



**HAL**  
open science

# Elaboration of thin nanocomposite layers based on Ag nanoparticles embedded in silica for controlled biocide properties

Alessandro Pugliara

► **To cite this version:**

Alessandro Pugliara. Elaboration of thin nanocomposite layers based on Ag nanoparticles embedded in silica for controlled biocide properties. Micro and nanotechnologies/Microelectronics. Université Paul Sabatier - Toulouse III, 2016. English. NNT : 2016TOU30324 . tel-01701079

**HAL Id: tel-01701079**

**<https://theses.hal.science/tel-01701079>**

Submitted on 5 Feb 2018

**HAL** is a multi-disciplinary open access archive for the deposit and dissemination of scientific research documents, whether they are published or not. The documents may come from teaching and research institutions in France or abroad, or from public or private research centers.

L'archive ouverte pluridisciplinaire **HAL**, est destinée au dépôt et à la diffusion de documents scientifiques de niveau recherche, publiés ou non, émanant des établissements d'enseignement et de recherche français ou étrangers, des laboratoires publics ou privés.



Université  
de Toulouse

# THÈSE

En vue de l'obtention du

## DOCTORAT DE L'UNIVERSITÉ DE TOULOUSE

Délivré par :

Université Toulouse 3 Paul Sabatier (UT3 Paul Sabatier)

---

**Présentée et soutenue par :**

**Alessandro PUGLIARA**

Le mardi 27 septembre 2016

**Titre :**

Elaboration of nanocomposites based on Ag nanoparticles embedded in dielectrics for controlled bactericide properties

---

ED SDM : Nano-physique, nano-composants, nano-mesures - COP 00

**Unité de recherche :**

CEMES (UPR 8011) et LAPLACE (UMR 5213)

**Directeur(s) de Thèse :**

Caroline BONAFOS (Directrice de Recherche CNRS, CEMES Toulouse)

Kremena MAKASHEVA (Chargée de Recherche CNRS, LAPLACE Toulouse)

**Rapporteurs :**

Francesco FRACASSI (Professeur, Université de Bari, Italy)

David HORWAT (Maître de Conférences, Université de Lorraine)

**Autre(s) membre(s) du jury :**

Fabrice GOURBILLEAU (Directeur de Recherche CIMAP Caen), Enrique NAVARRO (Senior Scientist IPE-CSIC Sarragose, Spain), Christine ROQUES (Professeure Université Paul Sabatier Toulouse), Nathalie TARRAT (Chargée de Recherche CEMES Toulouse), Christophe VIEU (Professeur INSA Toulouse)







# Remerciements

---

Cette aventure a commencé il y a 4 ans. Après l'obtention du diplôme de master, je ne pensais pas me retrouver en France pour faire un doctorat. Grâce à une série de coïncidences, j'ai eu la chance d'être pouvoir commencer cette expérience exceptionnelle. Le début de la thèse était difficile car cette activité exige beaucoup d'efforts et, en plus, je me suis retrouvé dans un pays étranger où je ne connaissais pas du tout la langue. A la fin, je suis arrivé à obtenir ma thèse grâce au soutien de toutes les personnes que j'ai rencontrées au cours de ce parcours. Pour cette raison, je tiens à remercier tous ces gens qui m'ont aidé à surmonter les obstacles que j'ai rencontrés pendant la thèse.

Je remercie mes directrices de thèse, Caroline Bonafos et Kremena Makasheva, qui ont me donné la possibilité de travailler dans deux prestigieux laboratoires qui sont au top dans leurs domaines, le CEMES pour la microscopie électronique en transmission (MET) et le LAPLACE pour la physique du plasma. Je voudrais leur remercier énormément pour la patience que vous avez eue avec moi, pour le temps que vous m'avez dédié, pour la confiance que vous m'avez donnée, pour les connaissances que vous m'avez transmises pendant ces inoubliables années de travail dans la recherche (merci, merci et merci encore à l'infini...).

Je voudrais remercier Monsieur Francesco Fracassi, Professeur de l'Université de Bari en Italie, et à Monsieur David Horwart, Maître de Conférences de l'Université de Lorraine en France, qui ont bien voulu accepter d'être mes rapporteurs. J'adresse mes remerciements aussi à Madames Christine Roques et Nathalie Tarrat à la fois pour avoir fait partie de mon jury de thèse et pour les discussions intéressantes et les échanges scientifiques qui m'ont permis d'élargir mes connaissances scientifiques. Egalement, je remercie Messieurs Fabrice Gourbilleau et Christophe Vieu pour m'avoir fait l'honneur d'être membres de mon jury de thèse.

En particulier, je tiens à remercier Enrique Navarro non seulement pour être membre de mon jury de thèse, mais aussi pour m'avoir accueilli à l'Instituto Pirenaico de Ecología de Saragosse et, en particulier, accompagné, guidé et soutenu avec ses précieux conseils pour aborder l'aspect le plus complexe de l'objet de la thèse, à savoir l'évaluation de la toxicité de mes nanostructures. Dans ce contexte, je voudrais remercier Maria Carmen Sancho Molina qui était un point de référence important qui m'a permis de développer mes compétences dans l'analyse de la toxicité de mes échantillons. Je lui remercie aussi pour les discussions approfondies et très enrichissantes, ses conseils et les explications particulières et détaillées sur les procédés de culture des algues qui ont rendu facile et claire une discipline aussi complexe que l'écotoxicologie. Merci, aussi, à Selene Muñiz pour m'avoir aidé plusieurs fois avec les algues et Alberto Barcos et Mercedes Garcia pour m'avoir accueilli dans leur bureau. Egalement, je remercie Yolanda Echegoyen pour sa disponibilité à analyser un nombre

"énorme" des échantillons avec les mesures de spectrométrie de masse. En fin, dans cette section, je voudrais remercier Jurgen Peci, Emna Zarrouk et Yosr Snoussi pour les très beaux moments passés ensemble à Zaragoza dans le week end.

Maintenant je voudrais remercier les différentes personnes qui j'ai rencontré dans les deux laboratoires au cours de cette expérience.

Je tiens à remercier la grande famille du CEMES qui m'a accueilli chaleureusement:

En particulier, je voudrais remercier beaucoup, tout d'abord, les personnes avec lesquelles j'ai travaillé en étroite collaboration. Merci donc à Robert Carles qui m'a régulièrement aidé avec ses précieux conseils et avec lequel j'ai eu l'honneur et le plaisir de discuter plusieurs fois de secrets de la plasmonique; Béatrice Pécassou qui m'a montré les mystères de monsieur *Implanter*, m'a aidé dans l'élaboration des échantillons, qui m'a permis d'améliorer mon français grâce à ses très agréables conversations que on a échangé, m'a « soutenu » avec ses très bonnes gâteaux quand j'ai été déçus à cause des difficultés dans la rédaction et à partir de laquelle j'ai appris le super proverbe « Le mieux est l'ennemi du bien » qui, maintenant, est très très très utile dans mon actuel travail (donc, merciiii Bea); Assia Haj-Salem qui était ma historique collègue de bureau du début et jusqu'à la fin de la thèse, m'a encouragé dans les moments difficiles; Maxime Bayle pour les simulations faites sur les spectres optique e pour le temps qui m'a dédié pour me enseigner à utiliser le model de la simulation développé au CEMES; Gérard Benassayag avec lequel j'ai eu le plaisir de discuté plusieurs fois sur le principe de l'implantation ionique; Adnen Mlayah qui m'a dédié du temps pour faire les mesures Raman sur mes échantillons.

Je remercie Cathy Crestou et Robin Cours qui m'ont enseigné une partie de la technique de préparation des échantillons MET. Merci aussi Dominique Lamirault du service prépa (maintenant je dois apprendre comme tu prépares les échantillons!).

Je tiens à remercier Cecile Marcelot, Sebastien Joulie et Florent Houdellier du service Microscopie qui m'ont accompagné à la découverte du monde de la microscopie électronique en transmission. Je voudrais aussi remercier, en particulier, Florent de m'avoir transmis sa passion pour cette incroyable technique (merciiii, Super Florent!). Merci encore à Cecile qui m'a donné beaucoup des conseils dans différences domaine (thèse, TP, concours ...).

Merci à Olivier Bancilhon, Jean-Noel Fillon et Christophe Collard du service informatique et à Mireille Trupin et Aurore Pruvost de l'administration.

Je voudrais aussi remercier toutes les chercheurs que j'ai eu le plaisir de rencontrer au labo mais avec qui, malheureusement, je n'ai pas beaucoup travaillé. Donc, merci à Marc Legros, Etienne Snoeck, Arnaud Arbouet, Joël Douin, Frederic Momprou, Muriel Hantcherli, Magali Benoit, Magali Brunet,

Nikolay Cherkashin, Aurelien Massboeuf, Fuccio Cristiano, Jesse Groenen... Peut-être un jour on pourrait trouver l'occasion de travailler ensemble.

Ensuite, je voudrais remercier aussi tous les autres personnes que j'ai rencontrées dans les couloirs et pas forcément, c'est-à-dire, Aurelie Royal, Lionel Pettiti, Pierre Abeilhou, Sebastien Weber, Winnie Vultos, Philippe Salles, Nicolas Ratel-Ramond, Bruno Melet, Pascal paiva, Christian Pertel, Nicolas Bello, Soumaya Naanani, Maxime Vallet, Abdelouahed Lasfar, Arthur Lantreibecq, Zofia Trzaska, Victor Boureau, Chloe Bayon, Luis Alfredo Rodríguez, David Reyes, Delphine Sordes, Iman Abdallah...

Maintenant, je voudrais également remercier l'autre famille qui m'a accueilli à Toulouse de la même façon que le CEMES, c'est-à-dire, le LAPLACE:

Je remercie Bernard Despax pour les importants conseils qui m'a donné sur le plasma au long de ces années. Je voudrais aussi remercier les chercheurs de mon équipe, c'est-à-dire, Antoine Belinguer, Hubert Caquineau, Richard Clergereaux, Simon Dap, Nicolas Gherardi, Nicolas Naudé, Patrice Raynaud.

Merci à Rick Verhorf et Stefania Vitale (detta anche Cristina!) qui m'ont aidé dans l'intégration dans le laboratoire; Jeremy Barbé qui était mon collègue de bureau et avec lequel je beaucoup discuté. Merci aussi à collègues doctorant and post-doc Laurent Milliere, Raphael Cozzolino...

Je remercie toutes les personnes ingénieurs, administratifs, techniques du laboratoire, c'est-à-dire, Cédric Trupin, Benoit Lantin, Benoit Schlegel, Agnès Gaunie-Picart, Patrick Ferre...

Je tiens à remercier Maria Carmen Monje Lacombe qui j'ai eu le plaisir de rencontré seulement dans ma dernière année de thèse par rapport la partie de la thèse qui concerne les protéines. J'espère dans le futur de pouvoir travailler ensemble sur d'autre sujet de rechercher.

Je voudrais remercier aussi les collègues de l'INSA qui m'ont aidé dans la préparation de TP et avec lesquels j'ai passé des moments inoubliables pendant mon activité d'enseignement, c'est-à-dire, Michel Bonnet, Cathy Crouzet, Pier-Francesco Fazzini (e grazie infinite anche per i consigli per preparare il colloqui per il posto di IE), David Vignolles, Isabelle Braud, Sawsen Azaizia, Catherine Béraud, Helene Carrere, Pascal Gérard, Thomas Blon, Gaelle Bœuf, Patrick Ferre (maitre du prisme!), Sylvain Augé, Muriel Hantcherli.

Je tiens à remercier Maria Teresa Hungria Hernandez qui m'a ouvert la route vers ma future carrière de microscopiste.

Je remercie Marie Christine Lafont pour m'avoir transmis ses connaissances sur la métallurgie et sur les techniques MET.



Je voudrais remercier mon actuelle famille, à savoir, toutes les personnes que petit à petit je commence à connaître au CIRIMAT-ENSIACET et à l'UMS Castaing.

Ora vorrei fare dei brevi ringraziamenti alla piccola comunità di italiani che mi hanno sempre aiutato e incoraggiato incessantemente in questi quattro anni.

Un immenso grazie lo voglio esprimere a due incredibili ricercatori italiani, Francesco Ruffino (il mio buon capo siculo per cui ho un debito di riconoscenza infinito) e a Simona Boninelli, che mi hanno appoggiato e incoraggiato ad intraprendere questa lunga avventura.

Grazie tante alla piccola delegazione di italiani del LAPLACE, Francesco Gullo e Jacopo profili, con i quali ho passato delle indimenticabili serate. Grazie inoltre a l'ultimo componente appena arrivato in questa congregazione di italiani, ovvero Adriana Scarrangella, che mi ha tirato fuori dai guai nel momento della preparazione del mio orale di "soutenance".

Anche se ho deciso di ringraziarli per ultimi, loro sono i primi ad avermi aiutato e sostenuto in ogni momento del mio percorso di tesi e sono le persone con cui ho molto legato qui in francia, sto parlando di Marzia Carrada, Patrick Benzo, Roberta Ruffilli e Giuseppe Caruso. Un infinite grazie a tutti loro.

Un profondo ringraziamento va ai miei amici fraterni che hanno sopportato tutte le mie lagne durante questi anni e senza i quali non sarei mai riuscito ad essere quello che sono oggi! Sto parlando di Francesca Inghilterra e Salvatore Messina, ovvero, due fratelli acquisiti. Senza dimenticare i rispettivi compagno o compagna, Dino Guarnaccia e Roberta Lavore, i quali mi hanno sempre sostenuto in questo percorso.

Un grosso grazie lo devo soprattutto ai miei cari amici Giuseppe Insolia, Eugenia Piselli, Angelo Fortuna e Lucia Calafiore. Loro sono i miei forti legami siculi!

Un grazie anche a Valentina Musumeci che per qualche tempo è stata una collega al CEMES ed, insieme agli altri siculi, abbiamo passato delle super serate tolosiane.

Infine voglio ringraziare la mia famiglia ovvero mia madre e mio padre che nonostante l'età avanzata sono venuti a vedere la difesa della mia tesi. Grazie a loro, oggi ho raggiunto questo importante traguardo, DOTTORE! Inoltre ringrazio i miei cari fratelli Fabrizio e Sebastiano con i quali non ci vediamo spesso ma che mi supportano sempre. Allo stesso modo le mie splendide cognate Alessandra e Irene e i miei super nipoti Riccardo e Gioele.

# List of Acronyms

---

This thesis involves different scientific domains in which a lot of acronyms are used. The used acronyms are summarized below to facilitate the reading of the text by readers.

<b>AC</b> Alternative Current	<b>PECVD</b> Plasma Enhanced Chemical Vapor Deposition
<b>AgNP</b> Silver NanoParticle	<b>PEG</b> PolyEthylene Glycol
<b>BF</b> Bright Field	<b>PL</b> PhotoLuminescence
<b>BSA</b> Bovine Serum Albumin	<b>PVD</b> Physical Vapor Deposition
<b>CAH</b> Contact Angle Hysteresis	<b>PV-TEM</b> Plan View Transmission Electron Microscopy
<b>C-FEG</b> Cold Field Emission Gun	<b>RBS</b> Rutherford Back Scattering spectrometry
<b>DC</b> Direct Current	<b>RF</b> Radio Frequency
<b>DP</b> Diffraction Pattern	<b>ROS</b> Reactive Oxygen Species
<b>DsRed</b> <i>Discosoma</i> Recombinant Red Fluorescent	<b>SACTEM</b> Spherical Aberation Corrected Trasmision Electron Microscope
<b>EC</b> Effective Concentration	<b>SDS-PAGE</b> Sodium Dodecyl Sulphate PolyAcrylamide Gel Electrophoresis
<b>EELS</b> Electron Energy Loss Spectroscopy	<b>SERS</b> Surface Enhanced Raman Scattering
<b>EPS</b> Extracellular Polymeric Substance	<b>S-FEG</b> Schottky Field Emission Gun
<b>ERDA</b> Elastic Recoil Detection Analysis	<b>TEM</b> Transmission Electron Microscopy
<b>FTIR</b> Fourier Transform Infrared Spectroscopy	<b>TEOS</b> Tetraethoxysilane
<b>HMDSO</b> Hexamethyldisiloxane	<b>TO</b> Transvers Optic
<b>HREM</b> High Resolution Electron Microscopy	<b>ULE-IBS</b> Ultra Low Energy Ion Beam Synthesis
<b>IBS</b> Ion Beam Synthesis	<b>ULE-II</b> Ultra Low Energy Ion Implantation
<b>ICP-MS</b> Inductively Coupled Plasma Mass Spectrometry	<b>XS-TEM</b> Cross Section Transmission Electron Microscopy
<b>LE-IBS</b> Low Energy Ion Beam Synthesis	
<b>LSPR</b> Localized Surface Plasmon Resonance	
<b>NP</b> NanoParticle	
<b>O.D.</b> Optical Density	
<b>OES</b> Optical Emission Spectroscopy	
<b>PAM</b> Pulse Amplitude Modulation	



# Contents

---

REMERCIEMENTS .....	I
LIST OF ACRONYMS.....	V
CONTENTS .....	VII
RESUME ETENDU DE THESE EN FRANÇAIS .....	XI
INTRODUCTION.....	1
CHAPTER I: STATE OF THE ART.....	5
1. INTRODUCTION: BACTERICIDE ACTIVITY OF SILVER AND “NANOSILVER” .....	5
1.1 History of silver use in human life.....	5
1.2 Recent applications of Ag compounds and AgNPs as antimicrobial agent .....	6
2. ION BEAM SYNTHESIS (IBS) OF AGNPs IN SILICA MATRIX .....	7
2.1. Principles of Ion Beam Synthesis of nanostructures .....	7
2.1.1 Accumulation and supersaturation .....	8
2.1.2 Nucleation or early phase separation .....	8
2.1.3 Growth processes .....	9
2.2. High-fluence ion implantation: reaching far-from-equilibrium states .....	10
2.3. Ion beam (direct) synthesis of AgNPs in SiO <sub>2</sub> matrix .....	11
2.3.1. Conventional energy ion beam synthesis.....	11
2.3.2. Low Energy Ion Beam Synthesis (LE-IBS) .....	11
2.3.3. Previous work at CEMES.....	12
3. PLASMA DEPOSITION TECHNIQUES FOR SYNTHESIS OF AGNPs IN SILICA MATRIX.....	14
3.1. Generalities on plasmas and in particular of RF capacitively-coupled discharges .....	15
3.1.1. Density of species .....	16
3.1.2. Plasma frequency .....	16
3.1.3. Plasma potential $V_p$ and electrostatic sheaths .....	17
3.1.4. Self-bias potential $V_{dc}$ of the RF electrode .....	18
3.2. Sputtering in an axially-asymmetric RF discharge.....	18
3.3. Elaboration of silica layers by PECVD .....	19
3.4. Elaboration of nanocomposite thin layer containing of AgNPs nanocomposite using plasma processes. Previous work at LAPLACE .....	22
4. AGNPs REACTIVITY IN DIFFERENT ENVIRONMENTS.....	25
4.1. Life-cycle of AgNP and alteration of AgNPs in the environment .....	25
4.2. Interaction of AgNPs with ambient air .....	26
4.2.1. Silver oxidation mechanism, from Ag <sup>0</sup> to Ag <sup>+</sup> .....	26
4.2.2. Silver sulfidation mechanism.....	29
4.3. Interaction of AgNPs with water .....	30
4.3.1. Phenomena affecting AgNPs dissolution in water .....	30
4.3.2. Phenomena affecting AgNPs dissolution in water .....	31
4.3.3. Implication of AgNPs sulfidation in the Ag <sup>+</sup> release .....	33
4.3.4. Interaction between AgNPs and chloride.....	34
4.3.5. Aggregation state of AgNPs.....	34
5. INTERACTION BETWEEN AGNPs AND MICRO-ORGANISMS .....	34
5.1. Structural parameters of AgNPs influencing the antimicrobial activity of silver.....	34
5.1.1. Effect of the NP size on the antimicrobial activity of silver .....	35
5.1.2. Effect of the shape and crystalline direction.....	37
5.1.3. Nature of nanoparticle shell.....	38

5.1.4. Effects of exposure medium on AgNPs antimicrobial activity.....	39
5.2. <i>Interaction between Ag and microorganisms: the particular case of green algae Chlamydomonas reinhardtii</i> .....	40
5.3. <i>Interaction between AgNPs and proteins</i> .....	42
5.3.1. Proteins properties affecting their interaction with solid surface .....	42
5.3.2. Surface properties related to proteins absorption.....	43
6. OPTICAL PROPERTIES OF AGNPs .....	44
6.1. <i>Electronic properties of noble metals</i> .....	44
6.2. <i>Optical properties of noble metals (bulk Electronic properties of noble metals)</i> .....	46
6.2.1. Drude model.....	46
6.2.2. Intraband and interband transitions in noble metals.....	47
6.3. <i>Optical response of noble metal nanoparticles</i> .....	48
6.3.1. Size effect .....	49
6.3.2. Localized Surface Plasmon Polariton (LSPP).....	50
6.3.3. Absorption and diffusion cross-sections .....	52
6.4. <i>Use of embedded AgNPs for SERS substrates</i> .....	53
7. CONCLUSIONS .....	55
<b>CHAPTER II: EXPERIMENTAL TECHNIQUES .....</b>	<b>57</b>
1. ION IMPLANTATION .....	57
1.1. <i>Basics of Ion Implantation</i> .....	57
1.2. <i>Ion Implanter</i> .....	58
1.3. <i>Ion Beam Synthesis</i> .....	58
2. PLASMA PROCESSES.....	60
2.1. <i>Plasma reactor description</i> .....	60
2.2. <i>Monitoring of the plasma process by OES</i> .....	62
2.3. <i>Experimental procedure for the elaboration of embedded AgNPs by plasma deposition process</i> .....	63
3. TRANSMISSION ELECTRON MICROSCOPY .....	64
3.1. <i>Image formation in a TEM</i> .....	65
3.2. <i>Conventional Bright Field TEM</i> .....	66
3.3. <i>High Resolution Electron Microscopy (HREM)</i> .....	67
3.4. <i>Specimen preparation</i> .....	68
4. OPTICAL BASED TECHNIQUES .....	68
4.1. <i>Fourier Transform InfraRed spectroscopy (FTIR)</i> .....	68
4.2. <i>Raman spectroscopy</i> .....	70
4.3. <i>Optical reflectance spectroscopy</i> .....	71
4.3.1. Reflectance definition .....	72
4.3.2. Experimental spectrophotometer .....	72
4.3.3. Characteristic reflectance spectrum of a thin silica layer on Si substrate and interest of using antireflective layers .....	73
4.4. <i>Ellipsometry</i> .....	75
5. ALGAE CULTURE.....	76
5.1. <i>Algae preparation</i> .....	76
5.2. <i>Turbidity and Optical Density</i> .....	77
6. PRINCIPLE OF FLUOROMETRY .....	79
6.1. <i>Principle of fluorometry</i> .....	79
6.2. <i>Procedure to evaluate released silver by fluorometry measurements</i> .....	80
6.3. <i>Concentration-response curves</i> .....	82
7. INDUCTIVELY COUPLED PLASMA MASS SPECTROMETRY (ICP-MS) .....	83

<b>CHAPTER III: CONTROLLED ELABORATION OF AGNPS EMBEDDED IN DIELECTRIC MATRIX BY PLASMA PROCESS</b>	<b>85</b>
1. INTRODUCTION.....	85
2. PLASMA DEPOSITION PROCESS.....	85
3. PLASMA SILICA ( $\text{SiO}_2^{\text{PLASMA}}$ ) COVER LAYER.....	88
4. STRUCTURAL AND OPTICAL PROPERTIES OF THE DEPOSITED PLASMONIC STRUCTURES.....	91
5. TOWARDS ELABORATION OF PLASMONIC SUBSTRATES BY SIMULTANEOUS AG-SPUTTERING AND PLASMA POLYMERIZATION.....	96
6. CONCLUSIONS.....	97
<b>CHAPTER IV: FULLY PREDICTIVE MODELING OF ELLIPSOMETRIC SPECTRA DESCRIBING THE DIELECTRIC RESPONSE OF PLASMONIC SUBSTRATES.....</b>	<b>99</b>
1. INTRODUCTION.....	99
2. STUDIED SAMPLES.....	100
2.1. Ion Implantation.....	100
2.2. Plasma deposition process.....	101
3. DESCRIPTION OF THE THEORETICAL MODEL USED FOR SIMULATION OF PLASMONIC STRUCTURES.....	102
4. NUMERICAL PROCEDURE FOR THE SIMULATIONS.....	104
5. RESULTS AND DISCUSSIONS.....	106
5.1. Advantages of the model describing the dielectric response of plasmonic structures.....	106
5.2. Critical assessment of the applicability of the model.....	108
6. CONCLUSIONS.....	111
<b>CHAPTER V: ASSESSING BIO-AVAILABLE SILVER RELEASED FROM SILVER NANOPARTICLES EMBEDDED IN SILICA LAYERS USING THE GREEN ALGAE <i>CHLAMYDOMONAS REINHARDTII</i> AS BIO-SENSORS.....</b>	<b>113</b>
1. INTRODUCTION.....	113
2. EXPERIMENTAL.....	114
2.1. Synthetic procedures.....	114
2.2. Structural and optical characterization of the nanocomposite layer.....	116
2.3. Experimental procedure for silver release assessment.....	116
2.4. Inductively Coupled Plasma–Mass Spectrometry measurements.....	117
2.5. Algal culture.....	117
2.6. Fluorometry measurement.....	117
3. RESULTS AND DISCUSSION.....	118
3.1. Structural analysis: silver reservoir in nanocomposite layer.....	118
3.2. Silver release in water.....	122
3.2.1. ICP-MS analysis.....	122
3.2.2. TEM Analysis.....	123
3.2.3. Optical Analysis.....	124
3.3. Silver toxicity on algal photosynthesis.....	125
3.4. Proposed mechanisms for $\text{Ag}^+$ release: water molecules uptake in silica matrix.....	128
4. TOWARDS REUSABLE NANOCOMPOSITE SAMPLES: ASSESSMENT OF THE AG RELEASE FROM ALREADY USED NANOCOMPOSITES.....	130
5. CONCLUSIONS.....	131
<b>CHAPTER VI: PHYSICO-CHEMICAL CHARACTERIZATION OF THE INTERACTION OF RED FLUORESCENT PROTEIN - DSRED WITH THIN SILICA LAYERS CONTAINING AGNPS.....</b>	<b>133</b>
1. INTRODUCTION.....	133
2. EXPERIMENTAL CONDITIONS.....	134
2.1. $\text{SiO}_2$ thin film preparation.....	134
2.2. DsRed protein and preparation procedure.....	135
2.3. Deposition of DsRed proteins on the silica layers containing or not AgNPs.....	136

3. STUDY OF THE INTERACTION DSRED/SiO <sub>2</sub> SURFACES.....	136
3.1. Adsorption and optical properties of DsRed sessile droplets.....	136
3.2. On the possibility to perform FTIR analysis of dehydrated DsRed adsorbed on solid surfaces.....	140
4. PRELIMINARY RESULTS OF SERS EFFECT OF DSRED PROTEINS DEPOSITED ON AgNPs BASED PLASMONIC SUBSTRATES.....	142
4.1. Selection of samples for the SERS study .....	142
4.2. Interaction of DsRed with thin silica layers with embedded AgNPs .....	144
4.3. SERS effect on DsRed proteins deposited on AgNPs based nanocomposites .....	145
5. CONCLUSIONS .....	146
<b>CONCLUSIONS AND OUTLOOKS.....</b>	<b>147</b>
<b>REFERENCES.....</b>	<b>151</b>
<b>SCIENTIFIC PRODUCTION.....</b>	<b>175</b>

# Résumé étendu de thèse en Français

---

Au cours des vingt dernières années, il y a eu une augmentation rapide dans le développement, la production et l'application des nanomatériaux manufacturés, qui jouent actuellement un rôle croissant dans de nombreux domaines, y compris les produits de consommation liés à divers secteurs: la santé, la cosmétologie, l'agriculture, l'alimentation, l'environnement, la communication, le transport et l'énergie [Peralta-Videa et al., 2011]. Ces nanomatériaux pourraient apporter des solutions aux défis technologiques dans les domaines de la conversion de l'énergie solaire, de la catalyse, de la médecine, et de l'eau, et du traitement de l'air à des fins de purification [Sharma et al., 2009]. Il est largement admis que l'émergence des matériaux à l'échelle nanométrique est due à leur grand rapport surface/volume et à leurs propriétés physiques exceptionnelles.

L'exemple le plus souvent cité concernant les nanoparticules métalliques et leur utilisation dans les applications industrielles est celui des nanoparticules d'argent (AgNPs). Les AgNPs sont bien connues non seulement pour leur activité chimique, mais aussi pour leurs propriétés plasmoniques. En effet, elles sont la meilleure antenne pour amplifier des signaux électroniques et vibratoires locaux à l'échelle nanométrique dans le domaine visible, fournissant des informations moléculaires uniques en champ lointain. Depuis sa découverte en 1974 sur les molécules de pyridine adsorbées sur des surfaces rugueuses d'argent, la Spectroscopie Raman Exaltée de Surface (SERS) s'est révélée être une technique analytique puissante pour la spectroscopie moléculaire, la reconnaissance biomoléculaire et la détection ultra-sensible (jusqu'à la molécule unique). Toutefois, la limitation dans la fabrication de substrats SERS reste un inconvénient majeur pour les applications potentielles.

En ce qui concerne leur activité chimique, les AgNPs ont montré la plus grande efficacité antimicrobienne contre les bactéries, les virus et autres micro-organismes eucaryotes. Elles sont maintenant présentes dans une gamme croissante de produits industriels [Silver et coll., 2006 ; Le Ouay et Stellacci, 2015]. Le "Nano-argent" est d'ailleurs une marque déposée (Samsung Company, 2003). AgNPs sont utilisées comme nouvelle génération de produits antimicrobiens dans les réfrigérateurs, les climatiseurs, les claviers d'ordinateurs, etc. [Rai et al., 2009]. Elles sont également exploitées pour leurs propriétés antimicrobiennes afin d'empêcher l'encrassement par les algues [Russell et Hugo, 1994]. Bien que certains de ces effets sont connus depuis l'Antiquité et que le nombre d'industries utilisant AgNPs dans leurs produits est en très forte augmentation de nos jours, les mécanismes exacts au niveau moléculaire de leurs effets sont encore mal compris.

Les applications les plus répandues des nanocomposites à base de AgNPs concernent les revêtements antibactériens. Il est généralement admis que l'adhésion microbienne représente une complication majeure pour toutes les applications biomédicales. Afin d'inhiber le développement d'un biofilm sur une surface, une possibilité consiste à utiliser des revêtements contenant un agent antibactérien comme les AgNPs, qui sont d'excellents candidats pour préserver simultanément une grande efficacité



antibactérienne et une exaltation importante des signaux vibratoires et luminescents provenant de molécules situées dans leur voisinage. C'est précisément cette ambivalence que nous souhaitons exploiter au moyen de couches diélectriques spécifiques contenant des AgNPs.

Les objectifs de cette thèse sont de développer des nanocomposites multifonctionnels à base de AgNPs enrobées dans un diélectrique permettant la libération contrôlée de l'agent antibactérien. Cela devrait permettre à la fois de cibler le type de micro-organisme à combattre et délivrer la bonne dose pour son inhibition, tout en préservant la microflore environnante. Pour atteindre ces objectifs, nous proposons d'utiliser la multifonctionnalité des AgNPs, qui sont à la fois des antennes plasmoniques pour détecter l'interaction avec les micro-organismes et des réservoirs d'ions connus pour leurs propriétés antibactériennes. Afin de stabiliser les nanoparticules et de contrôler la dose toxique (à savoir la concentration en ions  $\text{Ag}^+$  relargués) les AgNPs seront intégrées dans des matrices diélectriques. Les AgNPs dont la taille et la densité seront ajustées, seront positionnées à des distances variables de la surface du substrat, sur lequel les micro-organismes adhèrent.

Pour atteindre ces objectifs, deux étapes préalables sont demandées:

- (i) Evaluer la capacité des AgNPs enrobées dans les diélectriques à libérer des quantités contrôlées d'Ag ionique ( $\text{Ag}^+$ ) et / ou d'AgNPs, responsables de l'effet biocide. Cette étape constitue le cœur de ce travail de thèse. L'originalité de notre approche est double. Elle est d'abord basée sur l'ingénierie rationnelle de ces nanocomposites à base d'AgNPs: les nanoparticules sont incorporées dans des matrices diélectriques qui permettront un contrôle précis de la libération d'Ag en contrôlant les caractéristiques structurales des NPs. En second lieu, la libération d'Ag est évaluée par une méthode originale utilisant des algues vertes comme biocapteurs. Ainsi, la toxicité à court terme de AgNPs sur la photosynthèse des *Chlamydomonas reinhardtii* sera étudiée en utilisant la fluorométrie et la libération d'argent sera mesurée par spectrométrie de masse à plasma par couplage inductif (ICP-MS).
- (ii) Effectuer une analyse détaillée de la localisation et des interactions des molécules et des protéines déposées sur la surface de ces substrats contenant AgNPs enterrées en utilisant l'imagerie optique et les spectroscopies moléculaires. Cette étape sera initiée dans le dernier chapitre de ce manuscrit.

Ce travail, réalisé en co-direction entre CEMES et LAPLACE, est à l'interface entre la science des matériaux et de la biologie.

Le **chapitre I** rassemble l'état de l'art des différentes facettes qui constituent ce travail: l'élaboration des nanocomposites à base d'AgNPs en utilisant des méthodes physiques, l'interaction des AgNPs avec leur environnement (air et eau), l'activité biologique des AgNPs et leur propriétés optiques (plasmonique).

Les dispositifs expérimentaux principaux (élaboration et caractérisation) et les techniques utilisées au cours de cette thèse sont décrits dans le **chapitre II**.

Deux approches physiques ont été utilisées pour élaborer ces nanocomposites: (i) l'implantation ionique à basse énergie (LE-IBS) et (ii) la pulvérisation combinée à la polymérisation plasma. Ces techniques permettent l'élaboration d'une couche unique de AgNPs incorporées dans des films de silice, à des distances définies nanométriques (0-7 nm) au-dessous de la surface libre. La première technique (LE-IBS de AgNPs incorporées dans des couches de silice) a été développée au CEMES dans un précédent travail [Carles et al., 2009; Benzo et al, 2013], mais la quantité d'Ag qui peut être introduite dans le diélectrique est limitée, ce qui limite donc la taille, la densité et la fraction surfacique des AgNPs formées. C'est pour cette raison, qu'une technique complémentaire basée sur le dépôt par plasma a été développée dans ce travail à LAPLACE et est présentée dans le **chapitre III**.

Les propriétés structurales et optiques des nanocomposites ont été étudiées par microscopie électronique à transmission, spectroscopie de réflexion et ellipsométrie. Cette dernière technique, couplée à une modélisation basée sur l'approximation quasi-statique du formalisme classique de Maxwell-Garnett, a permis la détection de petites variations dans la taille et la densité des AgNPs. La potentialité de cette technique pour caractériser notre système est traitée dans le **chapitre IV**.

Le **chapitre V** est le cœur de ce travail et décrit la capacité de nos AgNPs enrobées à libérer des ions  $\text{Ag}^+$  lorsque les nanocomposites sont immergés dans l'eau. Pour cette évaluation, une méthode originale est présentée, ce qui utilise des algues vertes comme biocapteurs. Ce travail a été effectué à l'Instituto Pirenaico de Ecología (IPE-CSIC) à Saragosse (Espagne) au cours de 2 séjours d'un mois chacun.

Une dernière partie de ce travail, décrite dans le **chapitre VI**, est consacrée à l'étude des propriétés de stabilité et d'adsorption de protéines fluorescentes *Discosoma* rouge (DsRed) sur ces surfaces diélectriques. Ce travail a été réalisé en étroite collaboration avec le Laboratoire de Génie Chimique (LGC) à Toulouse.

Nous présentons dans ce résumé étendu les principaux résultats de cette thèse décrits dans les chapitres III, IV, V et VI du manuscrit.

Une première étape de cette thèse concerne donc **la synthèse par voie physique de ces nanocomposites**. Le but est d'élaborer des structures nanocomposites de  $\text{SiO}_2$  / AgNPs /  $\text{SiO}_2$  / Si (avec une seule couche de AgNPs, de taille, densité et distances entre nanoparticules bien contrôlées, et insérée dans une matrice  $\text{SiO}_2$  à une distance donnée de la surface). L'épaisseur de la couche de

silice incluant les NPs a été choisie de façon à ce que, pour des longueurs d'onde spécifiques, la réflectivité soit minimale, et par conséquent le champ électrique à la surface libre maximum.

La première technique de fabrication de AgNPs enrobées dans une matrice de silice utilisée dans ce travail est l'implantation ionique à basse énergie (ULE-IBS). Elle a été développée au CEMES dans le cadre de travaux antérieurs. Elle permet la synthèse d'un seul plan ("delta-layer") de AgNPs enterré près de la surface libre d'une couche de SiO<sub>2</sub> thermique que l'on a fait croître sur une plaquette de Si [Carles et al., 2009]. Sur la figure 1 (à gauche), une image typique de Microscopie Electronique en Transmission (MET) d'une coupe transverse (XS-MET) d'un échantillon implanté révèle la présence de AgNPs sous la forme d'un plan unique situé à quelques nanomètres sous la surface. Comme prévu, ces particules se forment au cours du processus d'implantation, sans la nécessité d'un recuit additionnel. Cela est dû au fort coefficient de diffusion de l'Ag dans la silice. Les AgNPs sont sphériques, cristallines, réparties de façon homogène et en argent pur, comme révélé par l'observation en Microscopie Electronique à Haute Résolution (MEHR, encart de la Fig.1). Elles sont réparties de façon homogène. En utilisant cette technique, différentes architectures à trois dimensions composées de AgNPs noyées dans la silice ont été ainsi conçues pour exploiter simultanément le phénomène d'interférence optique dans les milieux stratifiés et la résonance plasmon de surface (LSPR) de nanoparticules métalliques [Carles et al., 2011]. Ces structures sont basées sur un contrôle simultané des propriétés optoélectroniques à trois échelles (3S) (~ 2 / 20 / 200 nm) et le long des trois directions de l'espace (3D). En particulier, l'épaisseur de la couche diélectrique a été choisie pour avoir des propriétés antireflets imposant un maximum du champ électrique à proximité de la surface.

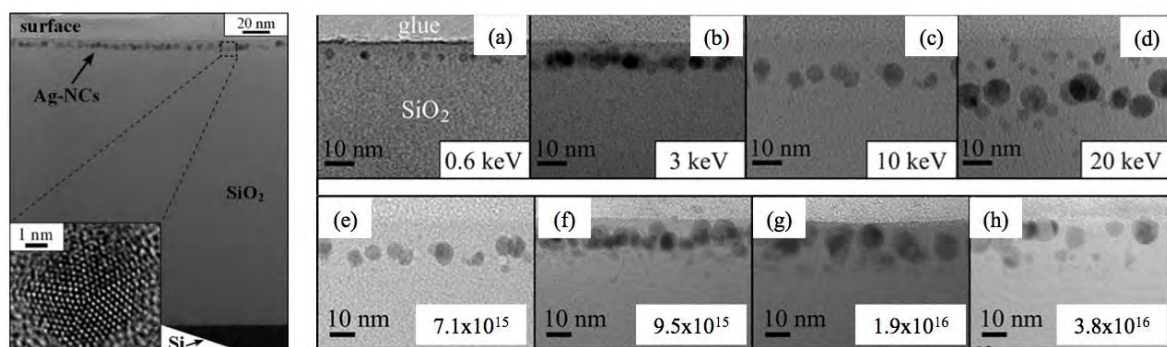


Figure 1: Côté gauche: image MET en champ clair (XS-MET) et vue sur la tranche d'un plan de AgNPs élaboré par ULE-IBS (énergie 3 keV et dose  $4,7 \times 10^{15}$  ions/cm<sup>2</sup>) avec en insert une image MEHR d'une AgNP. Côté droit: zoom d'images XS-MET des échantillons implantés (a) à (d) avec une énergie croissante et des doses conduisant à une concentration fixe de 20% atomique et (e) à (g) une faible énergie d'implantation (10 keV) et des doses croissantes. De [Benzo et al., 2013].

Contrôler l'énergie cinétique des ions implantés dans la gamme de la basse énergie offre la possibilité de contrôler à l'échelle nanométrique le positionnement sous la surface du plan des nanoparticules métalliques. Ainsi, la distance des NPs à la surface peut être variée entre 3,5 et 12 nm lorsque l'énergie d'implantation augmente de 0,6 à 10 keV (Fig. 1, du côté droit, (a) à (c)). Ces valeurs sont en bon

accord avec les valeurs théoriques du maximum (rang projeté,  $R_p$ ) du profil implanté calculé par TRIDYN [Möller et Eckstein, 1984]. L'augmentation supplémentaire de l'énergie d'implantation conduit à un élargissement du profil implanté et à la formation d'une bande de NPs spatialement réparties (Fig. 1 (d)). L'augmentation de l'énergie conduit également à une légère augmentation de la taille moyenne des particules de 2,5 nm à 4,9 nm, en raison d'un élargissement du profil d'implantation [Benzo et al., 2013].

Une saturation de la taille moyenne des AgNPs est clairement observée lorsque l'on augmente la dose d'implantation (Fig. 1(e) à (h)). En outre, la quantité d'Ag mesurée expérimentalement dans des nanoparticules à partir d'images MET est beaucoup plus faible que la dose nominale implantée, en particulier pour les doses élevées [Benzo et al., 2013]. Cette saturation est prédite dans la littérature par des simulations balistiques, et attribuée à la pulvérisation de surface et aux changements de stœchiométrie au cours de l'implantation [Stepanov et al., 2000; Stepanov, 2010]. Néanmoins, la dose maximale mesurée ici (environ  $10^{16}$  atomes/cm<sup>2</sup>) est beaucoup plus faible que celle prédite en utilisant le logiciel TRIDYN. Cet écart est la conséquence d'effets de diffusion. En effet, en plus de l'enrichissement en Ag dans la région proche de la surface en raison des effets balistiques, on observe une augmentation de la quantité d'Ag au voisinage de la surface due à la diffusion thermique de l'Ag. Les atomes d'Ag sont alors pulvérisés provoquant une diminution de la quantité totale de Ag dans la couche. À un certain point, les nanoparticules elles-mêmes sont pulvérisées par l'implantation en cours. [Benzo et al., 2013].

Il a ainsi été montré que l'implantation ionique à basse énergie était une technique prometteuse pour la fabrication d'un réseau 2D de AgNPs noyées dans une couche de silice. Le principal avantage de cette méthode reste l'incorporation directe des AgNPs dans une matrice diélectrique transparente, ce qui évite leur diffusion et leur altération, tout en préservant leurs propriétés plasmoniques et en gardant une surface plane et réutilisable. En particulier, un recuit post-implantation réduit fortement l'oxydation de l'argent, qui est la principale limitation pour l'utilisation de AgNPs déposées sur des surfaces [Benzo et al., 2011]. Néanmoins, la saturation de la quantité d'Ag introduite dans la matrice pour des doses élevées, limite le contrôle de la taille et de la fraction surfacique (et volumique) des AgNPs. Par conséquent, la synthèse d'AgNPs avec une taille moyenne supérieure à 10 nm et une fraction surfacique supérieure à 20% reste impossible avec cette méthode. Pour cette raison, nous avons développé dans cette thèse une nouvelle méthode, utilisant des techniques de dépôt de plasma, afin de fabriquer des AgNPs de taille moyenne > 10 nm noyées dans la silice à des distances nanométriques contrôlées de la surface, avec une fraction surfacique élevée (supérieure à 20%). Ce procédé implique la pulvérisation cathodique d'argent, suivie par le dépôt chimique à phase vapeur assisté par plasma, comme décrit dans la section suivante.

Les nanocomposites ont été élaborés en utilisant le dépôt physique en phase vapeur (PVD) comme première étape, et le dépôt chimique en phase vapeur assisté par plasma (PECVD) comme deuxième étape comme représenté sur la Fig. 2.

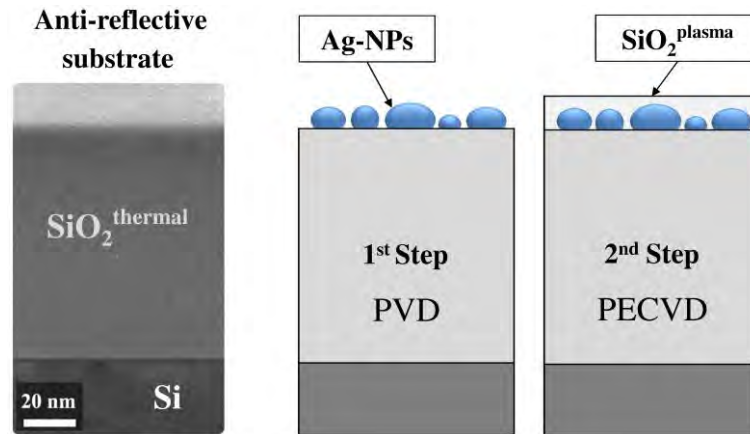


Figure 2: Elaboration d'un plan ("delta-layer") de AgNPs enrobées dans une matrice de SiO<sub>2</sub> par procédé plasma.

La figure 3 montre une image MET en champ clair en vue sur la tranche d'un échantillon élaboré par cette méthode. Il s'agit d'un plan de AgNPs déposé avec une puissance injectée  $P = 40$  W pour un temps de pulvérisation de  $t_s = 5$  sec et recouvert par une couche SiO<sub>2</sub> plasma d'épaisseur  $d_{\text{SiO}_2\text{plasma}} = 13$  nm (temps de dépôt pour la couche SiO<sub>2</sub> plasma,  $t_d = 60$  s). Les observations en MEHR (voir l'image en insert de la figure 3) montrent que les nanoparticules d'Ag sont cristallines et en argent pur. L'épaisseur totale de la structure est de 105 nm, qui remplit la condition anti-reflet.

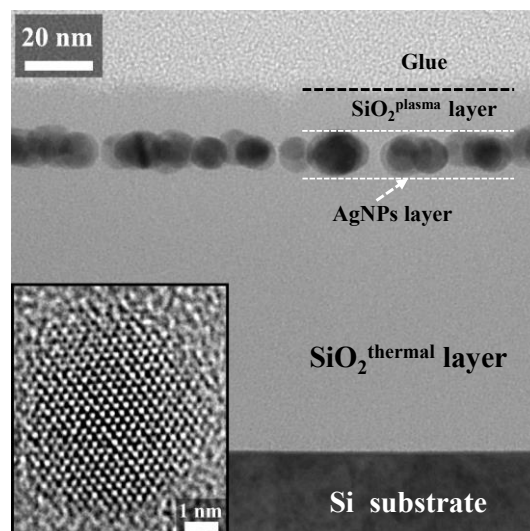


Figure 3: Image MET en champ clair en section transverse d'un échantillon élaboré par pulvérisation d'argent combinée au PECVD. Conditions:  $t_s = 5$  s,  $P = 40$  W ( $V_{cc} = -750$  V). Le temps de dépôt du SiO<sub>2</sub> plasma est  $t_d = 60$  s. En insert, image MEHR d'une nanoparticule d'Ag.

La taille, la densité et la forme des AgNPs varient avec la puissance injectée ou le temps de pulvérisation comme montré sur la figure 4. Lorsque le temps de pulvérisation est fixé, on observe en effet une augmentation de la taille et une diminution de leur densité, avec une surface de couverture à peu près constante. La même tendance est observée lorsque la puissance injectée est fixe et le temps de pulvérisation est augmenté. Pour un temps de pulvérisation fixé, l'augmentation de la puissance injectée modifie la forme des AgNPs de sphérique ( $P = 10 \text{ W}$ ) à sphéroïde ( $P > 60 \text{ W}$ ). L'augmentation du temps de pulvérisation de 5 s à 30 s n'influence pas la forme des AgNPs pour une faible puissance injectée ( $P = 10 \text{ W}$ ), alors qu'il conduit à dépasser le seuil de percolation pour la puissance injectée élevée ( $P = 80 \text{ W}$ ). Par conséquent, pour obtenir une couche unique de grandes AgNPs, une puissance injectée élevée et de courts temps de pulvérisation doivent être privilégiés.

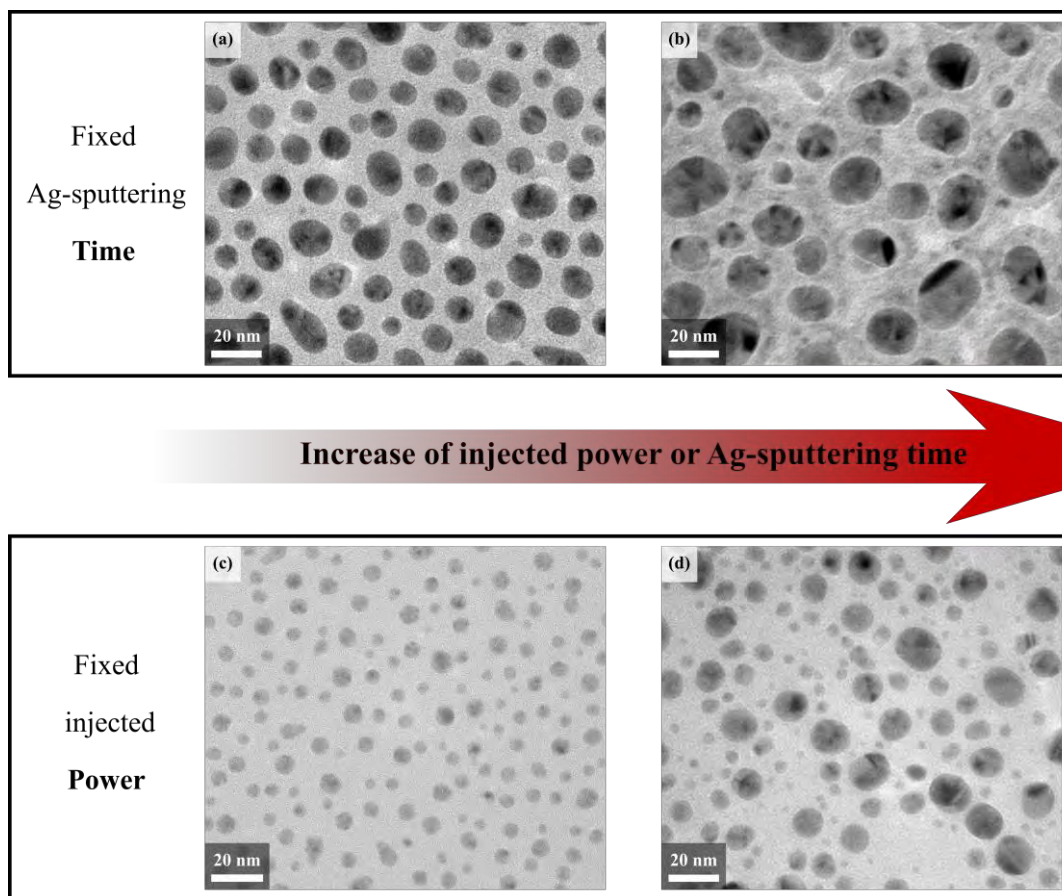


Figure 4. Images MET en vue plane observées en champ clair des substrats nanocomposites obtenus pour 2 puissances (a) 40W et (b) 80W et un temps de pulvérisation fixé  $t_s = 5 \text{ s}$ , et pour 2 temps (c) 10 s et (d) 30 s et une puissance injectée fixée  $P = 10 \text{ W}$ .

Un second défi dans l'élaboration de plasma de ces substrats est celle de la couche de couverture en  $\text{SiO}_2$ . Pour obtenir une couche  $\text{SiO}_2$  plasma ayant des propriétés proches d'une couche de silice thermique, la composition du plasma est ajustée en faisant varier le mélange gazeux. Ainsi, l'injection d'oxygène dans le mélange Ar-HMDSO du plasma introduit des espèces réactives qui favorisent l'oxydation des groupes méthyle et les espèces volatiles telles que l'eau et le dioxyde de carbone.

L'injection pulsée de HMDSO est une des originalités de ce procédé et permet un contrôle précis des paramètres du plasma. L'analyse par Spectroscopie Infra-Rouge à Transformée de Fourier (FTIR) de la couche de couverture en SiO<sub>2</sub> plasma ainsi élaborée montre une configuration proche de celle de la silice thermique.

Ainsi, nous avons montré comment les paramètres structuraux des nanostructures enterrées (taille, densité, distance à la surface) peuvent être contrôlés en réglant les conditions d'élaboration combinant pulvérisation d'argent et polymérisation plasma. En couplant ces échantillons à ceux élaborés par LE-IBS, nous avons maintenant deux techniques pour la fabrication d'une seule couche de AgNPs enrobées dans des couches minces de silice localisées à une distance nanométrique contrôlée sous la surface libre du diélectrique. Elles offrent la possibilité d'explorer différentes distributions de taille, densités surfaciques, et en particulier manipuler la distance de ces NPs à la surface libre.

Une fois les nanocomposites élaborés, nous nous sommes donc intéressés au développement, au test et à l'application d'un modèle prédictif pour l'interprétation des spectres ellipsométriques enregistrés sur les structures plasmoniques. L'ellipsométrie a en effet été utilisée comme technique de diagnostic efficace pour étudier ces systèmes nanostructurés et en particulier pour détecter de petites variations dans la taille et la densité des AgNPs.

Ce modèle est basé sur l'approximation quasi-statique du formalisme classique de Maxwell-Garnett, auquel est ajouté la prise en compte de l'effet de confinement électronique par l'intermédiaire du paramètre d'amortissement. Des échantillons ont été élaborés en utilisant: (i) l'implantation ionique à basse énergie et (ii) la polymérisation couplée à la pulvérisation cathodique. Le modèle permet l'extraction à partir des spectres ellipsométriques expérimentaux des caractéristiques de la population de NPs: taille moyenne, fraction volumique et distance de la couche de AgNPs à la surface libre de la matrice. La comparaison avec les résultats obtenus par microscopie électronique à transmission confirme l'applicabilité de ce procédé. Les limites de la méthode de diagnostic proposée ainsi que la poursuite du développement lié à la qualité de la comparaison entre les spectres générés par le modèle et les données expérimentales sont également abordés. Cet aspect de mon travail a été développé en étroite collaboration avec Maxime Bayle au cours de son doctorat au laboratoire CEMES.

La représentation schématique des structures plasmoniques modélisées est donnée sur la Fig. 5. Les structures plasmoniques sont considérées comme des systèmes multicouches. Chacune des couches est décrite par sa permittivité diélectrique. Les couches contenant des AgNPs sont considérées comme milieu effectif ayant donc une permittivité diélectrique effective. Cette hypothèse offre la possibilité de décrire par exemple la double couche de NPs avec des tailles et fractions volumiques différentes.

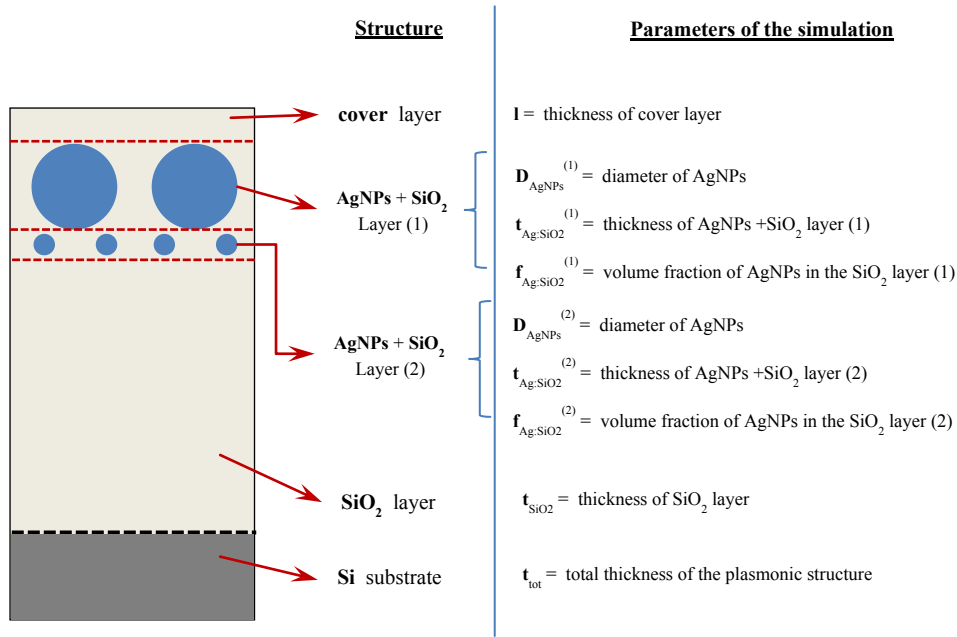


Figure 5: Représentation schématique des structures plasmoniques et des paramètres issus du modèle.

Cette structure stratifiée est bien adaptée pour tenir compte des différentes situations physiques qui peuvent survenir dans la représentation de l'empilement en fonction du type de procédé d'élaboration utilisé. Les propriétés diélectriques du substrat de Si ont été prises dans la référence [Palik, 1985] pour toute la gamme de longueurs d'onde, celles de la couche SiO<sub>2</sub> dans la base de données SOPRA [SOPRA Database, 1999] et la fonction diélectrique des AgNPs a été calculée selon l'équation (1) en utilisant les propriétés optiques de l'argent [Palik, 1985; Bayle, 2014].

$$\frac{\epsilon_{eff} - \epsilon_m}{\epsilon_{eff} + 2\epsilon_m} = \frac{N\alpha}{3\epsilon_m}. \quad (1)$$

Après l'introduction de la fraction volumique de AgNPs dans la matrice de silice  $f = NV$  et le remplacement de  $\alpha$  par son expression pour les NPs de forme sphérique ( $\alpha = 2$ ) [Garnett, 1904], on trouve l'expression générale de Maxwell-Garnett. Pour des fractions volumique suffisamment petites, la permittivité effective  $\epsilon_{eff}$  prend la forme:

$$\epsilon_{eff} = \epsilon_m + 3f\epsilon_m \frac{\epsilon_{NP} - \epsilon_m}{\epsilon_{NP} + 2\epsilon_m}. \quad (2)$$

avec  $\epsilon_{NP}$  qui représente la permittivité diélectrique des nanoparticules.

La réponse optique des métaux est affectée par trois caractéristiques principales: la taille, la forme et milieu environnant du métal [Kreibig et Vollmer, 1995; Maier, 2007]. La fonction diélectrique complexe des nanoparticules devient dépendante de la taille. En supposant que les nanoparticules sphériques métalliques, leur fonction diélectrique complexe peut être écrite suivant l'expression:

$$\epsilon_{NP}(\omega, D_{NP}) = \epsilon_{IB}(\omega) - \frac{\omega_p^2}{\omega^2 + i\gamma(D_{NP})\omega}, \quad (3)$$



où  $\varepsilon_{IB}(\omega)$  est la partie de la fonction diélectrique complexe due aux transitions interbandes dans les métaux massifs et  $\gamma(D_{NP})$  est liée au paramètre d'amortissement  $\gamma_b$  représentant les collisions des électrons avec d'autres électrons, avec le réseau cristallin (phonons), les défauts de réseau, ou des impuretés et prenant compte l'effet de la taille des nanoparticules. En conséquence, la dépendance de la fonction diélectrique avec la taille reste négligeable pour sa partie réelle tandis que sa partie imaginaire est fortement affectée.

Comme paramètres d'entrée dans le modèle nous commençons par faire des hypothèses sur les épaisseurs des différentes couches de la structure et les fractions volumiques des NPs. Après convergence des calculs de modélisation, les paramètres de sortie de la simulation sont répertoriés sur Fig. 5 ainsi que les spectres ellipsométriques ( $\tan(\Psi)$  et  $\cos(\Delta)$ ) dans la gamme de longueur d'onde 250-850 nm correspondant à la structure considérée. Ces spectres théoriques ont été comparés avec les spectres expérimentaux.

Le code numérique développé fonctionne sur le logiciel Matlab [Matlab, 2012] et utilise le formalisme d'Abélès pour le calcul du champ électrique dans les systèmes multicouches. Plus d'informations sur la modélisation et les hypothèses retenues peuvent être trouvées dans les références [Larivière et al., 1992; Poinsothe, 2006; Bayle, 2014].

Les spectres expérimentaux ont été acquis avec un ellipsomètre SOPRA GES5 dans la gamme de longueurs d'onde de 250 à 850 nm avec un angle d'incidence de  $75^\circ$ . Les paramètres des structures plasmoniques obtenues à partir de la modélisation ont été comparés de manière systématique aux résultats extraits des observations MET. La figure 6 montre les spectres ellipsométriques obtenus par modélisation superposés aux spectres expérimentaux sur l'échantillon implanté E1. L'image de MET en vue sur la tranche correspondant à cet échantillon est également montrée.

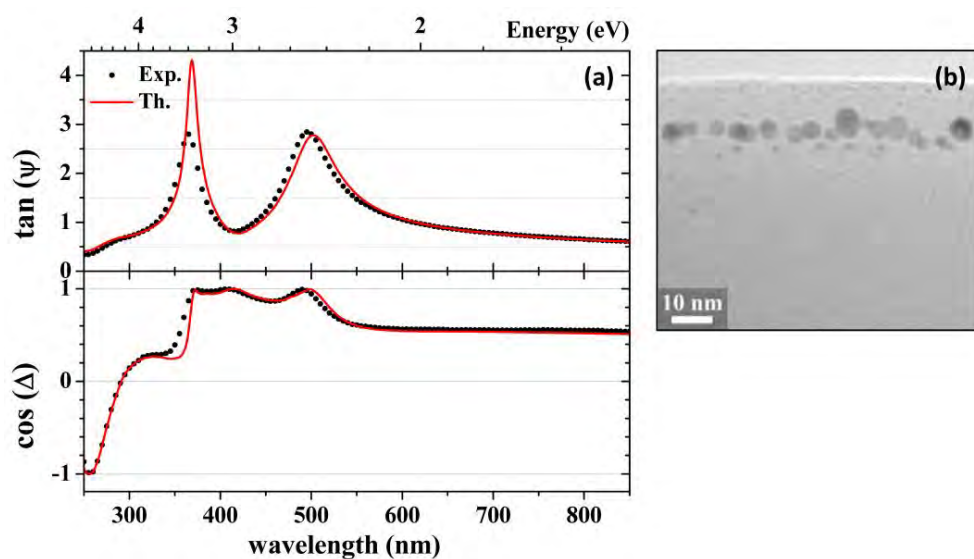


Figure 6 (a) Spectres d'ellipsométrie mesurés expérimentalement (points) et obtenus par modélisation (ligne rouge), et (b) images MET (champ clair) en vue sur la tranche de l'échantillon E1 implanté.

Les paramètres obtenus à partir de la modélisation et ceux mesurés sur les images MET sont résumés dans le Tableau 1. Une forte particularité de l'échantillon E1 est la présence d'un second plan de AgNPs en profondeur de l'échantillon. Dans ce cas, les couches constitutives de la structure modélisée sont au nombre de cinq, comme représenté sur la Fig. 5. Cet échantillon témoigne de la pertinence du modèle théorique développé.

Les spectres de la figure 7 correspondent à l'échantillon E3 déposé par plasma. La planéité de la couche de AgNPs dans ce cas permet de générer des spectres ellipsométriques identiques à ceux enregistrés expérimentalement. La très légère ondulation de la surface de l'échantillon imposée par le procédé de dépôt plasma ne conduit pas à la dépolarisation de la lumière incidente dans toute la gamme de longueurs d'onde.

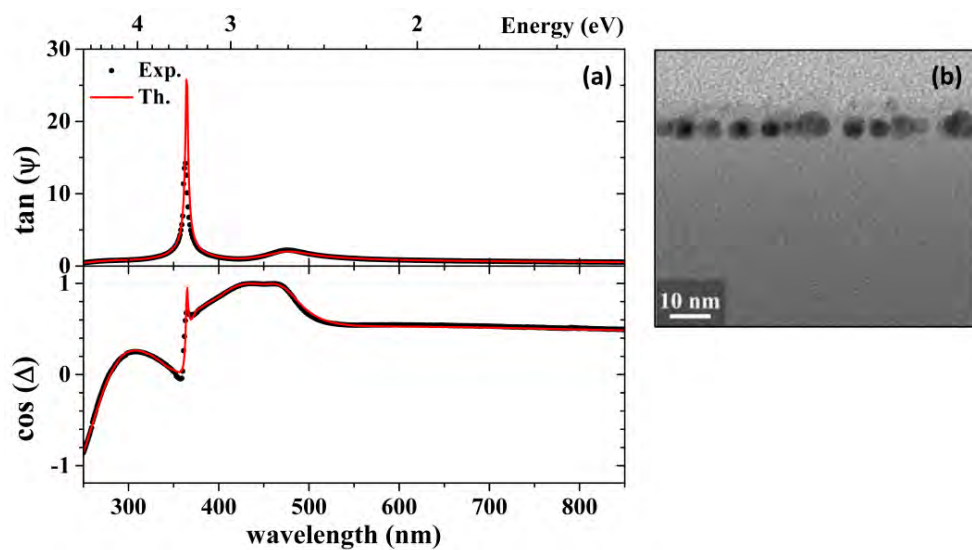


Figure 7: (a) Spectres d'ellipsométrie expérimentaux (points) et comme obtenus à partir de la modélisation (ligne rouge), et (b) images XS-MET en champ clair de l'échantillon E3 (dépôt plasma).

On peut remarquer l'excellent accord entre les paramètres décrivant les deux structures plasmoniques (E1 et E3) obtenus à partir de la modélisation des spectres ellipsométriques et ceux mesurés sur les images MET (tableau 1).

Le point commun de ces deux exemples est que leurs paramètres structurels satisfont complètement les hypothèses du modèle de Maxwell-Garnett. Les AgNPs sont de forme sphérique. Elles sont bien alignées dans un plan et ne forment qu'une seule couche dans laquelle l'épaisseur du milieu effectif peut être considérée comme égale au diamètre des AgNPs. La fraction volumique de AgNPs est suffisamment faible pour ne pas induire une forte modification du champ électromagnétique et être considérée comme une perturbation.

Des tests sur d'autres échantillons montrent un excellent accord entre les spectres calculés théoriquement et les spectres enregistrés expérimentalement lorsque les AgNPs sont quasi-sphériques avec une fraction volumique dans la matrice hôte jusqu'à 15-17%. En outre, une distribution de taille

étroite des AgNPs est nécessaire afin de permettre la représentation de l'épaisseur de la couche du milieu effectif par le diamètre des AgNPs. Une analyse statistique basée sur l'excentricité des échantillons montre qu'une valeur de 0,4 en terme d'écart à la sphéricité ne doit pas être dépassée, afin de rester dans le cadre de l'approximation de Maxwell-Garnett.

Tableau 1: Paramètres décrivant les échantillons E1 and E3 obtenus par ellipsometrie et MET.

Parameters	Sample E1		Sample E3	
	SE	TEM	SE	TEM
Cover layer thickness - $l$ (nm)	7.0	$7.0 \pm 2.0$	5.0	$4.7 \pm 0.5$
Layer 1: thickness - $t_{\text{Ag:SiO}_2}^{(1)}$ (nm)	9.0	$10.0 \pm 0.5$	6.0	$6.0 \pm 0.3$
AgNPs size - $D_{\text{AgNPs}}^{(1)}$ (nm)	9.0	$7.0 \pm 2.0$	6.0	$6.0 \pm 1.0$
Volume fraction of AgNPs - $f_{\text{Ag:SiO}_2}^{(1)}$	0.13	0.13	0.17	0.16
Eccentricity - $e_e$	n/a	0.35	n/a	0.36
Layer 2: thickness - $t_{\text{Ag:SiO}_2}^{(2)}$ (nm)	4.0	$4.1 \pm 0.5$	n/a	n/a
AgNPs size - $D_{\text{AgNPs}}^{(2)}$ (nm)	4.0	$3.2 \pm 0.9$	n/a	n/a
$f_{\text{Ag:SiO}_2}^{(2)}$	0.042	0.012	n/a	n/a
Silica layer thickness - $t_{\text{SiO}_2}$ (nm)	75.0	$69.0 \pm 3.0$	75.5	$76.0 \pm 4.0$
Total thickness of the structure - $t_{\text{tot}}$ (nm)	95.0	$90.0 \pm 5.0$	86.5	$87.0 \pm 4.0$

Nous avons ensuite testé la capacité de nos AgNPs enrobées, élaborées par LE-IBS (E1, E2) d'une part et par le procédé plasma décrit ci-dessus d'autre part (E4, E5), à libérer des ions  $\text{Ag}^+$  lorsque les nanocomposites sont immergés dans l'eau. Les images MET en XS et en VP de ces échantillons ainsi que leurs distributions de tailles sont données sur la Fig. 8.

Pour l'évaluation du relargage d'Ag par nos nanocomposites, une méthode originale a été mise au point utilisant des algues vertes comme biocapteurs. La libération d'argent a été mesurée par ICP-MS. La toxicité à court terme des AgNPs sur la photosynthèse des *Chlamydomonas reinhardtii* a été étudiée en utilisant la fluorométrie. La culture de *Chlamydomonas reinhardtii* a été préparée selon les modes opératoires décrits dans la référence [Le Faucheur et al., 2005]. Pour évaluer la libération d'argent, nous avons suivi la procédure décrite suivante (Fig. 9). Dans une première étape, on introduit 6 ml de solution 10 mM MOPS à pH ajusté de 7,5 (eau tamponnée) dans chacun des trois flacons. L'eau tamponnée a été préparée conformément à la procédure indiquée dans la référence [Navarro et al., 2008]. Nous utilisons l'un d'entre eux comme contrôle négatif. Dans le second, nous ajoutons une quantité appropriée de sel de nitrate d'argent ( $\text{AgNO}_3$ ) dissous dans de l'eau pure. Ce flacon est utilisé pour suivre les effets de la toxicité d'une quantité connue d'argent dissous (ions  $\text{Ag}^+$ ) sur les algues. Dans les conditions expérimentales adoptées, l' $\text{AgNO}_3$  est complètement dissocié [Navarro et al., 2008].

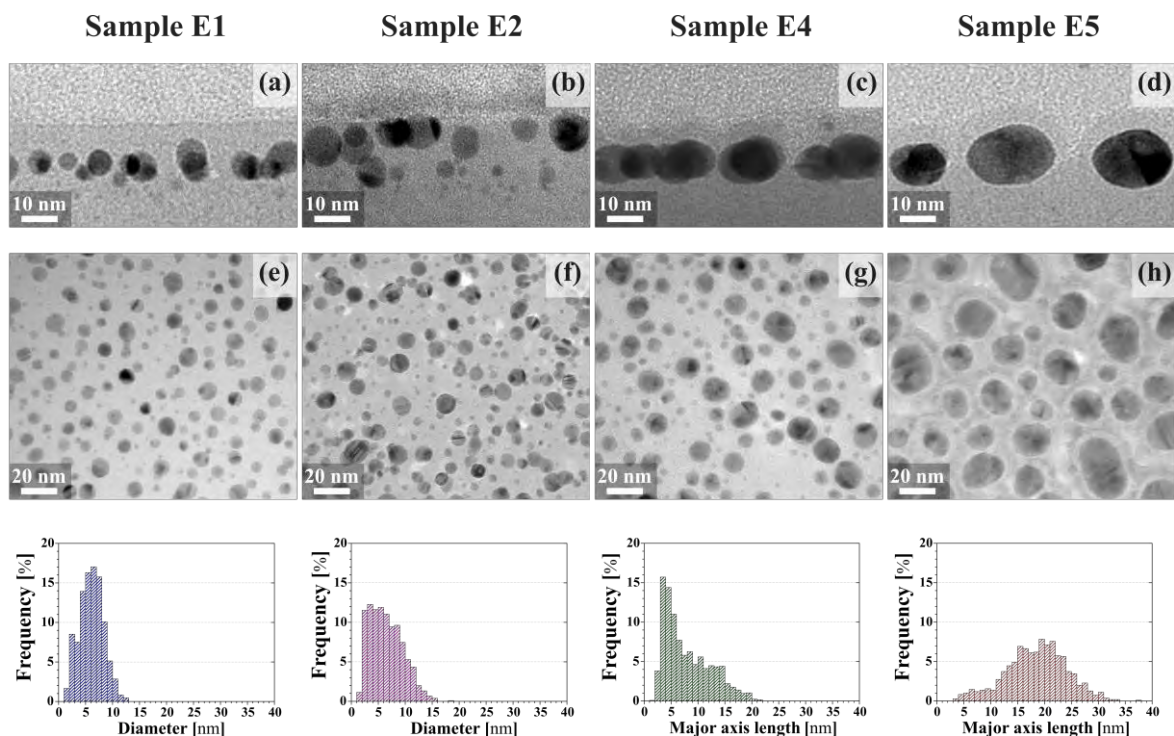


Figure 8: (a)-(d) Images XS-MET en champ clair, avec une zoom sur la partie supérieure des couches nanocomposites et (e) - (h) images en VP des échantillons exploités pour la mesure du relargage d'argent et distribution de taille associée.

Dans le troisième flacon nous ajoutons un échantillon solide avec AgNPs enrobées dans les couches minces de silice. Afin de comparer les différents échantillons, la même surface ( $4 \text{ cm}^2$ ) a été utilisée. Tous les flacons sont agités doucement à température ambiante dans l'obscurité. Afin d'améliorer la libération d'argent, une durée d'immersion de 20 heures a été choisie, l'essentiel du relargage d'Ag ayant lieu pendant les 24 premières heures d'immersion [Saulou et al., 2009].

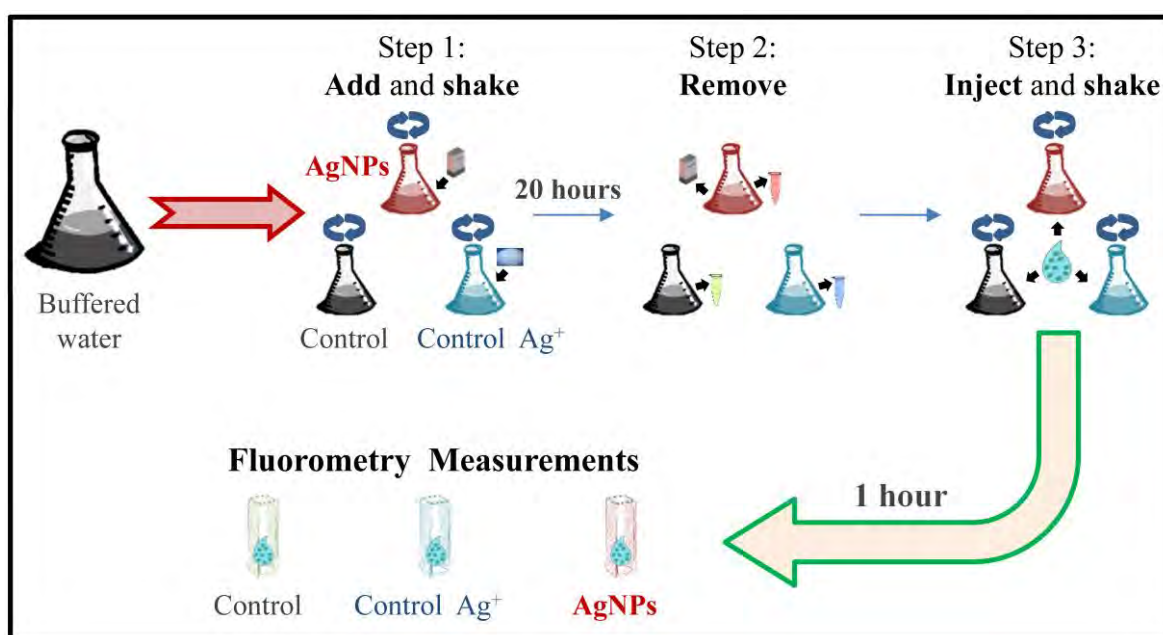


Figure 9: Schéma montrant la procédure pour la mesure du relargage d'Ag.

Dans une deuxième étape, nous enlevons l'échantillon solide de la solution et 2 ml de chaque flacon sont extraits pour les mesures ICP-MS afin d'évaluer la quantité totale d'argent en solution. Dans une troisième étape, on ajoute les algues dans les 3 ml de solution restante. Après une heure d'exposition, les mesures de fluorométrie sont effectuées sur 2 ml de cette solution. Pour assurer l'activité normale des algues, la solution a été maintenue sous un éclairage continu.

Pour une description précise du processus de libération d'argent, nous avons introduit trois paramètres caractéristiques des assemblées de AgNPs qui peuvent jouer un rôle important dans le relargage d'Ag<sup>+</sup> lorsque les échantillons sont immergés en solution. Le premier est la quantité maximale d'argent dans la couche de silice (réservoir initial d'Ag,  $K$ , exprimé en unité molaire). Le second paramètre que l'on peut estimer à partir de la taille et de la densité de surface des mesures est la surface totale des AgNPs, appelé  $M$ . Enfin, le troisième paramètre essentiel extrait des images XS-MET est la distance  $l$  séparant chaque AgNP de la surface de la silice libre.

Pour caractériser la dispersion spatiale dans la couche de SiO<sub>2</sub> des AgNPs nous évaluons  $l_{mean}$  leur distance moyenne et  $l^*$  la distance la plus probable. Celle-ci est définie comme étant la distance à laquelle le plus grand nombre de particules ( $n_{max}$ ) sont situés. Dans le cas des échantillons implantés, on observe en particulier une répartition spatiale non négligeable des AgNPs dans la couche (Fig. 8 (a) et (b)). Toutes ces valeurs sont compilées dans le tableau 2.

Tableau 2: Caractéristiques des AgNPs mesurées directement sur les images MET (taille, densité, distance moyenne et la distance la plus probable à la surface libre) et déduites de ces valeurs (surface totale des AgNPs, réservoir initial d'Ag). L'argent libéré mesuré par ICP-MS est également donné. Le pourcentage se réfère au réservoir Ag initial  $K$ .

Structural Characteristics	Implanted samples		Deposited samples	
	E1	E2	E4	E5
Mean size [nm]	6.1	6.5	7.9	18.5
St. Dev. of size-distribution [nm]	2.2	3.0	4.3	5.6
AgNPs surface density [ $10^{11}$ NPs/cm <sup>2</sup> ]	$10.4 \pm 0.7$	$10.1 \pm 0.8$	$6.9 \pm 0.4$	$1.7 \pm 0.2$
Average distance AgNPs-free surface, $l_{mean}$ [nm]	7.4	5.3	5.6	5.5
St. Dev. of the average distance, $\sigma$ [nm]	2.4	4.2	0.4	0.4
The most probable distance AgNPs-free surface, $l^*$ [nm]	7.5	0.5	5.5	5.5
Total AgNPs surface, $M$ [cm <sup>2</sup> ]	$4.7 \pm 0.5$	$5.4 \pm 0.5$	$5.6 \pm 0.6$	$5.7 \pm 0.6$
Initial Ag reservoir, $K$ [ $\mu$ M]	$9 \pm 1$	$12 \pm 2$	$17 \pm 3$	$29 \pm 4$
Released silver <sup>a</sup> [ $\mu$ M]	0.021 (0.2%)	0.491 (4.1%)	0.500 (2.9%)	0.480 (1.7%)
St. Dev. of the released silver [ $\mu$ M]	0.008	0.053	0.075	0.053

<sup>a</sup> La seuil de détection des mesures du relargage d'Ag par ICP-MS est de 0.003  $\mu$ M.

Les mesures de spectroscopie de masse montrent pour les échantillons déposés E4 et E5, qui présentent une faible dispersion des distances, des valeurs similaires de  $l^*$  et des valeurs similaires de  $M$ , un relargage d'Ag identique indépendamment de leur réservoir initial,  $K$  (E5 contient 74% atomes d'Ag en plus par unité de surface par rapport à E4). D'autre part, pour les échantillons implantés, bien que  $M$  soit multiplié que par 1,15 et  $K$  par 1,3 quand on passe de E1 à E2 (tableau 2), la perte d'argent est multipliée par 20 (de 0,2% d'Ag du réservoir initial pour E1 à 4,1% pour E2). Comme on le voit sur la Fig. 10, la principale différence entre ces deux échantillons réside dans la valeur  $l^*$  (7,5 nm dans E1, comparativement à 0,5 nm dans E2). Enfin, à partir de ces observations, on peut conclure que, dans tous les échantillons étudiés: (i) le nombre d'atomes d'Ag disponibles dans les AgNPs est largement suffisant et ne constitue pas un facteur limitant pour le relargage, et (ii) le paramètre clé qui régit ce relargage est la distance  $l^*$  la plus probable.

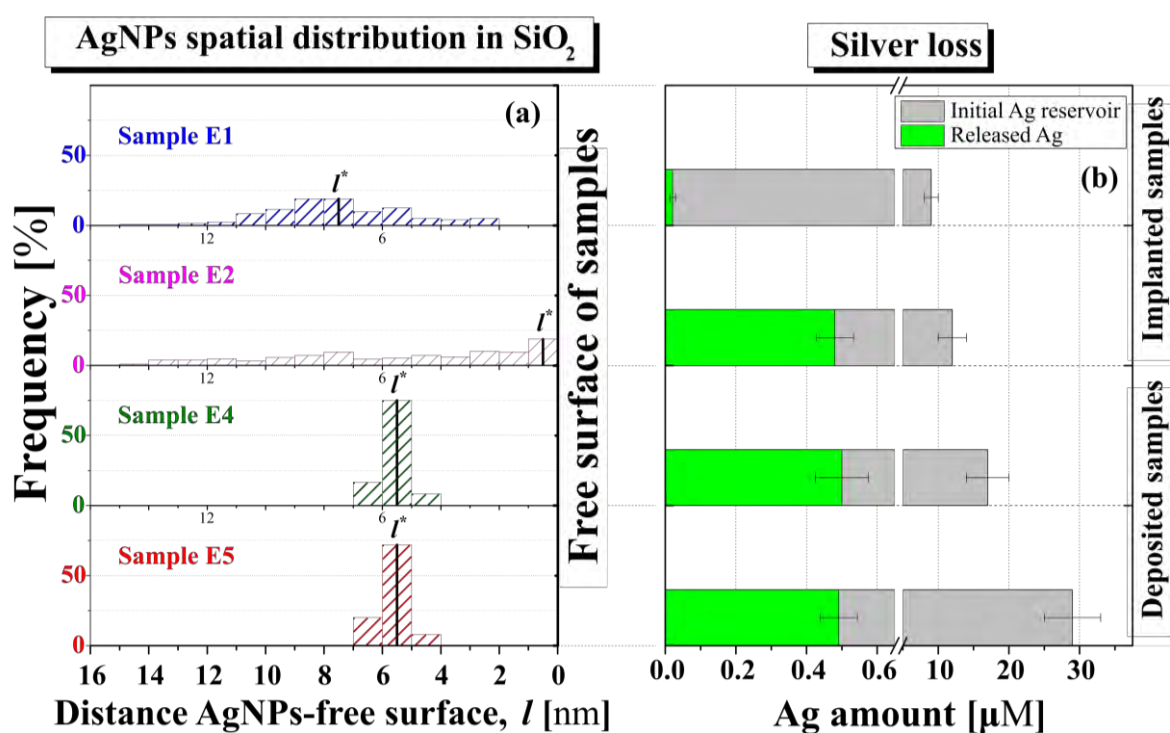


Figure 10: (a) distribution spatiale des AgNPs par rapport à la surface libre (distance  $l$ ) pour chaque échantillon; la distance la plus probable  $l^*$  est indiquée; (b) réservoir initial d'Ag (barre grise) et d'argent libéré (barre verte) pour chaque échantillon.

De manière plus quantitative, la distance seuil pour le relargage est comprise entre 5,5 et 7,5 nm puisque l'échantillon E1 a une très faible libération d'Ag. La libération d'argent la plus efficace est observée pour l'échantillon E2, qui possède la même distance moyenne que les échantillons E4 et E5 ( $l_{mean} \sim 5,5$  nm), mais un grand nombre de AgNPs plus proches de la surface libre (Fig. 10).

Les images XS-MET en champ clair (Fig. 11) montrent l'impact de l'eau tamponnée sur l'échantillon E2. En comparant les images avant (Fig. 11(a)) et après (Fig. 11(b)) immersion dans l'eau, on observe une diminution sensible du nombre de AgNPs touchant la surface libre.



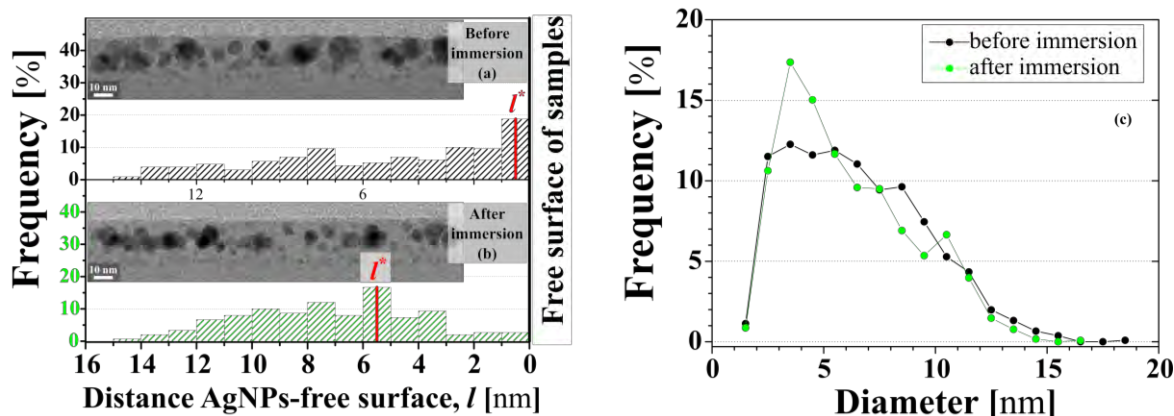


Figure 11: XS-MET de l'échantillon E2 et distribution des distances associée avant (a) et après (b) immersion dans l'eau tamponnée. (c) Distributions de tailles des AgNPs mesurées à partir des images en VP, avant (noir) et après (vert) immersion dans l'eau tamponnée.

Cela signifie que la libération d'argent est accompagnée par une dissolution partielle des AgNPs situées près de la surface libre. La distribution de la distance  $l$  entre AgNPs et la surface libre est représentée graphiquement sur la Fig. 11(b) avant et après immersion dans l'eau. Après immersion, la densité surfacique de AgNPs reste inchangée alors que la distance  $l^*$  augmente de 0,5 nm à 5,5 nm. Cela signifie que le nombre de AgNPs touchant la surface libre ( $l < 1$  nm) diminue fortement, tandis que celles enterrées plus profondément avec une distance  $5 < l < 6$  nm augmente considérablement. Au-delà de 6 nm, la forme de la répartition de distances ne change pas de manière significative. Ceci montre que la distance critique au-delà de laquelle la libération d'argent est négligeable, est de l'ordre de 6 nm. Ce résultat est en bon accord avec la distance seuil (entre 5,5 et 7,5 nm) évaluée plus haut.

En ce qui concerne la distribution de tailles mesurée à partir d'images VP-MET (Fig. 11(c)) on observe une diminution nette de la classe de AgNPs avec une taille supérieure à 6 nm, et en même temps une augmentation relative des classes comprises entre 3 et 5 nm. Les deux évolutions confirment la dissolution des plus grandes AgNPs situées à proximité de la surface libre après interaction avec l'eau. La perte d'atomes d'Ag peut être estimée à partir des images VP-MET de ces échantillons comme la différence entre le réservoir d'Ag ("Initial Ag reservoir",  $12 \pm 2 \mu\text{M}$ ) avant et après immersion dans l'eau ( $11 \pm 2 \mu\text{M}$ ). Même si la barre d'erreur cumulée sur cette mesure est importante (30%), cette valeur est du même ordre de grandeur que celle mesurée par ICP-MS (4,1%).

Pour mettre en évidence l'origine de la toxicité de l'argent observée sur les algues (les ions d'argent  $\text{Ag}^+$  et/ou des AgNPs), nous avons effectué des mesures de fluorométrie sur les solutions en présence de cystéine, connu comme ligand d'argent solide [Navarro et al., 2008]. La complexation équimolaire de  $\text{Ag}^+$  par la cystéine a été précédemment démontrée dans des conditions expérimentales similaires [Navarro et al, 2008; Navarro et al, 2015]. En raison des 30% d'AgNPs situés à 2 nm ou moins de la surface de la silice libre, l'échantillon E2 est le meilleur candidat pour évaluer la source de l'argent libéré. La Fig. 12 représente les mesures de fluorométrie, prises 1 heure après l'injection d'algues, d'une solution contenant de l'argent libéré par l'échantillon E2 et deux quantités différentes de cystéine.

Nous comparons les valeurs de fluorométrie obtenues sur l'échantillon E2 (triangles magenta) avec celles d'une solution de référence contenant de l'AgNO<sub>3</sub> avec une concentration de  $0,714 \pm 0,060 \mu\text{M}$  et différentes quantités de cystéine (cercles noirs). Les concentrations de cystéine d'environ 0,7 à 0,9  $\mu\text{M}$  suppriment la toxicité pour la photosynthèse des algues de Ag<sup>+</sup> (à partir d'AgNO<sub>3</sub>), ce qui confirme à la fois le rôle clé des ions Ag<sup>+</sup> dans la toxicité observée pour la photosynthèse des algues et la complexation équimolaire de cystéine et de Ag<sup>+</sup> [Navarro et al., 2008; Navarro et al, 2015]. L'échantillon E2 présente une restauration partielle de la photosynthèse des algues lorsque la concentration de cystéine est d'environ 0,35  $\mu\text{M}$ , ce qui indique la présence d'une plus grande quantité d'Ag<sup>+</sup> en solution. Une nouvelle addition de cystéine (1,5  $\mu\text{M}$ ) abolit la toxicité pour la photosynthèse des algues, en accord avec d'autres études [Navarro et al, 2008; Navarro et al, 2015]. Ces résultats confirment que la globalité de la toxicité de la suspension après contact avec l'échantillon E2 est due à la présence d'Ag<sup>+</sup> en solution.

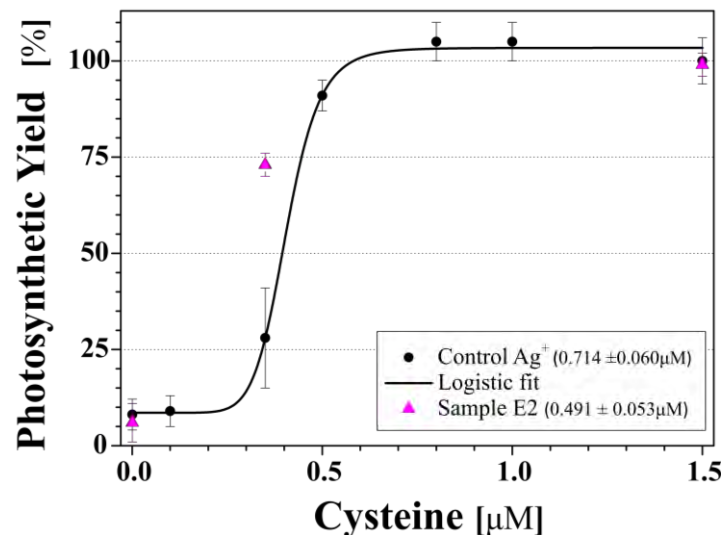


Figure 12: Mesures de rendement photosynthétique des algues après 1 heure d'exposition à l'argent libéré par l'échantillon E2 ou par une concentration fixe d'AgNO<sub>3</sub> (0.714 M) et différentes quantités de cystéine. La ligne noire retrace les quatre paramètres sous une forme logistique.

En regroupant les informations obtenues à partir des mesures de fluorométrie et des observations MET nous pouvons conclure que l'argent libéré en solution à partir des AgNPs enterrées est sous forme d'argent ionique.

L'architecture des échantillons utilisés dans cette étude est particulièrement bien adaptée pour contrôler la libération d'argent et par conséquent la toxicité de ces couches nanocomposites. En effet, les AgNPs enterrées sont situées à proximité de la surface libre du diélectrique et bien séparées les unes des autres permettant ainsi de maximiser leur surface de relargage. La distance nanométrique entre la couche de AgNPs et la surface libre, autrement dit l'épaisseur la fine couche de couverture de silice, agit comme une barrière protégeant l'argent métallique contre un relargage rapide et/ou un vieillissement prématuré, principalement par oxydation des AgNPs [Benzo et al., 2011].



Cependant, pour initier la libération d'Ag<sup>+</sup> les molécules d'eau doivent arriver à la surface des AgNPs. Les propriétés de la matrice environnante sont d'une importance capitale lorsque les structures de nanocomposites contenant des nanoparticules métalliques sont exposées à des agents externes de vieillissement (air, milieu aqueux, différents solvants, etc.). La libération d'Ag<sup>+</sup> se révèle être plus rapide lorsque la matrice hôte est moins stable, comme pour une matrice amorphe oxygénée et hydrophile à base d'hydrocarbures (a-CH:O) [Körner et al, 2010; Drabik et al, 2015] où les groupes d'oxygène fonctionnel permettent une pénétration de l'eau plus rapide. L'augmentation de l'hydrophobie de la matrice hôte, comme pour les matrices organo-siliciées amorphes (a-SiOC:H) [Saulou et al, 2009; Beer et al, 2012; Alissawi et al, 2013], conduit à plus lente libération d'Ag<sup>+</sup> principalement en raison du retard dans la pénétration des molécules d'eau. L'augmentation de la stabilité de la matrice par densification, comme pour les matrices de SiO<sub>2</sub> amorphes (ce travail), permet un réglage fin de la libération d'Ag<sup>+</sup>. L'absorption de molécules d' H<sub>2</sub>O de l'air a été étudiée dans le cas de fines couches de SiO<sub>2</sub> implantées (moins de 10 nm) [Schmidt et al., 2002; Claverie et al., 2006]. Le grand nombre de liaisons brisées dans les tétraèdres de SiO<sub>4</sub> en raison des atomes de Si et O déplacés au cours du processus d'implantation résulte dans des réarrangements de la structure fondamentale au sein du réseau vitreux, dans lequel l'humidité de l'air ambiant peut être absorbée. Les molécules d'eau adsorbées à la surface diffusent ensuite de manière accélérée dans la matrice endommagée. Par conséquent, des réactions chimiques des impuretés implantées avec l'hydrogène et l'oxygène peuvent se produire. Deux possibilités peuvent être envisagées: soit les molécules d'eau diffusent directement dans le réseau de SiO<sub>2</sub> endommagé par l'implantation, car H<sub>2</sub>O est une molécule de petit diamètre (inférieur à 0,3 nm) soit les molécules d'H<sub>2</sub>O se dissocient à la surface du diélectrique et ce sont les ions H<sup>+</sup> et OH<sup>-</sup> qui diffusent dans la silice. Les molécules et les complexes riches en O sont ainsi entraînés dans les couches jusqu'à environ 10 nm en profondeur. En fait, l'absorption et la concentration finale des molécules d'eau ne sont limitées que par le degré de dommage, à savoir la concentration des défauts dans la matrice de SiO<sub>2</sub>.

Dans le cas de la silice implantée avec de l'Ag, le recuit des couches à basse température (400-500°C) sous atmosphère N<sub>2</sub> permet une récupération partielle des dommages causés par l'implantation. Cette étape de recuit de la couche de silice est cependant suffisante pour éviter, ou tout au moins retarder la pénétration des complexes riches en O<sub>2</sub> de l'air [Benzo et al., 2011]. Dans le présent travail, nous démontrons que la silice implantée et recuite permet une forte interaction de l'argent avec les espèces réactives de l'eau jusqu'à 3 nm en profondeur. Au-delà de cette valeur, la pénétration d'espèces réactives diminue et devient négligeable à des profondeurs supérieures à 7 nm, tel que confirmé par la faible quantité d'argent libérée de l'échantillon E1. Cette profondeur critique peut être comparée à la longueur de diffusion de la vapeur d'eau dans la silice, qui est de 3 nm en une semaine [Muscat et al., 2001]. La diffusion de l'eau semble être accélérée dans nos échantillons. Ceci est probablement dû à la plus faible densité de la matrice de silice et à une porosité plus élevée comparée à la silice thermique pure, en particulier pour les échantillons implantés.

Dans les des échantillons déposés la stabilité de la matrice  $\text{SiO}_2$  lors de l'exposition à l'eau est également un processus dépendant des défauts. Elle est déterminée par la très petite quantité de groupes CH résiduels présents dans le réseau de la silice en raison du procédé de dépôt par polymérisation plasma. D'autres défauts structuraux dans le réseau de la silice plasma ne sont pas exclus. Une comparaison quantitative précise de la libération  $\text{Ag}^+$  pour différents types de matrices hôte est difficile d'autant plus que les caractéristiques de surface des échantillons étudiés ne sont généralement pas rapportées dans la littérature. Cependant il semblerait que le taux de libération d' $\text{Ag}^+$  soit le plus élevé lors des premières 24 heures. Par ailleurs, il a été montré [Schmidt et al., 2003] que les étapes consécutives d'interaction de l'oxygène et de l'argent impliquent une physisorption initiale de l' $\text{O}_2$  suivie par un état où l' $\text{O}_2$  est moléculairement chimisorbé précédant l'accrochage de l' $\text{O}_2$  aux clusters d'argent. En règle générale, la probabilité d'adsorption d' $\text{O}_2$  augmente avec la taille des AgNPs. Ce mécanisme est toutefois pondéré par les propriétés intrinsèques de la matrice de  $\text{SiO}_2$ , notamment par l'épaisseur de la couche de couverture.

En conclusion, nous avons donc mis au point une méthode originale pour évaluer le relargage d'Ag à partir d'AgNPs enrobées dans les nanocomposites, sur la base de la toxicité de l'Ag bio-disponible sur l'activité photosynthétique des algues. La distance des AgNPs à la surface libre du nanocomposite est le paramètre clé affectant la libération d'argent. En fonction de cette distance, la libération d'argent varie entre 0,2 et 4,1% de la quantité initiale d'Ag présente dans les échantillons. Les observations MET après immersion indiquent que la libération d'Ag est accompagnée par la dissolution des AgNPs qui sont situées à proximité immédiate de la surface libre alors que la densité d'AgNPs reste inchangée. Ceci permet de conclure que ces AgNPs sont la source de l'argent libéré en solution. Les mesures de réflectance confirment la présence d'argent métallique dans les NPs après immersion dans l'eau. La toxicité de l'argent libéré par ces nanocomposites sur la photosynthèse des algues est comparable à des concentrations similaires d' $\text{Ag}^+$  libérés par un sel d'argent  $\text{AgNO}_3$ . Ce résultat, ainsi que la capacité de la cystéine pour supprimer la toxicité des suspensions expérimentales démontrent que l'essentiel de l'argent libéré par les nanocomposites est sous forme d' $\text{Ag}^+$ . Pour la libération d'argent ionique, le contact avec les molécules d'eau est nécessaire, cette étape étant fortement dépendante des propriétés de la matrice.

Nos résultats montrent une approche physique pour moduler l'activité des surfaces d'argent nanostructurées. Ces nanocomposites sont donc de bons candidats comme revêtements pour inhiber le développement de films microbiens sur des surfaces solides. En outre, en couplant les propriétés bactéricides de ces AgNPs enterrées et leur qualité d'antenne plasmonique, ces revêtements peuvent être utilisés pour détecter et empêcher les premiers stades de formation de biofilms. De plus en plus, l'adhésion microbienne et la formation de biofilms provoquent des complications majeures dans le domaine biomédical et dans l'industrie alimentaire. Nous avons démontré dans une première partie de ce travail que la première condition nécessaire pour la fabrication de nanocomposites à propriétés anti-microbiennes est remplie. En effet, nos AgNPs enterrées dans la silice sont capables de libérer des ions

Ag et nous pouvons moduler ce relargage en jouant avec la distance des AgNPs et la surface libre diélectrique, en d'autres termes avec l'épaisseur de la couche de couverture en silice.

Dans ce contexte et fondé sur des modifications observées précédemment de la structure des protéines induites par le contact des AgNPs avec des micro-organismes l'étape suivante concerne la caractérisation physico-chimique de cette interaction. Ainsi la protéine fluorescente *Discosoma* rouge (DsRed) a été utilisée en raison de ses propriétés fluorescentes très prometteuses pour des applications en biotechnologie et en biologie cellulaire.

Une variété de techniques expérimentales ont été utilisées pour accéder et évaluer les propriétés structurales des protéines adsorbées sur des surfaces solides menant à la formulation d'un certain nombre de tendances communes [Arai et Norde, 1990; Matz et al., 1999; Baird et al., 2000; Vrzheschch et al., 2000; Wall et al., 2000; Larsericsdotter et al., 2005; Vo-Dinh, 2005; Barth, 2007; Hughes, 2012; Jachimska et Pajor, 2012]. Il est ainsi généralement admis que les protéines ayant une forte cohérence interne vont s'adsorber sur des surfaces hydrophobes. Au contraire, l'attraction électrostatique est nécessaire pour leur adsorption sur des surfaces hydrophiles. En revanche, les protéines à stabilité structurale beaucoup plus faible vont s'adsorber librement sur les deux surfaces hydrophobes et hydrophiles, même dans des conditions défavorables, comme c'est le cas des surfaces hydrophiles électrostatiquement répulsives.

Nous nous sommes donc intéressés au comportement des protéines DsRed et aux mécanismes sous-jacents en terme de stabilité et d'adsorption sur des surfaces de silice « nues » puis contenant des AgNPs enterrées. Par ailleurs, ces mêmes AgNPs enterrées près de la surface libre d'une couche anti-reflet en SiO<sub>2</sub> peuvent être utilisées pour la détection de substances chimiques sur leurs surfaces [Carles et al., 2011]. Dans ce contexte, nous illustrons les résultats préliminaires d'un effet SERS observé sur la protéine DsRed déposée sur nos substrats nanocomposites.

Quand une gouttelette contenant une concentration donnée de protéines est amenée en contact avec une surface solide, l'organisation et le comportement des protéines reposent principalement sur l'hystérésis de l'angle de contact aux interfaces solide-vapeur et liquide-vapeur. La figure 13 montre le comportement lors de la déshydratation de DsRed pour différentes concentrations de protéine. La décroissance linéaire au cours du temps de l'angle de contact est observée pour toutes les concentrations de DsRed étudiées. La déshydratation des gouttelettes est plus rapide pour les faibles concentrations de DsRed (jusqu'à 0,1 g/L). Cet effet est lié à la grande variation de l'énergie de surface du profil de gouttelettes à proximité du point triple (solide-liquide-vapeur) et aux mécanismes d'adsorption des protéines induits par la convection du liquide à l'intérieur de la gouttelette (effet Marangoni).

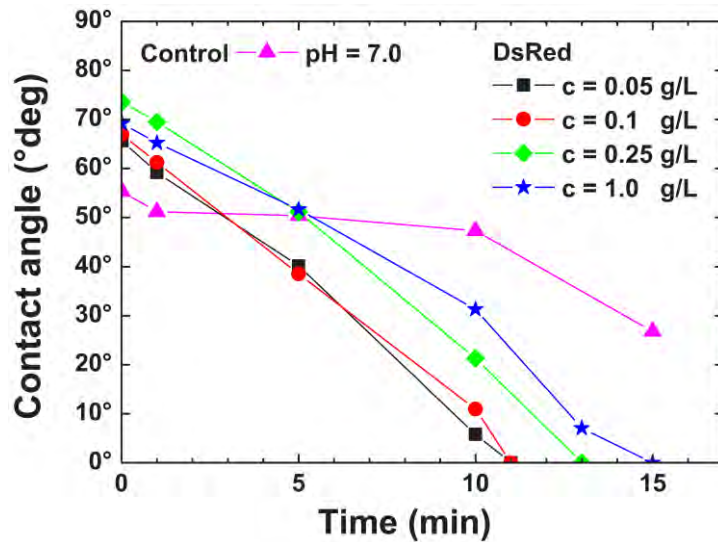


Figure. 13: Mesure des angles de contact à 23°C en fonction du temps au cours de la déshydratation de gouttes sessiles pour différentes concentrations de DsRed.

Comme on le voit dans le tableau 3, toutes les valeurs caractéristiques des gouttelettes sont augmentées lorsque la concentration de la DsRed est plus grande.

Tableau 3: Dynamiques de la déshydratation des gouttes sessiles.

DsRed (g/L)	Droplet image at 1s	Contact angle $-\theta_A$	Optical image after dehydration	Dehydrated sessile droplet <sup>a</sup>
Control pH=7.0		54.3° ± 0.1°	n/a	n/a
0.05		65.4° ± 0.2°		$d = 2.8 \text{ mm};$ $e = 20 \text{ nm};$ $l = 46 \text{ }\mu\text{m};$ $h = 0.6 \text{ }\mu\text{m}$
0.10		65.5° ± 1.6°		$d = 2.8 \text{ mm};$ $e = 30 \text{ nm};$ $l = 67 \text{ }\mu\text{m};$ $h = 1.4 \text{ }\mu\text{m}$
0.25		73.7° ± 1.5°		$d = 2.7 \text{ mm};$ $e = 30 \text{ nm};$ $l = 84 \text{ }\mu\text{m};$ $h = 3.0 \text{ }\mu\text{m}$
1.00		72.0° ± 2.7°		$d = 2.6 \text{ mm};$ $e = 60 \text{ nm};$ $l = 200 \text{ }\mu\text{m};$ $h = 5.2 \text{ }\mu\text{m}$

<sup>a</sup> Les caractéristiques de la gouttelette de DsRed après déshydratation sont les suivantes: "d" est le diamètre de la gouttelette; "e" est l'épaisseur de la gouttelette mesurée à l'intérieur de la gouttelette, juste avant l'anneau de la gouttelette; "l" est la largeur de l'anneau de la gouttelette; et "h" est la hauteur de l'anneau de gouttelette.

Cela signifie que la DsRed s'adsorbe sur l'ensemble de la zone couverte par la gouttelette avec dépôt préférentiel près de la ligne triple, à savoir à la frontière des gouttelettes. L'épaisseur de la couche de DsRed adsorbée sur des surfaces solides peut-être finement contrôlée par la concentration en protéines.

Les spectres de photoluminescence obtenus sont présentés sur la Fig. 14. L'intensité de l'émission de photoluminescence augmente lorsqu'augmente la concentration de DsRed. Cependant, cette variation n'est pas linéaire très probablement due à des phénomènes de "quenching" (Fig. 14, encart). La bande d'émission de photoluminescence présente un pic à 590 nm. Le léger décalage vers le rouge par rapport à l'émission de la DsRed en solution peut être attribué à des effets de conformation et d'interaction de la DsRed avec la couche mince de silice. L'analyse physico-chimique des interactions de la protéine fluorescente rouge DsRed avec des surfaces de SiO<sub>2</sub> thermique montre que l'épaisseur de la couche adsorbée peut être ajustée finement par la concentration en protéines. Les angles de contact mesurés à partir de très petites gouttelettes sessiles contenant différentes concentrations de DsRed montrent que l'interaction est hydrophile. Les protéines DsRed semblent stables aux variations de pH. L'adsorption de DsRed sur les surfaces de SiO<sub>2</sub> et les processus de déshydratation suivants ne conduisent pas à la dénaturation des protéines. Le pic d'émission de photoluminescence des protéines DsRed déshydratées adsorbées sur des couches de SiO<sub>2</sub> est situé à 590 nm, ce qui est légèrement décalé vers le rouge par rapport à la valeur mesurée pour une solution (583 nm).

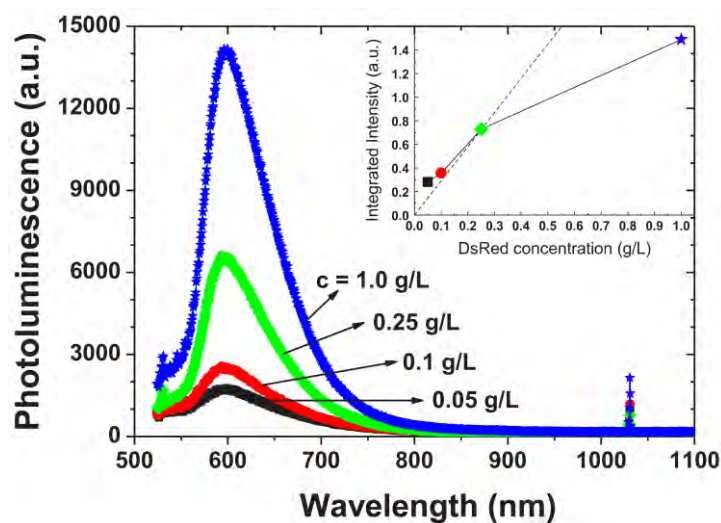
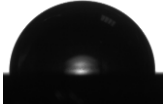
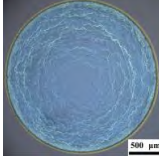
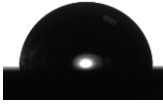
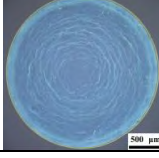
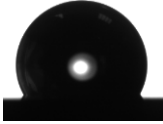
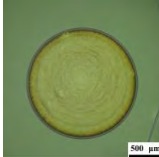
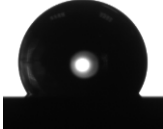
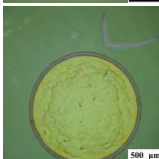


Figure 14. Spectres de photoluminescence des gouttelettes déshydratées de DsRed adsorbées sur la surface de SiO<sub>2</sub> pour différentes concentrations à pH = 7.0 et 23°C. L'encart représente l'intensité intégrée du pic de photoluminescence en fonction de la concentration de DsRed.

L'interaction des protéines avec nos substrats nanocomposites contenant les AgNPs présente un caractère hydrophobe ( $\theta \geq 90^\circ$ ). Le tableau 4 montre les caractéristiques morphologiques obtenues pour deux concentrations de DsRed (0,1 et 0,25 g/L). Les gouttelettes s'étalent et atteignent leur diamètre maximal immédiatement. Après séchage des gouttelettes sur le substrat, l'aspect visuel du dépôt des gouttelettes est plus homogène lorsque la teneur en Ag augmente (tableau III). En outre, les

substrats Ag nanocomposites élaborés par procédé plasma présentent des angles de contact supérieurs ( $120^\circ$ ) à ceux élaborés par LE-IBS ( $90^\circ$ ). Cela influe sur le diamètre final de la goutte sessile avec une réduction de son diamètre lorsque l'angle de contact augmente (tableau 4).

Tableau 4: Caractéristiques des gouttelettes de DsRed déposées sur les échantillons E2 et E5, pour des concentrations comprises entre 0.1 et 0.25 g/L à pH = 7.0 et  $23^\circ\text{C}$ .

Elaboration process	DsRed (g/L)	Droplet image at 1s	Contact angle - $\theta_A$	Optical image after dehydration	Dehydrated sessile droplet
<b>LE-IBS (E2)</b>	0.10		$91.8^\circ$		$d = 2.4 \text{ mm}$
	0.25		$89.7^\circ$		$d = 2.4 \text{ mm}$
<b>Plasma deposited samples (E5)</b>	0.10		$117.8^\circ$		$d = 1.7 \text{ mm}$
	0.25		$120.8^\circ$		$d = 1.8 \text{ mm}$

La figure 15 présente les spectres Raman de la DsRed obtenus en utilisant deux substrats différents (E2 et E5). Un spectre théorique de la DsRed a été utilisé comme référence pour déterminer la signature de la protéine. Les fréquences de vibration caractéristiques des liaisons moléculaires DsRed correspondent aux positions de la bande dans le spectre Raman.

Un effet SERS sur la protéine DsRed est observé pour l'échantillon E5 élaboré par procédé plasma. En particulier, un effet de clignotement est observé, ce qui correspond à des variations d'intensité des différents pics Raman. Ceci est dû aux changements et aux fluctuations de l'orientation moléculaire et la conformation de la protéine DsRed sous l'excitation laser (532 nm). Au contraire, le signal Raman est faible lorsque les protéines DsRed sont déposées sur l'échantillon élaboré par LE-IBS (E2) et le phénomène de "clignotement" n'est pas détecté. La différence de comportement entre ces deux échantillons peut être attribuée à plusieurs facteurs: (i) la fraction la plus élevée de la surface de AgNPs pour l'échantillon E5 conduisant à une forte concentration de points chauds, (ii) l'effet de la rugosité de surface, qui permet le piégeage des protéines dans les vallées entre deux NPs.

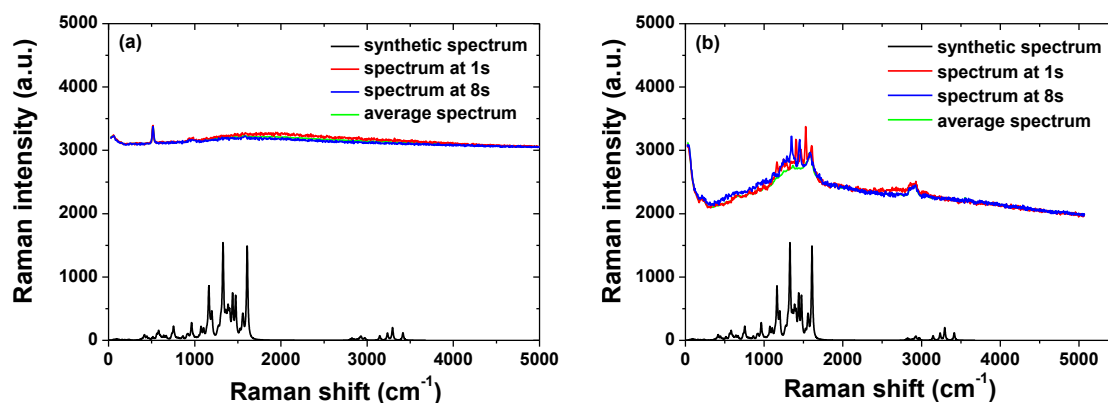


Figure 15: Spectres Ramans obtenus en excitant avec un laser à une longueur d'onde d'excitation de 532 nm lorsque les protéines Dsred sont déposées sur les substrats E2 (a) et E5 (b).

En conclusion de ce travail de thèse, les objectifs de cette thèse étaient de fabriquer des nanocomposites multifonctionnels à base de nanoparticules d'Ag enrobées dans des diélectriques à libération contrôlée de l'agent antibactérien. Ces revêtements innovants devraient permettre à la fois de cibler le type de micro-organisme à combattre et de délivrer la juste dose pour son inhibition, tout en préservant la microflore environnante. Pour atteindre ces objectifs, nous avons proposé d'utiliser la multifonctionnalité de nanoparticules d'Ag, qui sont à la fois (i) des antennes plasmoniques permettant d'exalter les signaux optiques et de détecter l'interaction avec les micro-organismes et (ii) des réservoirs d'ions connus pour leurs propriétés antibactériennes. Afin de stabiliser les nanoparticules et contrôler la dose toxique (i.e., la concentration en ions Ag<sup>+</sup> libérés) les AgNPs ont été incorporées dans des matrices diélectriques et positionnées à des distances variables de la surface du substrat, sur lequel les micro-organismes adhèrent.

Des couches de silice contenant des AgNPs ont été fabriquées par deux procédés très différents, mais complémentaires: (i) Synthèse par implantation ionique à basse énergie et (ii) Pulvérisation plasma d'Ag combinée à la polymérisation. Ces techniques permettent l'élaboration d'un plan unique de AgNPs enterrées dans des films de silice, à des distances nanométriques définies (0-7 nm) au-dessous de la surface libre du diélectrique. En ce qui concerne la technique de dépôt, spécialement développée dans ce travail de thèse, nous avons montré comment les paramètres clés des nanostructures enrobées (taille, densité, distance à la surface) peuvent être contrôlés en modifiant les conditions d'élaboration combinant pulvérisation d'argent et polymérisation plasma. Ces deux techniques offrent la possibilité d'explorer différentes distributions de taille, densités surfacique, et en particulier différentes distances de ce plan de NPs à la surface libre. Les propriétés structurales et optiques de ces nanocomposites ont été étudiées par microscopie électronique à transmission, spectroscopie de réflexion et ellipsométrie. Cette dernière technique, associée à une modélisation basée sur l'approximation quasi-statique du

formalisme classique de Maxwell-Garnett s'est révélée être une technique efficace de diagnostic pour la détection de petites variations dans la taille et la densité des AgNPs.

Afin d'évaluer la capacité des AgNPs enrobées dans des diélectriques pour libérer des quantités contrôlées d'ions Ag, nous avons mis au point une méthode originale, où l'évaluation de la dose et de l'activité biocide de l'ion  $\text{Ag}^+$  a été testée en utilisant un système modèle eucaryote, les *Chlamydomonas reinhardtii*. Le système photosynthétique de ces algues vertes a été utilisé comme biocapteur sensible et fiable pour détecter l'argent ionique bio-disponible en solution. La distance des AgNPs à la surface libre du nanocomposite est le paramètre clé affectant la libération d'argent. En fonction de cette distance, la libération d'argent varie entre 0,2 et 4,1% de la quantité d'Ag initialement présente dans les échantillons. Les observations MET après immersion indiquent que la libération d'Ag est accompagnée par la dissolution des AgNPs qui sont situées à proximité immédiate de la surface libre alors que la densité de AgNPs reste inchangée, suggérant que ces AgNPs sont la source de l'argent libéré en solution. La toxicité de l'argent libéré par ces nanocomposites sur la photosynthèse des algues est comparable à des concentrations similaires à celle du sel d'argent. Ce résultat, ainsi que la capacité de la cystéine à abolir la toxicité des suspensions expérimentales, démontre que l'essentiel de l'argent relargué par ces nanocomposites est sous la forme d' $\text{Ag}^+$ , excluant ainsi l'implication de AgNPs directement relarguées. Pour la libération de l'argent ionique, le contact avec les molécules d'eau est nécessaire, cette étape étant fortement dépendante des propriétés de la matrice. Nos résultats montrent une approche physique pour moduler l'activité des surfaces nanostructurées d'argent. Ces nanocomposites sont donc de bons candidats comme revêtements pour inhiber le développement microbien de films sur des surfaces solides.

Pour aller plus loin dans cette voie, l'analyse physico-chimique des interactions de la protéine fluorescente rouge (DsRed) avec des surfaces de  $\text{SiO}_2$  thermique a été réalisée visant à mieux comprendre la stabilité structurale des protéines DsRed et leur comportement d'adsorption. Les caractéristiques obtenues sur des gouttelettes de DsRed déshydratées montrent que l'épaisseur de la couche adsorbée sur des surfaces solides peut être modulée finement par le biais de la concentration en protéines. Les angles de contact mesurés sur de très petites gouttelettes contenant différentes concentrations de protéines DsRed montrent une interaction de type hydrophile, mais avec de plus grands angles de contact pour de plus grandes concentrations DsRed. L'adsorption de DsRed sur les surfaces  $\text{SiO}_2$  et les processus de déshydratation suivants ne conduisent pas à la dénaturation des protéines. L'émission de photoluminescence des protéines DsRed déshydratées adsorbées sur des couches de  $\text{SiO}_2$  est conservée avec un pic caractéristique de la DsRed situé à 590 nm, ce qui est légèrement décalé vers le rouge par rapport à la valeur indiquée pour une solution. Enfin, des résultats préliminaires montrent un effet SERS pour les protéines DsRed déposées sur nos AgNPs enrobées en particulier pour l'échantillon élaboré par procédé plasma présentant la fraction surfacique de AgNPs la plus élevée, et des NPs situées à 5 nm de la surface conforme du diélectrique. Ce résultat préliminaire



nous encourage à poursuivre dans l'avenir avec l'optimisation des conditions d'élaboration afin d'obtenir un effet SERS encore plus prononcé. Pour les échantillons déposés, où un réseau 2D des AgNPs de taille moyen environ 20 nm et supérieure est obtenu, l'influence de la densité/porosité de la couche de couverture sera par exemple étudiée. En ce qui concerne les échantillons élaborés par LE-IBS, le module basse température qui sera disponible au CEMES très prochainement, devrait permettre l'insertion dans la matrice d'une plus grande quantité d'Ag en supprimant sa diffusion vers la surface pendant le processus d'implantation. Des réseaux 2D percolés de AgNPs devraient être donc formés au cours du recuit post-implantation.

A court terme, la prochaine étape sera maintenant d'utiliser ces nanocomposites anti-bactériens dans des «conditions réelles» pour traiter la prolifération de micro-organismes, par exemple *Candida Albicans* IP48.72, qui peuvent coloniser les surfaces des instruments chirurgicaux, les dispositifs implantables (prothèses, stents) ou percutanés (cathéter) et les murs des salles d'interventions dans les hôpitaux. Cette étude sera réalisée en collaboration avec le LGC à Toulouse.

En parallèle, il serait intéressant d'effectuer une étude approfondie des mécanismes de libération des ions Ag et de leur diffusion à travers la couche mince de silice. Des expériences dédiées seront menées afin de mieux comprendre le relargage des ions Ag après immersion dans l'eau, impliquant FTIR, XPS, STEM-EELS et EDX. Elles devraient mettre en évidence la présence éventuelle d'une fine coquille d'Ag<sub>2</sub>O entourant les AgNPs. L'effet sur la libération des ions Ag de la densité (porosité) de la couche de couverture sera également exploré. La modélisation à l'échelle atomique du processus de libération des ions Ag pour des NPs enrobées dans de la silice et de la diffusion de ces ions dans la matrice devrait permettre de mieux appréhender les mécanismes réactionnels et les forces motrices impliquées dans le relargage.

A plus long terme, ce type d'étude approfondie des propriétés des matériaux nanocomposites et de l'interaction des nanoparticules métalliques avec des molécules biologiques (protéines et cellules) est très demandé pour mieux appréhender les principaux effets causés par ces matériaux ainsi que leurs effets secondaires. L'application généralisée des nanocomposites à base de AgNPs dans les produits de consommation de la vie quotidienne devrait inciter les acteurs de la recherche et les industriels à mieux évaluer les avantages de ce type de matériau versus les éventuels risques de santé et environnementaux. Ce genre d'étude multidisciplinaire sur l'ingénierie rationnelle de matériaux nanocomposites multifonctionnels s'inscrit ainsi dans une démarche de type "**safe-by-design**".

# Introduction

---

In the last twenty years there has been a rapid increase in the development, production and application of engineered nanomaterials, which are currently playing a growing role in many fields, including consumer products related to various sectors: health, cosmetology, agriculture, food, environment, communication, transport and energy [Peralta-Videa et al., 2011]. Especially, nanomaterials might provide solutions to technological challenges in the areas of solar energy conversion, catalysis, medicine, water, and air treatment for purification purposes [Sharma et al., 2009]. It is largely accepted that the nanoscale materials have emerged up owing to their high surface area to volume ratio and their unique chemical and physical properties. In particular, in the time of fast development and application of nanocomposite containing customer products, it is highly demanded to develop a new class of nanocomposites based on nanosized metal and/or metal oxide inclusions in dielectric matrices. The most frequently given example about metallic nanoparticles and their large use in the industrial applications, and the only one discussed here, concerns silver nanoparticles (AgNPs). The AgNPs are well known above all for their plasmonic properties. Indeed, they realize the best nanoscale antenna in the visible range for amplifying local electronic and vibrational signals, providing unique molecular information in the optical far-field regime. In the field of scientific research, two main spectroscopies have emerged based on Localized Surface Plasmon Resonance (LSPR) and Surface-Enhanced Raman Scattering (SERS). Since its discovery in 1974 on pyridine molecules adsorbed on rough silver surfaces [Fleischmann, 1974], SERS has received a great deal of attention as a powerful analytical technique for molecular spectroscopy, biomolecular recognition and ultra-sensitive detection (down to a single molecule). However, the limitation in fabricating SERS substrates remains a major drawback for potential applications.

Nevertheless, most of the applications of AgNPs rely on their chemical activity. The AgNPs have indeed proved the largest antimicrobial efficiency against bacteria, viruses and other eukaryotic microorganisms. They are now present in an expanding range of industrial products [Silver et al., 2006; Le Ouay and Stellacci, 2015]. “Nano-silver” is even a trademark name (Samsung Company, 2003). AgNPs are used as a new generation of antimicrobials in refrigerators, air conditioners, computers keyboards, etc. [Rai et al., 2009] They are also exploited for their antimicrobial properties to prevent of algal fouling [Russell and Hugo, 1994]. Although some of these effects are known since Antiquity, and the number of industries using AgNPs in their products is rapidly increasing nowadays, the exact mechanisms at molecular level are still poorly understood. In general, the antibacterial activity and toxicity of AgNPs is reported in terms of a dose, which should be respected for the purpose of drawing benefits rather than suffering hazards. It seems more objective to consider the beneficial effects of these products to prevent microbial contamination versus their potentially toxic risks. Nevertheless,

knowledge on the causes and the consequences provoked by the AgNPs is strongly required in order to completely reveal the potentialities of using these nanocomposite materials.

One of the most widespread applications of AgNPs based nanocomposites is the antibacterial coating. It is generally acknowledged that the microbial adhesion represents a major complication for all biomedical applications. To inhibit the development of biofilm on a surface, one possibility is to use coatings containing an antibacterial agent as AgNPs, which are excellent candidates for supporting simultaneously high antibacterial efficiency and huge enhancement of vibrational and luminescent signals originating from molecules located in their vicinity. We would like to exploit this ambivalence by means of specific dielectric layers containing AgNPs.

The objectives of this PhD work is to develop multifunctional nanocomposites based on Ag nanoparticles embedded in dielectric allowing controlled release of the antibacterial agent. This should allow both to target the type of microorganism to fight and to deliver it the right dose for its inhibition, while preserving the surrounding microflora. To achieve these objectives we propose to use the multifunctionality of Ag nanoparticles, which are both plasmonic antennas for detecting interaction with microorganisms and ion reservoirs known for their antibacterial properties. In order to stabilize the nanoparticles and control the toxic dose (i.e. the released  $\text{Ag}^+$  ion concentration) the AgNPs will be embedded in dielectric matrices. Ag nanoparticles with adjusted size and density will be positioned at varying distances from the surface of the substrate, on which microorganisms will adhere. These different degrees of freedom provide precise control of the amount of  $\text{Ag}^+$  released.

To achieve these objectives, two prerequisite steps are requested:

- (i) To assess the ability of the AgNPs embedded in dielectrics to release controlled amounts of ionic Ag ( $\text{Ag}^+$ ) and/or AgNPs, both responsible of the biocide effect. **This point is the core of this work.** The originality of our approach is here twofold. First, it is based on rational engineering of these AgNPs based nanocomposites: the nanoparticles are embedded in dielectric matrices which will allow fine control over the Ag release by controlling the NPs structural characteristics. Second, the Ag release will be evaluated by an original method using green algae as biosensors. Hence, the short-term toxicity of AgNPs to photosynthesis in *Chlamydomonas reinhardtii* will be studied using fluorometry and the silver release will be measured through inductively coupled plasma mass spectrometry.
- (ii) To perform a detailed analysis of the localization and interactions of molecules and proteins deposited on the surface of these substrates containing buried AgNPs by using enhanced optical imaging and molecular spectroscopies. **This step will be just touched in the last chapter of this manuscript.**

This work, performed in co-direction between CEMES and LAPLACE, is at the interface between material science and biology.

**Chapter I** gathers the state-of-the-art of the different facets that constitute this work: the elaboration of Ag based nanocomposites using physical methods, the interaction of AgNPs with their environment (air and water), the biological activity of AgNPs and their particular optical (plasmonics) properties. The main experimental (elaboration and characterization) techniques used during this PhD work are described in **Chapter II**.

Two physical approaches were used to elaborate these nanocomposites: (i) Low Energy Ion Beam Synthesis (LE-IBS) and (ii) combined silver sputtering and plasma polymerization. These techniques allow elaboration of a single layer of AgNPs embedded in silica films at defined nanometer distances (from 0 to 7 nm) beneath the free surface. The first technique (LE-IBS of AgNPs embedded in silica layers) has been developed at CEMES in a previous work [Carles et al., 2009; Benzo et al., 2013] but the amount of Ag that can be introduced in the dielectric is limited, limiting hence the size, density and surface fraction of the formed AgNPs. For this reason, a complementary technique based on plasma deposition has been developed in this work at LAPLACE and is presented in **Chapter III**.

The structural properties and optical of the nanocomposites were studied by transmission electron microscopy, reflectance spectroscopy and ellipsometry. This last technique, coupled to modelling based on the quasi-static approximation of the classical Maxwell-Garnett formalism, allowed detecting small variations in the size and density of AgNPs. The potentiality of this technique for characterizing our system is treated in **Chapter IV**.

**Chapter V** is the core of this work and is focused on the ability of our embedded AgNPs to release  $\text{Ag}^+$  ions when submersed in water. For this assessment, an original method, implying green algae as biosensors was employed. This work has been performed at Instituto Pirenaico de Ecología (IPE-CSIC) laboratory in Zaragoza (Spain) during 2 stays of one month each.

The last part of this work, described in **Chapter VI** is dedicated to the study of the structural stability and adsorption properties of *Discosoma Red* (DsRed) fluorescent proteins on these dielectric surfaces. This work has been performed in close collaboration with Laboratoire de Génie Chimique (LGC) in Toulouse.



# Chapter I: State of the Art

---

## 1. Introduction: bactericide activity of silver and “nanosilver”

Silver species (salt, powder, nanoparticles, etc.), even in low concentration, possess very high activity (that is, the capacity to disturb cell biochemical processes) against a broad range of microbes (antibacterial [Sondi and Salopek-Sondi, 2004], antifungal [Panáček et al., 2006], antiviral [Elechiguerra et al., 2005a] capabilities) and parasites, yet presenting very little systemic toxicity toward humans [Rai et al., 2009; Schröfel et al., 2014]. This harmful effect is mainly due to the interaction between cells and  $\text{Ag}^+$ , which are released in aqueous media from silver structures [Liu and Hurt, 2010]. In particular ionic Ag ( $\text{Ag}^+$ ) is a soft Lewis acid that has affinity to sulphur, but also to nitrogen. Thereby, there are many possibilities for the  $\text{Ag}^+$  to disturb biochemical processes of cell, *e.g.* interacting with thiol ( $-\text{SH}$ ) and amino groups ( $-\text{NH}_2$ ) of proteins, with nucleic acids, with cell wall, and with internal cell components (plasma membrane, DNA, ribosome, protein, enzyme) [McDonnell and Russell, 1999; Chernousova and Epple, 2013]. These multifaceted bactericidal mechanisms acting in synergy to perturb a broad range of targets in the cell metabolism are the key to low microbial resistance rates observed towards elemental silver. In fact, the microorganisms would have to develop a host of simultaneous mutations to protect themselves from this type of attacks.

### 1.1 History of silver use in human life

The antimicrobial properties of silver in the form of different silver compound, *i.e.* metallic silver or silver salt, are known to successfully fight infections and prevent spoilage since time immemorial. For example, going as far back as to the ancient Greece and Rome the antimicrobial property of silver was exploited by using Ag pots, vessels and coins to keep water sterile [Brett, 2006, Silver et al., 2006]. This particular application is preserved even today. The ionic silver is currently used for purifying and storing water on the space shuttle fleet and international space station [Barillo and Marx, 2014]. Further, since the seventeenth century by varying the concentration of Ag compounds, *i.e.* silver nitrate ( $\text{AgNO}_3$ ) or silver sulfadiazine ( $\text{C}_{10}\text{H}_9\text{AgN}_4\text{O}_2\text{S}$ ), Ag compounds have been applied for the treatment of burns, chronic wounds and several bacterial infections [Klasen, 2000; Castellano et al., 2007; Rai et al., 2009; Barillo and Marx, 2014]. The discovery of penicillin by Alexander Fleming in 1929 and the consecutive emergence of several antibiotics in 1940, made that the use of silver compounds has been minimized for the treatment of bacterial infections. The recent development of antibiotic-resistant microorganisms was prompting to the clinicians to return their attention to silver wound dressings containing various levels of silver amount [McDonnell and Russell, 1999; Chopra, 2007]. In the present scenario, Ag nanoparticles (AgNPs) sometimes called “nano-silver”, have emerged up as innovative and powerful antimicrobial agents with high efficacy owing to their high

surface area to volume ratio, possessing high thermal stability and low volatility, and maintaining most importantly lower toxicity to humans [Foldbjerg and Autrup, 2013; Barillo and Marx, 2014]. Besides, AgNPs can release continuously a quite high concentration of ions over a long time. Beyond the highly efficient  $\text{Ag}^+$  reservoir, AgNPs have intrinsic antibacterial properties that do not depend on the elution of  $\text{Ag}^+$ . In fact, the AgNPs can induce the production of Reactive Oxygen Species (ROS), such as oxygen superoxide  $\text{O}_2^-$  that can potentially be formed at the surface of the AgNPs inside the cell or directly can damage and penetrate the cell wall and plasma membrane [Schröfel et al., 2014]. To illustrate these processes some examples will be given in section 5 of this chapter.

## 1.2 Recent applications of Ag compounds and AgNPs as antimicrobial agent

In medicine the Ag compounds and “nano-silver” are exploited in diverse forms ranging from silver based dressings, burn treatment, wound dressings, dental materials, AgNPs impregnated textile fabrics, silver coated medicinal devices, etc. [Duran et al., 2007; Rai et al., 2009]. Different examples of the usefulness for human health of both Ag compounds and AgNPs are presented in figure I.1 [Chaloupka et al., 2010]. Beyond the known antibacterial effects, there are also recent evidences that AgNPs possess a potential anti-inflammatory [Nadworny et al., 2008] and anti-tumor [Ortega et al., 2015] effects and, they can accelerate wound healing [Tian et al., 2007; Sundaramoorthi et al., 2009].

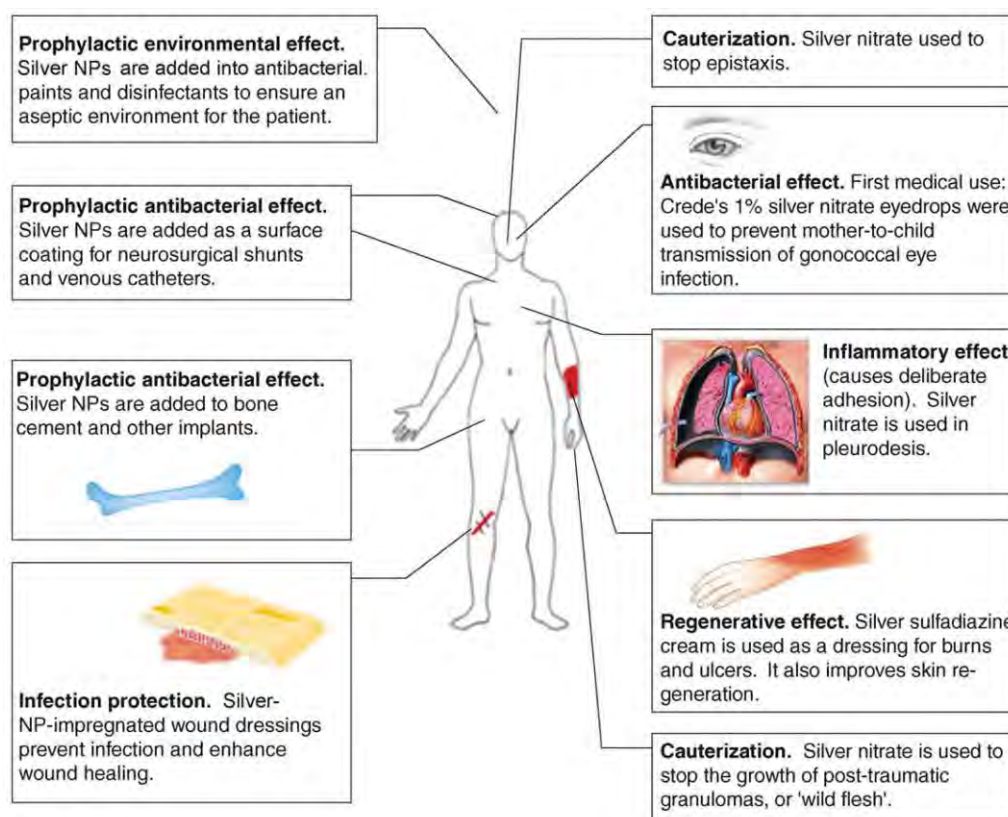


Figure I.1: Uses of Ag compounds (right-hand side) and AgNPs (left-hand side) in medicine for human health. From [Chaloupka et al., 2010].

In food industry and consumer products “nano-silver” has been integrated into various materials to inhibit the growth of microorganisms. This is useful for food industry to preserve the aliments within longer time (spoilage control). Some examples in the food domain can be found in food packaging or for refrigerator surfaces [Chaudhry et al., 2008]. In consumer area, *i.e.* water or air quality and personal healthcare, AgNPs are applied inside water or air filters for disinfection, or to elaborate antimicrobial surfaces of electronic appliances, to product odor-resistant textile fabrics and cosmetic products such as deodorants [Rai et al., 2009].

Because of their antimicrobial properties, the AgNPs have the potential of impacting on human and environmental health. These issues have been addressed by no less than 25 reviews during the period 2008–2015 [Hansen and Baun, 2012; Reidy et al., 2013; Haider and Kang, 2015; Le Ouay and Stellacci, 2015]. The development of reliable diagnostic methods for evaluating the biological activity of AgNPs, and to disentangle the contribution of the silver ions and silver nanoparticles to the whole antibacterial effect of AgNPs [Agnihotri et al., 2013], would be an asset for the appropriate design and use of silver-based nanotechnologies. The modulation of the silver ion release from AgNPs would eventually allow the release of the appropriate dose of  $\text{Ag}^+$  for biomedical uses and the environmental protection [Liu et al., 2010; Sabella et al., 2014]. One of the methods for controlling the Ag release from AgNPs is their inclusion in nanocomposites. The host matrices can stabilize AgNPs and at the same time allow a controlled release of ionic silver to inhibit the microbial colonization and biofilms formation in biological and medical applications [Despax et al., 2011; Beer et al., 2012; Alissawi et al., 2013]. In this PhD thesis, two physical approaches were applied to elaborate the nanocomposite structures: (i) low energy ion beam synthesis and (ii) combined silver sputtering and plasma polymerization. These techniques allow fabricating of a single layer of AgNPs embedded in thin silica films at controlled nanometric distance beneath the free surface. The physical principles of these two elaboration techniques are described in **section 2 and 3** of this chapter. The biological activity of AgNPs being closely related to ionic Ag ( $\text{Ag}^+$ ) activity, the way that the AgNPs interact with the environment (air and water) and give rise to this  $\text{Ag}^+$  release will be discussed in **section 4**. The biocide properties of AgNPs and the way they interact with micro-organisms will be described in **section 5**. At last, in **section 6**, another facet of AgNPs, *i.e.* their particular optical properties, that have lead in the 2000’s to the emergence of a growing thematic called “*plasmonics*” [Maier et al., 2001] will be described.

## **2. Ion Beam synthesis (IBS) of AgNPs in silica matrix**

### **2.1. Principles of Ion Beam Synthesis of nanostructures**

Nanostructure formation by means of ion beam synthesis (IBS) has now been studied for many years, but has not lost its initial appeal. With the combined use of ion-solid interactions that lead to far-from-equilibrium states and thermodynamic processes through which these could relax toward equilibrium,



tiny nanostructures of controlled composition can be formed in virtually any matrix. By now literature contains a wealth of publications on different ion-matrix combinations that potentially might trigger applications of these novel nanoscale materials. A review of various dielectrics with implanted silver nanoparticles can be found in references [Stepanov, 2010; Stepanov et al., 2013]. The basics principles of ion implantation are described in Chapter II.

Phenomenologically, IBS can be divided into several stages, described below.

### 2.1.1 Accumulation and supersaturation

After ions have been slowed down by electronic and nuclear stopping to thermal energy, they are incorporated into the target material. Thermal activation at common implantation temperatures is usually too low to allow for impurity diffusion over larger length scales. The impurity distribution remains frozen in, especially at low impurity concentrations. This is the case for low diffusing species as of  $\text{Si}^+$  implanted at high doses into  $\text{SiO}_2$  matrices [Bonafos et al., 2004; Bonafos et al., 2012]. This is not the case for fast diffusing species as  $\text{Ag}^+$  implanted in  $\text{SiO}_2$ , as we will see in the following.

### 2.1.2 Nucleation or early phase separation

In high dose implantation, nucleation of NPs can be encountered during implantation and/or during a post-implantation heat treatment. For a given ion-substrate system, the primary nucleation stage can roughly be classified with respect to the diffusion length  $L_{diff} = \sqrt{2D_{diff}t}$  of impurity monomers during implantation, with  $t = \phi_o/j$  the implantation time ( $\phi_o$  being the nominal fluence or dose and  $j$  the ion flux) and  $D_{diff}$  the diffusion coefficient of the implanted species in the matrix. Furthermore, the local accumulation of impurities is function of the ratio  $j / D_{diff}$ . Different scenario can be proposed depending on the comparison of  $L_{diff}$  with the two following characteristics distances [Strobel, 1999]:

- $\tilde{R}$ , which is the radius of the hypothetical sphere defined by  $(4/3)\pi R^3 \bar{c}(\phi) \leq i^*$  ( $\bar{c}(\phi)$  denotes the averaged local concentration after a fluence  $\phi$  has been implanted and  $i^*$  the number of atoms in the critical nucleus).
- $\Delta R_p$  which corresponds to the width of the implanted profile. The ions species are indeed distributed into the matrix according to a Gaussian law around the mean projected range  $R_p$  with a mean square deviation given by  $\Delta R_p$  (see Chapter II).

(i)  $L_{diff} < \tilde{R}$ : this condition states that thermal fluctuation do not initiate nucleation during the implantation process. A thermal treatment is necessary for the phase separation. This is the case of Si or Ge implantation in  $\text{SiO}_2$  at room temperature [Bonafos et al., 2004; Bonafos et al., 2012]. Upon annealing thermal fluctuations could initiate phase separation through the (homogeneous) nucleation of precipitates.

(ii)  $L_{diff} \approx \Delta R_p > \tilde{R}$ : nucleation starts during implantation when the monomer concentration exceeds the nucleation threshold. Due to the implantation profile, the first stable precipitates appear close to  $R_p$ , the projected range of the implantation profile. Since the concentration increase is proportional to the implanted profile, a larger supersaturation is reached in the centre of the profile than in the tails. Accordingly, the critical NP size is supposed to increase in the centre to the tails. In the course of implantation, the nucleation region spreads outside, whereas behind the nucleation front, the growth stage sets in. In this case, the NPs are formed essentially across the whole deposition range with a density roughly proportional to the impurity profile.

(iii)  $L_{diff} \gg \Delta R_p > \tilde{R}$ : the resulting monomer fluxes prevent spreading of the nucleation region across the profile, because in the tails the critical monomer concentration will not be exceeded. Therefore, the nucleation region is restricted close to  $R_p$ .

Implantation modes (ii) and (iii) are usually met for metal implantation into insulators. These processes are named “Ion Beam Direct Synthesis”. This is in particular the case for  $Ag^+$  implanted in  $SiO_2$  for which the high diffusion coefficient allows for the NPs nucleation during the implantation process itself [Carles et al., 2009; Stepanov, 2010]. In the case of low energy ion implantation of  $Ag^+$  (typically less than 10 keV), the implantation profiles are so narrow that the NPs form a plane (delta-layer) located at  $R_p$  [Carles et al., 2009; Benzo et al., 2013].

### 2.1.3 Growth processes

Nucleation can be followed by 3 growth regimes.

**Pure growth:** Second phase precipitates formed by nucleation grow as long as the local monomer concentration is above the equilibrium concentration of these precipitates. All precipitates grow on the expense of the reservoir of dissolved impurity atoms.

**Coarsening and Ostwald ripening:** The monomer concentration decreases during further annealing and a competitive coarsening process called Ostwald ripening. Large NPs grow on the expense of smaller ones, which finally dissolve [Bonafos et al., 2002].

**Coalescence and percolation:** During NP growth, neighboring NPs might touch each other and coalesce to a larger one. This process is more likely for high ion-fluences.

The division of IBS in a set of consecutive stages is to some degree artificial. The borders between the individual steps are rather ill-defined and depend on the specific implantation and annealing parameters. These three stages are resumed in Figure I.2.

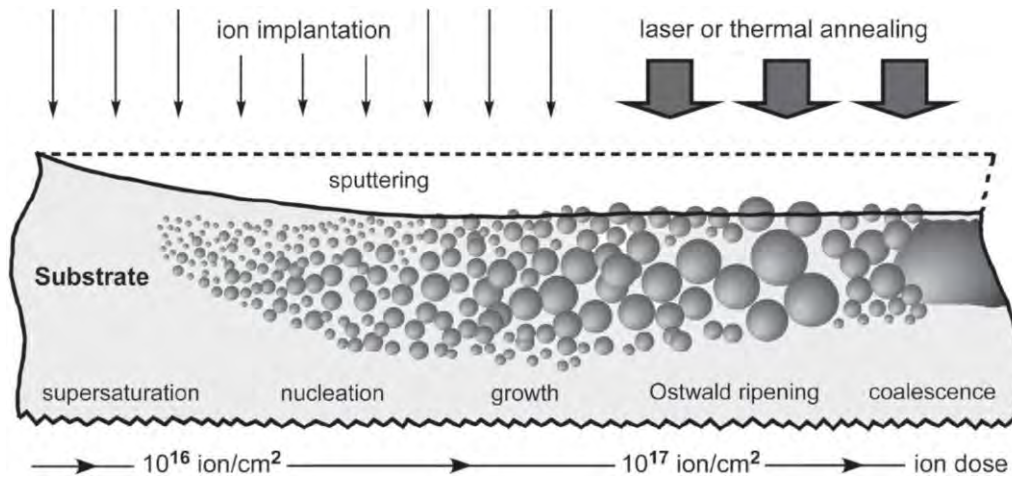


Figure I.2: Basic physical processes (from left to right) involved in the formation of NPs from an implant versus the ion dose with regard to surface sputtering under irradiation. From [Stepanov et al., 2013].

## 2.2. High-fluence ion implantation: reaching far-from-equilibrium states

High-fluence ion implantation as used for IBS leads to cumulative effects as surface erosion by sputtering, target swelling due to the incorporated atoms and ion beam mixing that might alter the target composition and its depth dependence.

**Target swelling:** implanted material has to be accommodated within the host material and requires additional volume there. Consequently, high fluence implantation leads to swelling of the implanted target and distortion of the impurity profile. The total target swelling is roughly given by the equivalent layer thickness of the implanted (deposited) material  $\phi N^{-1}$  with  $\phi$  being the ion fluence (dose) and  $N$  the density of atomic ion species.

**Ion sputtering:** The opposite is achieved by ion sputtering, which is the erosion of the target surface by energetic ions. Part of the recoil cascade created by the ion impact could reach the target surface. Some of such backward recoils will approach the surface with enough energy to escape the surface. During implantation, ion erosion removes target atoms as well as implanted species. Eventually, some equilibrium is reached where on average one implanted atom is sputtered for each introduced ion. The concentration distribution peaks under these conditions at the target surface and falls off over a distance comparable to the projected ion range. For high fluences, where sputtering becomes dominating, the concentration profile becomes asymptotically an error function (instead of a Gaussian distribution for low fluences). We will see in section 2.3.3 that sputtering effects lead to a saturation of the quantity of the Ag introduced and therefore of the average size and surface fraction of AgNPs.

High-fluence ion implantation as used for IBS leads to cumulative effects as surface erosion by sputtering, target swelling due to the incorporated atoms and ion beam mixing that might alter the

### **2.3. Ion beam (direct) synthesis of AgNPs in SiO<sub>2</sub> matrix**

Ion implantation technique, which can control energy and dose amount of ions, is one of the candidate methods to obtain embedded metal nanoparticles in a desired size and depth distribution. As mentioned before, the nucleation of the AgNPs occurs usually during the implantation process of silver ions in silica matrix without the need of any annealing step as widely reported in the literature [Liu et al., 1998; Tsang et al., 2006; Arai et al., 2007; Xiao et al., 2007]. This takes place when the Ag concentration is higher than the solubility threshold, which ranges between 3 and  $14 \times 10^{19}$  atom/cm<sup>3</sup> in silica matrix [Carles et al., 2009], and it is due to the high diffusion coefficient of Ag in silica [Nason et al., 1991; Stepanov, 2010].

#### **2.3.1. Conventional energy ion beam synthesis**

In the literature, most of the papers dealing with the synthesis of AgNPs in silica matrix concern the conventional energy range, typically of the order of 100 keV. At these energies, a large AgNPs band is usually formed following the profile of implanted ions with the biggest ones in correspondence of the projected range  $R_p$  [Tsang et al., 2006; Yang et al., 2014]. The exo-diffusion of Ag is often observed, leading to the formation of a plane of big AgNPs close to the silica free surface [Ren et al., 2007; Xiao et al., 2007; Takahiro et al., 2012]. For similar reasons, a plane of smaller AgNPs can be observed at the interface between silica and its supporting silicon substrate [Takahiro et al., 2012]. Owing to their optical properties, these nanocomposite materials have been studied for different application domains such as optical detectors, laser, sensor, imaging, display, solar cell, photocatalysis, photoelectrochemistry and biomedicine [Zhang, 2009]. For example, exploiting their large third-order nonlinear susceptibility with picoseconds response time, these materials are also interesting for the elaboration of nonlinear optical devices [Takahiro et al., 2012]. Another example concerns the field emission properties of AgNPs elaborated by ion beam synthesis for applications in flat panel displays and as an electron source in vacuum microelectronic devices [Tsang et al., 2006]. There is no example in the literature of the use of AgNPs ion beam synthesized in SiO<sub>2</sub> used for antibacterial coatings.

#### **2.3.2. Low Energy Ion Beam Synthesis (LE-IBS)**

Only few work concern low energy (typically less than 30 keV) implantation of Ag<sup>+</sup> ions for the synthesis of AgNPs embedded in silica matrix. LE-IBS leads to non-uniform distribution of Ag<sup>+</sup> ions in the depth of the silica matrix, which is different from the Gaussian profile traditionally predicted by statistical theory. This is mainly due to the effective atom sputtering of silica matrix free surface during the implantation, the implantation profile being very close to the surface. At these energies, both sharp size and spatial distributions of nanoparticles are obtained [Stepanov, 2010]. Some of these works concern implantation of negative silver ions (Ag<sup>-</sup>), which is possible in specific ion implanters and requires a mandatory subsequent heat treatment to nucleate the AgNPs [Arai et al., 2006; Arai et

al., 2007]. A recent research about the synthesis of quasi two-dimensional AgNPs arrays involves the irradiation of silica substrate by Xe ion before the Ag ion implantation at low energy (21 keV). This irradiation process allows the formation of localized defects inside the silica matrix, which in turn will be preferential nucleation and growth sites for AgNPs [Wang et al., 2013].

### **2.3.3. Previous work at CEMES**

At CEMES, *Ultra Low* (i.e., few keV) Energy Ion Beam Synthesis (ULE-IBS) was first used in the 2000's to synthesize a single plane of Si nanocrystals embedded in the thin gate oxide of MOS devices, for nonvolatile memory applications [Bonafos et al. 2005]. We recently extended this concept to the synthesis of a single plane (delta-layer) of AgNPs is embedded near the free surface of a SiO<sub>2</sub> layer thermally grown on a Si wafer [Carles et al., 2009]. In figure 1.3 (left), a typical TEM image of a cross section on an implanted sample reveals the presence of AgNPs in a single plane located a few nanometers under the surface. As expected these particles are formed during the implantation process; they are spherical, crystalline, homogeneously distributed and made of pure silver, as revealed by HREM observation (inset of Fig.1.3). They are homogeneously distributed. Different architectures consisting of three-dimensional (3D) patterns of AgNPs embedded in silica have been thus conceived to simultaneously exploit the optical interference phenomenon in stratified media and LSPR of metal nanoparticles [Carles et al., 2011]. These structures are based on a simultaneous control of optoelectronic properties at three scales (3S) ( $\sim 2/20/200$  nm) and along three directions (3D). In particular, the thickness of the dielectric layer has been chosen to have antireflective properties imposing maximum of the electric field close to the surface. It has been shown that the reflectance contrast is strongly enhanced when resonance conditions between the stationary electromagnetic field in the dielectric matrix and the LSPR in the AgNPs are realized. Silica has been preferred to SiN as antireflective and embedding layer for the AgNPs despite the highest electromagnetic confinement obtained in the last matrix, as mentioned previously. This choice is justified by the better control of the matrix properties (porosity, density) obtained in particular for thermal silica. More details in the optical and vibrational properties of these systems can be found in [Carles et al., 2009; Farcau et al., 2010; Carles et al., 2011; Bayle et al., 2014; Bayle et al., 2015; Carles et al., 2015]. In the following section, the main results concerning the control of the main characteristics of the AgNPs delta layer (distance to the surface, average size, surface density) are briefly resumed. More details can be found in refs [Benzo et al., 2011; Benzo et al., 2013].

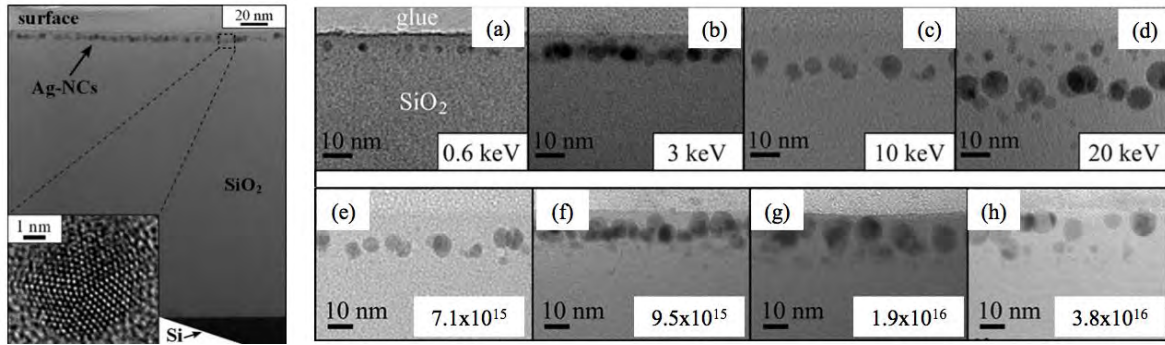


Figure I.3: Left side: XS-TEM bright-field image of a plane of AgNPs elaborated by ULE-IBS (energy 3 keV and dose  $4.7 \times 10^{15}$  ion/cm<sup>2</sup>) with in inset HREM image of a AgNP. Right side: zoom of XS-TEM images of the samples implanted with, from (a) to (d) an increasing energy and doses leading to a fixed concentration of 20 at.% and from (e) to (g) a fixed low implantation energy (10 keV) and increasing doses. From [Benzo et al., 2013].

**Effect of implantation energy.** Controlling the kinetic energy of the implanted ions in the low energy range offers the possibility to control in the nanometer range the subsurface positioning of the delta-layer of metal nanostructures. Hence, the distance to the surface can be tuned from 3.5 to 12 nm when the implantation energy increases from 0.6 to 10 keV (Fig. I.3, right side, (a) to (c)). These values are in good agreement with the projected range  $R_p$  of the implanted profile calculated by TRIDYN [Möller and Eckstein, 1984]. The further increase of the implantation energy leads to an expected broadening of the implanted profile and to the formation of a spatially distributed band of NPs (Fig. I.3(d)). Energy increase also leads to a slight growth of the mean particle size, from 2.5 nm to 4.9 nm due to a widening of the implantation profile [Benzo et al., 2013].

**Effect of implantation dose.** The three main effects are related to the increase of the implanted dose are: (i) shift of the nanoparticles towards the surface, (ii) the loss of the 2D organization of AgNPs, and (iii) the growth of the Ag nanoparticles (Fig. I.3, (e) to (h)). In particular, high implanted doses lead to the formation of bimodal size distribution of AgNPs with large nanoparticles located near the surface (up to touch the free surface) and small ones deeper into the silica matrix. [Benzo et al., 2013] This is due to Ag diffusion in the volume, where the Ag excess becomes then larger than the solubility threshold, allowing for nucleation of additional small Ag nanoparticles.

**Dose saturation.** A saturation of the average size of the AgNPs is clearly observed when increasing the implantation dose. In addition, the quantity of Ag experimentally measured in the nanoparticles from TEM images is much smaller than the nominal implanted dose, especially in the high dose range [Benzo et al., 2013]. Saturation effects have been predicted in the literature by ballistic simulations, and attributed to surface sputtering and stoichiometry changes during implantation [Stepanov et al., 2000; Stepanov, 2010]. Nevertheless, the measured dose saturation (around  $10^{16}$  atoms/cm<sup>2</sup>) is also much lower than those predicted using TRIDYN. This discrepancy has been attributed as originating in diffusion effects. Indeed, in addition to Ag enrichment in the region close to the surface due to pure

ballistic effects, the Ag redistribution results in an increase of the quantity of Ag at the surface vicinity. Ag atoms are sputtered instead of Si and O atoms causing a decrease of the total amount of Ag finally remaining in the layer. At some point, the nanoparticles themselves are sputtered by the ongoing implantation. [Benzo et al., 2013].

Hence, ULE-IBS is a promising technique for the wafer-scale fabrication of AgNPs planar arrays embedded in a silica layer on a silicon substrate. The main advantage of this method remains the direct embedding of the AgNPs in a transparent dielectric matrix, which avoids their dissemination and their alteration, while preserving their plasmonic properties and keeping a flat and reusable surface. In particular, a post-implantation annealing strongly limits silver oxidation, which otherwise excludes the use of AgNPs on free surfaces [Benzo et al., 2011]. An overview of the reactivity of AgNPs in contact with environment will be discussed in Section 4 of this chapter. Nevertheless, the saturation of the quantity of Ag introduced in the matrix saturates at high doses thus limiting the control of the size and surface (and volume) fraction of the AgNPs. Hence, AgNPs with average size significantly larger than 10 nm and coverage surface fraction larger than 20% could not be reached. The fabrication of percolated array of NPs, which is easily obtained by ULE-IBS of Si at high dose in SiO<sub>2</sub> [Bonafos et al., 2005] cannot be obtained in the case of Ag. For this reason, we have developed in this work a new method, using plasma deposition techniques, in order to fabricate a plane of large (>10 nm) AgNPs embedded in silica at controlled nanometric distances from the surface, with high surface coverage (much larger than 20%). This method involves silver sputtering followed by Plasma Enhanced Chemical Vapor Deposition (PECVD), which are described in the next section.

### **3. Plasma deposition techniques for synthesis of AgNPs in silica matrix**

Plasma based deposition of thin films is largely applied in industrial applications [Lieberman and Lichtenberg, 2005]. Starting in the microelectronic domain in the early 80's of the last century, the plasma technologies for deposition have now place in different areas of our every day's life, like for example in optics for coating layers, for surface treatment in the food industry, for biomedical applications, in photovoltaics', etc. Depending on the type of the used gas discharge, the main plasma characteristics (electron density and electron energy), the reactive gases injected as precursors and the gas pressure, one can obtain a quite large variety of composition of deposited thin layers, including elaboration of nanocomposite materials. Principally, the Physical Vapor Deposition (PVD) and the Plasma Enhanced Chemical Vapor Deposition (PECVD) are used in the surface modification of a wide range of substrates. In particular, PVD involves the evaporation or sputtering of a solid material while in PECVD the plasmas are used to activate the chemical precursors and consists of applying different types of gas discharges. The advantage of these deposition methods concerns the huge versatility and the excellent control of thin film growth at micrometric and nanometric scale [Kay and Hecq, 1984; Massines et al. 2004; Despax and Raynaud, 2007; Kortshagen, 2009; Belmonte et al.,

2011; Despax et al., 2011; Lukaszewicz, 2011]. Industrial plasma reactors are usually supplied with alternative current (AC) and depending on the used gas discharge they work in the whole range of pressure variation, from low pressure up to atmospheric pressure. Without loss of generality the discussion here is limited to an axially-asymmetric radio-frequency (RF) capacitively-coupled discharge sustained at 13.56 MHz at low gas pressure. This plasma deposition process has been chosen to elaborate a single layer of AgNPs embedded in the silica layer for our studies. At first, we recall the principals of plasma physics and the key points of using plasmas for thin film deposition processes.

### 3.1. Generalities on plasmas and in particular of RF capacitively-coupled discharges

Ignition of a gas discharge between two conductive plates requires an electric field with strength higher than the dielectric strength of the medium. For this reason, one applies a voltage higher than the breakdown voltage  $V_b$  depending on the pressure  $p$  and the nature of the gas as well as the inter-electrode distance  $d$ . This breakdown voltage is defined by the Paschen's law:  $V_b = f(p \times d)$  [Lieberman and Lichtenberg, 2005; Moisan and Pelletier, 2006;]. When the applied field is sufficiently high, the free electrons present in the media acquire energy required to ionize the atoms/molecules of the gas after electron impact. The gas ionization allows development of the electron avalanche. This charge multiplication phenomenon leads to a self-sustained discharge, called plasma [Lieberman and Lichtenberg, 2005; Moisan and Pelletier, 2006;]. Plasma is a collection of charged particles (electrons and ions) free to move in random directions. One of the main characteristics of the plasma is its global electrical neutrality (Fig. I.4), the other specific characteristic being its collective behavior.

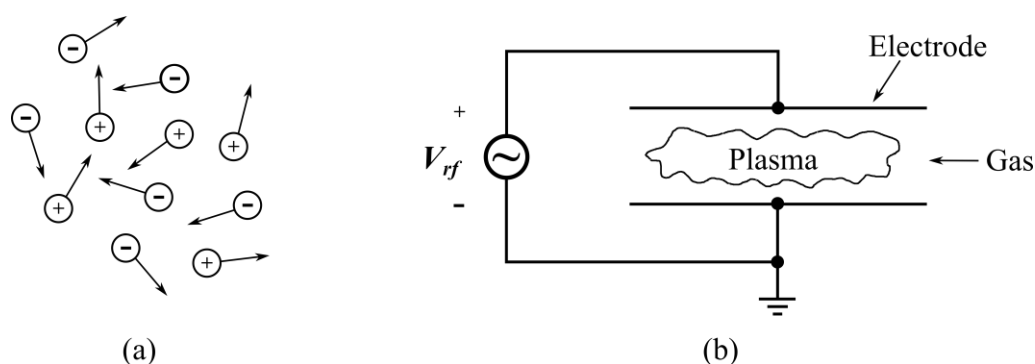


Figure I.4: Schematic view of (a) a plasma and (b) a discharge. From [Lieberman and Lichtenberg, 2005].

The laboratory plasmas and their industrial counterparts are usually far from thermodynamic equilibrium. The average energy of electrons in the plasma (characterized by the associated temperature  $T_e$ ) is much greater than that of the ions ( $T_i$ ) with the latter being not much far from the room temperature, *i.e.*  $T_e \gg T_i$ . The electrons give rise to energy transfer toward heavy species of gas



(atoms, molecules) through elastic collisions for momentum transfer or inelastic collisions for excitation, dissociation and ionization of these species.

### 3.1.1. Density of species

The species that can be found in the plasma are: electrons  $n_e$ , positive  $n_i^+$  and negative  $n_i^-$  ions, neutral species (atoms and/or molecules)  $n_0$ , radicals  $n_r$  and species in an excited state. The density of a given type of species is defined by the average number of these species per unit volume and time. Owing to the global neutral character of the plasma, the electron density is almost identical to the density of positive ions. In the general case of presence of negative ions and multi-charged ions, the quasi-neutrality condition takes the form:

$$-(e n_e + e n_i^-) + \sum_z Z e n_{iz}^+ = 0. \quad (\text{I.1})$$

In laboratory plasmas sustained at low pressures the quasi-neutrality condition is fulfilled and the density of charged species is typically in the range of  $10^{10} \div 10^{12} \text{ cm}^{-3}$  [Moisan and Pelletier, 2006].

### 3.1.2. Plasma frequency

After applying a local perturbation to initially neutral plasma, the charged species (electrons and ions) undergo a displacement from their equilibrium position. Under electric field, electrons displace collectively in the opposite direction with respect to the positive ions determining a temporary separation. Space charge field develops counteracting this displacement and leading the species toward their initial equilibrium state. This behavior of charged species defines another important characteristic of the plasma: the plasma frequency  $\omega_p$ . Hence, the angular *electron plasma frequency* is:

$$\omega_{pe} = \sqrt{\frac{n_{e0} e^2}{\epsilon_0 m_e}}, \quad (\text{I.2a})$$

where  $n_{e0}$  is the density of electrons in unperturbed plasma and  $m_e$  is their mass,  $e$  being the elementary charge and  $\epsilon_0$  the vacuum permittivity. In a similar way, one can define the *ion plasma frequency* as:

$$\omega_{pi} = \sqrt{\frac{n_i e^2}{\epsilon_0 m_i}}, \quad (\text{I.2b})$$

where  $n_i$  and  $m_i$  are the density and mass of ions, respectively.

The value of plasma frequency affects the ability of the charged species to follow the periodic variation of the applied electric field. Therefore, if the frequency of electric field is greater than the plasma frequency of a type of charged species, this kind of species cannot follow the oscillations of the electric field. The common excitation frequency of RF discharges at 13.56 MHz allows instant oscillation of electrons (electron plasma frequency of about 1 GHz). Because  $m_i \gg m_e$ , the ion plasma

frequency is much lower than the electron one (ion plasma frequency of approximately 1 MHz). For RF discharges, the ions remain virtually immobile and only experience the averaged value of the oscillating electric field.

### 3.1.3. Plasma potential $V_p$ and electrostatic sheaths

For a RF discharge with electrodes of given cross sectional area separated by a given distance, the sinusoidal current flows across the electrodes. Because of the quasi-neutrality, the density of electrons and ions is equal almost everywhere except within thin sheaths near the electrodes (or near the reactor walls) where the  $n_i^+ \gg n_e$  (Fig. I.5) [Lieberman and Lichtenberg, 2005].

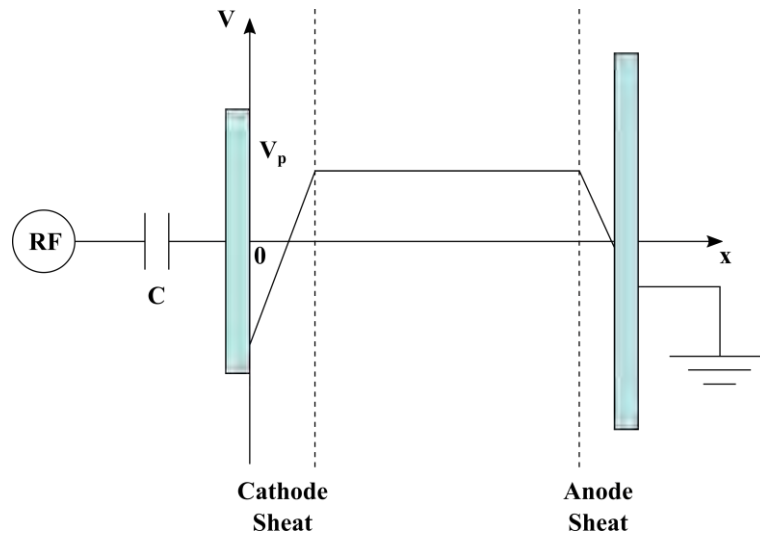


Figure I.5: The schematic formation of plasma sheaths in axially-asymmetric RF capacitively-coupled discharge.

It is possible then to distinguish three different zones: plasma (central zone) and two electrostatic sheaths (near electrodes). Because of the formation of these sheaths, a drop in the electrical potential occurs in these zones. On contrary, a stationary potential  $V_p$  (called *plasma potential*) takes place at the plasma region. In these conditions, the space charge region is defined by the *electrostatic sheath* whose width  $l_g$  is represented by [Chapman, 1980]:

$$l_g = \lambda_D \left[ \frac{e(V_p - V_f)}{k_b T_e} \right]^{3/4}, \quad (I.3)$$

where  $V_f$  is the floating potential (due to the presence of a foreign body in the plasma),  $\lambda_D$  is the Debye length (*i.e.* the maximum distance at which the plasma quasi-neutrality condition breaks down). These sheaths are then called capacitive and the RF capacitively-coupled discharge.

### 3.1.4. Self-bias potential $V_{dc}$ of the RF electrode

In an asymmetric RF discharge (Fig. I.5) the ratio between the potential located at the sheath of the smaller electrode ( $V_{g1}$ ) and the one of the larger electrode ( $V_{g2}$ ) varies following the inverse of ratio of the electrode surfaces ( $A_i$ ) at power  $m$ .

$$\frac{V_{g1}}{V_{g2}} = \left( \frac{A_2}{A_1} \right)^m. \quad (I.4)$$

For low pressure,  $m$  experimentally ranges between 1.5 and 2 [Pointu et al., 1997]. This relation of electrode surfaces is the source of continuous self-bias potential  $V_{dc}$  on the electrode wherein the RF field is applied with respect to the ground. This asymmetry gives rise to  $V_{g1} \neq V_{g2}$ . If  $A_1 < A_2$ , the self-bias potential of the electrode with smaller area  $A_1$  is generally negative. In addition, the spontaneous polarization is favored by the presence of the capacity that blocks the reverse conduction current from the plasma to the generator [Bergmann, 2014]. Hence, one obtains a variable charge density as function of the polarity of the applied RF field (Fig. I.6).

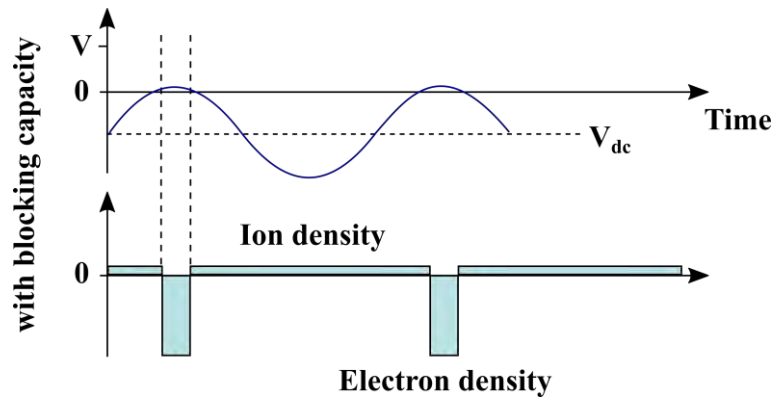


Figure I.6: RF potential and current on the electrode with the blocking capacity. From [Bergmann, 2014].

### 3.2. Sputtering in an axially-asymmetric RF discharge

Sputtering, as deposition process, results from the momentum transfer between incident ions from the plasma and atoms of a solid source (target). There are several sputtering systems for deposition purposes among which: ion beam, DC, RF and magnetron sputtering [Wasa et al., 2004]. In axially-asymmetric RF capacitively-coupled plasma, the efficiency of the sputtering depends among other parameters on the geometrical configuration of the reactor. A strong asymmetry between the two electrodes promotes the sputtering of the smaller electrode (which is often the electrode connected to the RF signal) (Fig. I.5). In an axially-asymmetric RF discharge maintained in argon at low pressure in which the smaller electrode is a silver target, the atoms from the silver target are ejected under the action of bombardment with argon ions ( $Ar^+$ ). To ensure the beginning of the sputtering mechanism, the ions have to acquire threshold energy  $E_s$  following the expression [Bohdansky et al., 1980]:

$$E_s = \frac{2E_B}{\gamma(1-\gamma)} \quad (I.5)$$

where  $E_B$  is the surface binding energy which is approximated by the heat of sublimation and  $\gamma$  is the mass ratio of the impinging ion over the released atom. At low pressure, the sheaths are non-collisional. Thus, ions acquire an energy  $E$  determined by the value of the self-bias potential to bombard the target.

The influence of the RF injected power and of gas pressure on nanoparticle growth can be described as follows. After imposing a specific injected power with the RF generator the estimation of the transmitted energy to the plasma becomes more complex due to the electric line losses. It requires the use of an impedance matching network to maximize the injected power into the plasma [Chapman, 1980]. In addition, in an RF capacitively-coupled discharge, it is more correct to describe the injected power through the self-bias potential. Because of the conduction stating that the output current of the plasma is zero, an increase of injected power intensifies the self-bias potential [Lieberman and Lichtenberg, 2005]. In this case, the bombarding  $\text{Ar}^+$  and free electrons of plasma acquire a higher energy. This leads to a strong intensification of the flow of sputtered silver species (*i.e.* atoms and/or clusters) and determines an increase of the rate of AgNPs growth. As the ion dynamic is strongly involved in the sputtering process, the gas pressure is the second important parameter after the injected power in this process. A gas pressure increase might influence the silver sputtering in the following ways: (i) through an increase of the plasma density, thus the ion density, if quasi-neutrality of the plasma is considered; (ii) through the plasma sheath close to the smaller electrode, mainly through its width and its nature (collisional or collisionless) and (iii) through the effect of scattering of sputtered atoms. The experimental results show that for a fixed injected power the self-bias voltage decreases when increasing the gas pressure [Milliere et al., 2016]. It is due to the thinner plasma sheath close to the powered electrode that will have a larger capacitance per unit area, thus setting up a smaller self-bias voltage. Moreover, the electrons can transfer their energy through elastic collisions to the deposited silver species on the substrate. This allows improving the surface diffusion of these species favoring the AgNPs growth. Summarizing, the AgNPs size is mainly controlled by the balance of two parameters in the gas discharge: injected power and gas pressure.

### 3.3. Elaboration of silica layers by PECVD

The use of silica thin films in many applications in different domains (like optics, food packaging interlayer dielectrics and corrosion protection layer) explains the increasing interest for these films. Among different deposition techniques, the PECVD has become one of the most important thin film deposition processes because of the possibility of preparing good quality coatings at low substrate temperature. High quality silica thin films are deposited by plasma processes from the most utilized silicon precursors (silane ( $\text{SiH}_4$ ), Tetraethoxysilane (TEOS;  $\text{Si}-(\text{O}-(\text{C}_2\text{H}_5))_4$ ) or Hexamethyldisiloxane

(HMDSO;  $O-(Si-(CH_3)_3)_2$ ) together with noble gas (normally helium or argon) and mixed with molecular oxygen ( $O_2$ ) or nitrous oxide ( $N_2O$ ). When using organosilicon precursors the gases forming the mixture are added to the organosilicon vapor in order to oxidize organic groups and to deposit near stoichiometric silica film. Both TEOS and HMDSO are non-toxic, nonexplosive, and much safer than silane. HMDSO has the further advantage of a higher room temperature vapor pressure which offers easier use.

**Deposition of silica film by PECVD in RF capacitively-coupled discharge at 13.56 MHz.** HMDSO molecule presents the advantage to be in liquid stable form at  $25^\circ C$  and atmospheric pressure (boiling point  $101^\circ C$ ) with purity of 99.5% in the gas form. However, the pure use of HMDSO in the plasma process yields polymer-like films on a substrate temperature as low as  $50^\circ C$  [Tkachuk et al., 1968]. This is an advantage for temperature sensitive substrates like polymers [Milliere et al., 2016]. A *Cram* representation of HMDSO molecule is illustrated in figure I.7.

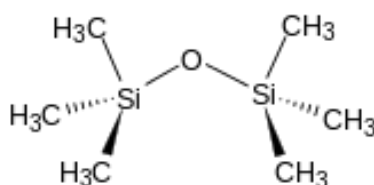


Figure I.7: The *Cram* representation of the HMDSO molecule ( $C_6H_{18}OSi_2$ ).

Formation of organosilicon film from HMDSO precursor by PECVD was studied for the first time in the 70s [Vasile and Smolinsky, 1972]. The results of this study indicate that the deposited film is composed of an organosilicon polymer of type  $SiO_xC_yH$ . Hence, the elaboration of silica film from plasma polymerization of HMDSO requires the elimination of carbon (C) and hydrogen (H) from the organosilicon polymer. To perform this, two operating parameters have to be taken in account: injected power in the plasma and introduction of oxygen in the gas mixture.

**Injected power in the plasma.** An increase of the injected power per monomer flow provokes a stronger fragmentation of the HMDSO molecules due to the increase of the electron energy [Lamendola et al., 1997; Aumaille et al., 2000; Goujon et al., 2004; Despax and Raynaud, 2007]. However, the dissociation of the HMDSO molecules may be not complete whether electron density and temperature are lower, as this is the case in RF discharges. In situ FTIR absorption analyses of a pure HMDSO gas for two different RF injected powers (100 and 150 W) show that the absorption bands that are the fingerprint of  $CH_3$ ,  $Si(CH_3)_x$ ,  $Si-O-Si$  in the HMDSO molecule decrease when the RF injected power is increased (Fig. I.8, left image) [Goujon et al., 2004] and (Table I.1) [Despax and Raynaud, 2007]. FTIR analysis of thin films deposited after HMDSO decomposition in the plasma when the RF injected power increases is represented in figure I.8, right image [Despax and Raynaud, 2007].

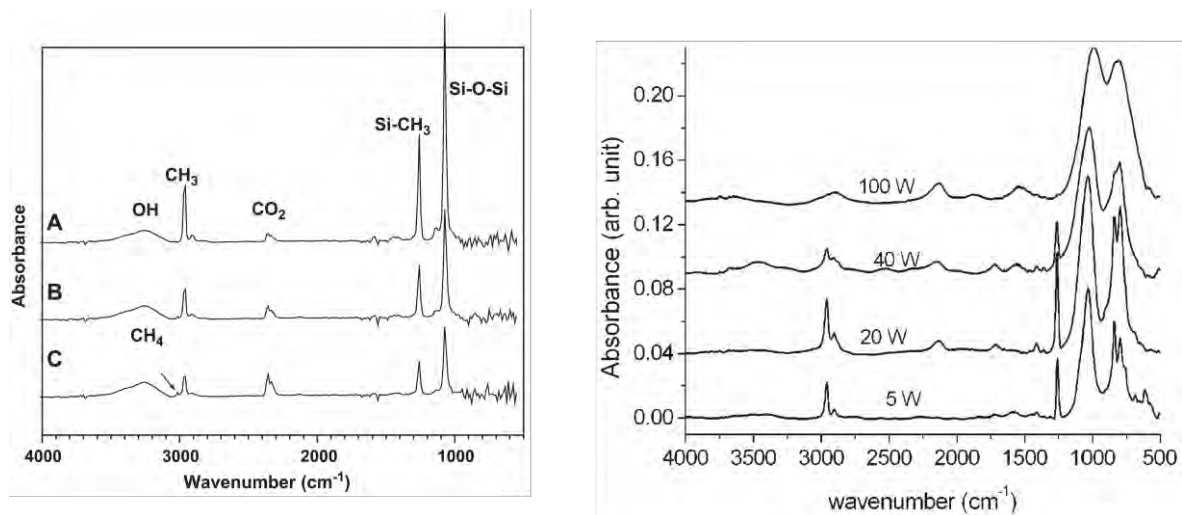


Figure I.8: FTIR spectra obtained under different RF injected power of: (left image) pure HMDSO gas (in situ measurement at RF injected power: (A) plasma off; (B) 100 W; (C) 150 W. No absorption of the plasma species can be investigated below  $1000\text{ cm}^{-1}$ ). From [Goujon et al., 2004]. (Right image)  $\text{SiO}_x\text{C}_y\text{H}_z$  deposited films (spectra normalized with respect to the film thickness). From [Despax and Raynaud, 2007].

A higher dissociation of the precursor and of its by-products occurs when the injected power is increased. Increasing the RF injected power up to 100 W, leads to the  $\text{CH}_3$  band and  $\text{Si}(\text{CH}_3)_x$  peak decrease until complete disappearance, while the aromatic  $\text{C}=\text{C}$  bands ( $1539\text{ cm}^{-1}$ ) appear, confirming the dissociation and the subsequent polymerization of HMDSO molecule [Despax and Raynaud, 2007]. Quantitative analysis of O/Si, C/Si and H/Si ratios as a function of the RF injected power carried out by Rutherford Back Scattering spectrometry (RBS) and Elastic Recoil Detection Analysis (ERDA) confirms the chemical evolution of the deposited film as a function of the injected power [Despax and Raynaud, 2007].

**Introduction of oxygen in the gas mixture.** A further reduction of the C and H content can be achieved by adding oxygen into the plasma. This generates new reactions that give rise to new species inside the plasma gas phase. This oxygen induced combustion process produces formaldehyde ( $\text{COH}_2$ ), formic acid ( $\text{CO}_2\text{H}_2$ ), carbon monoxide (CO), carbon dioxide ( $\text{CO}_2$ ) and water vapor ( $\text{H}_2\text{O}$  molecules) [Magni et al., 2001]. Moreover, the carbonated radicals of high masses resulting from the incomplete fragmentation of the HMDSO molecule, such as  $\text{SiO}_x\text{C}_y\text{H}$ , first diffuse to the surface and then the carbon is removed by oxygen etching to form  $\text{CO}_2$ . Hence, the oxygen content as well as the chemical kinetics in the gas phase of  $\text{O}_2$ -HMDSO plasma will largely control the stoichiometry and the characteristics of the deposited  $\text{SiO}_2$  film [Hegemann et al., 1999; Aumaille et al., 2000; Magni et al., 2001; Goujon et al., 2004; Barni et al., 2012].

Table I.1: Infrared absorption bands (in  $\text{cm}^{-1}$ ) of the HMDSO plasma deposits obtained under different power conditions. The values come from FTIR spectra of figure I.8 right image. From [Despax and Raynaud, 2007].

5 W	20 W	40 W	100 W	Mode	Chemical Groups
			3024 (vw)		H-C=C
2960 (s)	2960 (s)	2960 (qs)	2954 (vw)	$\nu^a$ C-H <sub>3</sub>	sp <sup>3</sup> CH <sub>3</sub>
2906 (w)	2906 (w)	2906 (w)	2910 (w)	$\nu^s$ C-H <sub>3</sub>	sp <sup>3</sup> CH <sub>3</sub>
	2876 (w-sh)	2876 (w-sh)	2875 (sw)	$\nu^s$ C-H <sub>2</sub>	sp <sup>3</sup> CH <sub>2</sub>
	2131 (w)	2140 (w)	2131 (qs)		
			1870 (vw)		
1721 (vw)	1718 (vw)	1716 (w)		$\nu^s$ C=O	
1575 (vw)	1570 (vw)	1556 (w)	1539 (qs)		X-C=C aromatic (X is H or Si)
1410 (vw)	1410 (vw)	1410 (vw)		$\delta^a$ C-H <sub>3</sub>	SiMe <sub>x</sub> (Me is CH <sub>3</sub> )
1358 (vw)	1359 (vw)	1359 (vw)		$\delta^a$ C-H <sub>2</sub>	Si-CH <sub>2</sub> -Si
1255 (vs)	1256 (vs)	1257 (s)		$\delta^s$ C-H <sub>3</sub>	SiMe <sub>x</sub>
1034 (vs)	1031 (vs)	1026 (vs)	1000 (vs)	$\nu^a$ Si-O-Si $\omega$ Si-CH <sub>2</sub> -Si	Si-O-Si
839 (vs)	837 (vs)	835 (w-sh)	835 (vw-sh)	$\nu$ Si-C $\rho$ CH H-SiO	SiMe <sub>x</sub>
796 (s)	796 (vs)	794 (vs)	802 (vs)	$\nu$ Si-C or $\delta$ Si-O $\rho^a$ CH	SiC <sub>x</sub> SiMe, SiMe <sub>2</sub>
756 (w-sh)	754 (vw-sh)				SiC <sub>3</sub> in Si(Me) <sub>3</sub>
686 (vw)				-	-
613 (w)				-	-

Summarizing, high RF injected power and O<sub>2</sub>-HMDSO ratio have to be used in order to obtain high quality plasma silica films. However, one should bear in mind that a small but detectable amount of carbon is always present into the deposited films elaborated in different experimental conditions.

### 3.4. Elaboration of nanocomposite thin layer containing of AgNPs nanocomposite using plasma processes. Previous work at LAPLACE

A way to elaborate nanocomposite thin layers containing metal nanoparticles by plasma process is to utilize the energetic ion-enhanced plasma sputtering of a metal in an axially-asymmetric RF discharge. The sputtered metal atoms are then present in the plasma volume as a volatile species and subsequently incorporated into the film formed in the same reactor [Kay and Hecq, 1984]. Exploiting this approach, for the first time, gold nanoparticles were uniformly dispersed into polymeric dielectric films (fluorocarbon matrix) combining PVD and PECVD simultaneously in one process [Kay and Hecq, 1984]. Controlled metal incorporation into polymeric dielectric matrices is of considerable interest because the metal species can dramatically influence both the chemical and physical properties of the resultant nanocomposites. Several ways can be applied to obtain metallic nanocomposite [Perrin

et al., 1985; Despax and Flouttard, 1989; Dilonardo et al., 2010; Alissawi et al., 2013; Drábik et al., 2015]. These include plasma polymerization of organometallic gaseous monomers or their copolymerization with other organic monomers. However, both the metal nanoparticles and the surrounding matrix can be modified to obtain a huge variety of metallic nanocomposites. This can be further increased by thermally induced processes, also occurring in the plasma gas phase and/or by post-deposition annealing.

By exploiting the deposition process that involves simultaneous silver sputtering and HMDSO plasma polymerization in an axially-asymmetric RF capacitively-coupled discharge at 13.56 MHz, one can grow Ag containing nanocomposites with well dispersed Ag nanoparticles in an  $\text{SiO}_x\text{C}_y\text{H}$  matrix (Fig. I.9). A strong originality of this plasma process is the pulsed injection of the reactive gas [Despax and Flouttard, 1989]. The silver volume fraction is controlled by adjusting the pulsed gas injection of HMDSO in argon (Fig. I.9) [Despax et al., 2011; Despax and Raynaud, 2007].

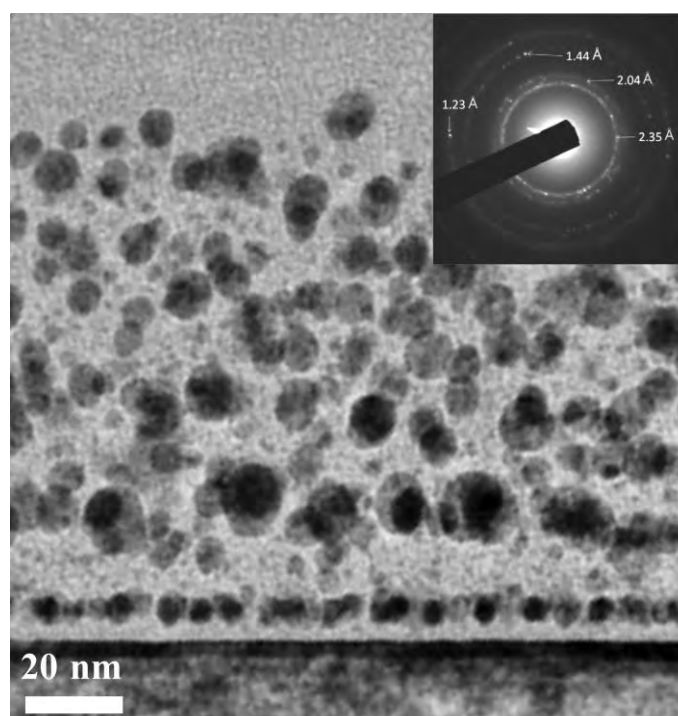


Figure I.9: XS-TEM bright field image of the nanocomposite thin layer containing dispersed pure Ag nanoparticles in  $\text{SiO}_x\text{C}_y\text{H}$  matrix deposited on a silicon substrate (silver volume fraction 0.25; RF injected power 80W). In the corner, the electron diffraction pattern of Ag nanoparticles in which are indicated Ag plane distances. From [Despax et al., 2011]

On the contrary, continuous injection of precursor gas determines a progressive coverage of the silver target up to the total target poisoning. In these conditions, the Ag containing nanocomposite present a gradient in the Ag content [Körner et al., 2012]. In fact the pulsation of the HMDSO mass flow rate with a given period ( $T = t_{\text{on}} + t_{\text{off}}$ ) and a variable duty cycle ( $t_{\text{on}}$ ) allows monitoring the HMDSO amount in the plasma chamber. The coverage rate on the silver target and, thus, the Ag sputtering and the Ag volume fraction into the nanocomposite, are adjusted through the  $t_{\text{on}}$  parameter at a given RF



injected power. This method requires a period of stabilization in which the polymer deposition and the sputtering rate reach a steady state.

FTIR measurements show that deposited Ag nanoparticles in  $\text{SiO}_x\text{C}_y\text{:H}$  matrix exhibit qualitatively the same spectra of  $\text{SiO}_x\text{C}_y\text{:H}$  films (Fig. I.10, left image) [Despax and Raynaud, 2007]. The only difference concerns the relatively marginal changes in composition which are revealed by the shift or/and the increase of some bands. In particular, the bands at around  $1\,000\text{ cm}^{-1}$  associated to the Si–O–Si stretching mode shift to greater energy while the  $\text{CH}_3$  peaks ( $1\,410$ ,  $1\,256$ ,  $835\text{ cm}^{-1}$ ) and Si– $\text{CH}_2$ –Si peak reappear with the increase in silver volume fraction. These results indicate that the presence of silver seems to favor the incorporation of both oxygen ( $1\,024\text{ cm}^{-1}$ ) and methyl groups in the film network. RBS and ERDA measurements of the C/Si, O/Si and H/Si ratios plotted as a function of the Ag/Si atomic ratio show that the H, C and O percentages rise in respect to the Ag amount present in the layers (Fig. I.10, right image). These results are in perfect agreement with the presence of methyl groups and with the shift of Si–O–Si stretching mode to the greater energy in the FTIR spectra.

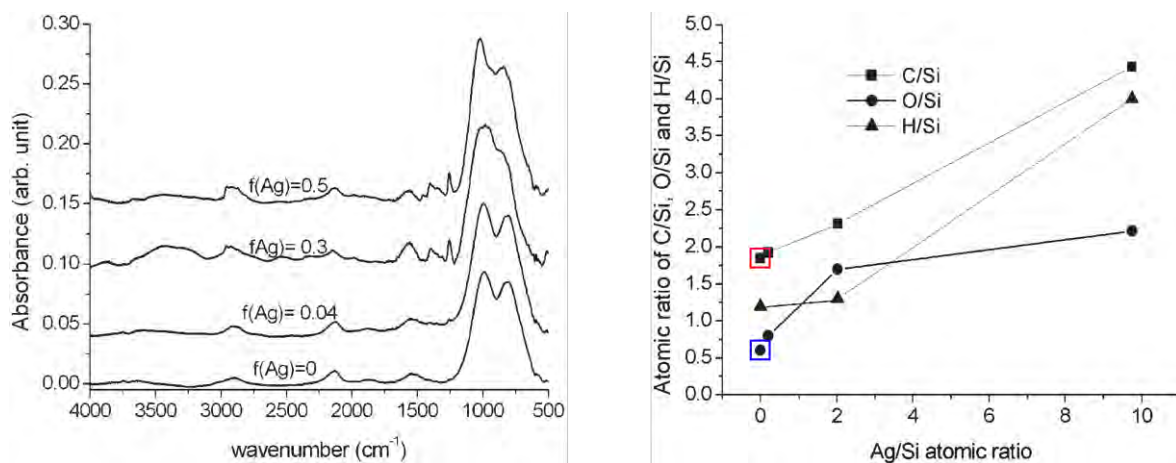


Figure I.10: FTIR spectra of  $\text{SiO}_x\text{C}_y\text{:H}$  films containing different Ag-volume fractions (RF power of 100 W) (left panel). Evolution of the film composition as a function of the Ag/Si ratio obtained by RBS and ERDA measurements (right panel). From [Despax and Raynaud, 2007].

Two dimensional (2D) arrangements of Ag nanoparticles can be prepared by successive plasma deposition: sputtering of Ag-atoms (Fig. I.11) [Makasheva et al., 2013] to form the AgNPs, then covered by plasma deposited thin layer. The basic model of nucleation and growth processes occurring during the initial stages of Ag deposition. The arriving Ag atoms diffuse on the surface for certain time duration until they encounter each other on their diffusing path and the nucleation starts. Tiny Ag clusters are formed at certain sites on the substrate which grow by continued deposition via surface diffusion and direct impingement. Afterwards, this single layer of Ag nanoparticles can be coated in the same reactor, obtaining finally Ag nanoparticles embedded in plasma elaborated host matrix.

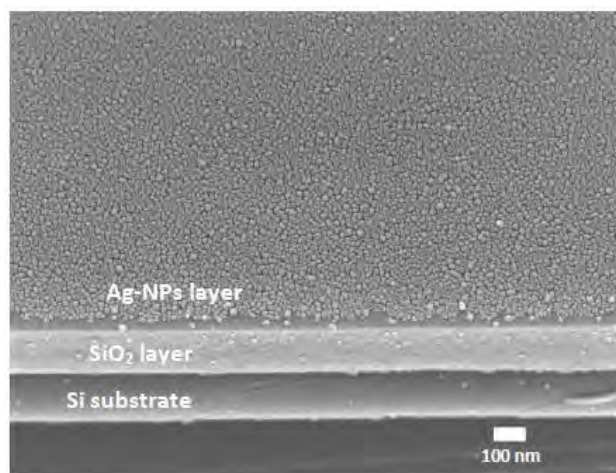


Figure I.11: Tilted at 30° degrees SEM image of the Ag-nanoparticle single layer deposited on SiO<sub>2</sub>-layer over Si-substrate. From [Makasheva et al., 2013].

The preliminary results of a single layer of AgNPs embedded in organosilicon matrix [Makasheva et al., 2013] obtained by successive plasma deposition, alongside with the long time accumulated experience in LAPLACE in plasma deposition of thin layers, including nanocomposites [Despax and Flouttard, 1989; Despax and Raynaud, 2007; Despax et al., 2011], served as a basis for the developed in this work method to elaborate a plane of large AgNPs embedded in silica matrix at well controlled nanometric distances from the surface.

#### **4. AgNPs reactivity in different environments**

The interaction of AgNPs with different species (like chemical elements, inorganic or organic compounds) is of primary importance to understand the AgNP environmental behavior. The result of this interaction can affect silver reactivity, bioavailability and, eventually, toxicity towards the environmental media. In the following sections, the life-cycle of AgNPs will be discussed first and afterward the main abiotic (without organisms) interactions between AgNPs and two important environments: (i) ambient air and (ii) water.

##### **4.1. Life-cycle of AgNP and alteration of AgNPs in the environment**

Once synthesized, AgNPs can undergo chemical and physical alterations, which strongly influence both their unique optical properties and their availability towards any biological system, if released into the environment. In general, the abiotic interaction between NPs and different agents in atmospheric, aquatic or terrestrial environment (for example, presence of light, oxidative species, presence of other potential ligands for silver, ionic strength, etc.) is the first step of their structural modification (graphically represented as changes at the NPs' surface in figure I.12) [Navarro et al., 2008a].

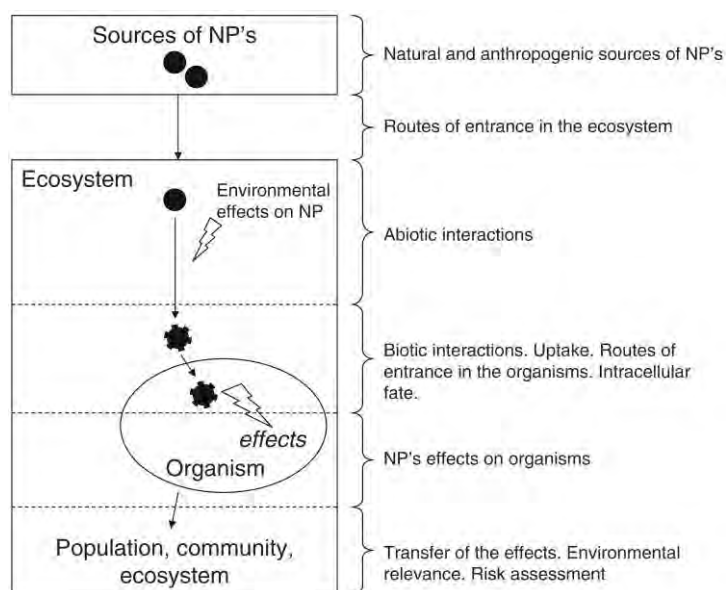


Figure I.12: General chain of events that can lead NPs to be a potential risk for the environment. From [Navarro et al., 2008a].

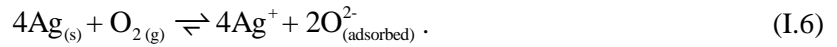
The alterations of AgNPs will greatly determine their fate in the environment and thus their bioavailability to organisms for a given biological system. They can increase, or reduce, different mechanisms determining the interaction at biological interfaces (biotic interactions), like AgNPs or their sub-products (such as silver ions) uptake, the route of entrance in the organisms or their availability inside the cell. All these interactions may cause toxic effects on the targeted organisms by AgNPs and also offer the possibility of transferring these effects to the food webs, thus affecting communities and ecosystems. In the next sections we will focus our attention on two particular environments, ambient air and water, which are of primary importance to the fate of AgNPs.

## 4.2. Interaction of AgNPs with ambient air

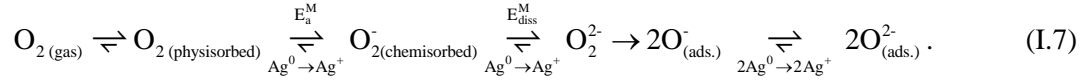
Two well-known elements present in atmospheric air can mainly interact with AgNPs: (i) oxygen to form silver oxide (oxidation) and (ii) sulphur to obtain silver sulphide (sulfidation).

### 4.2.1. Silver oxidation mechanism, from $\text{Ag}^0$ to $\text{Ag}^+$

The oxygen, present naturally in ambient air at standard environmental conditions (temperature  $25^\circ\text{C}$  and total pressure 100 kPa [Lide, 2009]), is the main element, which strongly reacts with silver. It is now known that at least three states of oxygen can be identified on Ag surfaces: (i) physisorbed molecular species ( $\text{O}_2$ ), which are very close to the gas phase structure, (ii) chemisorbed molecular species (the superoxide molecule  $\text{O}_2^-$ ), and (iii) atomically adsorbed states ( $\text{O}^-$ ) [Campbell, 1985]. At standard environment conditions, the oxygen chemisorption gives rise to oxidation of metallic silver ( $\text{Ag}_{(s)}$ ) following the reaction [Kilty and Sachtler, 1974]:



The following series of charge transfer events between silver and oxygen can explain the formation of reactive oxygen atoms from oxygen molecules at room temperature (Fig. I.13) [Czanderna, 1964; Campbell, 1985; Katz et al., 1999]:



After physisorption of the oxygen molecule, the electron transfer from silver to oxygen during the oxygen molecule adsorption on the silver surface provokes weakening of the oxygen molecular bonds (O–O) [Yoshida et al., 1973]. After overcoming the activation barrier with energy  $E_a^M$  (Fig. I.13), the interaction between silver atom and physisorbed molecular oxygen allows obtaining chemisorbed superoxide molecule  $\text{O}_2^-$ . Afterwards, by overcoming the activation barrier with energy  $E_{\text{diss}}^M$ , the interaction  $\text{Ag}_{(s)} - \text{O}_2^-$  leads the peroxide molecule  $\text{O}_2^{2-}$ , which is instable and dissociates in two reactive oxygen atoms  $\text{O}^-$  (highlighted by the one direction of the reaction) [Birks et al., 2006]. Finally, interacting with other two metallic silver atoms, the two anions  $\text{O}^-$  can reach the oxidation state of 2– (eq. I.6) [Backx et al., 1981]. At standard temperature, this adsorbed reactive oxygen atom in the state 2– will strongly interact with metallic silver [Bukhtiyarov et al., 2003], allowing possible formation of different silver oxide forms ( $\text{AgO}$ ,  $\text{Ag}_2\text{O}$  and  $\text{Ag}_2\text{O}_3$ ). Typically, a layer of the silver oxide in the form of  $\text{Ag}_2\text{O}$  (the most common one) forms on the metallic silver surface following the reaction [Cai et al., 1998]:



**Case of Ag Bulk.** For bulk silver at chemical equilibrium, the standard molar formation free energy of  $\text{Ag}_2\text{O}$  (*i.e.* the change of Gibbs free energy that accompanies the formation of 1 mole of silver oxide from molecular oxygen and solid silver at standard environmental conditions [Lide, 2009]) following the reaction I.8 can be written as [Cai et al., 1998]:

$$\Delta G_0^{\text{bulk}}(T) = \frac{1}{2} RT \ln p_{\text{O}_2}^0, \quad (\text{I.9})$$

where  $R$ ,  $T$ , and  $p_{\text{O}_2}^0$  are the gas constant, the absolute temperature and the equilibrium partial pressure of oxygen, respectively. At 25°C and oxygen equilibrium partial pressure of  $p_{\text{O}_2}^0 = 12.43 \text{ Pa}$ , the formation of  $\text{Ag}_2\text{O}$  compound is thermodynamically favored due to the negative standard molar formation free energy ( $\Delta G_{\text{bulk}}^0(25^\circ\text{C}) = -11.25 \text{ kJ/mol}$ ) [Lide, 2009].

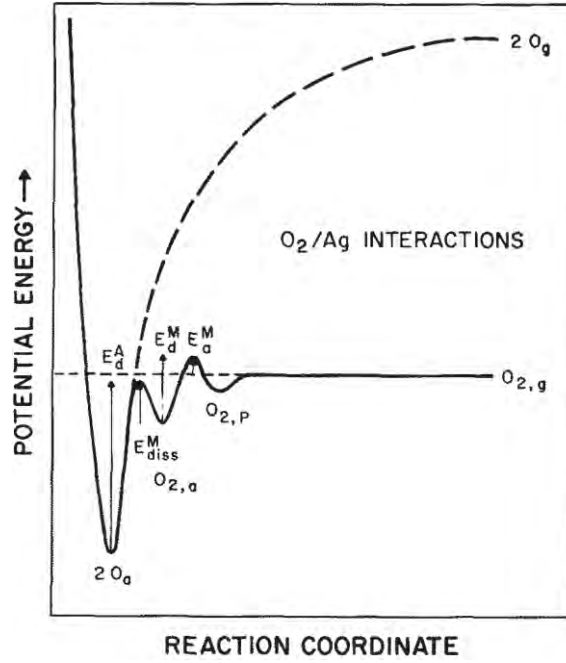


Figure I.13: Potential energy diagram for the interaction of  $O_2$  with a silver surface. From [Campbell, 1985]).

In ambient air, at standard environmental conditions, the oxygen partial pressure is increased, about 20.26 kPa ( $p_{O_2}$ ) and the molar formation free energy of  $Ag_2O$  for the bulk silver  $\Delta G_{bulk}$  remains negative ( $\Delta G_{bulk}(25^\circ C) = -8.43 \text{ kJ/mol}$ ) [Bi et al., 2002]). It implies that the oxidation of Ag may also occur in ambient air. Moreover, the  $Ag_2O$  compounds are stable at atmospheric pressure up to  $200^\circ C$  [Benton and Drake, 1932], the threshold temperature at which thermal decomposition of bulk  $Ag_2O$  begins production of  $O_2$  and  $Ag_{(s)}$ .

**Case of AgNPs.** The oxidation mechanism of bulk silver can also apply to silver nanoparticles. In particular, for silver cluster, the oxygen chemisorption is favored at temperatures above  $-196^\circ C$  if the loss of one electron optimizes the cluster free electron configuration [Schmidt et al., 2003]. Moreover, the smaller the AgNPs are, the easier they would be oxidized [Bi et al., 2002]. This is due to the free energy changes depending both of surface and curvature effect of the nanosized particle, unlike bulk in which these effects are negligible [Cai et al., 1998]. The free energy variation,  $\Delta g$ , to form a spherical silver nanoparticle of radius  $r$  is inversely proportional to its radius according to the expression [Verhoeven, 1975]:

$$\Delta g^{NP}(r) = \frac{2\sigma M}{\rho_{Ag}} \cdot \frac{1}{r}, \quad (I.10)$$

where  $\sigma$  is the surface energy per unit area of silver nanoparticles,  $M$  is the silver atomic weight and  $\rho_{Ag}$  is the silver density. Hence, the standard formation free energy  $\Delta G^{NP}(T, r)$  of  $Ag_2O$  for the silver nanoparticles with radius  $r$  at oxygen equilibrium partial pressure  $p_{O_2}^{0-NP}$  will be [Cai et al., 1998]:

$$\Delta G_0^{\text{NP}}(T, r) = \Delta G_0^{\text{bulk}}(T) - 2\Delta g^{\text{NP}}(r). \quad (\text{I.11})$$

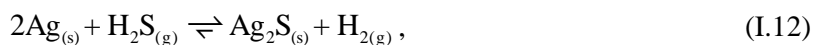
Considering a surface energy (defined as the energy involved in forming a new surface) per unit area equal to  $0.97 \text{ J/m}^2$  for a free silver nanoparticle of radius 2.5 nm according to reference [Medasani et al., 2007], the standard molar formation free energy of  $\text{Ag}_2\text{O}$  for silver nanoparticles at standard temperature is  $\Delta G_{\text{NP}}^0(25^\circ\text{C}, 2.5 \text{ nm}) = -19.3 \text{ kJ/mol}$ . This increment of  $\Delta G_{\text{NP}}^0(25^\circ\text{C}, 2.5 \text{ nm})$  in module is more than 70% compared with that of the bulk silver. This implies that, thermodynamically,  $\text{Ag}_2\text{O}$  formation on AgNPs should occur more easily than that on bulk silver at room temperature. Theoretical studies of the surface energy per unit area for free AgNPs show also that the surface energy increases significantly when the nanoparticle size decreases below 1 nm [Medasani et al., 2007]. It means that these small nanoparticles would be oxidized easier than the big ones. Moreover, the high ratio of surface to bulk atoms for Ag nanoparticles that increases drastically with reduction of their size can modify their chemical activity [Beyer et al., 1975; Henglein, 1988]. Usually, oxidation begins from the surface of AgNPs and forms  $\text{Ag}_{\text{core}}@ \text{Ag}_2\text{O}_{\text{shell}}$  structure. During oxidation, the thickness of the  $\text{Ag}_2\text{O}$  shell increases and, consequently, the size of Ag core decreases. The oxidation of originally pure Ag nanoparticles can occur and a stable  $\text{Ag}_2\text{O}$  shell can exist even for nanoparticles of radius of 6 nm. Moreover, the  $\text{Ag}_2\text{O}$  shell becomes larger when decreasing the nanoparticle size and the possibility of AgNPs complete oxidation can even occur.

**Dependence of AgNPs oxidation on the relative humidity.** Another key parameter for the kinetics of Ag nanoparticles oxidation is the relative humidity of ambient air. High level of moisture enhances Ag nanoparticle oxidation. More details on this effect are given in section 4.3 where we consider the interaction between silver and water. For example, although embedded in porous silica, Ag nanoparticle with mean radius 1.5 nm exposed to the air with relative humidity of 80% at room temperature can form a dense oxide film in 2 h. On contrary, the same system exposed to the air with relative humidity less than 30% do not show important oxidation over several months [Cai et al., 1998]. However, for Ag nanoparticles with larger radius ( $R_0 = 30 \text{ nm}$ ) deposited on silica the oxidation effects appear within 20 days of exposure and a strong oxidation within 50 days when exposed to the air with relative humidity of 40% at  $22^\circ\text{C}$  [Sachan et al., 2013]. It means that the AgNPs oxidation upon variation of the relative humidity is size dependent effect.

#### 4.2.2. Silver sulfidation mechanism

The presence of common gaseous sulphur compounds in the atmosphere (hydrogen sulphide  $\text{H}_2\text{S}$ , carbonyl sulphide  $\text{OCS}$ , sulphur dioxide  $\text{SO}_2$  and carbon disulphide  $\text{CS}_2$ ) can provoke formation of silver sulphide  $\text{Ag}_2\text{S}$  (argentite) on Ag surfaces (sulfidation process). This phenomenon causes the tarnishing for example of jewellery, household silverware or electrical equipment [Franey et al., 1985]. At total gas exposure of 100 ppm/h, temperature of  $21^\circ\text{C}$  and relative humidity of 92% the thickness

of Ag<sub>2</sub>S due to H<sub>2</sub>S and OCS (over 20 nm) is at least one order of magnitude more than that of SO<sub>2</sub> and CS<sub>2</sub> (under 2 nm). Starting from pure solid Ag and H<sub>2</sub>S gas, the initial step of Ag<sub>2</sub>S formation is the adsorption of H<sub>2</sub>S molecules, probably at grain boundaries or defects in the surface structure where the normal bonding in the silver crystal is unsatisfied [Phillips, 1962]. At the end of process, a molecular hydrogen is released. The Ag<sub>2</sub>S is thus formed following the reaction:



with standard formation free energy of Ag<sub>2</sub>S,  $\Delta G_{0-\text{Ag}_2\text{S}}^{\text{NP}}(25^\circ\text{C}) = -7.1 \text{ kJ/mol}$  at thermodynamic equilibrium, standard temperature and oxygen equilibrium partial pressure. Once the nucleation of Ag<sub>2</sub>S occurs, the growth of sulphide proceeds laterally across the silver surface until formation of a continuous layer. Further growth involves diffusion of the H<sub>2</sub>S molecules through the Ag<sub>2</sub>S layer. This diffusion process provides the limit to sulfidation by H<sub>2</sub>S at long exposure times [Graedel et al., 1985].

**Sulfidation dependence on the relative humidity.** Similar to the case of silver oxidation discussed previously, the sulfidation rate could be increased by more than an order of magnitude if the relative humidity is increased from 0 to 100% [Graedel et al., 1985]. Moreover, when the relative humidity is over 90% the formation of several monolayers of water on silver surface can occur [Graedel et al., 1985]. Since the interaction of OCS with water gives rise to H<sub>2</sub>S as a final product of the reaction and the H<sub>2</sub>S is very soluble in water, it seems likely that the function of the water is to absorb H<sub>2</sub>S and make it more readily available to the silver [Graedel et al., 1985].

**Case of AgNPs.** Since sulfidation kinetics partly depends on the surface orientation and the presence of steps, AgNPs can sulfidize faster than bulk Ag due to the intrinsic characteristic of NPs related to both the edge-dominated structure and the high surface exposed. For example, bare AgNPs when exposed to laboratory air, present sulfidation rate of 7.5 times higher than that the one of bulk silver under the same conditions, giving a Ag<sub>2</sub>S growth rate around 3 nm per day, even at low relative humidity (~ 20%) [Mcmahon et al., 2005].

### 4.3. Interaction of AgNPs with water

#### 4.3.1. Phenomena affecting AgNPs dissolution in water

The formation of all environmentally relevant Ag-species from metallic AgNPs in water can be modified by several parameters, either inherent to the nanoparticles (size, shape, coating), or attributable to the medium (presence of light, oxidative species, presence of other potential ligands for silver, ionic strength, pH, electrolyte species) [Le Ouay and Stellacci, 2015]. These parameters have influence on several phenomena that can contribute to the increase or the decrease of the solubility of Ag-species in water. A summary of the phenomena affecting the AgNPs is presented in figure I.14.

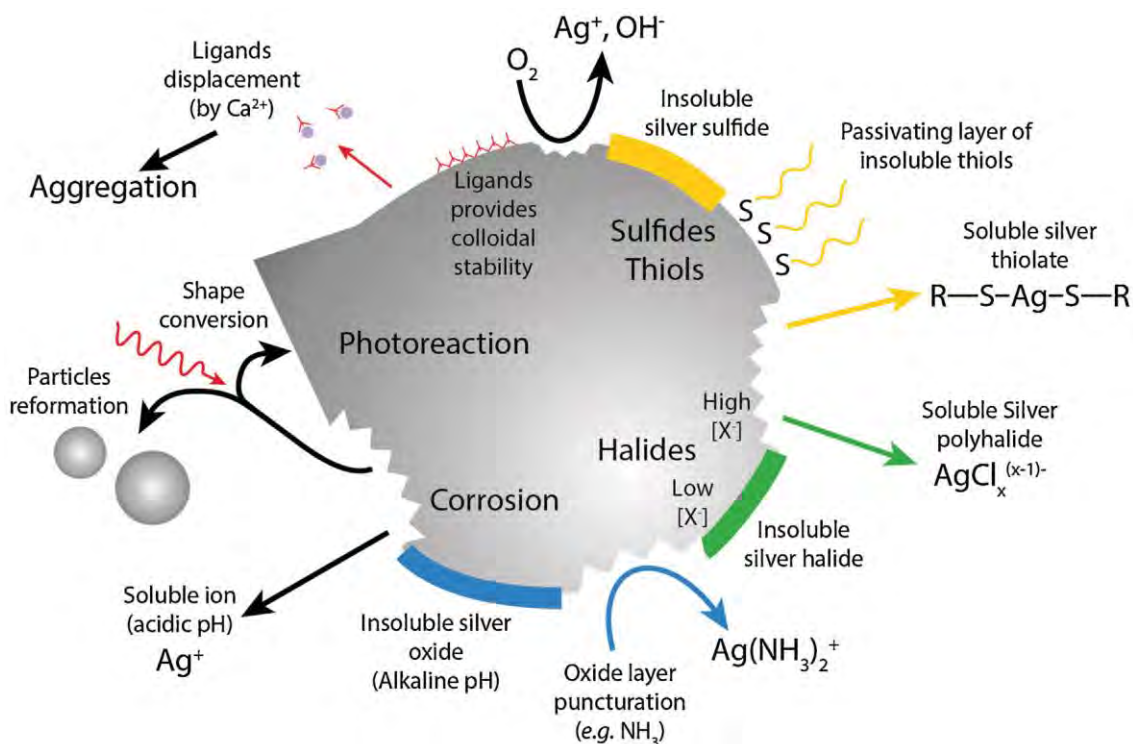


Figure I.14: Summary of different phenomena affecting AgNPs dissolution in water. From [Le Ouay and Stellacci, 2015].

Among the different phenomena affecting AgNPs dissolution in water, one can distinguish four important categories: (i) corrosion by reactive species (oxygen, sulphurous and chloride) [Liu and Hurt, 2010; Liu et al., 2010; Levard et al., 2011], (ii) aggregation of the nanoparticles [El Badawy et al., 2010; Prathna et al., 2011] (iii)  $\text{Ag}^+$  reduction (chemical- or photo-induced) [Liu et al., 2010; Glover et al., 2011], and (iv) surface passivation by inorganic (insoluble silver oxide, sulfide or halide, and colloidal ligand) or organic (thiols - R - SH, where R represents a carbon-containing group of atoms and colloidal ligand, such as the most used PVP and citrate) capping layer [Liu et al., 2010]. In the following sections, we focus our attention on the first two categories of AgNPs transformations that are primary critical steps for understanding the environmental fate, transport, and biological impacts of AgNPs.

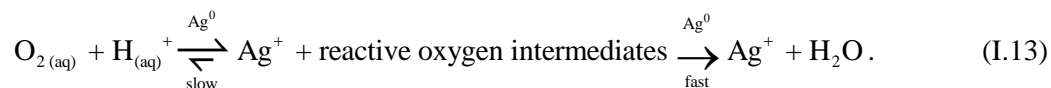
#### 4.3.2. Phenomena affecting AgNPs dissolution in water

When AgNPs are dispersed in water, various and rather complex processes can take place. Characterization of  $\text{Ag}^+$  release by AgNPs dissolution is an important environmental behavior of AgNPs. In any case, the initiation of AgNPs dissolution takes into account the oxidation of atomic Ag by the release of  $\text{Ag}^+$  because the zero-valent silver metal ( $\text{Ag}^0$ ) is insoluble in water [Petrucci et al., 1997; Sotiriou et al., 2012]. Similar to the impact of molecular oxygen on AgNPs in ambient air, discussed in the previous section, the molecular oxygen dissolved in water ( $\text{O}_{2(\text{aq})}$ ) represents an essential oxidizing species for the AgNPs surface [Lide, 2009; Liu and Hurt, 2010;]. However, the



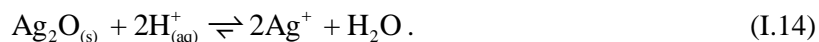
solution pH-value is an important parameter for the  $\text{Ag}^+$  release because protons ( $\text{H}^+_{(\text{aq})}$ ) and  $\text{O}_{2(\text{aq})}$  cooperate to oxidize the AgNPs surface [Liu and Hurt, 2010].

**Ion Release Mechanisms.** In water environment, the AgNPs oxidation to give  $\text{Ag}^+$  is not likely to take place through a four-electron transfer process that reduces  $\text{O}_{2(\text{aq})}$ , but rather through simpler redox reactions that produce reactive oxygen intermediates (hydrogen peroxide  $\text{H}_2\text{O}_2$ , superoxide anion radical  $\text{O}_2^{\bullet-}$ , and hydroxyl radical  $\bullet\text{OH}$ ) that are more powerful oxidizing agent and stronger nucleophile (i.e. more likely to share an electron pair and form a chemical bond) than  $\text{O}_{2(\text{aq})}$  [Liu and Hurt, 2010]. The most probable mechanism of AgNPs dissolution can be written as follows:



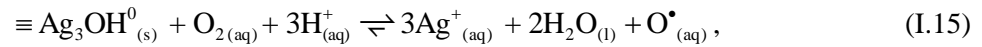
In this mechanism, the initial nanoparticle oxidation via reaction with oxygen is a limiting factor. In the first part of the reaction the possibility that a strong oxidant like  $\text{H}_2\text{O}_2$  could reduce  $\text{Ag}^+$  just present in solution to  $\text{Ag}^0$  is also taken into account [He et al., 2011; He et al., 2012a]. This effect can produce either a shape change of the AgNPs or a particle reformation, or an increase of the NPs sizes [Liu et al., 2010; Peretyazhko et al., 2014].

Another scenario has to be considered for AgNPs coated by  $\text{Ag}_2\text{O}$  surface layer. One or more atomic layers of  $\text{Ag}_2\text{O}$  can be formed as a consequence of the exposure of AgNPs to oxygen either dissolved in solution or present in ambient air before water immersion. In water, the  $\text{Ag}_2\text{O}$  layer is covered with surface hydroxyl groups ( $\text{Ag}-\text{OH}$ ) [Peretyazhko et al., 2014]. Although the  $\text{Ag}_2\text{O}$  solubility in water is low (0.0025 g  $\text{Ag}_2\text{O}$  /100 g  $\text{H}_2\text{O}$  at  $25^\circ\text{C}$  - solubility product  $K_{\text{sp}}^{\text{Ag}_2\text{O}} = 4 \times 10^{-11}$  [Lide, 2009]), in acidic aqueous environment ( $\text{pH} < 7$ , excess of protons  $\text{H}^+$ ), the  $\text{Ag}-\text{O}$  bonds weaken and break because the hydroxyl groups undergo protonation ( $\text{Ag}-\text{OH}_2^+$ ) [Stumm et al., 2012]. In this condition the  $\text{Ag}^+$  release into solution can occur following the reaction [Peretyazhko et al., 2014]:



**Incomplete dissolution of nanoparticles.** Dispersed AgNPs in aqueous environment can dissolve partially or completely depending of different factors like AgNPs functionalization and concentration, environmental temperature, amount of dissolved molecular oxygen in water, solution pH and nanoparticle aggregation [Kittler et al., 2010; Liu et al., 2010; Sotiriou et al., 2012; Mittelman et al., 2013]. In any case, the AgNPs dissolution follows the same distinct two-step behavior observed for the time release of  $\text{Ag}^+$  [Mittelman et al., 2013]. The first step concerns an initial rapid release of  $\text{Ag}^+$  in the first few hours after exposure to water. Afterwards, the second step involves a gradually declining  $\text{Ag}^+$  release, tending to a saturation value, observed over long water exposure time (several days). The interpretation of this AgNPs dissolution behavior remains controversial in the literature because of different experimental conditions [Liu et al., 2010; Mittelman et al., 2013].

**Interpretation of Ag<sup>+</sup> release behavior.** Recently, a new conceptual approach was used to interpret the large range of phenomena influencing the Ag<sup>+</sup> release in solution [Molleman and Hiemstra, 2015] considering previously developed ideas [Schmidt et al., 2003]. It includes the particle size [Zhang et al., 2011; Ma et al., 2012; Peretyazhko et al., 2014], the solid-solution ratio [Kittler et al., 2010; Zhang et al., 2011;], the pH of the solution [Liu and Hurt, 2010; Peretyazhko et al., 2014;], the quantity of dissolved oxygen [Liu and Hurt, 2010; Xiu et al., 2012;] and their consequences (*i.e.* incomplete dissolution of AgNPs [Kittler et al., 2010; Zhang et al., 2011; Sotiriou et al., 2012; Ma al., 2012; Peretyazhko et al., 2014]). In this approach the subvalence of Ag (*i.e.* +1/3 valence unit per Ag atom), which can be created upon partial oxidation of the AgNPs surface, is the key to understand the oxygen induced release of Ag<sup>+</sup> from AgNPs. In this context, the solid-water interface of AgNPs will release Ag<sup>+</sup> upon a circular process with: (I) the oxidative dissolution of ≡Ag<sub>3</sub>OH<sup>0</sup> groups with a two-electron step (eq. I.15), (II) the creation of new metallic sites at the underlying lattice, and (III) subsequent oxidation to ≡Ag<sub>3</sub>OH<sup>0</sup>.



where ≡Ag<sub>x</sub> represents the underlying metallic Ag lattice with which OH<sup>-</sup> (or O<sup>•</sup>) interacts.

Moreover, the released radicals O<sup>•</sup> penetrate inside the lattice and contribute to the formation of highly stable ≡Ag<sub>6</sub>O<sup>0</sup> groups (eq. I.16) that protect AgNPs from further oxidation:



In conclusion, the Ag<sup>+</sup> release is rather the result of formation of a protective oxidized Ag layer that kinetically prevents from full oxidation of AgNPs [Molleman and Hiemstra, 2015].

#### 4.3.3. Implication of AgNPs sulfidation in the Ag<sup>+</sup> release

The sulfidation process of AgNPs in water, to form Ag<sub>2</sub>S, is strongly enhanced because of the high solubility of H<sub>2</sub>S in this liquid [Lee and Mather, 1977]. Acting the water as an appropriate intermediary liquid, the contact probability between the solid Ag surface and H<sub>2</sub>S increases and the formation of stable Ag<sub>2</sub>S in solution can occur because of the insolubility of this compound in water (solubility product  $K_{\text{spa}}^{\text{Ag}_2\text{S}} = 6 \times 10^{-30}$ ) [Franey et al., 1985; Graedel et al., 1985; Lide, 2009]. Moreover, Ag<sup>+</sup> released in solution tends to complex with soft bases such as sulphur [Stumm et al., 2012], reducing Ag<sup>+</sup> availability in solution. In the case of AgNPs the sulfidation in water is enhanced owing to its edge-dominated surface structure affecting AgNPs surface properties in terms of aggregation state and surface charge. This leads to a decrease of the AgNPs dissolution rate [Levard et al., 2012]. In addition to inorganic sulphurous compounds, AgNPs or released Ag<sup>+</sup> species can also bind strongly to organosulfur compounds. The strong affinity of Ag<sup>+</sup> is illustrated by the high stability constant of Ag<sup>+</sup>-organosulfur complexes [Bell and Kramer, 1999]. Indeed, Ag<sup>+</sup> have the greatest affinity for thiol-

containing ligands as cysteine. In particular, cysteine can form two complexes AgCys and AgCys<sub>2</sub>, with a ratio of Cys/Ag in the range of 1–2, depending on the concentrations of Cys and Ag<sup>+</sup> [Adams and Kramer, 1999].

#### **4.3.4. Interaction between AgNPs and chloride**

The dissolution behavior of AgNPs in the presence of Cl<sup>-</sup> depends on the chloride concentration in the solution. In the presence of low concentration of Cl<sup>-</sup>, the dissolution rate of AgNPs in presence of oxygen can be decreased because of the formation of relatively insoluble AgCl shells on the surfaces of AgNPs, which inhibits the molecular oxygen penetration and as a consequence the Ag<sup>+</sup> release [Li et al., 2010]. At high concentration of Cl<sup>-</sup>, possible formation of bioavailable anionic Ag complexes (such as AgCl<sup>2-</sup>, AgCl<sup>2-3</sup>, and AgCl<sup>3-4</sup>) can modify the dissolution rate of AgNPs. The formation of these complexes leads to enhancement of bioavailability of silver for the microorganisms [Gupta et al., 1998].

#### **4.3.5. Aggregation state of AgNPs**

Aggregation is another parameter that might have an important impact on silver release rate in solution. This mainly concerns “free” (non embedded) AgNPs in solution but also embedded AgNPs that have left their matrix after water immersion. The main effect imposed by AgNPs aggregation is the reduction of reactive surface exposed to the environment [Levard et al., 2012]. The high surface area to volume ratio and the surface charge of AgNPs determinate a high reactivity of nanoparticles with each other. Considering Brownian diffusion in liquid, nanoparticle surfaces can be in contact with each other and short-range attractive interactions (like van der Waals attraction forces) can overcome the electrostatic repulsion forces allowing particle–particle attachment to occur [Hotze et al., 2010]. This aggregation process is strongly affected by both AgNPs coating layer and by the surrounding environmental conditions, such as pH, ionic strength and electrolyte species in solution [El Badawy et al., 2012]. High level of aggregation can result in AgNPs settling out, making these particles able to release in the environment small amount of ionic silver for long time.

### **5. Interaction between AgNPs and micro-organisms**

#### **5.1. Structural parameters of AgNPs influencing the antimicrobial activity of silver**

AgNPs morphology of both physically or chemically elaborated AgNPs can influence (enhance or reduce) their antimicrobial activity that is strictly related to the toxicity on microorganisms present in the environment [Misra et al., 2012]. Relation can be established according to the three main physical characteristics of AgNPs (Fig. I.15): **size**, **shape** and **crystalline direction** of the nanoparticle core, and the **nature** of nanoparticle shell (for surface-coated or embedded AgNPs).

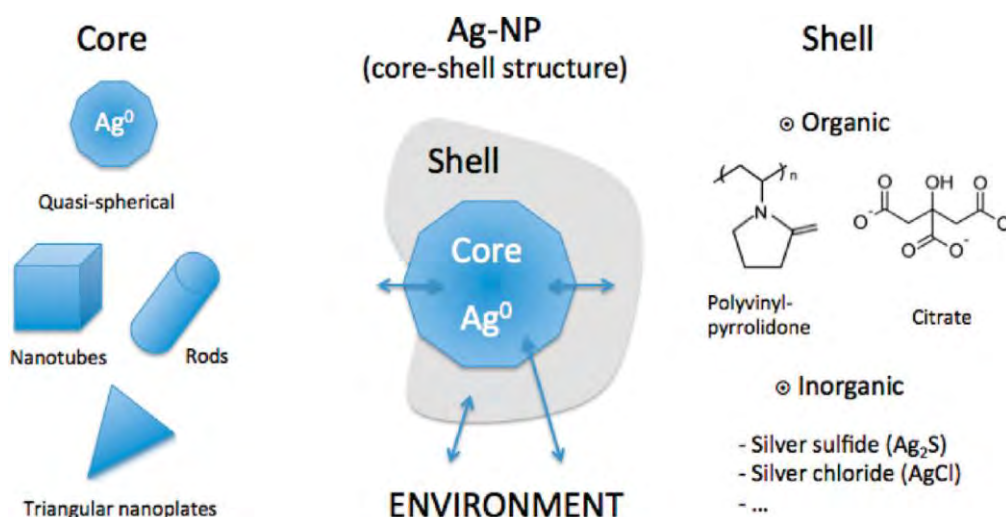


Figure I.15: Typical AgNPs structure with a polymorph metallic silver core and a continuous or discontinuous capping layer (shell). Double arrows represent the reactions that might occur between the shell (organic or inorganic) or silver core (directly or indirectly) with the environment and also at the interface between core and shell. From [Levard et al., 2012].

### 5.1.1. Effect of the NP size on the antimicrobial activity of silver

Numerous experimental studies, sometimes coupled with modelling, show a size dependency of the antimicrobial activity of (quasi-spherical) AgNPs; smaller (with diameter less than 10 nm) being more active on the basis of equivalent total silver mass content [; Morones et al., 2005; Lok et al., 2007; Sortiriou and Pratsinis, 2010; Zhang et al., 2011]. The improved antimicrobial activity can stem from two main factors. The first one is the AgNPs dissolution in the form of Ag<sup>+</sup> that plays the most important role in toxicity against microorganisms. Considering spherical AgNPs of uniform size, a reduction in the particle size from 10  $\mu\text{m}$  to 10 nm will increase the surface area by a factor of 10<sup>9</sup>. Hence, smaller AgNPs exhibit more active surface (that is, reacting to the oxidative species in solution to obtain Ag<sup>+</sup>, also in chemisorbed state) per unit of mass and are thus more prone to high grade of dissolution [Lok et al., 2007; Sortiriou and Pratsinis, 2010]. However, a constant release of Ag<sup>+</sup> ion per unit surface area was not observed as expected for such nanoparticles [Ma et al., 2012]. This indicates that the surface area alone does not explain the high dissolution rate of smaller AgNPs. A possible reason for this behavior can be found in connection with the nanoparticles enhanced curvature (highly convex surface) that facilitates mass transfer from their surface [Sortiriou and Pratsinis, 2010; Ma et al., 2012;]. As a consequence, aggregates of AgNPs possess lower antimicrobial impact because they have less exposed surface to the medium. [Baker et al., 2005; Bae et al., 2010].

The second factor that may also explain the size-dependent antimicrobial activity is the difference in the levels of association of the AgNPs with cells. Smaller AgNPs still present in solution can directly and more easily attach to the surface of the cell membrane and drastically disturb its proper function [Morones et al., 2005]. This effect can be related to the electronic structure of metal nanoparticles smaller than 5 nm. When the nanoparticle size is reduced, the number of surface atoms increases and

the mean coordination of these atoms decreases. This provokes three effects: the valence band becomes sharper, the density of state at the Fermi level drops and the gravity centre of this band can shift. The latter can significantly influence the reactivity of nanoparticle surface. A shift of the valence band toward the Fermi level can determine a strong interaction between the electrons of this band and ones of species close to the nanoparticle surface [Henry, 1998].

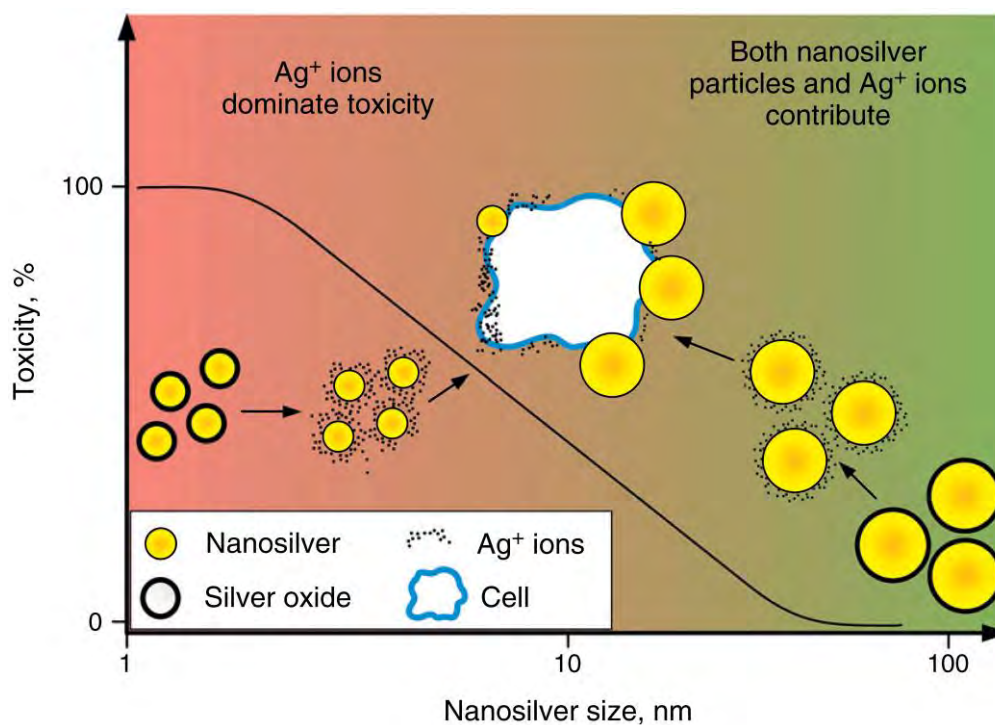


Figure I.16: Size-dependent antimicrobial behavior expressed in terms of toxicity on the basis of equivalent total silver mass content. From [Sotiriou and Pratsinis, 2011].

These two size-dependent features are in competition with each other and contribute in different importance degrees to the antimicrobial activity. For small AgNPs (less than 10 nm), this activity is dominated by  $\text{Ag}^+$  rather than undissolved nanoparticles. In fact, the survival small AgNPs do not have a chance to play a significant role on toxicity against microorganisms. On the contrary, for relatively large (average size larger than 10 nm) AgNPs, the toxicity against microorganisms is lower than the previous case but nanoparticles and ions influence the antimicrobial activity in similar proportion [Sortiriou and Pratsinis, 2010]. In figure I.16 is shown a general picture resuming the size-dependent antimicrobial behavior (expressed in terms of toxicity as a function of the AgNPs size) [Sotiriou and Pratsinis, 2011]. This emphasizes the importance of the released  $\text{Ag}^+$  and nanoparticles in the mechanisms of the antimicrobial activity of nanosilver.

### 5.1.2. Effect of the shape and crystalline direction

Although the interactions between microorganisms and AgNPs can be similar for nanoparticles with similar size for markedly different shapes the antimicrobial activity can differ. This difference can be explained in terms of crystallographic nature of facets, of sharp edges and corners, and of polycrystalline structure present in AgNPs of different shapes. It is well-known that different crystallographic surfaces of bulk solids (and, on particular, of nanoparticles) have different reactivity. It was extensively explored theoretically and experimentally in surface passivation or heterogeneous catalysis [Xu et al., 2006; Kilin et al., 2008]. AgNPs with the same surface areas but different shapes may have different effective surface areas in terms of facets with antimicrobial activity. These differences concern the packing densities of different crystal planes; more packing means lower energy and higher stability. In the case of silver, the close-packed  $\{111\}$  family planes (facets) are the lowest energy crystal planes with maximum packing, and therefore have the lowest surface tension [Marzbanrad et al., 2015]. In the mechanism of small AgNPs formation the cost of an increase in the internal strain is offset by the reduction in surface tension achieved through growth of the lower energy  $\{111\}$  facets [Wiley et al., 2004]. In biology, this finding promotes enhancement of the direct reactivity of AgNPs containing mainly  $\{111\}$  facets (*i.e.* quasi-spherical nanoparticles with icosahedral, twinned, or decahedral morphologies (Fig. I.17)) towards sulphur containing proteins present at the microorganism surface [Morones et al., 2005]. In this context, sulphur presents a high affinity towards these high atom density surfaces of silver due to, likely, easier formation of the stoichiometric  $\text{Ag}_2\text{S}$  on the silver surface [Hatchett and White, 1996].

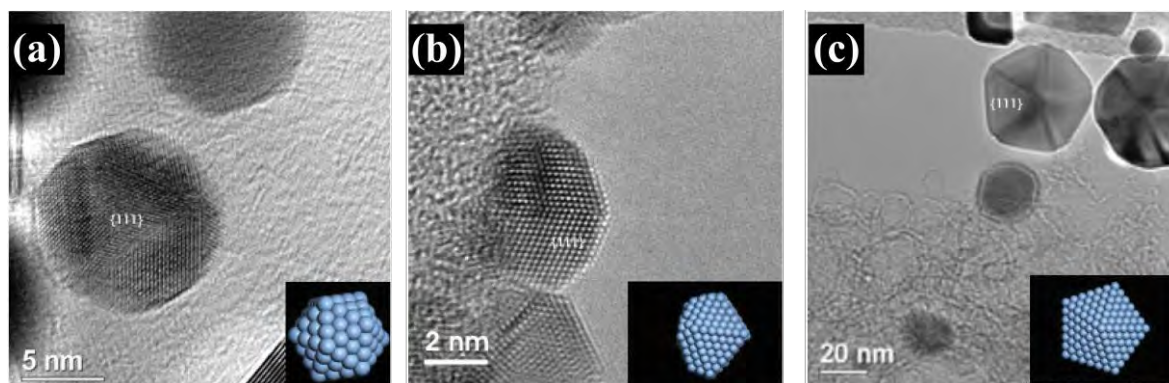


Figure I.17: The most common morphologies of the quasi-spherical AgNPs. The  $\{111\}$  facets are labelled and their respective models are shown as insets: (a) icosahedral particle, (b) twinned particle and (c) decahedral particle seen in the  $[100]$  direction. From [Morones et al., 2005].

The second aspect of shape dependency of AgNPs antimicrobial activity concerns the presence of sharp edges and corners mainly in non-spherical AgNPs (*i.e.* triangular nanoplates, nanorod, nanocubes). These portions of nanoparticles possess a locally enhanced curvature, which determines a preferential  $\text{Ag}^+$  dissolution at these locations [Zhang et al., 2005; Sortiriou and Pratsinis, 2010;]. Additionally, polycrystalline silver nanostructures will dissolve more rapidly than the single-

crystalline ones because of, likely, the high-energy defects contained at the grain boundaries that provide active sites for their oxidative dissolution in  $\text{Ag}^+$  [Wiley et al., 2004; Elechiguerra et al., 2005b;].

### 5.1.3. Nature of nanoparticle shell

AgNPs need a shell to stabilize them in the environment (stabilizing coating). These coatings do not concern only the AgNPs elaborated by chemical ways and coated by ligands but also the AgNPs elaborated by physical routes and embedded in dielectric matrices, the coating being here the matrix itself. The nature of the coating can affect physicochemical properties of the nanoparticles provoking changes in their antimicrobial activity [Navarro et al., 2015]. One of these changes concerns the release of  $\text{Ag}^+$ .

**Physical effect** of coating implies modification of the exposed silver surface to the aqueous solution, which involves changes in the amount of released  $\text{Ag}^+$ . Decrease of  $\text{Ag}^+$  can occur when the aggregation state of nanoparticles increases, as detailed before. The AgNPs aggregation depends on the shell category. For example, AgNPs coated with organic polymers have worse surface stabilization (corresponding to high aggregation state of NPs) and therefore weaker antimicrobial activity than those coated with organic anionic surfactant [Kvítek et al., 2008]. The released  $\text{Ag}^+$  amount can be reduced by the partial or total coverage of the AgNPs surface by a shell. This effect is observed both in organic coating discussed previously and in inorganic coating like insoluble silver oxide, sulphide and halide (produced through interaction of silver with environment) [Levard et al., 2012]. In the case of nanoparticles embedded in a solid matrix, such as silica, it has been shown an increase of the  $\text{Ag}^+$  release proportional to the NP surface (without coating) directly exposed to the medium [Sotiriou and Pratsinis, 2010; Sotiriou et al., 2011].

**Chemical effect** of coating can influence the released amount of silver ions in solution by  $\text{Ag}^+$  complexation due to the nature of coating. Citrate (a carboxylic acid) and PEG (a polymer) coatings are the two examples that highlight the modification of  $\text{Ag}^+$  concentration in solution. In particular, citrate might complex  $\text{Ag}^+$  retaining the ions at the AgNP surfaces [Tejamaya et al., 2012] and possibly leads to renewed reduction of dissolved  $\text{Ag}^+$  to metallic Ag [Rivas et al., 2001]. This leads to a decrease the  $\text{Ag}^+$  concentration in solution and the related toxicity on different organisms [Yang et al., 2012; Navarro et al., 2015]. Despite the fact that the PEG shell is not a good  $\text{Ag}^+$  ligand, this polymeric coating can retain  $\text{Ag}^+$  close to the nanoparticle surface that can be released by interactions with microorganisms or their by-product, increasing the antimicrobial activity of nanoparticle [Navarro et al., 2015]. Another example of chemical effect concerns biological macromolecules such as proteins like bovine serum albumin (BSA) that, at low concentration, increases stability and allows AgNPs to exert bactericidal effects. On the contrary, an excess of BSA in solution appears to block the activities of  $\text{Ag}^+$  ions delivered from the nanoparticles [Lok et al., 2007].

Another important antimicrobial activity alteration associated to the stabilizing coating involves the physical interactions between the AgNPs and the microorganisms. These alterations concern mainly the surface charge and hydrophobicity of AgNPs. The modification of **surface charge** due to the coating plays also a role in the  $\text{Ag}^+$  release. Indeed, uncoated AgNPs possess a natural negative surface charge throughout the pH range (2 to 10) common in the environment [El Badawy et al., 2010]. This is due to the surface atoms that are coordinately unsaturated and can interact with nucleophilic molecules (*i.e.* OH and  $\text{H}_2\text{O}$ ) leading to negative charge excess in the metal interior. This charge excess can be picked up by electron acceptors [Mulvaney et al., 1991]. Applying a stabilizing coating, the AgNPs surface charge, at solution pH 7, can be modified from more positive or more negative values compared to the one of uncoated nanoparticles [El Badawy et al., 2010; El Badawy et al., 2011; Ivask et al., 2014]. This variable surface charge may play a large role in AgNPs antimicrobial activity, depending on the charge type of both cell and nanoparticle. For example, when the magnitude of negative surface charge of AgNPs decreases, the AgNPs toxicity on microorganisms with negative charge wall (*i.e.* Gram-positive bacteria) exhibits an increase due to reducing of the electrostatic barrier that limits the cell-nanoparticle interactions [El Badawy et al., 2011]. In this case, AgNPs with positive surface charge coating show electrostatic cell-nanoparticle attraction determining a significantly higher toxicity than both nanoparticles with negative surface charge and positively charged silver ions. The attachment of AgNPs to the negatively charged bacterial cell walls is the primary mechanism for enhancement of AgNPs antimicrobial activity when compared to the only chemical effect caused by the  $\text{Ag}^+$  alone [El Badawy et al., 2011].

An additional factor that plays an important role in the antimicrobial activity is the **hydrophobicity** of AgNPs, which is the affinity of a surface to receive water and polar solvent. To evaluate the antimicrobial activity of AgNPs with respect to their hydrophobicity, it must be taken into account that different categories of microorganisms can possess hydrophobic or hydrophilic behaviour. Generally, microorganisms with hydrophilic characteristics (*i.e.* yeasts) prefer to adhere to hydrophilic material surfaces, such as metals or glasses (*i.e.* stain steel or silica, respectively); ones with hydrophobic properties (*i.e.* bacteria) prefer hydrophobic material surfaces, such as polymers [An and Friedman, 1998; Saulou et al., 2009;]. Considering these phenomena, hydrophobic microorganisms (in particular bacteria) adhere to a greater extent than hydrophilic ones [An and Friedman, 1998].

#### **5.1.4. Effects of exposure medium on AgNPs antimicrobial activity**

Solution chemistry must also be considered when studying AgNPs antimicrobial activity because its role can be crucial for the ultimate form of silver (Ag speciation) that organisms will encounter in the exposure medium [Liu et al., 2010]. Solution pH, ionic strength and electrolyte species (*e.g.* NaCl,  $\text{NaNO}_3$  and  $\text{CaCl}_2$ ), generally influence the amount of released silver through changes in aggregation state and dissolution rate of AgNPs [Fabrega et al., 2009; Liu and Hurt, 2010; Loza et al., 2014]. For



example, AgNPs are more likely to be found as aggregates in high ionic strength media [Li et al., 2010] or in presence of electrolytes [Zhang et al., 2011]. Moreover, an increase of the solution temperature leads to an increased degree of dissolution [Kittler et al., 2010]. All these parameters can provoke changes in the antimicrobial activity of nanoparticles [Axson et al. 2015]. Also, ligand (*e.g.*  $\text{Cl}^-$ ,  $\text{S}^{2-}$ ,  $\text{SO}_4^{2-}$ ,  $\text{PO}_4^{3-}$ ,  $\text{Ca}^{2+}$  and cysteine) and Natural Organic Matter (NOM), which has mostly a biological origin including the organic matter released from plants, algae and fungi (*e.g.* proteins, polysaccharides, nucleic acids, lipids, etc.), present in solution might chelate free  $\text{Ag}^+$  (*i.e.* to create a strong bonding of ions and molecules to metal ions). They may also chemically reduce  $\text{Ag}^+$  to  $\text{Ag}^0$  or cause  $\text{Ag}^+$  to precipitate in one of its many insoluble complexed forms (such as  $\text{AgCl}$  or  $\text{Ag}_2\text{S}$ , as discussed in the previous paragraph). They can at last alter the reactivity of AgNPs by displacing the surface coating and adsorbing to their surfaces [Navarro et al., 2008a; Choi et al. 2009; Fabrega et al., 2009; Liu and Hurt, 2010; Levard et al., 2011; Xiu et al., 2011; Levard et al., 2012; Cumberland and Lead, 2013].

Another important example concerns cysteine, a common amino acid representative of thiol ligands that bind monovalent silver. Cysteine is widely used in AgNPs toxicity experiments to assess the effects of dissolved  $\text{Ag}^+$ . This proteinogenic amino acid is able to reduce silver toxicity to organisms exposed to silver nanomaterials due to the relatively strong affinity between  $\text{Ag}^+$  and cysteine [Navarro et al., 2008b]. Although the complexation of dissolved  $\text{Ag}^+$  by cysteine is the likely mode of action, an excess of cysteine (Cysteine/Ag concentration ratio about 50) can also induce aggregation of the AgNPs over long exposure time, leading to a secondary mechanism by which the presence of cysteine could decrease AgNPs toxicity [Gondikas et al., 2012].

## **5.2. Interaction between Ag and microorganisms: the particular case of green algae *Chlamydomonas reinhardtii***

In the literature, antimicrobial and toxicity effects of AgNPs were studied for two main categories of micro-organisms: prokaryotes and eukaryotes [Marambio-Jones and Hoek, 2010; Chernousova and Epple, 2013]. The main difference between the two categories involves the cell structure. Prokaryotes are organisms in which cells have a simpler internal structure without organelles (membrane-enclosed structures in the cytoplasm). In contrast, eukaryotes present different kinds of organelles inside the cytoplasm [Madigan et al., 2012]. These organelles include, first and foremost, the nucleus, which house the cell's genome and key processes of DNA like replication and transcription, but also mitochondria and chloroplasts, which are dedicated to energy conservation and carry out respiration and photosynthesis, respectively. However, chloroplasts are only present in photosynthetic cells of organisms like plants or algae. One of the two prokaryotic groups is that of bacteria. Among them, some are pathogenic bacteria and are at origin of related human diseases. For this reason, a lot of Ag toxicity and release studies are performed on bacteria evaluating mainly the antibacterial efficiency and mechanism of Ag nanocomposites [Sondi and Salopek-Sondi, 2004; Shahverdi et al., 2007; Ivask

et al., 2014; Le Ouay and Stellacci, 2015]. Moreover, these microorganisms are relatively easy to culture and can be considered a “screening tool” for the toxicity of nanosilver. Animals, plants, fungi and algae are different types of eukaryotic organisms. In particular, fungi cells are most closely related to animal ones and some fungi grow as single-celled forms (the yeasts). Among yeasts, *Saccharomyces Cerevisiae* has been studied as a model eukaryote for many years. For this reason, studies of the interactions between *Saccharomyces Cerevisiae* and Ag nanocomposites is an important step to evaluate both toxicity consequences and antifouling properties of these nanomaterials [Saulou et al., 2010; Despax et al., 2011].

Owing to the random dispersion of AgNPs contained into the Ag nanomaterials in ecosystem, many researches are performed now to evaluate the risk of these nanomaterials towards organisms in the environment [Behra et al., 2013]. Algae are sensible and powerful tools to understand effects of these nanocomposite materials [Navarro et al., 2008b; Miao et al., 2009; He et al. 2012b;]. The unicellular green algae belong to a particular class of algae, with chloroplasts containing a and b chlorophylls, which give them their characteristic green color. By the composition of their photosynthetic pigments, they are similar to plants and are phylogenetically closely related to land plants. Among these algae, *Chlamydomonas reinhardtii* represents a model eukaryotic organism to study the toxicity effect of dispersed AgNPs. It is mandatory to highlight that the bacteria, yeast, and unicellular green algae present an additive external structure with respect to other eukaryotic organisms. This is the rigid cell wall that is the first protective barrier against toxic agents. However, the toxicity effects of Ag are similar towards internal components of cell for together organisms (with and without cell wall). Similar to bacteria, *Chlamydomonas reinhardtii* is a microorganism relatively easy to culture (for details see Chapter 2). Moreover, this alga presents two important advantages to evaluate the Ag release from AgNPs:

- Ag uptake in *Chlamydomonas reinhardtii* from AgNPs has been observed to occur rapidly [Fortin and Campbell, 2001] and to be dependent on dissolved  $Ag^+$ . No evidence of substantial AgNPs uptake was found for this microorganism [Piccapietra et al., 2012; Navarro et al., 2015;]. In contrast, bactericidal properties of the AgNPs were mainly related to direct effects based on nanoparticles found to accumulate intracellularly and at the cell membrane [Morones et al., 2005].
- *Chlamydomonas reinhardtii* is an extremely sensitive tool for the indirect measurement of  $Ag^+$  released in solution under realistic exposure scenarios due to changes in its chlorophyll fluorescence (inhibition of algal photosynthesis yield). Moreover, its photosynthetic yield is not affected by the algal translocation into buffered water or by exposure to Ag-ligand like cysteine [Navarro et al., 2008b; Navarro et al., 2015].

However, during the normal living cycle of algae,  $H_2O_2$  is a metabolic product of algae, which may be secreted in the nearest layer of exposure medium around the cell depending on the algae species and

conditions [Suggett et al., 2008; He et al., 2012c; Pospíšil, 2012]. AgNPs in contact with H<sub>2</sub>O<sub>2</sub> would lead to an enhancement of the Ag<sup>+</sup> release as discussed previously. These reactions would result in increasing Ag<sup>+</sup> availability close to algae cells and thus in increased Ag<sup>+</sup>-uptake (enhanced toxicity effect) [Navarro et al., 2015; Sigg and Lindauer, 2015]. In this context, the Ag release from solid Ag nanocomposite can be tested in both absence (abiotic condition) and presence (biotic condition) of algae.

### **5.3. Interaction between AgNPs and proteins**

Microbial adhesion to surfaces followed by cell growth and colonization results in the formation of an Extracellular Polymeric Substance (EPS) capable of protecting the underlying microorganisms from antimicrobials, chemical biocides and host defense mechanisms [Hoyle and Costerton, 1991; Costerton et al., 1999]. The system composed by the microbial population adhered to a surface and surrounded by EPS represents a biofilm. The formation of biofilms is a significant problem in various areas (medical device, food industry, distribution of drinking water etc.) [Briand et al., 1999; Pradier et al., 2005; Ramage et al., 2006]. A surface treatment can prevent biofilm formation by limiting the initial microbial adhesion and/or by killing microorganisms as they come in close contact with the solid surface. This microbial adhesion on the solid surface is induced by proteins [Saulou et al., 2010]. In the last decade, a growing interest has been focused on nanocomposite coatings containing AgNPs as antimicrobial agent [Favia et al., 2000; Jiang et al., 2004; Saulou et al., 2012; Sambhy et al., 2006; Sardella et al., 2006]. These nanocomposite coatings (about 300-400 nm thickness) are typically consisted of AgNPs (< 50 nm in size) embedded in polymer or polymer-like matrices. Wet chemical or plasma assisted methods were used to mediate the coatings. The interaction between microorganisms and nanocomposite containing AgNPs leads to changes in structures of intracellular (like enzymes) and cell wall (like mannoproteins) protein, probably through interacting with their thiol groups [Feng et al., 2000; Saulou et al., 2010; Saulou et al., 2012;]. In the literature, the first studied step was the protein adsorption on a solid surface [Jenney and Anderson, 2000; Wyre and Downes, 2002; Sakiyama et al., 2004; Shen and Zhu, 2016]. Understanding of interaction mechanisms between proteins and AgNPs represents a route to elucidate the role of proteins in the formation of biofilms. A brief description of proteins and solid surface properties related to their mutual interaction is given below.

#### **5.3.1. Proteins properties affecting their interaction with solid surface**

A protein is an assembly of amino acids (*i.e.* an organic compound containing amine (-NH<sub>2</sub>) and carboxylic (-COOH) functional groups) held together by covalent bonds between a carbon atom and a nitrogen atom of two amino acids. More than 100 amino acids linked in a chain are required to create a simple protein. Owing to the chemical and physical properties of amino acids, one or more amino acid chains forming the protein fold into three-dimensional shapes held by chemical bonds. This three-dimensional shape of a protein is critical to its function. Principal bonds holding the protein three-

dimensional shape typically are hydrogen bonds that are weaker than the covalent ones [Lartundo-Rojas, 2007]. These bonds can easily be broken by chemical product or heat. In this context, protein properties important for their adsorption on sample surface can be summarized as [Lartundo-Rojas, 2007; Shen and Zhu, 2016]:

- **Size.** Big proteins present more contact sites to interact with the surface;
- **Structure stability.** Proteins that have a less stable structure (*i.e.* ones presenting less intramolecular bonds) can easily enlarge on surface. As consequence, these proteins improve the number of contact sites with the surface;
- **Charge.** Depending on the amino acid sequences in a given region, the outer hydrophilic surface of a protein is heterogeneously charged at neutral pH;
- **Hydrophobicity.** A protein consists of hydrophobic/hydrophilic domains in structure. The inner hydrophobic core of the protein is favorable for a hydrophobic surface with a relatively high water contact angle;
- **Heterogeneity.** Protein surface can present regions with different charge and hydrophobic/hydrophilic behavior.

All these properties give to the proteins the ability to adapt to different solid surfaces.

### 5.3.2. Surface properties related to proteins absorption

In the same way, the surface properties implied to the protein adsorption process involve chemical and physical characteristics of solid surfaces [Shen and Zhu, 2016]. Principal surface characteristics are:

- **Topography.** High roughness of the solid surface improves the exposed surface able to interact with the proteins;
- **Charge.** The electrical surface potential influences the charge distribution at solid surface which in turn modifies ions in solution close to the interface between the solution and the solid surface. As consequence, this alters the electrostatic interaction between proteins and substrate surface;
- **Composition.** Surface chemical composition determines the kind of intermolecular forces that rules the interaction between proteins and the surface;
- **Hydrophobicity.** Hydrophobic surfaces promote the formation of bonds between proteins and the surface. Together with the topography characteristic, a curved hydrophobic surface enhances the amount of adsorbed proteins;
- **Heterogeneity.** The presence of heterogeneity on the surface, such as heterogeneously charged or amphiphilic surfaces (e.g. possessing at the same time hydrophobic and hydrophilic groups), define regions that can interact with proteins in different way.

However, the protein adsorption mechanisms are not only due to the proteins and surface properties. This adsorption also depends on the availability of proteins. Moreover, proteins can be brought to the

surface by one or more of the four main transport mechanisms: diffusion, natural convection, forced convection and coupled transport. Variables such as the concentration and size of the proteins are important to determine their access to the surface [Ratner et al., 2004]. Once proteins are present on the surface, they can interact with the substrate via intermolecular forces such as ionic bonding (electrostatic interactions), hydrophobic interactions and charge transfer interactions (electron exchange) [Lartundo-Rojas, 2007]. Hydrogen bonds, which are important as stabilizers for the protein structure, do not play a key role in the interactions between proteins and the surface. Protein adsorption is virtually irreversible except if dramatic changes occur in the environment, such as an increment of ionic strength, a decrease in pH or the use of detergents.

## 6. Optical properties of AgNPs

In addition to their bactericide properties, nanocomposite materials containing noble metallic NPs are widely studied for their exceptional optical properties. In the past decade, attention was focused on nanoparticles composed of noble metals, because they support localized surface plasmon resonances (LSPRs). These collective oscillations of the conduction band electrons enable strong optical absorption and scattering in subwavelength structures, with spectral properties dependent on the NP material, size, shape, electronic charge and surrounding medium. The LSPR of noble metal NPs is widely exploited for enhanced optical spectroscopies of molecules, [Nie and Emory, 1997] nonlinear optics, [Toudert et al., 2008; Traverse et al., 2008] photothermal therapy, [Baffou and Quidant, 2013] photovoltaics, [Atwater and Polman, 2010; Linic et al., 2011] or more recently in plasmoelectronics [Spinelli and Polman, 2012; Warren et al., 2012] and photocatalysis. [Prieto et al., 2012; Mukherjee et al., 2013; Zhang et al., 2013]. Among the noble metal NPs, we will see that AgNPs realize the best nanoscale antennae. In this last section, we will describe the electronic and optical properties of noble metals, from the bulk material to the NPs. Development of solid Surface Enhanced Raman Scattering (SERS) substrates based on metal nanostructures embedded in dielectrics will be introduced. Even if not the heart of this work, this other facet of our nanocomposite materials could be coupled to their bactericide properties for a multifunctional use in the biofilm detection and prevention (see Chapter 6). In addition, their optical response has been used all along this work for a fast and non-destructive characterization of these nanocomposite materials. In particular, ellipsometry measurements have been shown to be a wealth of information, as it will be shown in Chapter IV.

### 6.1. Electronic properties of noble metals

To understand the optical properties of noble metal nanoparticles, we have to start with the electronic band structure a bulk noble metal. The classification of noble metals requires a solid with fully occupied  $d$ -valence levels and energy  $E_F$  of Fermi level, which identifies the last occupied energy level at temperature of 0 K in metals that does not cross the  $d$ -valence levels (Fig. I.18). The three metallic

elements that satisfy these conditions are copper, silver and gold [Eckardt et al., 1984]. These metals have an atomic structure of electron configuration: [noble gas]  $(n-1) d^{10} ns^1$ . From the point of view of solid state physics, the electronic band structure of noble metals is composed by a band of fully occupied levels (called valence band - blue in Fig. I.18) and a band of partially occupied levels (called conduction band - green in Fig. I.18) [Kittel, 2004]. The overlapping of  $(n-1) d^{10}$  discrete atomic levels gives rise to the valence band while the hybridization of discrete atomic levels  $ns$  and  $np$  leads to the formation of the conduction band.

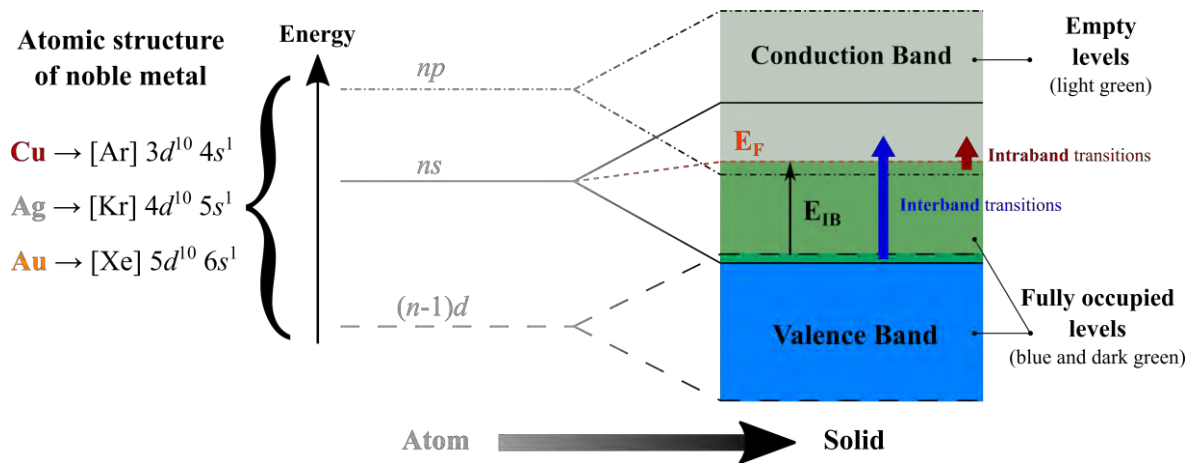


Figure I.18: Schematic of the electronic structure evolution of noble metals Cu, Ag and Au with  $n = 3, 4$  and  $5$ , respectively, starting from atomic levels towards the band structure of the bulk solid. Two types of band transitions (interband and intraband), the energy threshold of interband transitions between valence and conduction band  $E_{IB}$  and the energy of Fermi level  $E_F$  are shown. The atomic structure of these noble metals is reported on the left side.

The valence band of noble metals results from 5 overlapping  $d$  electronic dispersion curves, each one varying in a narrow energy range (orange points in figure I.19). On the contrary, the conduction band contains only the hybrid  $sp$  dispersion curve that varies in a broad energy range (blue points in figure I.19).

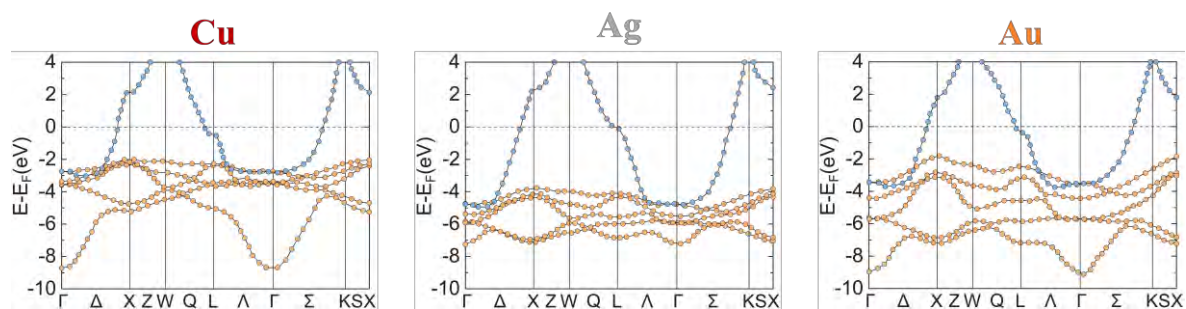


Figure I.19: Electronic energy dispersion curves in Cu, Ag and Au as function of the wave vector  $\mathbf{k}_e$ . From [Eckardt et al., 1984]. In the ordinate axis, the zero value corresponds to the Fermi level. In the abscissa axis, the standard labels of symmetry points and axes of the Brillouin zone (*i.e.* face centred cubic (fcc) are reported [Kittel, 2004]).

This implies that the density of electronic states (*i.e.* the number of electronic states per unit of energy) in the valence band is much higher than the one in the conduction band, in particular close to the energy of Fermi level. This finding will strongly affect the electronic transition rates of these metals due to an external excitation (*e.g.* an electromagnetic wave as the light). In this context, optical characteristics of noble metals are strictly related to their band structure.

## 6.2. Optical properties of noble metals (bulk Electronic properties of noble metals)

### 6.2.1. Drude model

The properties of the metal free electrons can be adequately explained by using the Drude model. This model describes the metals as a system in which the free electron gas of density  $n$  can move in a fixed array of positive ions. When an oscillating external electric field  $\mathbf{E}$  is applied, the electrons collectively oscillate around their equilibrium position. This motion in bulk metals is damped via collisions of electrons with other electrons, crystal lattice (phonons), lattice defects, or impurities. This occurs with a characteristic collision frequency  $\gamma_b = 1/\tau$ , where  $\tau$  is the time between two consecutive collisions (known as the relaxation time of the free electron gas).

The motion of an electron in the plasma sea subjected to an external electric field  $\mathbf{E}(t)$ , is described by the fundamental classical equation of motion:

$$m_e \frac{\partial^2 \mathbf{r}}{\partial t^2} + m_e \gamma_b \frac{\partial \mathbf{r}}{\partial t} = e \mathbf{E}_0 e^{-i\omega t}, \quad (\text{I.17})$$

where  $m_e$  is the electron mass,  $e$  is the elementary charge,  $\omega$  is the electric field angular frequency.

The particular solution of this equation describing the forced oscillation of the electron is:

$$\mathbf{r}(t) = \frac{e}{m_e (\omega^2 + i\gamma_b \omega)} \mathbf{E}(t). \quad (\text{I.18})$$

The ensemble of displaced electrons provokes a macroscopic polarization of metal  $\mathbf{P} = -n_e e \mathbf{r}(t)$ . Inserting this expression for  $\mathbf{P}$  into the equation for dielectric displacement  $\mathbf{D}(r,t) = \epsilon_0 \mathbf{E}(r,t) + \mathbf{P}(r,t)$  yields:

$$\mathbf{D}(t) = \epsilon_0 \left( 1 - \frac{\omega_p^2}{\omega^2 + i\gamma_b \omega} \right) \mathbf{E}(t), \quad (\text{I.19})$$

where  $\omega_p = \sqrt{\frac{n_e e^2}{\epsilon_0 m_e}}$  is the Drude plasma frequency of the free electron gas. This angular frequency can be recognized as the natural frequency of a free oscillation of the plasma sea around a positive background of the ion cores in which all electrons move in phase (collective oscillations). In a quantum description of this harmonic oscillation, one introduces energy quanta  $E_p$  called *volume plasmons*. For most of the metals, the energy associated with these excitations ranges between 5 and

15 eV depending on the band structure details [Kittel, 2004].  $E_p$  of noble metals ranges between 9 and 11 eV [Rakić et al., 1998]. Considering equation I.17, the complex dielectric function of the free electron gas  $\varepsilon_d(\omega)$  in the Drude model is expressed as:

$$\varepsilon_D(\omega) = 1 - \frac{\omega_p^2}{\omega^2 + i\gamma_b\omega}. \quad (\text{I.20a})$$

The dielectric response is thus described by a complex function where the real part  $\varepsilon'_D(\omega)$  accounts for the dispersion and the imaginary part  $\varepsilon''_D(\omega)$  for the absorption:

$$\varepsilon'_D(\omega) = 1 - \frac{\omega_p^2}{\omega^2 + \gamma_b^2} \stackrel{\omega \gg \gamma_b}{\cong} 1 - \frac{\omega_p^2}{\omega^2}, \quad (\text{I.20b})$$

$$\varepsilon''_D(\omega) = \frac{\omega_p^2\gamma_b}{\omega(\omega^2 + \gamma_b^2)} \stackrel{\omega \gg \gamma_b}{\cong} \frac{\omega_p^2}{\omega^3}\gamma_b. \quad (\text{I.20c})$$

The remarkable feature of the real part of the dielectric function for bulk metals is its ability to be positive (propagation) or negative (extinction) following the frequency and to be zero at  $\omega = \omega_p$  when the damping factor  $\gamma_b$  is negligible ( $\omega \gg \gamma_b$ ).  $\varepsilon'_D(\omega) = 0$  defines the resonance condition of bulk metals. At the plasma frequency  $\omega_p$ , we can observe two important features of the free electron gas. First, the propagation direction of the collective oscillation of the free electron gas is parallel to the applied electric field (longitudinal waves) [Maier, 2007]. Due to the longitudinal nature of this excitation, volume plasmons do not couple to transverse electromagnetic waves, and can be excited only by particle impact. Second, the electric field becomes a pure depolarization field ( $\mathbf{E} = -\mathbf{P}/\varepsilon_0$ ). This provokes a restoring force on displaced free electrons.

### 6.2.2. Intraband and interband transitions in noble metals

In the band structure described in figures I.18 and I.19, two types of electronic transitions can be distinguished:

- *Intraband* transitions within the sp hybrid band (conduction band) involving the direct excitation of electrons in levels close to the  $E_F$ . At room temperature ( $T = 25^\circ\text{C}$  equivalent to 26 meV by the relation  $E \propto k_b T$ , where  $k_b$  is the Boltzmann constant), electrons have enough energy to reach the empty levels. These electrons can be considered as **free electrons** and the Drude model is a good approximation.
- *Interband* transitions between the d valence band and the conduction hybrid sp band allowing electrons of full levels of valence band to directly reach empty ones of conduction band. The **minimum energy** required for this type of interband transition is  $E_{IB}$ , which is of the order of



magnitude of few eV (Fig. I.18). These electrons are considered **bound electrons** at room temperature.

The frequency (or wavelength) dependence of the dielectric function of a bulk noble metal does result from these two types of electronic transitions. When plotting the real and imaginary parts of the dielectric function, we can see that after the energetic threshold of  $E_{ib} = 3.9$  eV for Ag (2 eV and 2.1 eV for Au and Cu, respectively), the experimental data move away from the Drude model predictions (Fig. I.20). Above this energy, the interband transitions become important and strongly modify the imaginary part of the metal dielectric function.

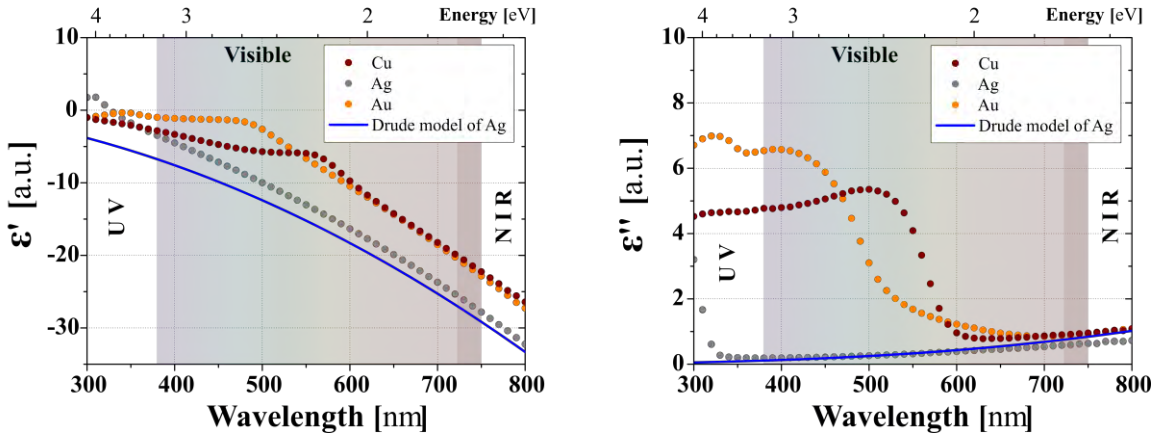


Figure I.20: Experimental  $\epsilon_D'(\lambda)$  and  $\epsilon_D''(\lambda)$  of Cu, Ag and Au (color points). It also reports the real and imaginary part of  $\epsilon_D(\lambda)$  of Ag calculated using equations I.20 (at room temperature, in energy units,  $\omega_p$  is 9.08 eV and  $\gamma_b$  is 0.28 eV [Hollstein et al., 1977]) (blue line). It is possible to distinguish the energy threshold of interband transition  $E_{IB}$  of each noble metal (around 2.1 eV (590 nm) for Cu, 3.9 eV (320 nm) for Ag and 2.4 eV (520nm) for Au [Kreibig and Vollmer, 1995]). For each element, dielectric function points are extracted from experimental ellipsometric spectrum. From [McPeack et al., 2015].

### 6.3. Optical response of noble metal nanoparticles

Scaling down to nanometer size, the optical response of metals is affected by three features: size, shape and surrounding medium of the metal [Kreibig and Vollmer, 1995; Maier, 2007]. In this section, we focus our attention to small and spherical metallic nanoparticles with dimensions much lower than the bulk electronic mean free path  $l_b$  (around 50 nm for noble metals) and greater than the Fermi wavelength  $\lambda_F$  (around 0.5 nm for noble metals) [Maier, 2007; Hartland, 2011]. The latter defines the 3D-0D quantum limit for which the spacing between electronic states at the Fermi level becomes larger than  $k_b T$ . As a consequence, the band structure of metallic nanoparticles does not change for nanoparticle dimensions above one nm.

### 6.3.1. Size effect

The complex dielectric function of metals nanoparticles develops size dependency for nanoparticle of dimensions in the nanometer range. The size dependency of dielectric function stems from both interband transitions and damping contributions. The contribution of interband transitions is related to local changes in the properties, like electron density and atomic distances, close to the particle surface, for example. The damping contribution involves changes in the electronic mean free path due to the scattering of conduction electrons against the nanoparticle surface. Usually, the latter contribution exceeds the former one by far [Coronado and Schatz, 2003]. Hence, when the nanoparticle size is smaller than  $l_b$ , the damping increases and can be written as [Coronado and Schatz, 2003]:

$$\gamma(D_{NP}) = \gamma_b + g_s \frac{v_F}{l_{eff}(D_{NP})}, \quad (I.21)$$

where  $g_s$  is dimensionless parameter depending on the surface scattering, usually assumed to be close to unity [Coronado and Schatz, 2003; Baida et al., 2009],  $v_F$  is the Fermi velocity, and  $l_{eff}$  is the effective electronic mean free path. The latter depends on the size and shape of the nanoparticles and can be expressed by  $l_{eff} = 4V/S$  where  $V$  is the volume and  $S$  is the surface area of the nanoparticle. For spherical nanoparticles, the effective electronic mean free path is directly proportional to the size  $D_{NP}$  of nanoparticles, *i.e.*  $l_{eff}(D_{NP})$  [Kreibig and Vollmer, 1995; Coronado and Schatz, 2003]. Finally, the complex dielectric function of metallic spherical nanoparticles  $\varepsilon_{NP}(\omega, D_{NP})$  can be written as:

$$\varepsilon_{NP}(\omega, D_{NP}) = \varepsilon_{IB}(\omega) - \frac{\omega_p^2}{\omega^2 + i\gamma(D_{NP})\omega}, \quad (I.22)$$

where  $\varepsilon_{IB}(\omega)$  is the part of complex dielectric function due to the interband transitions in bulk metals.

In the visible frequency range, the condition  $\omega \gg \gamma(D_{NP})$  remains valid and the real  $\varepsilon'_{NP}(\omega)$  and imaginary  $\varepsilon''_{NP}(\omega, D_{NP})$  components of  $\varepsilon_{NP}(\omega, D_{NP})$  read:

$$\varepsilon'_{NP}(\omega) = \varepsilon'(\omega) \cong \varepsilon'_{IB}(\omega) - \frac{\omega_p^2}{\omega^2}, \quad (I.23)$$

$$\varepsilon''_{NP}(\omega, D_{NP}) \cong \varepsilon''(\omega) + \frac{\omega_p^2}{\omega^3} g_s \frac{v_F}{l_{eff}(D_{NP})}. \quad (I.24)$$

Hence, the size dependency of the dielectric function is negligible for the real component of the dielectric function (which is equal to the bulk value) meanwhile it significantly influences the imaginary part.

### 6.3.2. Localized Surface Plasmon Polariton (LSPP)

To describe the electric interaction between metal nanoparticles and an electromagnetic wave, the *quasi-static approximation* is fulfilled because the nanoparticle size  $D_{NP}$  is much smaller than the wavelength  $\lambda$  of the external electric field  $E(z, t)$  in the visible range ( $D_{NP} \ll \lambda$ ) (Fig. I.21).

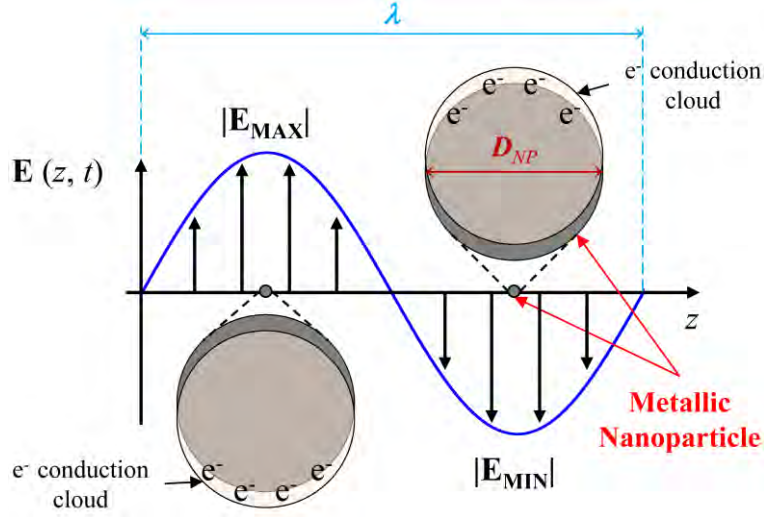


Figure I.21: Interaction between the electromagnetic wave of harmonic time dependence and metallic spherical nanoparticles under *quasi-static approximation*. The displacement of conduction electronic cloud with respect to positive charges is shown at minimum ( $E_{MIN}$ ) and maximum ( $E_{MAX}$ ) of electric field.

Within this approximation, the phase of the harmonically oscillating electromagnetic field is practically constant over the particle volume and this allows neglecting the spatial retardation effects over this volume. Therefore a uniform displacement of the conduction electrons cloud from the positive charges occurs (Fig. I.21).

One can calculate the spatial field distribution by assuming the simplified problem of a homogeneous isotropic spherical nanoparticle of radius  $R = D_{NP}/2$  and dielectric function  $\epsilon_{NP}(\omega, D_{NP})$  located at the origin in a uniform static electric field  $\mathbf{E}_0 = E_0 z$ . The surrounding medium is assumed to be isotropic and non-absorbing with a real dielectric constant  $\epsilon_m$  (Fig. I.22).

We only report here (for an overview see [Maier, 2007]) the final result concerning the spatial distribution of the electric field inside ( $\mathbf{E}_{in}$ ) and outside ( $\mathbf{E}_{out}$ ) the spherical nanoparticle due to the applied electric field  $\mathbf{E}(z, t) = \mathbf{E}_0 e^{-i\omega t}$ :

$$\mathbf{E}_{in} = \frac{3\epsilon_m}{\epsilon_{NP}(\omega, D) + 2\epsilon_m} \mathbf{E}(z, t) \quad (1.25)$$

$$\mathbf{E}_{out} = \mathbf{E}(z, t) + \frac{3\mathbf{n} \cdot \mathbf{p} - \mathbf{p}}{4\pi\epsilon_0\epsilon_m} \frac{1}{r^3}, \quad (1.26)$$

where  $\mathbf{n}$  and  $\mathbf{r}$  are the unit vector and the module of the vector position (the origin is taken at the center of the nanoparticle), respectively.  $\mathbf{p}$  is the dipolar moment of the nanoparticle induced by the applied electric field and defined as  $\mathbf{p}(z,t) = \varepsilon_0 \varepsilon_m a(\omega, D_{NP}) \mathbf{E}_0 e^{-i\omega t}$ , where  $a(\omega, D_{NP})$  is the polarizability.

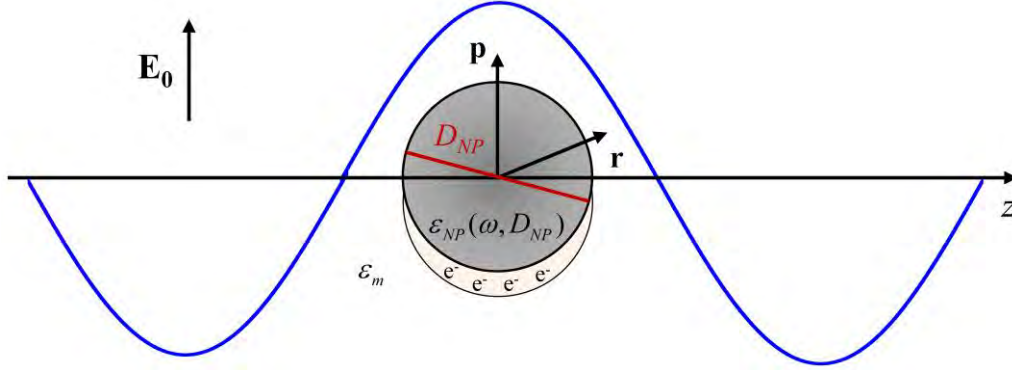


Figure I.22: Sketch of a spherical nanoparticle placed into an electrostatic field.

The latter can be expressed as:

$$a(\omega, D_{NP}) = \frac{\pi}{2} D_{NP}^3 \frac{\varepsilon_{NP}(\omega, D_{NP}) - \varepsilon_m}{\varepsilon_{NP}(\omega, D_{NP}) + 2\varepsilon_m} \quad a(\omega, D_{NP}) = \frac{\pi}{2} D_{NP}^3 \frac{\varepsilon_{NP}(\omega, D_{NP}) - \varepsilon_m}{\varepsilon_{NP}(\omega, D_{NP}) + 2\varepsilon_m}. \quad (I.27)$$

The polarizability presents a resonance when the term  $|\varepsilon_{NP} + 2\varepsilon_m|$  is minimal, i.e., for  $\varepsilon_{NP} = -2\varepsilon_m$ . For this value, a resonance of the electric field inside and outside the nanoparticle is also observed.

In the same way that we have described the volume plasmons for bulk materials, we can define the localized surface plasmon as the quantum of collective oscillations in a NP. The corresponding resonance or LSPR (for Localised Surface Plasmon Resonance) takes place for a frequency:

$$\omega_{LSPR} = \frac{\omega_p}{\sqrt{\varepsilon_{IB} + 2\varepsilon_m}}. \quad (I.28)$$

This frequency depends on the NP material and shape (here the factor 2 is the shape factor for a sphere) but also on the environment ( $\varepsilon_m$ ) of the NP. Thanks to their small size, the NPs allow to concentrate the electromagnetic field at a scale drastically smaller than the corresponding wavelength. Indeed, following Eqs I.25 and I.26, one sees that the electromagnetic energy will be concentrated inside the NP and at its immediate vicinity. This is particularly suitable to the use of the exaltation effects of the light diffusion by objects localized in their near field as the well-known SERS (Surface Raman Spectroscopy) effect [Cho et al., 2012]). In addition, according to equation I.27, this phenomenon will be particularly exalted at frequencies near that of the LSPR.

### 6.3.3. Absorption and diffusion cross-sections

When an electromagnetic wave interacts with a NP, the NP absorbs a part of the incident power and another part is diffused. Using the Mie theory [Maier, 2007], one can calculate the associated cross-sections. They are defined as the ratio between the electromagnetic power absorbed, or radiated, and the incident energy flux. Their sum is called “extinction cross-section”.

$$C_{ext} = C_{abs} + C_{diff}, \quad (I.29)$$

with,

$$C_{abs} = k \text{Im}(\alpha) = 4\pi k R^3 \text{Im} \left( \frac{\varepsilon - \varepsilon_m}{\varepsilon + 2\varepsilon_m} \right), \quad (I.30)$$

and

$$C_{diff} = \frac{k^4}{6\pi} |\alpha|^2 = \frac{8\pi}{3} k^4 R^6 \text{Im} \left| \frac{\varepsilon - \varepsilon_m}{\varepsilon + 2\varepsilon_m} \right|^2, \quad (I.31)$$

The absorption cross-section varies with  $R^3$  meanwhile the diffusion one is function of  $R^6$ . In the dipolar approximation  $R \ll \lambda$ , the absorption clearly dominates the diffusion and we can write:

$$C_{ext} \approx C_{abs} = \frac{24\pi^2 R^3 \varepsilon_m^{3/2}}{6\pi} \frac{\varepsilon''(\lambda)}{|\varepsilon'(\lambda) + 2\varepsilon_m| + \varepsilon''^2(\lambda)}. \quad (I.32)$$

These quantities are homogeneous to surfaces and can be represented in a schematic way (Fig. I.23): in resonant conditions (LSPR frequency), the “effective projected area” of the NP becomes larger than its geometrical value.

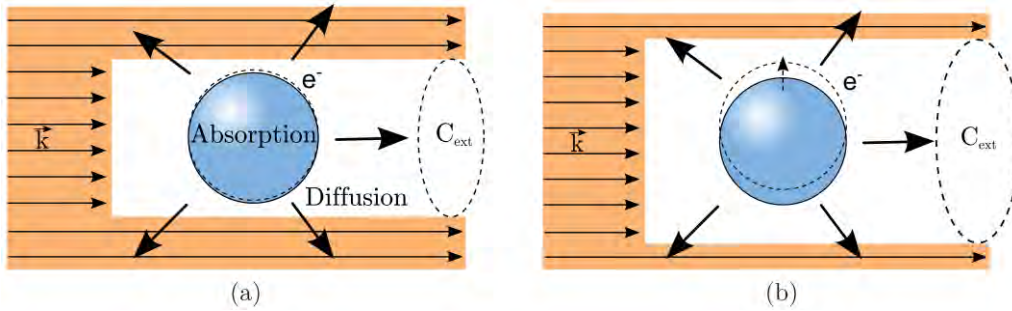


Fig. I.23: Schemes representing the extinction cross-section  $C_{ext}$  of a metal NP in an electromagnetic field, out of resonance (a) and at the resonance (b). From [Bayle, 2014]

Consequently, in order to compare the amplitude and acuity of the LSPR of different systems (NP+matrix), we can define the extinction efficiency as the ratio between the extinction cross-section and the geometric surface:

$$Q_{ext} = \frac{C_{ext}}{\pi R^2}. \quad (I.33)$$

The resonance frequency  $\omega_{\text{LSPR}}$  of a spherical NP, and therefore the associated photon energy, depend on the nature of NP material but also on that of its embedding matrix. We can hence calculate the resonance energy of the composite system if we know the dielectric functions of the both materials [Polyanskiy, 2016]. The calculation of the extinction efficiency gives information on the resonance profile (frequency location, width and intensity) and allows the best choice of the couple (NP material/matrix). In figure I.24, the extinction coefficient for NPs made of 3 noble metals (Ag, Au and Cu) in two different matrices ( $\text{SiO}_2$  and  $\text{Si}_3\text{N}_4$ ) is plotted [Bayle et al., 2014]. The relative amplitude of each curve clearly shows an important resonance for Ag and Au that can be used for plasmonic applications in these two types of matrices. Nevertheless, the Ag resonance is clearly higher than the one of Au and this material will be chosen for maximum field exaltation. Indeed, the resonance quality factor, defined as  $Q = \lambda_{\text{LSPR}}/\Delta\lambda$  where  $\Delta\lambda$  is the FWHM, is higher for AgNPs than for AuNPs (metal effect) because of the supplementary damping by interband transitions in Au. As discussed in section 6.2.2 of this chapter, the interband transitions are located at higher energy for Ag (3.9 eV) compared to Au (2 eV).

Now by changing the embedding medium from  $\text{SiO}_2$  to  $\text{Si}_3\text{N}_4$  for example a strong enhancement of the LSPR and its tuning in the middle of the visible were obtained. The LSPR of Ag-NPs shifts from the near UV range (400 nm) to the visible range (475 nm). Owing to the fact that the higher the refractive index, the better the electromagnetic energy confinement is, the quality factor is doubled when changing the surrounding medium from  $\text{SiO}_2$  to  $\text{Si}_3\text{N}_4$  for example. Nevertheless, most of the studies in the literature involving AgNPs embedded in dielectrics for plasmonic applications involve silica matrices, this material being widespread and easiest to synthesize.

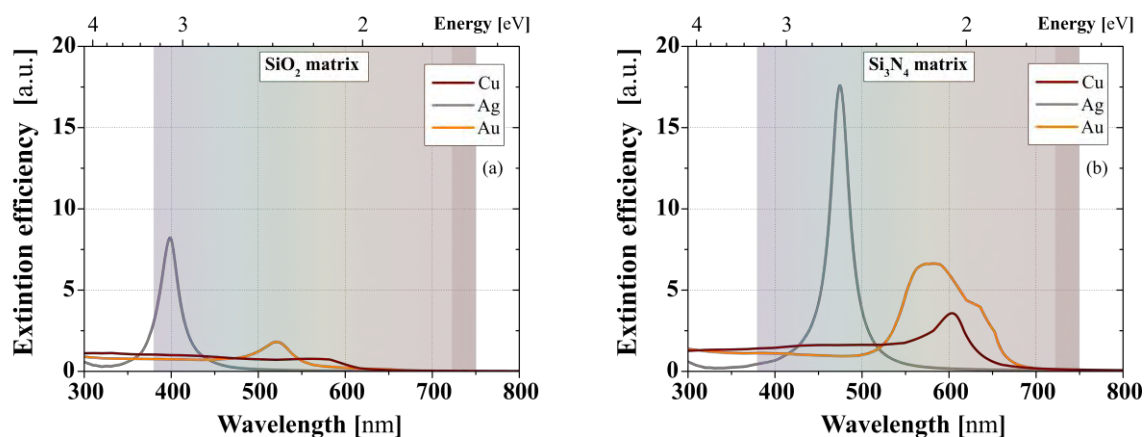


Figure I.23: Extinction efficiency of noble metal NPs embedded in a  $\text{SiO}_2$  (a) and  $\text{Si}_3\text{N}_4$  (b) matrix [Bayle et al., 2014].

#### 6.4. Use of embedded AgNPs for SERS substrates

Hence AgNPs realize the best nanoscale antenna for amplifying local electronic and vibrational signals in the visible range, providing unique molecular information in the optical far-field regime. In the field

of scientific research, two main spectroscopy techniques have emerged based on localized surface plasmon resonance (LSPR) and surface-enhanced Raman scattering (SERS). Advances in micro and nano-fabrication technology have made available integration of sensitive LSPR to lab-on-a-chip platforms. They are increasingly popular in fundamental biological studies, health science research and environmental monitoring [Vo-dinh et al., 2005; Stewart et al., 2008; Rycenga et al., 2011]. Since its discovery in 1974 on pyridine molecules adsorbed on rough silver surfaces [Fleischmann et al., 1974], SERS has received a great deal of attention as powerful analytical technique for molecular spectroscopy, biomolecular recognition and ultra-sensitive detection (down to a single molecule). Many effective ways have been explored [Lacy et al., 1996; Evanoff and Chumanov, 2005; Rycenga et al., 2011] for the synthesis of Ag plasmon-active surfaces as an aggregation of colloids, electrochemically roughened electrodes, atom beam sputtering, or pulsed laser deposition. Most of the currently available lithographic techniques are developed for the fabrication of two-dimensional metallic nanostructure arrays and often carry with them limitations that prohibit their widespread use for biological spectroscopy and imaging [Le Ru et al., 2006; Jones et al., 2011;]. In particular, the limits imposed by the fabrication of SERS substrates remain the major drawback for their large application, due to the drastic requirements for controlling on large area and, in a reproducible way, a well-defined spacing between the metallic nanostructures and the probing molecules. Generally, the enhancement of the scattering cross-section for SERS substrates is attributed to an electromagnetic mechanism (based on surface “plasmon resonance”) and/or to a chemical one (based on “charge transfer”). Whatever the mechanism, the requirement for an efficient SERS substrate is the fine control on nanometer scale of size and shape of the metallic particles, and of the distance between their surface and the probed molecules. A key point to overcome is control of the thickness and porosity of the coverlayer. The thickness of the coverlayer must be selected at nanoscale level as a compromise between the preservation of SERS enhancement and the protection of AgNPs against oxidation, for example [Benzo et al., 2011], and against direct interaction of the AgNPs with the probing molecules [Vo-Dinh et al., 2005].

Development of solid SERS substrates based on metal nanostructures covered by a polymer [Pal et al., 1995], or by inorganic materials (ultrathin SiO<sub>2</sub> layers) [Lacy et al., 1996] allowed improving their stability and performance. The SiO<sub>2</sub>-coated SERS substrates proved to be especially useful in SERS-based biosensors because of the well-defined hydrophilic and stabilizing properties, which actually motivated the current study. Different elaboration methods have been applied for the synthesis of solid SERS substrates. The explored ways are either via chemical reactions, lithographic fabrication, and template-direct growth [Stewart et al., 2008 and the references therein; Rycenga et al., 2011], via thermal evaporation [Lacy et al., 1996] or more recently via low energy ion implantation beam synthesis (LE-IBS) [Carles et al., 2009; Carles et al., 2011; Bayle et al., 2014], all of them emphasizing the large interest for applications and the importance of strict control during the synthesis of SERS substrates. This recent work on “embedded” plasmonics is the starting point of this work.

## 7. Conclusions

In this Chapter, we have presented the two facets of AgNPs that are at the same time (i) Ag<sup>+</sup> ion reservoirs with powerful bactericide and anti-microbial properties and (ii) the best plasmonic antenna in the UV-visible range. The main results on the physical approaches used in the literature to elaborate solid nanocomposite substrates based on AgNPs embedded in dielectrics have been introduced. These nanocomposites being intended to interact with biological objects, the reactivity of AgNPs with the different media (air, water) has also been described. In the next Chapter, the main techniques used in this work for the elaboration of these nanocomposites and the characterization of their structural and optical properties are presented. In addition, the original method that we have used for the assessment of the Ag<sup>+</sup> released and implying green algae as biosensors is detailed.





# Chapter II: Experimental techniques

---

In this chapter, the main experimental techniques used in this work will be detailed.

## 1. Ion Implantation

Ion implantation is a process of material engineering used as ages for semiconductor doping. This technique has been diverted from its initial use to introduce high doses and perform Ion Beam Synthesis (IBS) as explained in Chapter I. Hence, tiny nanostructures of controlled composition can be formed in virtually any matrix.

### 1.1. Basics of Ion Implantation

After each interaction with the target atoms, nuclear or electronic, the impinging ion losses part of its energy until it implants into the matrix. The total path travelled by the ion, due to all the random collisions, is  $R$ . However, the important distance is the projected range along the axis normal to the matrix surface,  $R_p$ . During the implantation process, the ions species are distributed into the matrix according to a Gaussian law: ions are distributed around the mean projected range  $R_p$  with a mean square deviation given by  $\Delta R_p$ :

$$N(z) = \frac{F_o}{\sqrt{2\pi}\Delta R_p} \exp\left\{-\frac{(z - R_p)^2}{2(\Delta R_p)^2}\right\}, \quad (\text{II.1})$$

$\Phi$  denotes the implanted fluence (or dose),  $R_p$  the projected range along the normal axis and  $\Delta R_p$  is the width of the profile due to straggling. Energy transfer by nuclear stopping the primary ions creates recoils which themselves could displace further substrate atoms giving rise to a recoil cascade. This is achieved if energy higher than a threshold value – the displacement threshold  $E_d$  – is transferred in a collision to a target atom. In this case a stable Frenkel pair being a pair of interstitial and vacancy is created, which is immobile at low temperatures. Then, damages can accumulate during implantation and eventually lead to the amorphization of the crystal structure. At higher temperatures though damages could anneal out dynamically in the course of implantation the number of Frenkel pairs does not exceed a temperature dependent steady state level.

The depth profiles of implanted impurity atoms are usually calculated with the help of Monte Carlo methods using the binary collision approximation codes among which TRIM/SRIM [Ziegler et al., 2010] is the most common one. For the extreme case of high dose implantation, Möller et al. [Möller et al., 1984] developed a dynamic modification of TRIM – TRIDYN – that accounts for target changes during the course of the implantation (sputtering, stoichiometry changes, swelling, ion mixing...).

## 1.2. Ion Implanter

The simplified scheme of an ion implanter is shown in Figure II.1. Ions are generated from a solid source (or a powder) in a plasma and then are extracted and accelerated. A separating magnet coupled to a selection slit allows the ions selection as a function of their ratio mass versus charge. In this work, silver ions  $^{107}\text{Ag}$  of atomic mass 106,90 uma are selected. They are then accelerated with the selected energy. The ion beam is shaped by using electrostatic lenses and a scanning system in X and Y-directions allows a uniform wafer implantation. The ion beam is deviated just before reaching the implantation chamber in order to eliminate the neutralized ions. The decelerator located just after the implantation chamber allows, by the application of a potential, to decelerate the ions, in order to reach kinetic energy lower than 5 keV. The initial energy  $E_i$  of the incoming ions delivered by the ion implanter is divided by 8 before bombarding the wafer. This means that for initial energies  $E_i$  ranging from 5 to 25 keV, the final implantation energies  $E_f$  range from 0.6 to 3.1 keV [Benassayag et al., 2000]. The ion flux (ions/cm<sup>2</sup>/s) reaching the sample surface can be deduced from the current measurement and is defined by:

$$j = \frac{I}{Se} \quad (\text{II.2})$$

By integration of this flux over time one obtains the amount of impurities implanted in the matrix. This quantity is called dose (or fluence)  $\Phi$ .

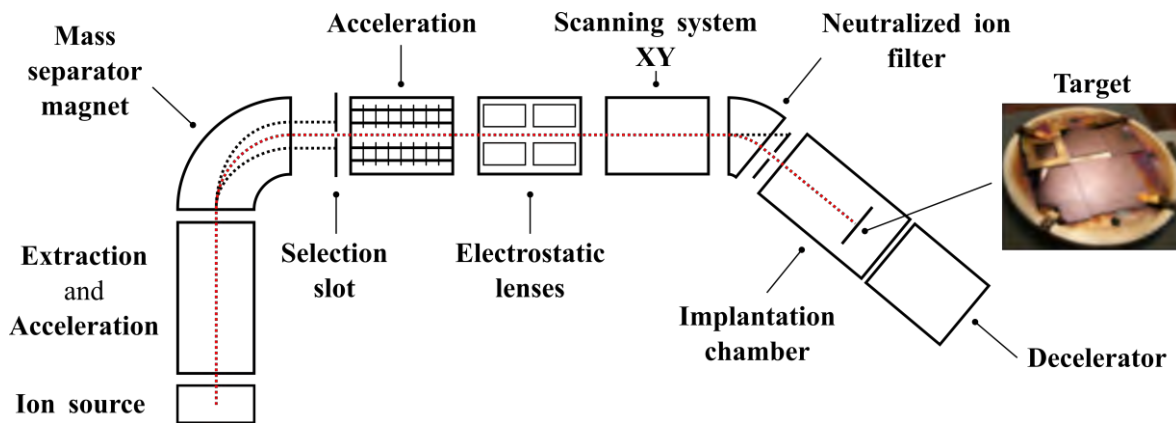


Figure II.1: Simplified scheme of the ion implanter.

## 1.3. Ion Beam Synthesis

The ion beam synthesis of AgNPs embedded in dielectrics is a one-step process (Fig. II.2). Substrate is composed of thermal silica layer grown on top of a Si wafer. As explained in Chapter I, the thickness of the dielectric layer has been chosen to be an antireflective layer (90 nm) with maximum of the electric field close to the surface [Carles et al., 2011].  $\text{Ag}^+$  are implanted for a fixed energy (in the range from 0.6 to 20 keV), which determined the projected range of the implanted profile. In this

energy range, a quasi 2D array of NPs can be formed. The ion dose is varied from some  $10^{15}$  to some  $10^{16}$   $\text{cm}^{-2}$  and fixes the amount of Ag introduced in the matrix. These high doses correspond to Ag concentrations at the mean projected range ( $R_p$ ) larger than 10 at.%. The ion current plays a key role for the silver diffusion in the silica matrix and has been fixed to 5  $\mu\text{A}$  for all the implantations. Finally, to recover the matrix damage and protect the AgNPs from fast oxidation [Benzo et al., 2011] a post-implantation rapid-thermal-annealing is carried out under  $\text{N}_2$  atmosphere at  $500^\circ\text{C}$  for 30 minutes. The choice of the annealing time and the temperature is restricted as to maintain unchanged the AgNPs size distribution and their position inside the  $\text{SiO}_2$  matrix.

Patterning in the plane of such AgNPs assembly can be obtained by implanting  $\text{Ag}^+$  ions through a stencil mask in close contact with the  $\text{SiO}_2$  surface. Hence different embedded plasmonic architectures (lines or dots arrays, gratings) made of AgNP metallic assemblies can be fabricated. This stencil mask is fabricated by focused ion beam milling of a 200 nm thick  $\text{Si}_3\text{N}_4$  membrane. After implantation, the mask is simply removed from the substrate leaving the patterns implanted on it ready to be investigated. More details on this masking process can be found in [Benassayag et al., 2012]. These particular masked samples have been fruitfully exploited for the optical studies.

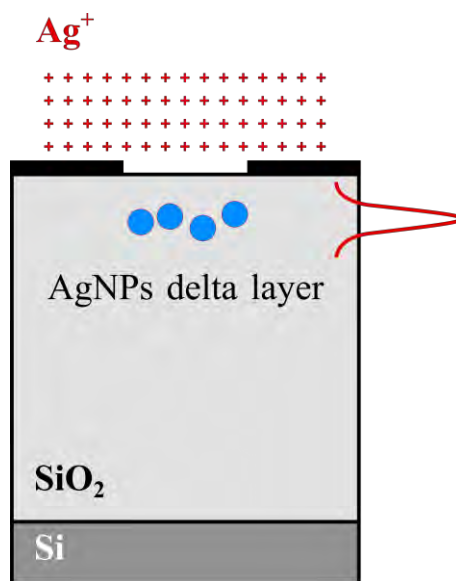


Figure II.2: Scheme of the implantation process in the case of low energy ion implantation (some keV).

The conditions for the controlled ion beam synthesis of AgNPs embedded in silica matrix have been previously optimized in the group [Benzo et al., 2011; Benzo et al., 2013] and resumed in Chapter 1. In this PhD thesis, we have selected 2 sets of operating conditions from this previous work, representing samples implanted with  $\text{Ag}^+$  at a fixed energy of 10 keV and two different doses, 0.71 and  $3.8 \times 10^{16}$   $\text{ions}/\text{cm}^2$ . These two samples present a quasi 2D array of AgNPs, with similar mean diameter and surface density (see Figs. I.9 (e) and (h)). The main difference consists in the distance of

the AgNPs from the free surface, which slightly increases when increasing the implantation dose. The samples obtained by ULE-II are called hereafter “implanted samples”.

## **2. Plasma processes**

Plasma-based deposition processes are versatile techniques largely applied in industrial applications for elaboration of thin layers including nanocomposites containing metal clusters. In this section, at first we will present the specific details of the plasma reactor used for nanocomposite synthesis, after that the diagnostic method to monitor the plasma characteristics and, finally, the experimental procedure for the elaboration of a layer of AgNPs embedded in silica matrix. For simplicity the plasma elaborated samples are called hereafter “plasma deposited samples”.

### **2.1. Plasma reactor description**

The reactor used in this study exploits the plasma of an axially-asymmetric capacitively-coupled RF (13.56 MHz) discharge sustained at low gas pressure. This reactor was built in LAPLACE by Bernard Despax and coworkers. It is illustrated in Figure II.3. For dimensional and other details see Despax and Raynaud, 2007.

The axial-asymmetry of the discharge is related to the large difference between the surface area of the RF powered (upper) smaller electrode and the grounded (lower) electrode, including the reactor walls. This type of discharges allows efficient sputtering from the powered electrode which in the current case is a silver target. The inter-electrode distance is of 35 mm. The RF electrode is coupled to a Sairem generator (delivered power up to 300 W) by means of a LC matching network. The axially-asymmetric design of that RF capacitively-coupled discharge produces axially-asymmetric plasma inducing a self-bias voltage on the powered electrode (the smaller electrode). The self-bias voltage scales up with the injected power in the discharge for a fixed gas pressure.

The vacuum chamber is evacuated by a standard pumping system sustained of primary (rotary) and secondary (turbomolecular) pumps. Before performing the deposition the reactor is usually pumped overnight by the turbomolecular pump (down to  $5 \times 10^{-2}$  Pa). The working gas pressure is of few Pa. It is measured by a Baratron gauge. The operating gases used in this study are Ar (Air Liquide alphagaz 2, 99.9995%) and O<sub>2</sub> (Air Liquide alphagaz 2, 99.9995%). As silicon precursor we have used HMDSO purchased from Sigma Aldrich (purity greater than 99.5%). The HMDSO line and the reactor walls are constantly heated at 50°C to avoid condensation of the HMDSO monomer. The purely technological interest of using HMDSO as precursor in plasma processing is maintained by the possibility of deposition of plasma polymers or thin oxide films (in HMDSO-O<sub>2</sub> mixture) depending on the ratio of the partial pressures of injected gases. Furthermore, HMDSO is non-toxic, non-explosive, and much safer than silane.

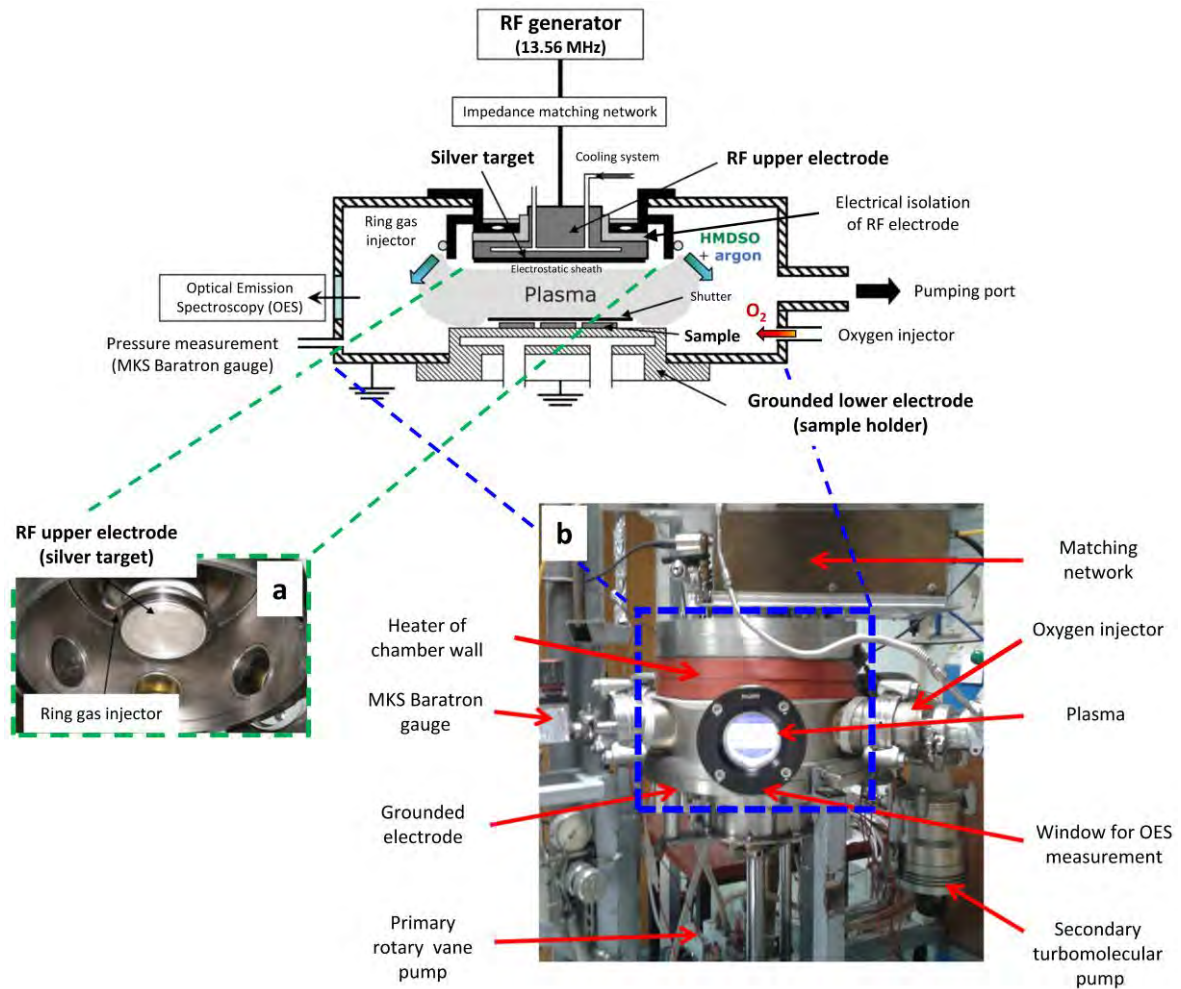


Figure II.3: Schematic representation of the plasma reactor: (a) image of the inner upper part of the reactor chamber. (b) image of the reactor when the plasma is switched on.

One of the unique features of the experimental procedure is the pulsed injection of HMDSO with an injection time,  $t_{on}$ , and a total period,  $T$  ( $T = t_{on} + t_{off}$ ), see Figure II.4. The maximum accessible HMDSO flow rate is 0.4 sccm, which actually corresponds to a continuous HMDSO gas injection. The HMDSO flow rate is adjusted by a mass flow controller OMICRON, switched by a pulse generator AGILENT.

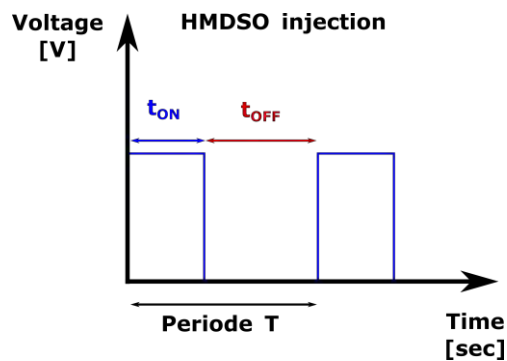


Figure II.4: Illustration of duty cycle of HMDSO injection.

The Ar gas and the Ar-HMDSO mixture are introduced into the reactor by means of a ring gas injector located in the upper part of the reactor at the periphery of the RF electrode. The Ar and HMDSO are mixed in a buffer chamber before being injected in the reactor. The O<sub>2</sub> is introduced in the plasma by a port located at the sample holder (lower electrode) level. A metallic shutter is positioned in the lower part of the reactor to hide the substrate during the plasma stabilization phase in order to prevent from continuous deposition on the sample once the plasma is switched on. It allows strict control over the deposition time.

The plasma electrical behavior is followed through measurements of the self-bias voltage  $V_{dc}$ . Due to the asymmetrical design of the used plasma process the self-bias voltage of the RF electrode is strictly related to the acceleration of Ar<sup>+</sup> ions towards the silver target, thus to the Ag-sputtering. The glow emission from the plasma is followed by Optical Emission Spectroscopy (OES). OES spectra are acquired through an optical fiber positioned at 5 mm above the grounded electrode, connected to a spectrometer Princeton Instrument (Acton Advanced Sp 2500A) for further analysis.

## 2.2. Monitoring of the plasma process by OES

The Optical Emission Spectroscopy is a non-contact diagnostic method largely applied for characterization of the main plasma parameters (electron energy and electron density) by means of measurements of the atomic optical transitions. The analysis consists of collecting light directly emitted by the excited species present in the discharge and further signal processing using theoretical models to describe the plasma [Donnelly, 1990].

In the plasma the glow emission occurs when species, atomic or molecular, in an excited energy (initial) level  $E_k$  totally or partially lose the acquired energy by a radiative decay mechanism (de-excitation) into a lower (final) energy level  $E_j$ , if the radiative transition between two energy levels is permitted. During this transition, a photon of wavelength  $\lambda_{kj}$  corresponding to the difference of the two energy levels is emitted. According to the Einstein relation of spontaneous emission the intensity of emitted light  $I_\lambda$  can be written as:

$$I_\lambda \propto \frac{h c}{\lambda_{kj}} N_k A_{kj} \quad (\text{II.3})$$

where  $N_k$  is the population density of the initial excited level,  $A_{kj}$  is the transition probability between the energy levels  $k$  and  $j$ ;  $h$  and  $c$  being the Plank constant, and the speed of light in vacuum, respectively.

The most convenient way to use OES for real-time monitoring of a plasma process is to rely on the ratio between the intensities of two spectral lines. At steady state conditions it reads:

$$\frac{I_1}{I_2} = \frac{g_1 A_1 \lambda_2}{g_2 A_2 \lambda_1} \exp\left[\frac{E_2 - E_1}{k_B T_e}\right] \quad (\text{II.4})$$

where  $k_B$  is the Boltzmann constant,  $T_e$  is the mean electron energy and  $g_1$  and  $g_2$  are the corresponding atomic level degeneracies. The selection rules for a couple of emission lines are as follow:

- quite intense emission lines in order to collect a sufficient number of photons;
- high enough transition probabilities  $A$ ;
- emission lines with close to each other wavelengths.

In our plasma process, we follow the ratio between an argon emission line and a silver one. Both emission lines originate from highly excited atomic levels (Table II.1). It is important to estimate both the quantity of sputtered silver for the AgNPs deposition and the plasma efficiency for the elaboration of the plasma silica layers and the line ratio method appears the most appropriate one.

Table II.1: Physical parameters of the selected optical emission lines [NIST].

Element	$\lambda$ (nm)	$A$ ( $10^6 \text{ s}^{-1}$ )	$E_j$ (eV)	$E_k$ (eV)	Energy level - $j$	Energy level - $k$
Ag I	546.5	86.0	3.78	6.05	$4d^{10} ({}^1S) 5p [{}^2P^{\circ}]$	$4d^{10} ({}^1S) 5d [{}^2D]$
Ar I	549.6	1.69	13.08	15.33	$3s^2 3p^5 ({}^2P^{\circ}_{3/2}) 4p$	$3s^2 3p^5 ({}^2P^{\circ}_{3/2}) 6d$

### 2.3. Experimental procedure for the elaboration of embedded AgNPs by plasma deposition process

Given the targeted architecture of the samples consisting of a stack of plasma  $\text{SiO}_2$ /AgNPs/thermal  $\text{SiO}_2$  layers on a Si-substrate (Fig. II.5) that fulfill the antireflective condition (Chapter I, indispensable one for reflectance and ellipsometric analysis as well as for SERS measurement [Carles et al., 2011]), the plasma deposited samples are elaborated according the procedure described below. Moreover, the gas pressure, the self-bias voltage and the line intensity ratio are monitored during the plasma deposition process.

**1<sup>st</sup> step: substrates pre-treatment.** Substrates (thermally grown  $\text{SiO}_2$  layer of thickness of 90 nm on a Si substrate) of surface  $1 \text{ cm}^2$  are cleaned in Piranha solution ( $\text{H}_2\text{O}_2 + \text{H}_2\text{SO}_4$ ) for 2 min to remove surface contaminations. Afterwards, a chemical etching using HydroFluoric acid (HF) removes the native oxide and reduces the  $\text{SiO}_2$  layer thickness to 80 nm. After each step of the cleaning procedure the substrates are rinsed with deionized water until obtaining zero conductivity. After the pre-treatment the samples are immediately transferred to the reactor for plasma deposition.

**2<sup>nd</sup> step: single layer of AgNPs.** The silver sputtering is performed in argon plasma, which is maintained at gas pressure of 5.32 Pa. Ar flow of 2.8 sccm fixes this gas pressure in the reactor. The plasma is ignited and the targeted input power is set. Cautions are taken to avoid signal reflection by adjusting the impedance of the matching network. Maximum of the self-bias voltage is used as criterion for efficient power absorption in the plasma. After a short stabilization time (usually 3



minutes) the plasma is ready for the Ag-sputtering. The Ag-sputtering is performed at fixed input power in the range 10-80 W and sputtering time in the range 5-30 s for the given Ar-gas pressure of 5.32 Pa. These parameters control the size, density and shape of the obtained AgNPs. OES spectra are recorded during the stabilization phase and the Ag-sputtering.

**3<sup>rd</sup> step: plasma silica layer.** The elaboration of a plasma silica layer requires a gas mixture of HMDSO and O<sub>2</sub>. We use a mixture of Ar-HMDSO-O<sub>2</sub>. The HMDSO is injected by pulses. The procedure for silica deposition was optimized and the following operating parameters were identified: Ar flow of 2.8 sccm, O<sub>2</sub> flow of 1.25 sccm and HMDSO pulses with  $t_{on} = 3.1$  s over a period of 5 s, which corresponds to an average flow of 0.248 sccm. With the above gas flows, the total gas pressure is set to  $p_{tot} = 7.68$  Pa, slightly oscillating according to the pulsed injection of HMDSO. To achieve a strong decomposition degree of the HMDSO the discharge is sustained by injected power of 120 W. Similar to the sputtering process, the plasma sustained in Ar-HMDSO-O<sub>2</sub> mixture requires a stabilization period. In this type of deposition, the plasma stabilization phase takes typically 30 min. Again the OES spectra are recorded during both the stabilization phase and during silica layer deposition.

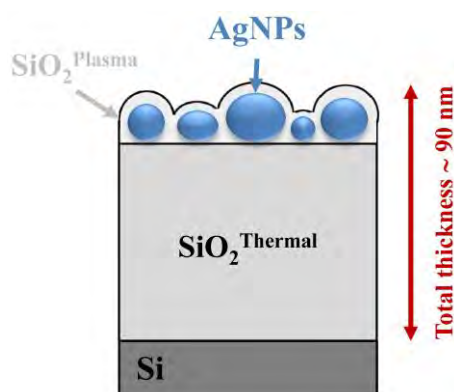


Figure II.5: Typical architecture of plasma deposited samples.

In summary, the typical architecture of the samples is composed by a sequential superposition of single layer of AgNPs covered by thin plasma silica layer (Fig. II.5). The total thickness of the nanocomposite is about 90 nm in which the AgNPs with size in the ten – twenty nanometer range are covered by a this silica layer of thickness of few nanometers.

### 3. Transmission Electron Microscopy

The main contributions of Transmission Electron Microscopy (TEM) are its high resolution in real space, down to the atomic scale, with magnifications ranging from  $10^3$  to  $10^6$ , and also the possibility to combine information obtained in the real space in image mode with the information obtained in the

Fourier space (or reciprocal space) in diffraction mode. Moreover, the nature of the interaction electron-matter provides a link between structural or morphological and chemical local studies.

### **3.1. Image formation in a TEM**

The overall process of the image formation in TEM can be summarized in 6 steps, which follow the electron wave trajectory:

- creation and acceleration of an electron beam from the electron source,
- illumination of the specimen with (coherent) electron probe,
- scattering of the electron wave by the specimen,
- formation of a diffraction pattern in the objective lens back focal plane,
- projection of the image (or the diffraction pattern) on the detector plane.

In the first step, electrons are generated either by thermionic emission if a filament (tungsten or LaB<sub>6</sub>) is heated at high temperatures, by the cold-field emission (C-FEG) extraction from an extremely sharp tungsten tip at room temperature, or by the combination of both methods in a so-called Schottky Field Emission Gun (S-FEG). The C-FEG and S-FEG gun are highly coherent and bright electron sources while thermionic source provides more intense but poorly coherent beam. In the second step, the electron wave is accelerated (typically up to 60 kV - 300 kV) and the illumination system (a set of 2 or 3 condenser lenses) allows defining the beam (probe size, convergence angle, electron dose) but irradiates the top surface of the specimen. The electron wave then interacts with the sample through various processes of scattering (elastic and inelastic). The exit electron wave coming out from the specimen is processed by the objective lens to form a diffraction pattern of the specimen in the back focal plane and subsequently an image of the object. A schematic representation of the image formation in TEM is displayed on Figure II.6.

The electron-specimen interaction makes that the incident electron wave changes its initial state by elastic and inelastic scattering phenomena. Different signals are generated, resulting from the electron-specimen interaction. In the inelastic scattering processes, the electrons lose a small amount of their energy that is transferred to the specimen, producing the emission of a wide range of secondary signals (x-rays, visible light, secondary electrons, phonons and plasmons excitations), also damaging the specimen. The secondary signals are very useful to perform analytical TEM experiments such as X-ray Energy-Dispersive-Spectroscopy (XEDS) or Electron Energy loss spectroscopy (EELS). On the other hand, in the elastic processes the electrons are scattered without energy loss. In crystalline materials, the elastic scattering gives rise to Bragg diffraction related to the constructive interference of the scattered electron waves in a periodic crystal. Thus Bragg scattering results in a series of diffracted beams scattered at angles dependent on the lattice periodicities of the crystal structure. The elastically scattered electron beams are the ones used to form images in TEM techniques such as conventional (diffraction contrast) TEM and phase contrast High Resolution Electron Microscopy (HREM).

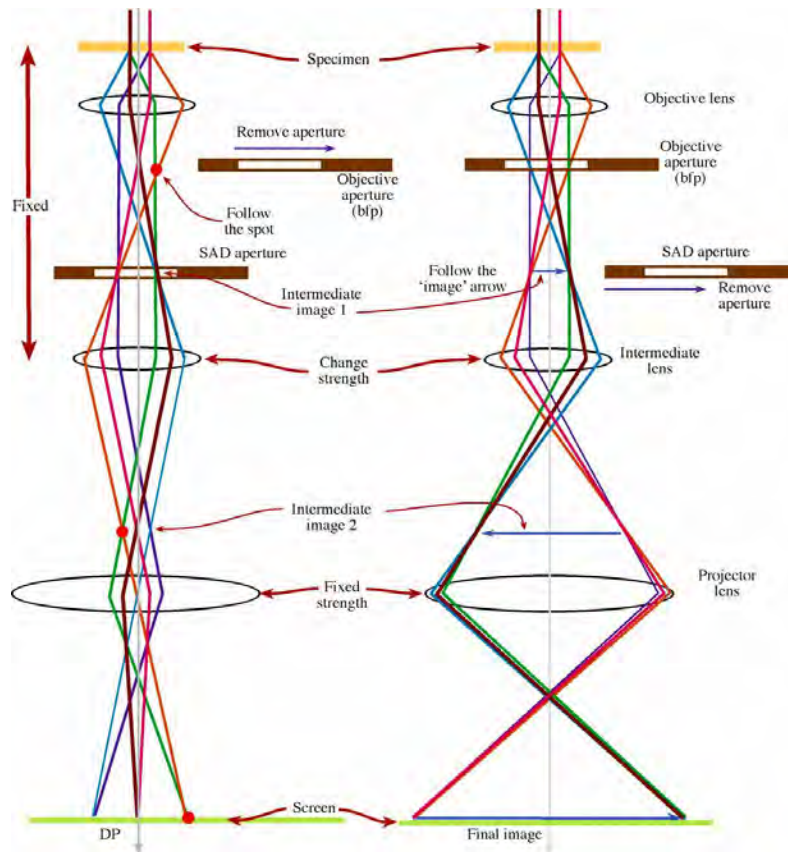


Figure II.6: The two basic operations of the TEM imaging system involve (left) diffraction mode: projecting the Diffraction Pattern (DP) onto the viewing screen and (right) image mode: projecting the image onto the screen. From [Williams and Carter, 2009].

### 3.2. Conventional Bright Field TEM

In the Bright Field (BF) mode of the TEM, an aperture is placed in the back focal plane of the objective lens, which allows only the transmitted beam to pass. In this case, the image results from a weakening of the direct beam by its interaction with the sample. Therefore, mass-thickness and diffraction contrast contribute to image formation: thick areas, areas in which heavy atoms are enriched, and crystalline areas appear with dark contrast. In the case of AgNPs embedded in silica, the difference in atomic number between Ag and SiO<sub>2</sub> is high so that the NPs show high amplitude contrast. In particular defocused bright-field imaging has proved to be successful for imaging individual nanocrystals at low magnification. The electrostatic potentials being strongly different in Ag and SiO<sub>2</sub>, a phase shift indeed exists between electron waves having propagated (or not) through the NPs. Provided the incident beam being highly coherent, this phase shift can be imaged by using defocused bright-field conditions, to reveal interfaces between the AgNPs and the surrounding silica matrix. The contrast in the image is increased by a pair of Fresnel fringes (black/white or white/black) that are located at the AgNPs/SiO<sub>2</sub> interface [Bonafos et al., 2001]. These imaging conditions are suitable for probing the spatial depth distribution of the AgNPs in cross-sectional specimen and for measuring their size-distribution in plan-view preparation (see Figure II.7).

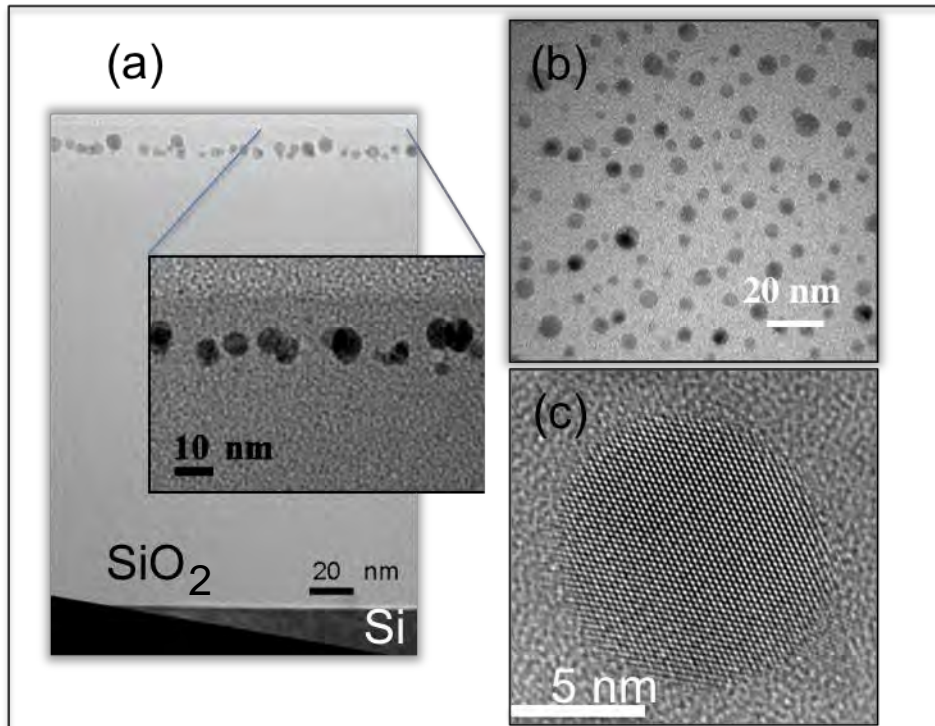


Figure II.7: TEM Bright Field image of AgNPs embedded in silica matrix observed in (a) cross-section and (b) in plan-view. (c) HREM of a AgNP.

### 3.3. High Resolution Electron Microscopy (HREM)

Contrast in the HREM image arises from the coherent superposition of the primary and elastically scattered beams. For a thin enough imaged area, it is directly connected to the projected atomic structure of the NPs. A crystal can be observed in HREM with significant contrast if it is crystalline, in Bragg orientation with respect to the incident electrons, and if the thickness of the imaged area is not greater than two or three times the diameter of the NPs. Thus, amorphous and misoriented particles are excluded from this image. Moreover, thin edges of the NPs are too thin to be imaged as atomic columns which results in slightly underestimated size of the NPs [Schamm et al., 2008].

TEM resolution is limited by the acceleration voltage of the electron beam and the ability to correct the spherical aberration of the objective lens. The most modern TEM microscopes operated at 300 kV and are equipped with Cs correctors that are able to reach a point-to-point resolution down to 0.5 Å. The TECNAI F20 SACTEM has been used in this work to acquire HREM images. It is equipped with spherical aberration corrector located below the objective lens, which achieves a spatial resolution of 1.2 Å. Nevertheless, in HREM images of AgNPs embedded in silica, the minimum detectable size that can be measured is equal to 4–5 planes, i.e. around 1 nm. A typical HREM image of an AgNP is shown in Figure II.7c.

### 3.4. Specimen preparation

To be observable in Transmission Electron Microscope the specimen must be thin enough to be transparent to the electrons, typically less than 100 nm for conventional TEM and 10 nm for HREM. Specimens from all samples were prepared for cross-sectional (XS-TEM) and plan-view (PV-TEM) observations using the standard procedure involving mechanical polishing and Ar<sup>+</sup> ion milling.

## 4. Optical based techniques

Optical based diagnostic techniques used in this thesis, and detailed in the following sections, (*i.e.* FTIR, Raman spectroscopy, reflectance spectroscopy and ellipsometry) allow us studying the composition, structural properties or the optical response of materials exploiting the interaction between light beam and the studied material. In this context, one distinguishes different kind of light/matter interactions:

- **Absorption** that occurs when the light beam passes through the material and part of it is absorbed. This interaction is important for FTIR spectroscopy, especially when the sample is studied in transmission mode like for the experiments performed in this PhD thesis.
- **Elastic diffusion** (or elastic scattering) that happens when photons of the scattered beam have identical energies as the ones of the incident beam. In this case, no energy exchange occurs between the light and the scattering material. If the material is homogeneous, it leads to well-known phenomena: *reflection* and *refraction*. If the medium is heterogeneous (defects, roughness), it diffuses the incident light beam into random-directions. This is the *Rayleigh scattering*. Reflectance and ellipsometric spectroscopy are based on this light behavior.
- **Inelastic diffusion** (or inelastic scattering) that occurs when photons of the diffused beam have different energy with respect to the ones of incident beam. In this case, the electromagnetic wave transfers energy to the material by phonons, the energy quantum of a lattice vibration in condensed matter. This kind of scattered light is fundamental for Raman spectroscopy.

### 4.1. Fourier Transform InfraRed spectroscopy (FTIR)

FTIR absorption spectroscopy is a non-destructive technique that allows studying the structural properties of materials, in particular, the nature of molecular bonds. This technique is based on the interaction between infrared light and vibrational states of the matter. At temperatures above absolute zero, all atoms are in continuous vibration with respect to each other. Atoms in molecules are able to vibrate in several modes. When the frequency of a specific vibration mode is equal to the frequency of the incident infrared radiation, the molecule absorbs the radiation. For this reason, FTIR spectroscopy is a powerful tool for structural clarification and compound identification in the sample and is even a common spectroscopic technique used for quantitative determination of compounds in mixtures.

Infrared radiation is absorbed and the associated energy is converted into different types of motions. The absorption involves discrete and quantized energy levels. However, the individual vibrational motion is usually accompanied by other rotational motions. These combinations lead to the absorption bands, not the discrete lines, commonly observed in the middle infrared region. The major modes of molecular vibrations are stretching, bending and rocking (Fig. II.8).

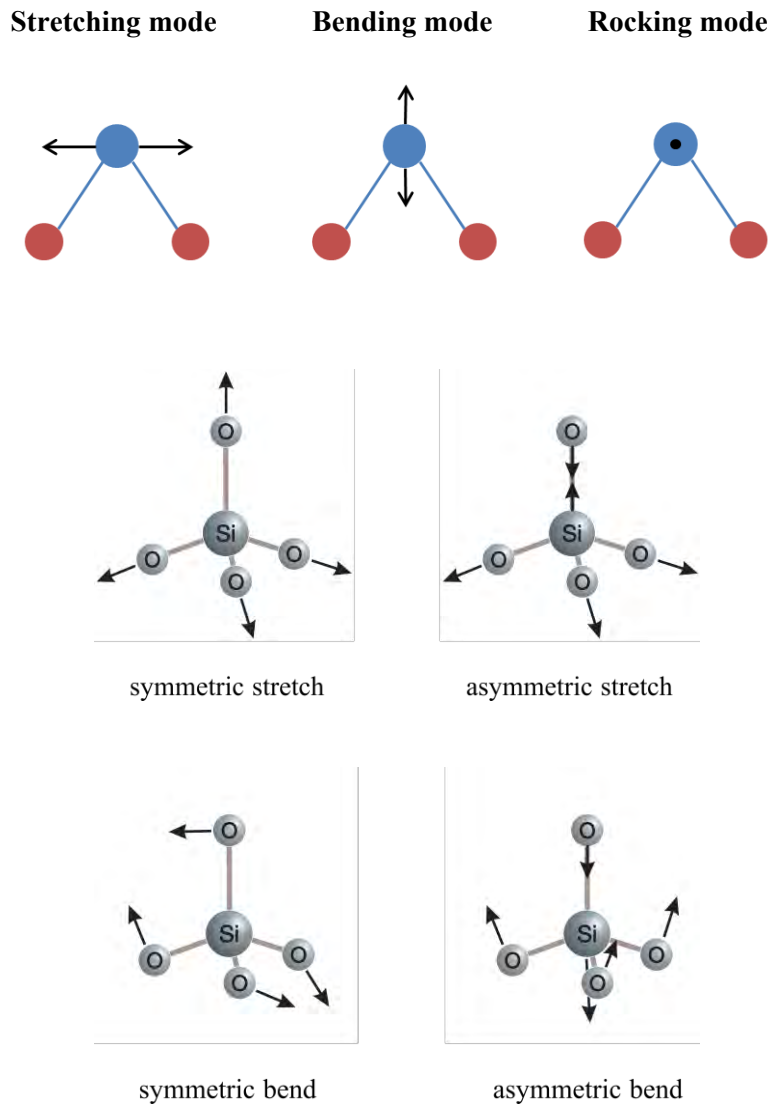


Figure II.8: Schematic representation of principal vibrational molecular modes, on the top, and of main vibration modes of silica structure, on the bottom. From [Salh, 2011].

FTIR spectra are obtained by detecting changes in transmitted (transmittance,  $T$ ) or absorbed (absorbance,  $A$ ) intensity as a function of frequency. Transmittance is the ratio of radiant power transmitted by the sample to the radiant power incident on the sample. Absorbance is the logarithm to the base 10 of the reciprocal of the transmittance. The infrared spectra presented in this thesis were performed on a Bruker spectrometer Vertex70 a resolution of  $0.2 \text{ cm}^{-1}$ . This spectrometer sends the infrared radiation onto the sample through a Michelson interferometer, which allows the simultaneous

collection information to all the wavelengths. For this, a pyroelectric detector DTGS is used, which enables measurement over a spectral range of 400 to 4000  $\text{cm}^{-1}$ . The interferogram obtained is then converted to an infrared spectrum using the Fourier transform. The measurement enclosure, wherein the sample is placed, is continuously purged with a dry nitrogen flow, to remove water and carbon dioxide molecules present in the ambient atmosphere. The measurements are performed in transmission mode and the spectra are shown as the difference between the sample absorbance ( $A_{sample}$ ) and the reference one ( $A_{reference}$ ) following the relation:

$$A_{diff} = A_{sample} - A_{reference} = \log_{10} \left( \frac{T_{sample}}{T_{reference}} \right)^{-1} = -\log_{10} \left( \frac{I_{sample}}{I_{reference}} \right), \quad (\text{II.5})$$

where  $I_{sample}$  and  $I_{reference}$  are the intensities transmitted through the sample and the reference, respectively. The reference is an intrinsic silicon substrate which is transparent to infrared light.

## 4.2. Raman spectroscopy

As FTIR, Raman spectroscopy provides information about the composition and structural properties of material observing the vibrational, rotational and low-frequency modes in a material. In this technique, a laser beam is sent to a given material, and it is possible to measure the scattered light intensity, or the number of scattered photons, as function of the difference between the frequency of the incident photons and that of the scattered ones expressed in  $\text{cm}^{-1}$ . At the microscopic level, the Raman scattering can be explained as a process of transitions between electronic states. In general, one distinguishes in Raman spectroscopy three different kinds of random scattering of light: *Rayleigh*, *Raman Stokes* and *anti-Stokes* scattering (Fig. II.9).

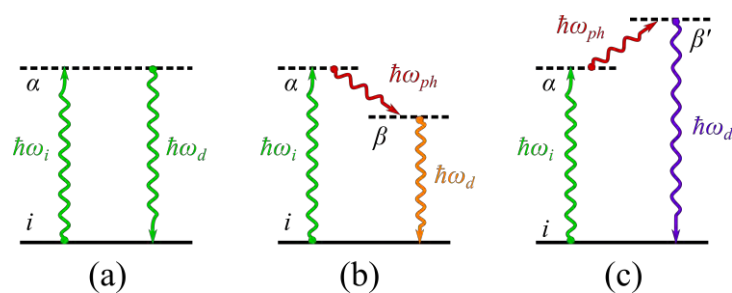


Figure II.9: Schematic representation of Rayleigh (a), Raman Stokes (b) and anti-Stokes (c) scattering.

All these processes have the same initial step. This concerns the transition of one electron from the real lower energy level  $i$  toward the virtual upper energy level  $\alpha$  by the absorption of an incident photon of energy  $\hbar\omega_i$ . Afterward the three processes follow different routes:

- *Rayleigh scattering*: this is a two-step process (Fig II.9a). The second step concerns the de-excitation of the electron of energy level  $\alpha$  toward the initial energy level  $i$ . This provokes the

emission of a photon of energy  $\hbar\omega_d = \hbar\omega_i$ . This kind of process represents the largest contribution to the random scattered light giving an intense peak at  $0 \text{ cm}^{-1}$  in Raman spectra.

- *Raman Stokes scattering*: that is a three-step process (Fig II.9b). In the second step, the excited electron of energy level  $\alpha$  transfers a part of its energy to create a phonon of energy  $\hbar\omega_{ph}$ . In this case, the electron goes toward a virtual energy level  $\beta$ . Afterward, from this energy level, the electron reaches the initial energy level  $i$  emitting a photon of energy  $\hbar\omega_d = \hbar\omega_i - \hbar\omega_{ph}$ .
- *Raman anti-Stokes scattering*: that is also a three-step process (Fig II.9c). In this process the second step involves the absorption of a phonon of energy  $\hbar\omega_{ph}$ . This permits to the excited electron of the energy level  $\alpha$  to reach a virtual energy level  $\beta'$ . From this energy level, the electron undergo a de-excitation towards the initial energy level  $i$  emitting a photon of energy  $\hbar\omega_d = \hbar\omega_i + \hbar\omega_{ph}$ .

The probability to have the emission of a photon of energy  $\hbar\omega_d$  depends on the ability of a crystal to absorb or to emit a phonon of energy  $\hbar\omega_{ph}$ . This is related to populations of levels  $\beta$  and  $\beta'$ . The statistic Boltzmann distribution relates the intensities of Raman Stokes and anti-Stokes scattering with populations of virtual energy levels as function of angular frequency  $\omega$  at fixed temperature by the following equation:

$$\frac{I_{Stokes}}{I_{anti-Stokes}} = \frac{n(\omega) + 1}{n(\omega)} = e^{\frac{\hbar\omega}{k_B T}}, \quad (\text{II.6})$$

where  $n(\omega)+1$  and  $n(\omega)$  are the populations of levels  $\beta$  and  $\beta'$ , respectively. From equation II.6 is evident that the energy level  $\beta$  is more occupied than that of  $\beta'$ . For this reason, the intensity of the Stokes scattering is higher than that of the anti-Stokes scattering.

Moreover, when the energy of the incident (or scattered) photon coincides with an electronic transition of the studied material, the energy level  $\alpha$  ( $\beta$  or  $\beta'$ ) is real. In this case, the transition probability is exalted and the Raman process is named *resonant incident photon* (or *scattered*). By selecting an opportune energy of the incident photon (excitation energy), it is possible to fully exploit the exaltation of the Raman scattering.

For the studies presented in this PhD work a high resolution Raman spectrometer (Horiba Jobin-Yvon Xplora) equipped with three lasers 532, 632 and 785 nm and a standard confocal microscope was used.

### 4.3. Optical reflectance spectroscopy

Optical reflectance spectroscopy is a macroscopic nondestructive technique useful to determinate rapidly relevant structural parameters at the nanoscale. For example, this technique has the potential of evaluating the average size of noble metal nanoparticles exploiting their LSPR for appropriately designed architectures [Carles et al., 2011].



### 4.3.1. Reflectance definition

The reflectance is defined as the ratio between the reflected,  $I_r$ , and incident,  $I_i$ , intensities of an impinging light beam expressed in percentage. Considering that the intensity scales as the square of the electric field,  $I = |E|^2$ , the reflectance can be written as:

$$R = \frac{I_r}{I_i} = \frac{|E_r|^2}{|E_i|^2}. \quad (\text{II.7})$$

### 4.3.2. Experimental spectrophotometer

In our work, we used a commercial spectrophotometer (Agilent Cary 5000 UV-Vis-NIR) equipped with a module measuring the specular reflectance. The measurement principle is the following: a light beam of variable wavelength incoming the module is sent on the sample by a conveniently placed mirror. The reflected from the sample beam is sent outside the module in the same direction as the incoming beam by another mirror (Fig. II.10). Hence, the reflected intensity is measured and compared to the incident one. The reflectance of sample is deduced from this comparison and expressed as a percentage. All measurements were performed in a wavelength range from 200 nm to 800 nm (6.2 eV to 1.55 eV) to cover a spectrum from the ultraviolet to the near infrared, with a resolution of 1 nm.

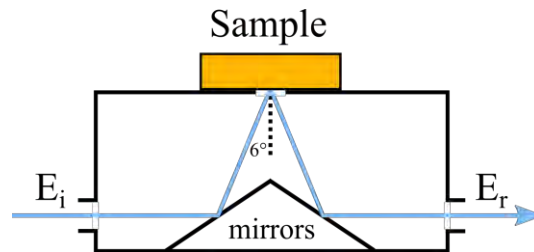


Figure II.10: Schematic diagram of the optical reflectance measurement. The incidence and reflected angle on the sample were deliberately emphasized in the figure.

Exploiting this configuration, the angle of incidence of the light beam  $\theta_1$  (as well as the reflected one) is tilted of  $6^\circ$  with respect to the sample normal direction. According to the Snell–Descartes law, the angle of the refracted light beam  $\theta_2$  can be calculated from the relation:

$$n_1 \sin\theta_1 = n_2 \sin\theta_2 \quad (\text{II.8})$$

where  $n_1$  and  $n_2$  are the air and matrix refractive indexes, respectively. Since the matrix refractive index is greater than the refractive index of the air, the refractive angle in the matrix will be less than the incidence angle in the air, *i.e.* below  $6^\circ$ . In this case, we will consider that this module provides the experimental reflectance to a quasi-normal incidence at the sample surface.

### 4.3.3. Characteristic reflectance spectrum of a thin silica layer on Si substrate and interest of using antireflective layers

When the incident light wave reaches the sample surface, part is directly reflected by the silica free surface (silica / air interface), while the other part passes through the layer to reach the silica / silicon interface (Fig. II.11). At this point, part of the wave is transmitted in the substrate and the remaining part is reflected and returns to the surface. The total reflected wave results from the different reflections and transmissions at the interfaces.

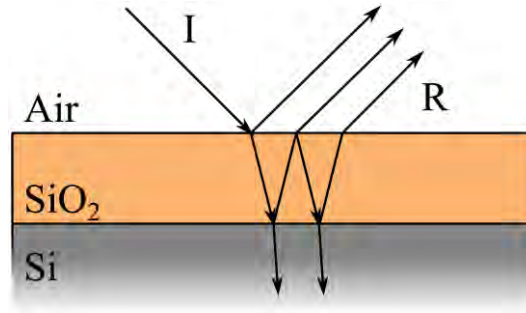


Figure II.11: Schematic diagram of the paths of light rays in our samples. The optical path difference is causing interferences observed on the reflectance response. From [Bayle, 2014]

Silicon is a high refractive index absorbing material in the visible range ( $n_{silicon} = 3.86$  against  $n_{silica} = 1.45$ ) and therefore well reflects the light rays in this range. Thus, the silica layer plays the role of Fabry-Perot half-cavity and one can therefore observe a reflection interference phenomenon. We can relate the various observed orders of interference  $m$  with the thickness  $e$  of the silica layer of refractive index  $n_\lambda$  that weakly depends on the wavelength. Since the measurement is performed at normal incidence, reflectance minima appear due to the destructive interference and follow the relation:

$$\lambda_m = 2n_\lambda e \left( m + \frac{1}{2} \right)^{-1}, \quad (\text{II.9})$$

where  $\lambda$  is the wavelength of the incident beam.

This reflectance curve can also be expressed as a function of the energy on the incident photons. The reflectance minima of a monochromatic electromagnetic wave enlightening a SiO<sub>2</sub>/Si sample under an oblique incidence occur for specific photon energies  $E_m$ . The phase condition corresponding to the successive destructive interference orders ( $m = 0, 1, 2, \dots$ ) in the silica layer writes, for an oblique incidence:

$$E_m = \left( m + \frac{1}{2} \right) \frac{hc}{2n_\lambda e \cos \theta_r}, \quad (\text{II.10})$$

where  $L$  is the optical path in the  $\text{SiO}_2$  layer,  $h$  is the Planck constant,  $c$  is the light speed in vacuum, and  $\theta_r$  is the refracted angle inside the silica layer.

Figure II.12 shows experimental reflectance (black curve) measured for our multilayer samples composed of 90 nm thick silica on top of a Si substrate, without (black curve) and with AgNPs localized just under the surface (red curve). The two reflectance minima (at  $m=0$  and  $m=1$ ) predicted by the anti-reflective condition appear at  $\lambda_0 = 527$  nm and  $\lambda_l = 203$  nm. In the UV range, the  $m=1$  shows high sensitivity to the presence of AgNPs by the absorption increase (i.e., decrease in the reflectance). On the contrary, due to the synergetic effect between plasmon resonance and optical interference, the fundamental mode  $m=0$  gives rise to a highest sensitivity in almost all the visible range (400-800 nm). Thus, when AgNPs are embedded in these layers and located close to the surface (red curve) a strong modulation of the reflectance spectra is observed near the LSPR resonance (413 nm). More generally, by selecting such anti-reflective condition, we can get an enhanced sensitivity to any modification at the surface of the sample. As a matter of fact, this high sensitivity comes out from the fact that the electromagnetic field is maximum at the surface in antireflective conditions. Localization of the AgNPs at the vicinity of the free surface (at an antinode of the electric field) has a strong effect: the resonant absorption by the AgNPs drastically modifies the electric field and in particular strongly reduces the reflected field amplitude in the air. At the end, the antireflective conditions will enhance coupling between the AgNPs and the electromagnetic field (for more details see [Carles et al., 2014]).

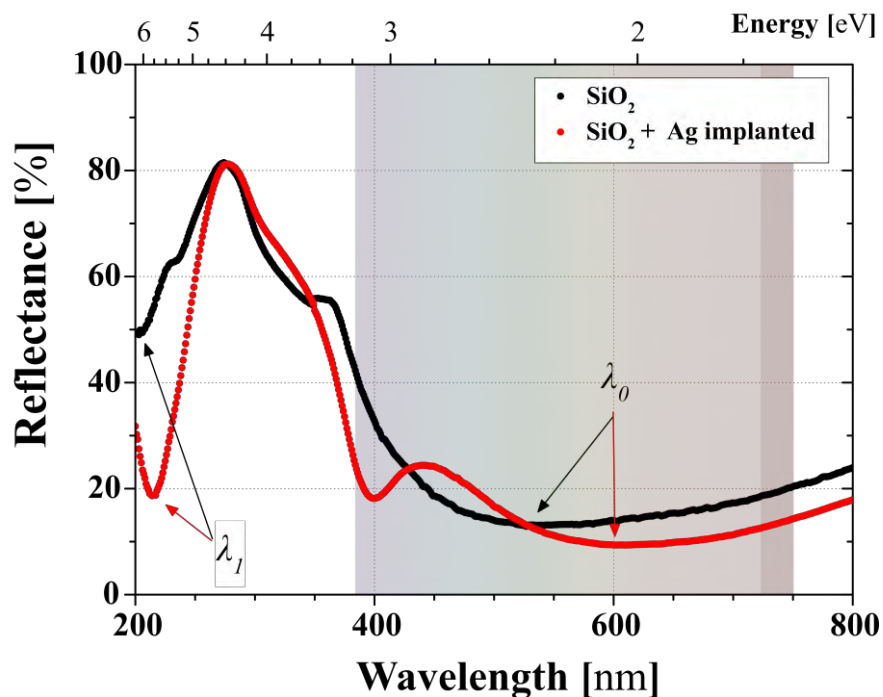


Figure II.12: Reflectance spectra of a 90 nm thick silica layer on top of silicon (black points) and silica layer with implanted AgNPs (red points) as function of wavelength.

#### 4.4. Ellipsometry

The ellipsometric spectroscopy is an optical technique commonly used in microelectronics for characterization of transparent thin layers, which enables to determine their optical and structural properties. As the optical reflectance, the advantages of this technique involve its non-destructive and non-contaminant character. The sensibility of this technique to the structural changes is at nanoscale. In this section, we present briefly the theoretical operation of ellipsometry. For more details about the technique refer to [Bernoux et al., 2003].

When an electromagnetic plane wave arrives on the flat surface of a sample, it can be transmitted, absorbed or reflected by this surface. The principle of spectroscopic ellipsometry consists in analyzing the variation of two important parameters of the electric field of an electromagnetic wave, *i.e.* the amplitude and the phase, after reflection on the sample (Fig. II.13).

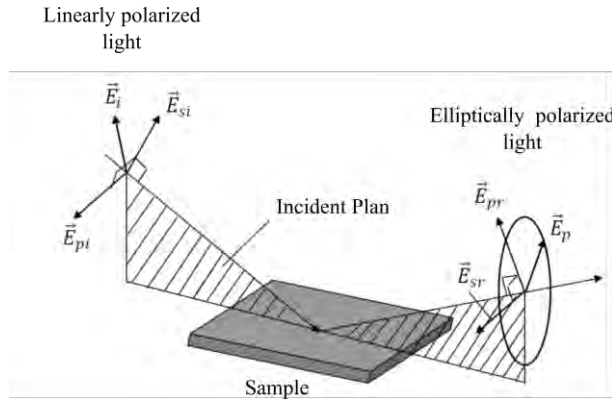


Figure II.13: Schematic representation of the principle of ellipsometric measurement. The polarization of the incidence and reflected beam on the sample are marked.

The electric field of a polarized incident electromagnetic wave  $E_i$  is represented by two components: one with parallel,  $E_{pi}$ , and the other one with perpendicular,  $E_{si}$ , directions with respect to the incidence plane of the impinging beam. The two components ( $E_{pr}$  and  $E_{sr}$ ) of the electric field after reflection  $E_r$  on the sample surface undergo modifications that can be represented by the reflection coefficients of parallel,  $r_p$ , and perpendicular,  $r_s$ , polarization to the incidence plane as:

$$r_p = \frac{E_{pr}}{E_{pi}} = |r_p| e^{i\delta_p}, \quad (\text{II.10})$$

$$r_s = \frac{E_{sr}}{E_{si}} = |r_s| e^{i\delta_s}. \quad (\text{II.11})$$

The real parts of these two complex coefficients ( $|r_p|$  and  $|r_s|$ ) represent the attenuation of the amplitude of the two electromagnetic wave components. The complex parts ( $\delta_p$  and  $\delta_s$ ) involve the phase change of these two components induced by the reflection. This provokes a change of the incident beam polarization (*i.e.*, from linear to elliptical polarization). Finally, spectroscopic ellipsometry measures

the ratio of these two coefficients ( $\rho_e = r_p/r_s$ ) that depends on the wavelength of the incident beam.  $\rho_e$  can be written as:

$$\rho_e = \tan \Psi e^{i\Delta}, \quad (\text{II.12})$$

where  $\tan \Psi = |r_p|/|r_s|$  is related to the amplitude of the two electromagnetic wave components and  $\Delta = \delta_p - \delta_s$  is the difference of phase change of these two components after reflection.

The measurement of  $\rho_e$  is performed by measuring the two quantities,  $\tan \Psi$  and  $\cos \Delta$ . Thus, measurement of these quantities at a fixed incidence angle as a function of the wavelength allows determining optical and structural properties of the sample by using different theoretical models.

In our study, the samples are composed by successive nanometric layers of different composition elaborated on a silicon substrate that well reflects the light in the UV-visible-near infrared range. One or more parameters of each layer are unknown. For interpretation of the recorded ellipsometry spectra modeling of the structure of these nanocomposites is required. The use of models as Effective Medium Approximation (EMA) turns to be appropriate for a quite accurate description of this kind of systems. The hypothesis and the model description developed in this study are detailed in Chapter IV along with the obtained results and the model validation.

The spectroscopic ellipsometer used in this work is a Sopra GES 5 phase modulated system operating in the UV-visible-infrared range of the light spectrum from 0.2 to 2.8 microns (6.2 – 0.4 eV). This ellipsometer exploits the measurement method with rotating polarizer and fixed analyzer. The advantage of this method is that measurements are not affected by the sensor sensitivity to the polarization.

## 5. Algae culture

The evaluation of bio-available silver released in environment requires specific analysis. To achieve this we employed a specific technique that uses algae as a sensible and reliable bio-sensor for measuring the dissolved silver released from silver nanoparticles. For this, we measured by fluorometry the extremely sensitive chlorophyll fluorescence changes of algae under realistic toxic exposure scenarios.

### 5.1. Algae preparation

The experiments were performed with eukaryote unicellular green algae *Chlamydomonas reinhardtii* (strain CR137C). Batch cultures were prepared by transferring an inoculum of algae (approx.  $1 \times 10^5$  cells/mL with an O.D.<sub>685</sub> = 0.05) to fresh growth media [Le Faucheur et al., 2005]. Algae were grown during 72 hours until reaching exponential growth phase at 25°C with continuous illumination of 120  $\mu\text{Mol photons s}^{-1} \text{ cm}^{-1}$  (Philips Coolwhite TLD 15W fluorescent lamps) and shaken at 90 rpm to avoid

algae aggregation and sedimentation in order to keep an homogeneous solution. The growth media culture was Talaquil, prepared as described in reference [Le Faucheur et al., 2005].

Experimental batch cultures were harvested by centrifugation (1500 g, 10 min), and then resuspending the cell pellet in the appropriate volume of 10 mM MOPS buffered solution (3-morpholinepropanesulfonic acid in double distilled water (Milli-Q)) adjusted at 7.5 pH using KOH. The resuspension of algae in MOPS solution is a fundamental step to avoid the presence of growth media during the experiments, since it can alter the speciation of silver. As example, EDTA (Ethylenediaminetetraacetic acid disodium salt dehydrate) is an important compound in growth media, and it is a well-known chelating agent that can capture the metal ions in solution.

Algae concentration in suspension (cells/mL) has been assessed by measuring the optical density (O.D.) at wavelength of 685 nm with a spectrophotometer Thermo Helios Alpha. Experimental batch cultures were prepared by transferring an inoculum of algae in the experimental growth phase at a starting density of approximately  $6 \times 10^5$  cells/mL, which corresponds to  $O.D._{685} = 0.15$ . All control and experimental flasks have got the same amount of algae and at the same stage of their growth phase.

Reliable and quick measurements of cell number require two common measures: cell count by microscope and turbidity by spectrophotometer [Madigan et al., 2012]. Cells were counted using a microscope equipped with a Neubauer counting chamber (Fig. II.14).

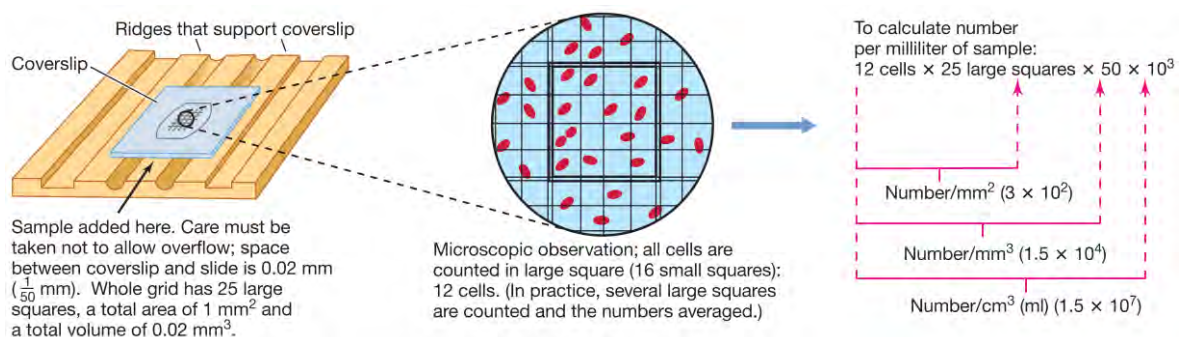


Figure II.14: Direct microscopic counting procedure using counting chamber. From [Madigan et al., 2012].

## 5.2. Turbidity and Optical Density

The turbidity is a quick and easy method to estimate cell numbers based on property of cells suspension to scatter light without destroying or significantly disturbing the sample. This phenomenon is measured using a spectrophotometer (Fig. II.15a). The unit of turbidity is called optical density (O.D.) at the specified wavelength. The Beer–Lambert’s law  $I = I_0 e^{-kz}$  allows measuring the unscattered light,  $I$ , passing through the suspension of cells measured by photocell, knowing the incident light intensity  $I_0$ , the thickness  $z$ , and the extinction coefficient  $k$ , of the cells suspension. Using a solution without algae, called blank solution, the O.D. is defined as:

$$O.D. = \text{Log} \frac{I_b}{I_s}, \quad (\text{II.13})$$

where  $I_b$  and  $I_s$  are the unscattered light intensities after passage through the blank solution and the cells suspension, respectively. Considering that the incident light is equal to the addition of scattered, unscattered and absorbed light interacting with cell suspension, the O.D. is direct proportionally to the absorption from cell suspension [Mitchell and Kiefer, 1988].

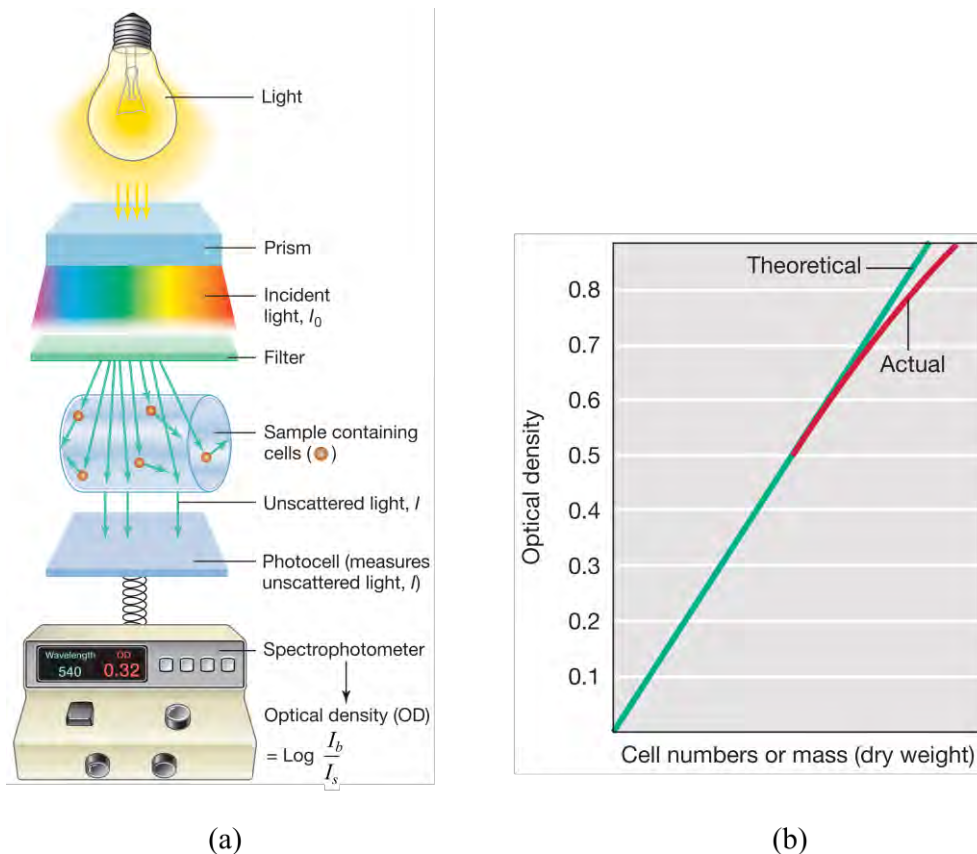


Figure II.15: (a) Measurements of turbidity made in a spectrophotometer. (b) Relation between cell number and turbidity readings. From [Madigan et al., 2012].

To avoid cell clumping and to have a one-to-one proportionality, typically, the O.D. measurements are performed at low cell concentrations accomplished by stirring, keeping the cells well mixed to prevent the formation of cell aggregates. After combining microscopic cell count and turbidity, it is possible to correlate O.D. measurements to the cell concentration for each growth phase of the algae cultures (Fig., II.15b).

In the morphology of green algae *Chlamydomonas reinhardtii*, the chloroplast containing chlorophylls  $a$  and  $b$  occupies the largest part in the algae volume. This alga presents a sharp absorption peak related to the chlorophylls  $a$  in the red part of light spectrum around 685 nm (Fig. II.16). Consequently, all the O.D. measurements were carried out at this wavelength ( $O.D._{685}$ ) [Berberoglu et al., 2008].

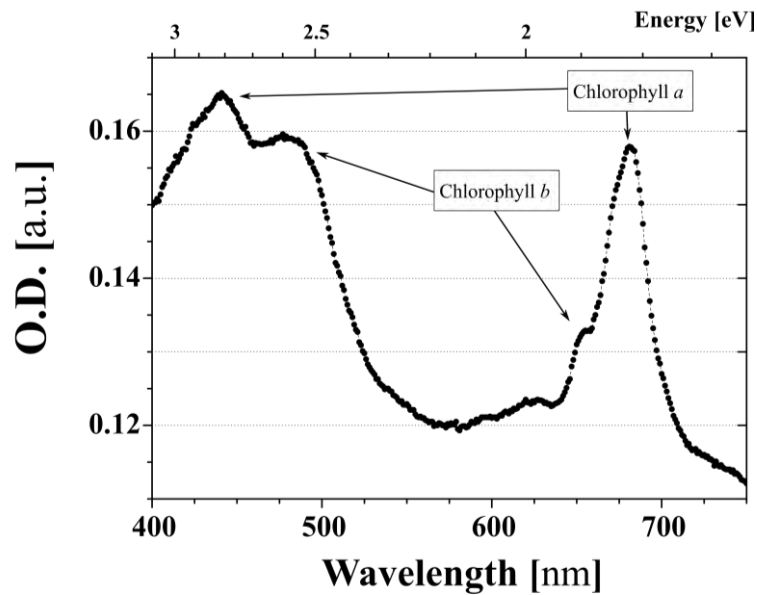


Figure II.16: Experimental O.D. spectrum of green algae *Chlamydomonas reinhardtii*. The associated chlorophylls *a* and *b* absorption peaks are indicated.

## 6. Principle of fluorometry

Fluorometry is routinely used as a method to assess the impact of different toxicants on the algal physiology; with specific demonstration of its suitability for nano-ecotoxicology [Navarro, 2008; Navarro, 2015]. This technique is based on the measurement of the fluorescence emitted from the photosynthetic system II in vegetal cells under excess light conditions [Schreiber et al., 2004; Consalvey et al., 2005]. In all eukaryotic plants and algae, photosynthetic systems are part of chloroplast in which different functional reactions take place during the photosynthesis to transform light energy in chemical energy (photochemistry) (for details see references [Schreiber et al., 1995] and [Consalvey et al., 2005]).

### 6.1. Principle of fluorometry

Light absorption in photosynthetic system II creates excited states for electrons in the reaction centre chlorophyll *a*-protein complex (energy captured) [Consalvey et al., 2005]. In ambient light conditions (normal state), this energy is divided in three competitive processes: photochemistry conversion, heat dissipation and fluorescence emission (Fig. II.17).

In excess light conditions (saturation state), molecules responsible of photochemistry conversion are saturated and this process is temporarily suppressed [Consalvey et al., 2005]. In this case the main part of absorbed light is re-emitted through fluorescence in the red band of visible spectrum (Fig. II.17).



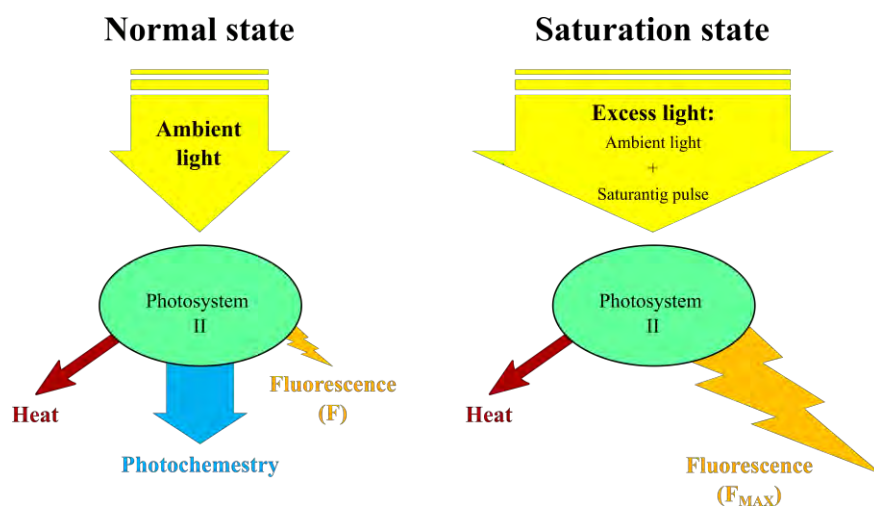


Figure II.17: Diagram showing the principle of Pulse-Amplitude-Modulation (PAM) fluorometer to determinate the effective quantum yield of photochemical energy conversion (PHOTOSYNTHETIC YIELD).

Short saturating amplitude modulated pulse (PAM) of a fluorometer is an efficient way to produce an excess light in the vegetal cell. Hence, we can define the characteristic parameter of fluorometry, the photosynthetic yield, as: the effective quantum yield of photochemical energy conversion (PHOTOSYNTHETIC YIELD). This parameter can be calculated by two consecutive measurements of the fluorescence yield, one briefly before ( $F$ ) and one during a short pulse of saturating light ( $F_{MAX}$ ), following the expression:

$$\text{PHOTOSYNTHETIC YIELD} = \frac{F_{MAX} - F}{F_{MAX}} \quad (\text{II.14})$$

## 6.2. Procedure to evaluate released silver by fluorometry measurements

To evaluate the effects of released silver on algae and well understand the fluorometry results, we followed the general procedure schematized in figure II.18.

- In a first step, we introduce fixed amount of buffered water (in our study 6 ml of MOPS) in each one of three flasks. We use one of them as control (black flask - control). This flask allows control of the algae behaviour in an ambient without nutrient and toxicant (normal health stage of algae). In the second flask, we add an appropriate amount of silver nitrate salt ( $\text{AgNO}_3$ ) (blue flask - control  $\text{Ag}^+$ ) dissolved in pure water. This flask allows following the toxicity effect of a well-known amount of bioavailable ionic silver ( $\text{Ag}^+$ ) on algae (under the adopted experimental conditions, the  $\text{AgNO}_3$  is completely dissociated [Navarro et al., 2008]). In the third flask, we add the sample containing AgNPs to analyse (red flask – AgNPs; in our study, a solid sample with AgNPs embedded in thin silica layers). All three flasks were kept at the same conditions of light, temperature, shaking and incubation time.

- In a second step, we take 2 ml from each flask for Inductively-Coupled Plasma Mass Spectrometry (ICP-MS) measurements to evaluate the total amount of silver in solution. In our study, at this procedure point, the solid sample with embedded AgNPs was removed from the solution (for details see Chapter V, section 4.5).

In the experiment, that involves cysteine, an appropriate amount of this strong silver-ligand was introduced to catch the  $\text{Ag}^+$  present in the solution [Navarro et al., 2008].

- In a third step, we add the same amount of algae in the solution left in the flasks (in our study 3 mL) up to a concentration of  $\text{O.D.}_{685} = 0.15$ . After one hour of the algae exposure, we perform the fluorometry measurements on 2 ml of solution.

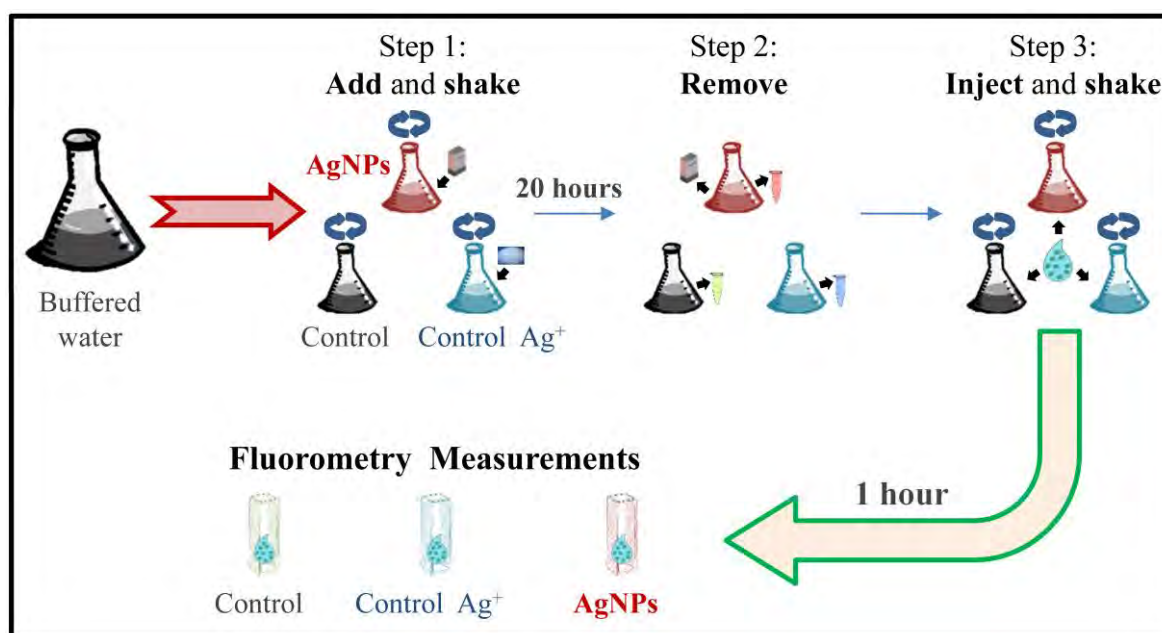


Figure II.18: Diagram showing the procedure pathway for silver release measurement.

After algae injection, all solutions were kept under continuous illumination of  $65 \mu\text{Mol photons s}^{-1}\text{cm}^{-1}$  to ensure normal activity of the algae. Each fluorometry experiment was repeated twice and three fluorometry measurements were taken for each experimental condition to assess the reproducibility of fluorometry results. The time delay between two consecutive fluorometry measurements was at least 30 seconds to allow the complete recovery of the photosynthetic activity of algae after the saturating pulse. The algal photosynthetic yield measured by fluorometry was not affected by the algal translocation into MOPS or by exposure to cysteine (for details see references [Navarro et al., 2008] and [Navarro et al., 2015]).

In our study three parameters were taken into account: (i) **the surface sample exposed to buffered water** that was fixed at  $4 \text{ cm}^2$  for all elaborated samples. This is important to compare samples elaborated at different conditions and to have enough silver in solution to obtain toxicity effect; (ii) **the**

**immersion duration of samples in buffered water** that was 20 h to improve the silver release from the coated or embedded silver nanocomposite samples as it has been shown in the literature where the most important delivery of silver takes place during the first 24 h of immersion [Saulou et al., 2009; Mittelman et al., 2013]; (iii) **darkness**, samples were kept in the dark to avoid redox reaction due to the light exposure [Liu et al., 2010].

Moreover, different experimental conditions were explored to obtain a good interpretation and comparison of the fluorometry measurements. The first one is the amount of buffered water that allows maximizing the concentration of the released in the solution silver from the embedded AgNPs and having enough solution to perform both the fluorometry and the ICP-MS analysis. The second one is the algae concentration of  $O.D._{685} = 0.15$  that permits to have enough bioavailable silver per cell to provoke detectable in fluorometry toxicity effect on the algae. The third one is the continuous shaking at 90 rpm of all solutions at room temperature during the entire fluorometry experiment. This is important to keep a homogeneous solution in the case of: (i) silver released from elaborated samples or  $AgNO_3$  salt, (ii) the system silver-cysteine and (iii) the interaction silver-algae. The last one is the algae short-term exposure to silver that allows minimizing accumulation of algal products in the exposure media and, thus, changes in the silver speciation.

### 6.3. Concentration-response curves

The interpretation of fluorometry measurements is based on concentration-response curve of algal photosynthetic yield after short-term exposure to increasing bioavailable ionic silver in solution [Navarro et al., 2008].

In the figure II.19 we represent the experimental algal photosynthetic yield concentration-response curve after short-term (1 hour) exposure to bioavailable ionic silver measured by ICP-MS. In this graph, the photosynthetic yield of algae in MOPS (the green point - **control**) denotes a reference in each fluorometry experiment for normal health stage of algae. The algal photosynthetic yields in presence of different ionic silver amounts (the black point – **control  $Ag^+$** ) are expressed in percentage of control yield. This allows comparing different experiments performed in similar conditions (same light exposure, temperature, algae concentration) referring the algal photosynthetic yield of samples to its own control solution. A decrease of algal photosynthetic yield indicates an alteration in the physiological state of algae affected by the ionic silver. A characteristic value mostly used in biology is the half-maximum effective concentration ( $EC_{50}$ ) of released ionic silver corresponding to a reduction of 50% of the photosynthetic yield.

This parameter is calculated using a four-parameter logistic fitting and identifies the threshold below which the ionic silver in solution has strong toxicity effect on algae. Algae concentration of  $O.D._{685} = 0.15$ , used to perform this concentration-response curve is a sensible and reliable sensor of silver concentration in solution ranging between 0.3 and 0.8  $\mu M$ .

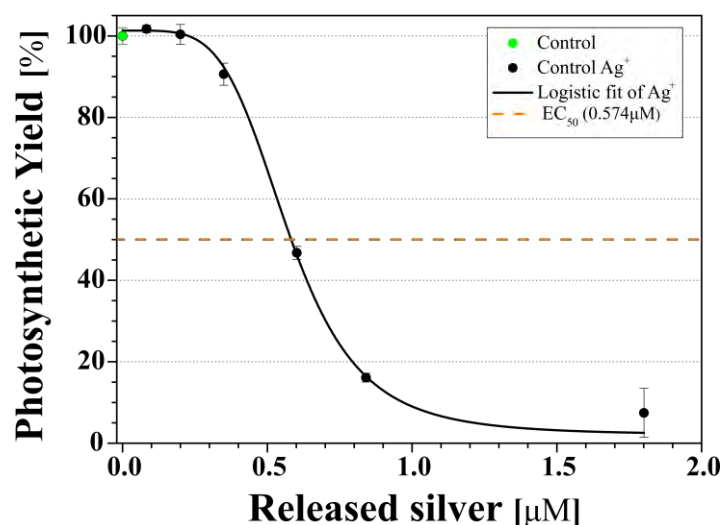


Figure II.19: Experimental algal photosynthetic yield concentration-response curve after short-term (1 hour) exposure to ionic silver measured by ICP-MS (released silver). The algae concentration was with  $O.D._{685} = 0.15$ .

## 7. Inductively Coupled Plasma Mass Spectrometry (ICP-MS)

Inductively Coupled Plasma Mass Spectrometry (ICP-MS) is an analytical technique used for elemental analyses. In our study, this technique allows evaluating the total amount of Ag released in solution. ICP-MS combines an inductively coupled plasma source with a mass spectrometer. The ICP discharge is used for ionization of the atoms of the sample. The created ions are then separated and detected by the mass spectrometer (Fig. II.20) [Nelms, 2005].

Argon gas flows inside the coaxial channels of the ICP torch. When power from a RF generator is supplied to the RF load coil, oscillating electric and magnetic fields are established at the end of the torch. Application of a spark to the argon gas flowing through the ICP torch part leads to creation of electrons and argon ions after ionization of the argon atoms. These primary electrons follow the oscillating fields acquiring enough energy to ionize other argon atoms after collisions and to initiate thus the avalanche and establish the argon plasma. The sample is typically introduced into the ICP plasma as an aerosol, either by aspirating a liquid or dissolved solid sample into a nebulizer or using a laser to directly convert solid samples into an aerosol. Once the sample aerosol is introduced into the ICP torch, the elements in the aerosol are converted first into gaseous atoms and then positively ionized towards the plasma end. The created in the plasma ions are then brought into the mass spectrometer via the interface cones.

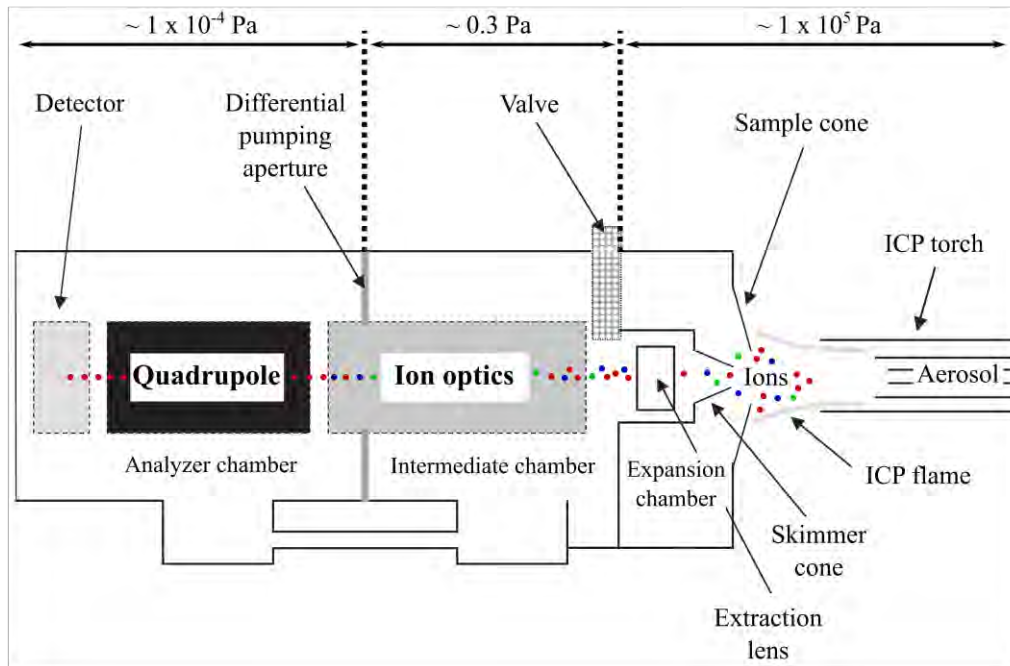


Figure II.20: A cross section through a typical quadrupole ICP-MS showing the three stages of differential pumping. From [Nelms, 2005].

The interface region in the ICP-MS transmits the ions traveling in the argon stream at atmospheric pressure into the low pressure region of the mass spectrometer ( $< 1 \times 10^{-4}$  Pa). This is done through the intermediate vacuum region created by the two interface cones, the sampler and the skimmer (Fig. II.20) in the expansion chamber. The sampler and skimmer cones are metal disks with a small hole ( $\sim 1$  mm in diameter) in the center. The purpose of these cones is to sample the center portion of the ion beam coming from the ICP torch. The ions from the ICP source are then focused by electrostatic lenses (ion optics part). Owing to this ion optic system in the intermediate chamber, it is possible to collimate the positively charged ion beam coming from the system and focus it into the entrance aperture of the mass spectrometer.

Once the ions enter into the analyzer chamber, they are separated through mass spectrometer by their mass-to-charge ratio. The most commonly used type of mass spectrometer is the quadrupole mass filter made by 4 rods. In this kind of mass spectrometer, AC and DC voltages are applied to opposite pairs of the rods. These voltages are then rapidly switched along with an RF-field. The result is that an electrostatic filter is established and ions of a single mass-to-charge ratio ( $m/e$ ) can pass through the rods to the detector at a given instant in time for their identification.

# Chapter III: Controlled elaboration of AgNPs embedded in dielectric matrix by plasma process

---

## 1. Introduction

Two physical approaches are used in this work to elaborate AgNPs embedded in thin silica layers are: (i) low energy ion beam synthesis (LE-IBS) and (ii) plasma deposition techniques comprising silver sputtering followed by plasma polymerization. The purpose is to fabricate multifunctional substrates that can be used for both (i) controlled Ag release and biocide action and (ii) efficient plasmonic enhancement. The two elaboration techniques are complementary and give the prospect to consider different physical situations. However, to overcome the main drawback of low energy ion beam synthesis which is the lack of possibility to attend a percolated array of NPs, as discussed in Chapter I, and to enlarge the variety of structures containing a single layer of AgNPs we have applied plasma deposition techniques. In order to fabricate a plane of large ( $>10$  nm) AgNPs at controlled nanometric distances from the surface and to attain a high surface coverage (larger than 20%) we have developed in this PhD a new method. It consists of successive steps of plasma deposition techniques combining silver sputtering and plasma polymerization, and will be described here. In this Chapter are presented the main results on the developed plasma deposition process to elaborate in a controlled way of large-area plasmonic substrates consisted of a single layer of AgNPs deposited on SiO<sub>2</sub> layer and coated by ultrathin SiO<sub>2</sub> plasma layer.

## 2. Plasma deposition process

Plasma based deposition processes are known to be quite versatile for deposition of nanocomposite thin layers containing metal clusters. Intensive research on the possibilities to obtain thin nanocomposite layers sustained of metallic nanoparticles embedded in dielectric matrices started with the works of E. Kay *et al.* [Kay and Hecq, 1984] where Physical Vapor Deposition (PVD) and Plasma Enhanced Chemical Vapor Deposition (PECVD) were combined in one process to obtain gold nanoparticles dispersed in fluorocarbon matrices. This approach, privileged also by other research groups [Kay and Hecq, 1984; Perrin *et al.*, 1985; Laurent and Kay, 1989; Despax and Floutard, 1989; Despax and Raynaud, 2007; Körner *et al.*, 2009; Dilonardo *et al.*, 2010; Kylián *et al.*, 2013; Drábik *et al.*, 2015], offers several advantages compared to other deposition techniques. It allows: (i) a quite easy control of the metal content in the thin film only by controlling the partial pressures of the plasma feeding gas and the gas precursors in the discharge, leading to the possibility to obtain materials with

metallic concentration from a few percent up to 100%; (ii) homogeneous dispersion of the metal nanoparticles in the film and (iii) fine control over the size of the metal nanoparticles.

Optical properties of this type of nanocomposite structures can finely be tuned by simply varying the metal volume fraction in the layer [Perrin et al., 1985]. Strong structural modifications of both the metal nanoparticles and the surrounding matrix can be achieved by thermally induced processes occurring in the plasma gas phase and/or by post-deposition annealing [Perrin et al., 1985; Laurent and Kay, 1989; Despax and Flouttard, 1989]. Stability of the plasma elaborated host matrix to exposure to different aging agents (air, aqueous media, *etc.*) is shown to be superior for amorphous hydrophilic matrices (plasma silica – a-SiO<sub>2</sub>, organosilicon – a-SiOC:H or oxygenated hydrocarbon – a-CH:O) compared to amorphous hydrophobic ones (fluorocarbon – a-F-C or hydrocarbon – a-C-H) [Perrin et al., 1985; Laurent and Kay, 1989; Despax and Flouttard, 1989; Despax and Raynaud, 2007; Drábik et al., 2015; Körner et al., 2009; Dilonardo et al., 2010; Kylián et al., 2013]. Although the stability of amorphous hydrophilic matrices is generally good, the more resistant matrix is the silica, compared to organosilicon or oxygenated hydrocarbon matrices, as it is the densest one. Moreover, release of metallic ions and/or metallic nanoparticles from the plasma mediated nanocomposite thin films, in particular Ag<sup>+</sup> and AgNPs [Saulou et al., 2009; Körner et al., 2010; Despax et al., 2011; Alissawi et al., 2012; Drábik et al., 2015], shows dependence on the size and density of metal nanoparticles and on the type of the host dielectric matrix (hydrophilic/hydrophobic properties and porosity) and the distance from the AgNPs to the substrate surface. Additionally to the possibility of large variation of the optical, structural and electrical properties of the nanocomposites, offered by the above described plasma process, the stability related issues must be considered when a given application of the nanocomposite thin films is pursued.

The purpose in this part of the study is to elaborate nanocomposite structures of SiO<sub>2</sub>/AgNPs/SiO<sub>2</sub>/Si (a single layer of AgNPs, with well controlled size, density and distance among the nanoparticles, is inserted in a SiO<sub>2</sub> matrix at a given distance from the surface) with highly pronounced anti-reflective properties. The thickness of the whole structure must be selected in a way that for specific wavelengths the reflectance is at minimum and consequently the electric field at the free surface is at maximum, as accounted for by modelling the propagation of electromagnetic waves in stratified media [Carles et al., 2011; Bayle et al., 2014]. In the current study a total thickness of 100 nm of the nanocomposite structure was intended.

The nanocomposite structures were elaborated by using the plasma of an axially-asymmetric capacitively-coupled RF (13.56 MHz) discharge combing PVD, as a first step, and PECVD as a second step in the applied deposition procedure as described in Chapter II and shown in Fig. 1. The discharge powered electrode (smaller electrode) was an Ag-made target to bear the silver sputtering. The axially-asymmetric design of this RF discharge induces a self-bias voltage  $V_{dc}$  on the powered electrode, controlling in that way the metal sputtering. Deposition of plasma silica coverlayer was performed in the same reactor. The plasma reactor and the experimental techniques for real-time

monitoring were described in details in Chapter II. The plasma behaviour during deposition was controlled by Optical Emission Spectroscopy (OES) and electrical measurements. For both deposition steps – sputtering and plasma polymerization – variation of the  $I_{\text{Ag}(546.6\text{nm})}/I_{\text{Ar}(549.6\text{nm})}$  ratio as a function of the injected power or the gas mixture composition was recorded. This kind of chart constitutes useful data to obtain reproducible results [Despax and Raynaud, 2007].

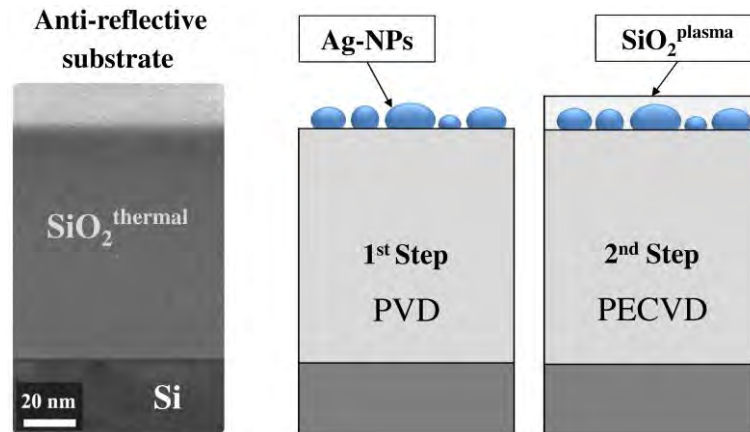


Figure III.1: Pathway for elaboration of large-area plasmonic substrates (single layer of AgNPs embedded in SiO<sub>2</sub> matrix) by plasma process.

The used plasma process is fully compatible with the standard microelectronic technologies. As discussed above it is versatile in terms of experimental conditions which enlarges the possibility to probe and, consequently, to optimize the optical response of the elaborated plasmonic structures. To realize the plasmonic structures a single layer of AgNPs was deposited by Ag-sputtering on the surface of thermally grown SiO<sub>2</sub>-layer (thickness of 80 nm) on Si-substrate (2" in diameter) in Ar-discharge maintained at low gas pressure ( $p_{\text{Ar}} = 5.2$  Pa). The substrate was fixed to the grounded electrode. It was previously cleaned in Piranha solution for 2 min, followed by chemical etching for 30 seconds in hydrofluoric acid (HF). At each step of the cleaning procedure the substrates were rinsed with deionized water. The cleaning procedure is indispensable for the elaboration of plasmonic substrates because it guarantees the removal of the surface contamination and the native oxide, known to be badly organized from structural point of view and presenting poor electrical properties.

The AgNPs size, density and shape were controlled through tuning the sputtering operating conditions. The sputtering time was varied between 5 s and 30 s for different input powers ( $P = 10 - 80$  W), corresponding to a self-bias voltage variation in the range  $V_{\text{dc}} = -400 - -1000$  V (Fig. III.2a). The plasma process was monitored by OES through the ratio of  $I_{\text{Ag}(546.6\text{nm})}$  to  $I_{\text{Ar}(549.6\text{nm})}$  line intensities. For the sputtering step the evolution of  $I_{\text{Ag}(546.6\text{nm})}/I_{\text{Ar}(549.6\text{nm})}$  ratio gives an image of the Ag amount in the plasma which can be related to the Ag volume fraction deposited on the substrate. Figure III.2a shows the measured self-bias voltages as a function of the applied power during the Ag-sputtering and the corresponding line intensity ratio of the silver line  $I_{\text{Ag}(546.6\text{nm})}$  to the argon line  $I_{\text{Ar}(549.6\text{nm})}$ . Prior to each



sputtering the Ag-target was mechanically polished, then cleaned in the Ar-discharge and the plasma process stability was followed by OES. When the emission spectrum from the plasma (Fig. III.2b), and in particular the  $I_{\text{Ag}(546.6\text{nm})}/I_{\text{Ar}(549.6\text{nm})}$  ratio, was found to be constant throughout at least 5 minutes the Ag-sputtering was performed. During the plasma stabilization phase the substrate was hidden behind a shutter [Despax and Raynaud, 2007]. Once the plasma process stability was attained, the shutter was removed for the time of sputtering. The possibility to hide the substrate during the plasma stabilization phase, and once the Ag-sputtering step has been performed, allows us to use very short deposition times (only of few seconds) and to obtain a strict control of the plasma deposition process.

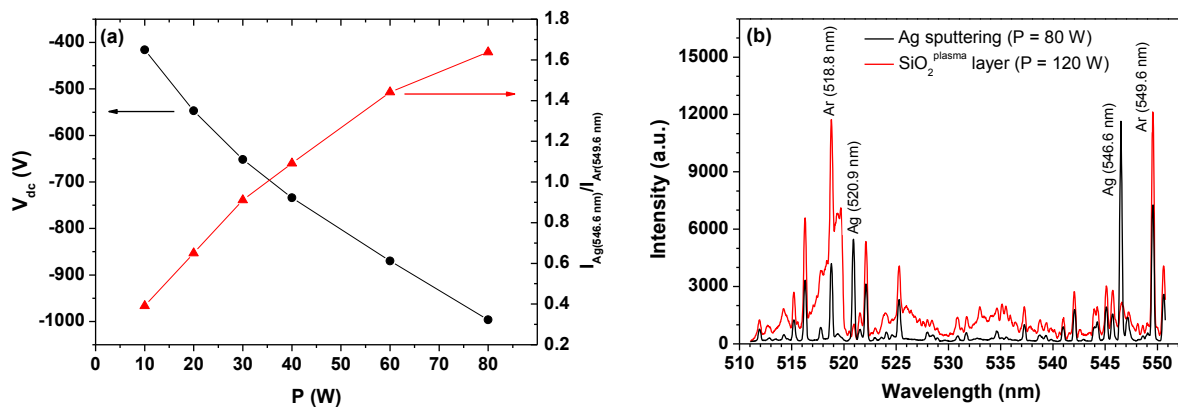


Figure III.2: (a) Evolution of the self-bias voltage  $V_{dc}$  and the ratio of the line intensities  $I_{\text{Ag}(546.6\text{nm})}$  to  $I_{\text{Ar}(549.6\text{nm})}$  as a function of the applied discharge power during the sputtering step ( $p_{\text{Ar}} = 5.2$  Pa) and (b) OES spectra from the plasma sustained in Ar at  $p_{\text{Ar}} = 5.2$  Pa and  $P = 80$  W during the Ag sputtering step (black curve) and of the plasma sustained in Ar/HMDSO/ $\text{O}_2$  mixture at average total pressure  $p_{\text{tot}} = 7.68$  Pa and  $P = 120$  W for the  $\text{SiO}_2$  plasma deposition step (red curve).

### 3. Plasma silica ( $\text{SiO}_2^{\text{plasma}}$ ) cover layer

The plasma silica ( $\text{SiO}_2^{\text{plasma}}$ ) coverlayer embedding the AgNPs was deposited in the plasma sustained in a gas mixture of argon (Ar flow - 2.8 sccm, where sccm stands for standard cubic centimeters) - hexamethyldisiloxane (HMDSO -  $[\text{CH}_3]_6\text{Si}_2\text{O}$ ) - oxygen ( $\text{O}_2$  flow - 1.25 sccm) at average total gas pressure  $p_{\text{tot}} = 7.68$  Pa. The HMDSO (Sigma Aldrich product with purity larger than 99.5%) and argon (AirLiquid AlphaGaz 2 - 99.9995%) flows were mixed in a buffer chamber before being introduced into the plasma chamber. The high quality oxygen flow (AirLiquid AlphaGaz 2 - 99.9995%) was introduced into the plasma chamber by means of an appropriate port situated at the level of the grounded electrode where the substrate was fixed. Strong particularity of our plasma process which makes it original and highly efficient is the pulsed introduction of the precursor. The HMDSO was introduced in the discharge by pulses with period  $T = 5$  s ( $T = t_{\text{on}} + t_{\text{off}}$ ) and injection time  $t_{\text{on}} = 3.1$  s which corresponds to an average HMDSO flow of 0.248 sccm. The maximal fluctuation of the total gas pressure induced by the pulsed injection of the HMDSO was of 0.4 Pa. The combined effect of pulsed introduction of HMDSO in the plasma and the specific location of  $\text{O}_2$  introduction, in the

vicinity of the substrate, has finally a strong impact on the quality of the deposited  $\text{SiO}_2^{\text{plasma}}$  coverlayer. It allows deposition of high quality  $\text{SiO}_2$  plasma layers for relatively low  $\text{O}_2$  to HMDSO ratios. The injected RF power for the  $\text{SiO}_2^{\text{plasma}}$  deposition was fixed to 120 W assuring high degree of HMDSO decomposition in the plasma. Obtaining high quality  $\text{SiO}_2^{\text{plasma}}$  layers, in a plasma process by using HMDSO as precursor, requires diagnostic of the plasma parameters as a function the gas discharge operating conditions - type of gas discharge, injected power, gas pressure and gas mixture [Lamendola et al., 1997; Hegemann et al., 1999; Aumaille et al., 2000; Goujon et al., 2004; Prasad et al., 2005; Camacho et al., 2008]. Once more, like in the Ag-sputtering step, previous to the  $\text{SiO}_2^{\text{plasma}}$  deposition the stability of plasma process was followed until obtaining constant values for the self-bias voltage, the total average gas pressure and the glow emission from the discharge for at least 5 minutes. For the  $\text{SiO}_2^{\text{plasma}}$  deposition step the plasma stabilization phase takes typically 30 minutes. All experiments for the  $\text{SiO}_2^{\text{plasma}}$  deposition were carried without any silver atomic presence in the plasma gas phase. This point was controlled through the absence of silver lines in the recorded optical emission spectra, like the example shown in Fig. III.2b (red curve). It is worth to point here that the OES shown in Fig. III.2b, corresponding to the plasma polymerization step, reflects the elementary processes occurring in the plasma gas phase. After each  $\text{SiO}_2^{\text{plasma}}$  deposition the plasma reactor walls and the Ag-target were cleaned, so that the initial conditions for the next deposition remained unchanged, guaranteeing in that way reproducibility of the elaborated plasmonic substrates. The thickness of the  $\text{SiO}_2^{\text{plasma}}$  coverlayer was controlled by the deposition time after a preliminary study on the deposition rate. The deposition rate, resultant from the above described plasma conditions, was found to be low, only of 13 nm/min. The low deposition rate used in this study gives place to deposition of a dense  $\text{SiO}_2^{\text{plasma}}$  coverlayer with well-ordered matrix. The  $\text{SiO}_2^{\text{plasma}}$  coverlayer should not only be of high quality (no C-H or Si-H content) but also exempt of any silver presence in it. To achieve a  $\text{SiO}_2^{\text{plasma}}$  layer with properties close to thermal silica layer the plasma composition was adjusted by varying the gas mixture. The oxygen injection into the plasma maintained in Ar-HMDSO mixture introduces reactive species that promote oxidation of the methyl groups and the volatile species, such as water and carbon dioxide. To improve the oxidation efficiency in the plasma reactor used for this study, the oxygen flow was introduced grazing the surface of the samples by means of an appropriate port. The parameters for plasma polymerization phase, like applied power, HMDSO injection time and  $\text{O}_2$  flow were optimized by OES and electrical measurements of the self-bias voltage. Typical OES spectrum of the plasma emission is shown in Fig. III.2b. The real-time monitoring of the plasma process by OES [Despax and Raynaud, 2007] is indispensable for obtaining plasma silica layers of high quality.

The pulsed injection of the precursor is one of the originality of the applied plasma process. Indeed, pulsed injection of HMDSO allows fine control over the plasma parameters. The suitable HMDSO injection time was determined in relation with the  $\text{O}_2$  flow in order to ensure both complete plasma organosilicon covering of the Ag-made electrode to prevent from Ag-sputtering and a plasma

deposition of SiO<sub>2</sub> layer with properties close to a thermal silica layer. It was found that the slot of plasma operation parameters that satisfies the above two requirements for the quality of SiO<sub>2</sub><sup>plasma</sup> layer is very narrow. In the preliminary study, where the optimization of the plasma operation conditions was performed, it was found that in the plasma of Ar-HMDSO-O<sub>2</sub> gas mixture, for HMDSO injection times larger than 3.0 s, over 5 s period, in the used in this study, axially-asymmetric capacitively-coupled RF discharge, the silver sputtering did not occur because of the rapid plasma polymer covering of the silver electrode with a thin SiOC:H film. One can see on Fig. III.3 that a slight increase of HMDSO injection time over the same period in insufficiently oxygen flow introduced in the plasma (HMDSO t<sub>on</sub> = 4.0 over T = 5 s period with O<sub>2</sub> flow = 1.0 sccm, green curve) leads to a very broad massive between 800 cm<sup>-1</sup> and 1000 cm<sup>-1</sup>. It signifies the presence of the asymmetric stretching Si-O-Si mode together with the CH<sub>x</sub>(x<2)-Si wagging mode although other carbon groups are not observed in the spectrum. Reducing the HMDSO injection time to t<sub>on</sub> = 3.1 for the same injected power in the discharge (Fig. III.3, blue curve) provides condition for deposition of SiO<sub>2</sub><sup>plasma</sup> layer. Effect of rapid thermal annealing (400°C for 30 min) of the plasma silica layer (Fig. III.3, red curve) did not induced any further changes in the silica matrix (densification or structural reorganization). The FTIR spectrum of thermal SiO<sub>2</sub> layer (Fig. III.3, black curve) is shown for comparison purposes only.

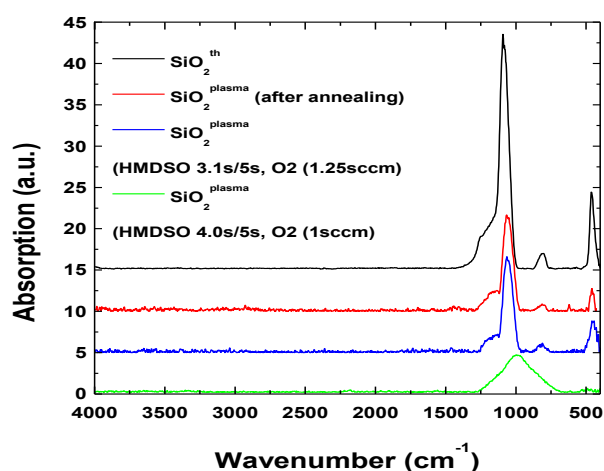


Figure III.3: FTIR spectra showing the evolution of the layer composition with the gas mixture parameters: t<sub>on</sub> and O<sub>2</sub> flow. The spectra are normalized to the corresponding layer thickness. The black curve represents FTIR spectrum of thermal silica layer.

Finally, to avoid Ag presence in the discharge, and consequently in the SiO<sub>2</sub><sup>plasma</sup> layer, the HMDSO injection time must be longer than 3.0 s, over 5 s period, for the O<sub>2</sub> gas flows of 1.25 sccm. However, to prevent from possible C-H content in the SiO<sub>2</sub><sup>plasma</sup> layer the HMDSO injection times must not be longer than 3.2 s for the O<sub>2</sub> gas flows of 1.25 sccm. The composition of deposited SiO<sub>2</sub> layer was determined by FTIR and ellipsometry. It is in accordance with the SiO<sub>2</sub> layers obtained by other authors using O<sub>2</sub> and HMDSO as precursors for silica deposition in a plasma process [Hegemann et al., 1999; Aumaille et al., 2000; Goujon et al., 2004].

The FTIR spectrum of  $\text{SiO}_2^{\text{plasma}}$  layer used to cover the AgNPs, in order to complete the plasmonic substrate, is shown in Fig. III.4. One can observe the three typical TO modes of molecular vibrations of amorphous silicon dioxide [Kirk, 1988]. In particular, the FTIR spectrum shows the Si-O-Si rocking vibration at  $457\text{ cm}^{-1}$ , the symmetric stretching mode at  $810\text{ cm}^{-1}$ , and the asymmetric stretching mode at  $1062\text{ cm}^{-1}$ . The shoulder centred around  $1250\text{ cm}^{-1}$ , characteristic of thermal  $\text{SiO}_2$  is clearly observable on the spectrum. The lack of Si-H stretching bond at  $2250\text{ cm}^{-1}$ , the C-H symmetric stretching bond in  $\text{CH}_3$  environment at  $2900\text{ cm}^{-1}$ , the C-H asymmetric stretching bond at  $2960\text{ cm}^{-1}$  and the OH bonds, both associated at  $3450\text{ cm}^{-1}$  and free at  $3630\text{ cm}^{-1}$ , that appear in plasma deposited organosilicon layers [Makasheva et al., 2013] when only HMDSO is used as precursor, testifies for the efficient process of oxidation and the high quality of the elaborated  $\text{SiO}_2^{\text{plasma}}$  layer. The FTIR spectrum presents a weak shift to lower frequencies in the peak position of the Si-O-Si asymmetric stretching mode,  $1062\text{ cm}^{-1}$  instead of  $1076\text{ cm}^{-1}$  as expected for thermal  $\text{SiO}_2$  layer, most likely due to the slight  $\text{SiO}_2$  disorder. Due to the small thickness of  $\text{SiO}_2^{\text{plasma}}$  layer, only 96 nm as measured by spectroscopic ellipsometry, a slight noise in the absorption FTIR spectrum is observed in Fig. III.4.

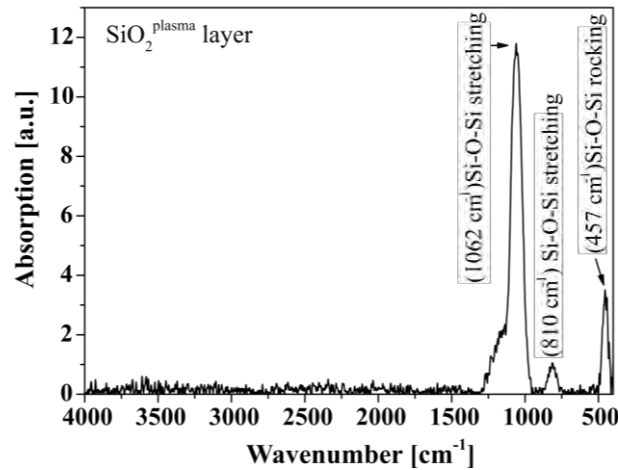


Figure III.4: FTIR spectrum of a deposited  $\text{SiO}_2^{\text{plasma}}$  layer of thickness  $d_{\text{SiO}_2^{\text{plasma}}} = 96\text{ nm}$ .

#### 4. Structural and optical properties of the deposited plasmonic structures

Figure III.5 represents a bright field TEM image in cross-section view of typical elaborated sample. It corresponds to the following structure: single layer of AgNPs deposited at injected power of  $P = 40\text{ W}$  for sputtering time of  $t_s = 5\text{ sec}$  and covered by  $\text{SiO}_2^{\text{plasma}}$  layer of thickness  $d_{\text{SiO}_2^{\text{plasma}}} = 13\text{ nm}$  (deposition time for the  $\text{SiO}_2^{\text{plasma}}$  layer,  $t_d = 60\text{ s}$ ).

One can clearly notice the planarity in the AgNPs single layer (the AgNPs layer average thickness is of 9 nm). High Resolution Electron Microscopy (HREM) observations (see image in insert of Fig. III.5) show that the Ag nanoparticles are crystalline and made of pure silver. The total thickness of the

structure is 105 nm, which fulfils the condition for anti-reflectivity of optical waves in the middle of the visible range [Carles et al., 2011; Bayle et al., 2014].

The evolution of the AgNPs size, density and shape with the injected power for Ag-sputtering is shown in Fig. III.6 for a fixed sputtering time  $t_s = 5$  s and two different powers 40W (Fig. III.6a) and 80W (Fig. III.6b) covered by a  $\text{SiO}_2^{\text{plasma}}$  layer of thickness  $d_{\text{SiO}_2^{\text{plasma}}} = 13$  nm ( $\text{SiO}_2^{\text{plasma}}$  layer deposition time,  $t_d = 60$  s). The size of AgNPs increases from  $11.1 \pm 2.4$  nm to  $19.6 \pm 7.8$  nm. Their density is reduced from  $4.6 \times 10^{11}$  NPs/cm<sup>2</sup> to  $1.7 \times 10^{11}$  NPs/cm<sup>2</sup>, covering an area of 45.8% and 42.6%, respectively. The same trend is observed when the injected power is fixed and the sputtering time is increased.

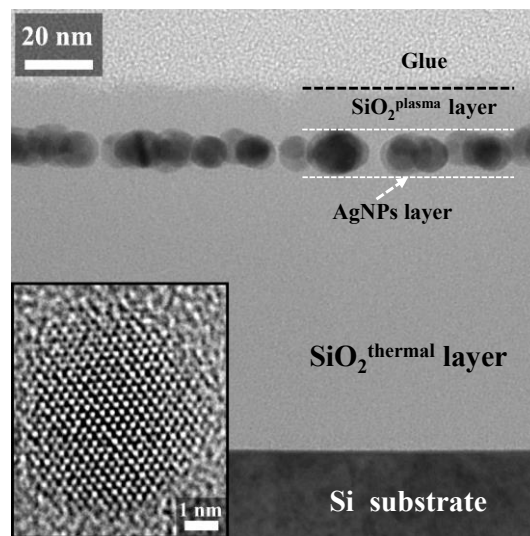


Figure III.5: Bright field TEM cross-section image of a sample elaborated by combined silver sputtering and PECVD. Conditions for the AgNPs single layer deposition  $t_s = 5$  s,  $P = 40$ W ( $V_{dc} = -750$  V). The  $\text{SiO}_2^{\text{plasma}}$  deposition time,  $t_d = 60$  s. In insert HREM image of a single nanocrystal.

For  $P = 10$  W, increasing the sputtering time from 10 s (Fig. III.6c) to 30 s (Fig. III.6d) leads to an increase of the mean diameter of the AgNPs from  $4.5 \pm 1.7$  nm to  $7.7 \pm 2.8$  nm corresponding to a coverage area of 13% and 19%, respectively. The density of AgNPs however decreases from  $7.6 \times 10^{11}$  NPs/cm<sup>2</sup> to  $6.9 \times 10^{11}$  NPs/cm<sup>2</sup>, for the two sputtering times ( $t_s = 10$  s and  $t_s = 30$  s), respectively.

For a fixed sputtering time by scaling up the injected power the shape of AgNPs changes from spherical ( $P = 10$  W) to prolate spheroid ( $P > 60$  W). This property has been observed for other types of metal nanoparticles embedded in dielectric matrices, like Au-nanoparticles dispersed in fluorocarbon or hydrocarbon matrices, in the same type of gas discharges [Perrin et al., 1985; Laurent and Kay, 1989]. Increasing the sputtering time from 5 s up to 30 s does not influence the AgNPs shape for low injected power ( $P = 10$  W), while it leads to overtaking the percolation threshold for high injected power ( $P = 80$  W). Consequently, to obtain a single layer of large AgNPs, high injected power and small sputtering times must be privileged.

The ellipsometric spectroscopy is an extremely sensitive and powerful method largely applied for diagnostic of thin transparent layers with the main advantage of being non-destructive. The ellipsometric spectrum of  $\text{SiO}_2^{\text{plasma}}$  layer (Fig. III.7a) was used to determine the refractive index and the thickness of the layer by applying the Forouhi-Bloomer dispersion law [Forouhi and Bloomer, 1986]. The obtained values are  $n = 1.45$  (at  $\lambda = 632.8$  nm) and  $d_{\text{SiO}_2^{\text{plasma}}} = 96$  nm, respectively. The ellipsometric spectrum of  $\text{SiO}_2^{\text{plasma}}$  layer is identical to the one of thermal  $\text{SiO}_2$  layer for the same thickness, which testifies for the high quality of the plasma deposited silica layer in this study. It means that the layer composition is close to thermal silica one and there is no silver contamination in this layer.

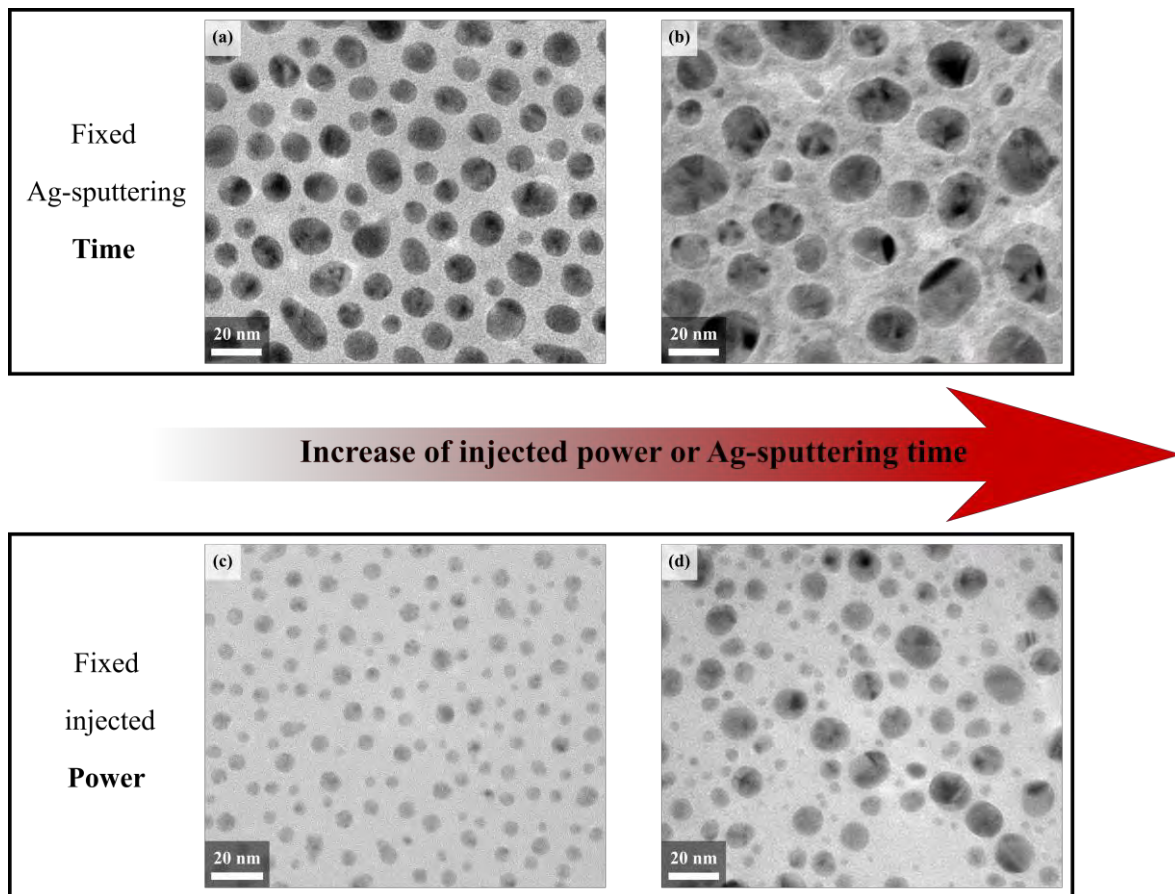


Figure III.6: Bright field TEM plan-view images of the obtained plasmonic substrates by using different powers (a) 40W and (b) 80W at fixed Ag-sputtering time  $t_s = 5$  s or increasing the Ag-sputtering time from (c) 10 s to (d) 30 s for fixed injected power  $P = 10$  W.

In fact, due to the electric field polarization, the ellipsometric measurements are extremely sensitive to changes in the refractive index and the extinction coefficient due to any silver presence inside the  $\text{SiO}_2$  matrix. Even a very small fraction of Ag-atoms in the  $\text{SiO}_2$  layer leads to a departure in the  $\cos\Delta$  variation, that gives the phase difference, induced by the reflection, between the perpendicular and parallel components of the polarized electric field as shown in Fig. III.7a.

To guarantee the performance of plasmonic substrates when integrated in devices one needs to characterize their dielectric response. A good way is to use reliable non-destructive diagnostic methods like ellipsometry and reflectometry. When AgNPs are embedded in the SiO<sub>2</sub> layer, the ellipsometric spectra indicate their presence by shift of the peak to higher energies in the tanΨ variation and by appearance of a peak in the cosΔ variation at the same wavelength as for the tanΨ variation, as shown in Fig. III.7b for the two plasmonic substrates presented on the TEM plan-view images in Fig. III.6a,b. The tanΨ variation is closely related to changes in the amplitudes of the polarized electric field after reflection. It means that even small variations in the size and density of AgNPs will be detected by spectroscopic ellipsometry. The larger the size of AgNPs, the larger the energy shift of their peak on the ellipsometric spectra is. This is an expected behaviour of ellipsometric spectra for AgNPs with different size and density as already presented in other studies [Kreibig and Vollmer, 1985; Oates and Mücklich, 1995].

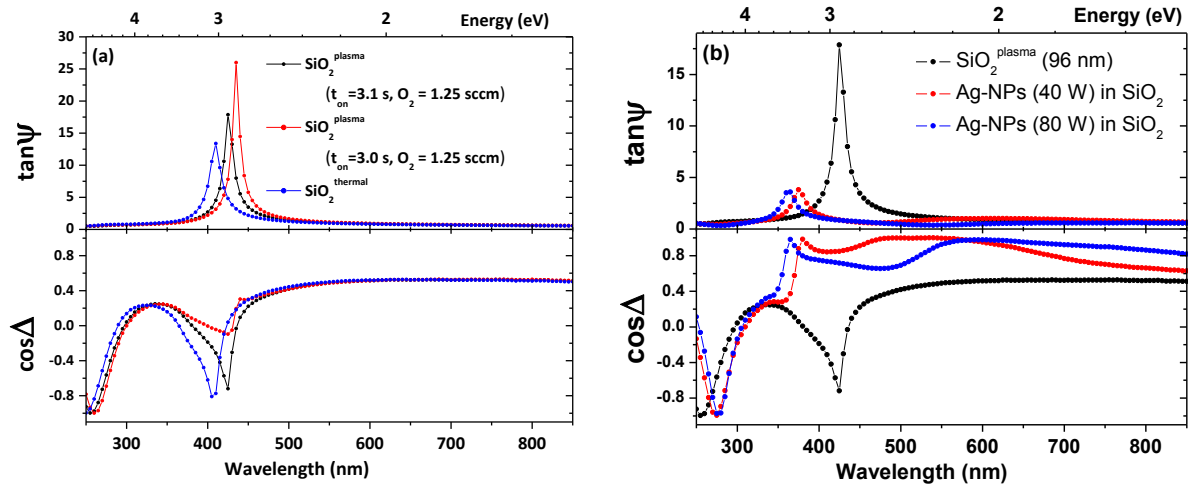


Figure III.7: Ellipsometry spectra of elaborated samples: (a) SiO<sub>2</sub><sup>plasma</sup> layer for t<sub>on</sub> = 3.1s (black curve), SiO<sub>2</sub><sup>plasma</sup> layer for t<sub>on</sub> = 3.0s (red curve) where one can see departure on the cosΔ variation due to small quantity of Ag in the SiO<sub>2</sub><sup>plasma</sup> layer and SiO<sub>2</sub><sup>thermal</sup> layer (blue curve) and (b) SiO<sub>2</sub><sup>plasma</sup> layer (black line) and two plasmonic substrates P = 40 and 80 W, t<sub>s</sub> = 5 s, and deposition time for the SiO<sub>2</sub><sup>plasma</sup> coverlayer t<sub>d</sub> = 60 s.

Alternatively to the ellipsometric spectra analysis presented by Oates *et al.* [Oates and Mücklich, 1995] where AgNPs deposited on SiO<sub>2</sub> layer are surrounded by air, the present plasmonic structures appear more complex as the AgNPs are embedded in the SiO<sub>2</sub> matrix and an appropriate description of the dielectric functions of different media and of the interface-related artefacts requires an in-depth analysis. Modelling of the recorded ellipsometric spectra, based on the quasi-static approximation of the classical Maxwell-Garnett formalism, however accounting for the electronic confinement effect through the damping parameter was developed in this PhD work and will be presented in Chapter IV. Details on the theoretical model, the developed diagnostic procedure and the interpretation of



ellipsometric spectra recorded on the plasma deposited thin silica layers containing AgNPs are described and commented alongside with the model limits.

Visible-UV reflectance spectra are particularly easy to obtain experimentally or model theoretically, and furthermore they display a notable sensitivity to the incorporation of AgNPs in the dielectric matrix, as shown in Figs. III.8a and III.8b. By changing either the injected power (Fig. III.8a) or the sputtering time (Fig. III.8a) one drastically affects the reflectance in the visible range (400 – 750 nm) where most of the potential applications of plasmonic substrates are expected. This enhanced sensitivity is a direct consequence of the design of our specific substrates, which allows simultaneously combining strong absorption at the LSPR (near 413 nm for spherical AgNPs in SiO<sub>2</sub> host matrix) and antireflective effect of the multilayer structure (near 600 nm) [Carles et al., 2011]. On Figs. III.8a and III.8b, one clearly observes that higher the embedded Ag amount, by increasing the deposition time or the injected power respectively, higher the reflectance in the middle of the visible range is (near 500 nm).

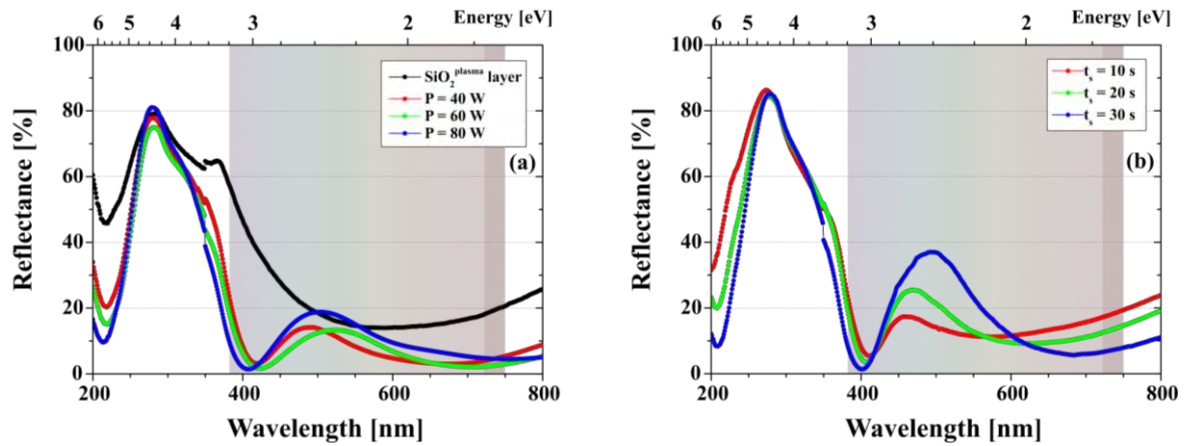


Figure III.8: Reflectance spectra of SiO<sub>2</sub><sup>plasma</sup> layer (thickness  $d_{\text{SiO}_2^{\text{plasma}}} = 96$  nm, black line in figure III.7a) and the elaborated plasmonic substrates. (a) The AgNPs delta-layers were deposited with  $P = 40$  W (red line), 60 W (green line) and 80 W (blue line) for fixed sputtering time  $t_s = 5$  s. The deposition time of the SiO<sub>2</sub><sup>plasma</sup> coverlayer is  $t_d = 60$  s ( $d_{\text{SiO}_2^{\text{plasma}}} = 13$  nm). (b) The AgNPs delta-layers were deposited with  $P = 10$  W for increasing sputtering times  $t_s = 10$  s (red line), 20 s (green line), 30 s (blue line). The deposition time of the SiO<sub>2</sub><sup>plasma</sup> coverlayer is  $t_d = 30$  s ( $d_{\text{SiO}_2^{\text{plasma}}} = 5$  nm).

One thus expects a high sensitivity in the elastic scattering response for LSPR-sensitive devices or inelastic scattering response for SERS substrates. It is worth to underline here the high sensitivity of the plasma elaborated plasmonic substrates for optical applications in the visible range: the reflectance is modified around 25% (on average) at 500 nm.



## 5. Towards elaboration of plasmonic substrates by simultaneous Ag-sputtering and plasma polymerization

Given the shape evolution of AgNPs (from spherical to prolate spheroid) in the Ag-sputtering step when increasing the injected power to sustain the discharge in order to obtain large particles, our next goal was to improve the properties of the nanocomposite layer through deposition of a single layer of large spherical AgNPs, with a narrow size-distribution of the NPs, embedded in silica matrix and covered by a flat silica coverlayer of few nanometers. Indeed, playing on the HMDSO injection time  $t_{on}$ , one can control the poisoning effect of the Ag-target. As discussed earlier, when depositing the  $\text{SiO}_2^{\text{plasma}}$  layer, HMDSO injection times of less than 3.1 s over 5 s period leads to deposition of silica layers containing a very small Ag-fraction (Fig. III.7a). It means that for these operating conditions the Ag-sputtering from the target occurs during the plasma polymerization process. To fully benefit the capacities of our plasma deposition system we have initiated a study on the elaboration and structural properties of plasmonic substrates by using simultaneously metal sputtering and plasma polymerization.

In the past, this method was exploited in LAPLACE to elaborate carbonaceous or organosilicon matrices containing dispersed metal nanoparticles aiming at applications in electrical systems for their modulated dielectric properties [Despax and Flouttard, 1989; Canet et al, 1992] or as coating layers containing AgNPs with antiadhesive and antimicrobial properties [Despax and Raynaud, 2007; Saulou et al., 2009; Despax et al., 2011; Saulou et al., 2012].

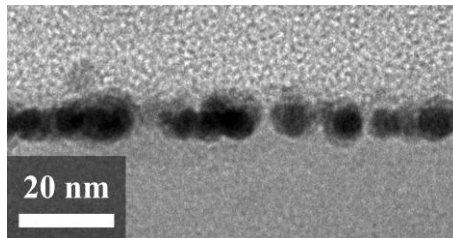


Figure III.9: Bright field TEM cross-section image of a sample elaborated by combined simultaneously Ag-sputtering and plasma polymerization. Conditions for the AgNPs single layer deposition  $t_{on} = 1.75$  s,  $P = 120$ W ( $V_{dc} = -1040$  V) and deposition time 1 min.

The preliminary deposition was performed by using the same operating conditions exploited for the plasma silica layer deposition, to keep the gas mixture and the  $\text{O}_2$  flow proper for the silica matrix, except for the HMDSO injection time that was fixed to  $t_{on} = 1.75$ s over 5s period. The deposition time was of 1 minute. Figure III.9 shows the bright field TEM cross-section image of a sample elaborated under these conditions on silica surface. One can see in the figure the formation of a single layer of spherical AgNPs touching the free surface. The nanocomposite layer thickness is of 10 nm. These first results open the way for future studies on the synthesis and applications of embedded AgNPs targeting

both their use as plasmonic substrate and as coating layers containing strong biocide agent, and confirming their multifunctionality.

## **6. Conclusions**

In this Chapter, we have shown that the potentialities of plasma based deposition can be exploited to perform rational engineering of targeted nanostructures, in this case plasmonic substrates and how the key parameters of the embedded AgNPs (size, density, distance to the surface) can be controlled by tuning the plasma operating conditions combining silver sputtering and plasma polymerization in one process. Two different deposition routes were followed: the first one based on successive silver sputtering and plasma deposition of silica cover matrix and the second one (although only in preliminary phase of development) consisting of simultaneous Ag-sputtering and plasma polymerization. The structural and optical characterizations of the obtained plasmonic structures confirm the efficiency of the plasma deposited plasmonic substrates. By coupling these samples to the ones elaborated by LE-IBS, we have now two techniques for fabricating of a single layer of AgNPs embedded in thin silica films at controlled nanometric distance beneath the free surface. They offer the possibility to explore different AgNPs size distributions, surface densities and particularly their separation from the free surface. This set of samples will be used in Chapter V to evaluate if, even if embedded in a dielectric matrix, our AgNPs are able to release  $\text{Ag}^+$  ions when submersed in water. For this assessment, an original method will be described, implying green algae as biosensors. Before testing the biocide properties of these solid layers, the next chapter (Chapter IV) will be focused on the optical properties of these layers by going deeper in the potentialities of ellipsometry as an efficient diagnostic technique for the detection of small variations in the size and density of AgNPs.



# Chapter IV: Fully predictive modeling of ellipsometric spectra describing the dielectric response of plasmonic substrates

---

## 1. Introduction

The properties of nanocomposite materials are nowadays widely studied aiming at a large spectrum of applications. In particular, nanostructures containing a layer of silver nanoparticles (AgNPs) embedded in silica matrix close to the free surface have a strong potential for plasmonic devices. The main advantage of these structures is the possibility to manipulate, localize and enhance the electromagnetic field at their surface. Currently, well-established microscopy techniques, including Atomic Force Microscopy (AFM), Scanning Electron Microscopy (SEM) and TEM allow visualisation and characterisation of the nanostructures, although being “local”, intrusive, and unsuitable for real-time and in-line monitoring of the processes, especially on the surface/interfaces modifications [Losurdo et al., 2009]. However, to guarantee the performance of plasmonic structures when integrated in devices one needs to characterize their dielectric response during the elaboration phase. A good way is to use reliable non-destructive diagnostic methods. In general, many fundamental and functional properties of nanocomposites can be conveniently probed using several variants of optical spectroscopy. In particular, using polarized light in ellipsometric measurements proves to be highly efficient. Spectroscopic ellipsometry (SE) actually turns out to be the most appropriate among the various tools for characterization of nanocomposite materials. It is a non-destructive, non-intrusive, and non-invasive, contactless optical technique, that has been developed and applied extensively over the last 50 years, not only for the optical characterization of bulk materials and thin films, but also for in situ real-time measurement of multilayered film structures, interfaces, and composites, during fabrication and processing [Tompkins and Irene, 2005]. Ellipsometry is routinely used to measure thickness and optical constants of dielectric, semiconductor, and metal thin films and a critical review discussing how to reduce the correlation between film thickness and optical constants was recently provided in the literature [Hilfiker et al., 2008].

In this Chapter we report on the development, test and application of a fully predictive model appropriate for interpretation of ellipsometric spectra recorded on plasmonic structures. It is based on the quasistatic approximation of the classical Maxwell-Garnett formalism, however accounting for the electronic confinement effect through the damping parameter. Samples were elaborated by using: (i) low energy ion beam synthesis and (ii) combined sputtering and plasma polymerization. The model allows extracting from the experimental ellipsometric spectra the characteristics of the NPs

population: average size, volume fraction and distance of the AgNPs layer from the matrix free surface. Comparison with results obtained from transmission electron microscopy confirms the applicability of this method. The limits of the proposed diagnostic method along with further development related to the quality of comparison between the model-generated spectra and experimental data is also discussed. This aspect of my work was developed in close collaboration with Maxime Bayle during his PhD at CEMES laboratory.

## 2. Studied samples

The two different elaboration techniques described previously were applied here to elaborate the AgNPs embedded in 90 nm thick silica layers thermally grown on (100) Si substrate: ion implantation and plasma deposition process. They offer the possibility to explore different AgNPs shapes, size distributions, surface densities and particularly their separation from the free surface. For clarity of presentation the selected samples elaborated by ion implantation are called “implanted samples” and labelled E1 and E2 hereafter, and those prepared by plasma deposition process are called “plasma deposited samples” and labelled E3 and E4. The elaboration conditions of the studied samples by using these two physical methods are described below.

### 2.1. Ion Implantation

As described in Chapter I, we have recently developed a synthesis technique based on implantation of  $\text{Ag}^+$  ions with low kinetic energy (few keV) and doses of few  $10^{16}$  ions/cm<sup>2</sup> by which a layer of AgNPs is embedded near the free surface of a  $\text{SiO}_2$  layer thermally grown on a Si wafer [Carles et al., 2009; Benzo et al., 2013]. A specifically modified Varian 200A2 implanter was used in order to work in the low energy range. The layers have been implanted at fixed energy  $E$  of the  $\text{Ag}^+$  ions and with two ion doses  $D$  (see Table IV.1). The ion density current  $I$  plays a key role for the silver diffusion in the silica matrix and has been fixed to 5  $\mu\text{A}$  for all the implantations. Under these conditions the nucleation of the AgNPs takes place during the implantation process without the need of any annealing step [Liu et al., 1998; Tsang et al., 2006; Benzo et al., 2013] due to the high diffusivity of Ag in  $\text{SiO}_2$  [Nason et al., 1991; Stefanov, 2010].

To recover the matrix damage and protect the AgNPs from fast oxidation [Benzo et al., 2011] a post-implantation rapid-thermal-annealing was carried out under  $\text{N}_2$  atmosphere at 500°C for 30 minutes. The choice of the annealing time and temperature was restricted as to maintain unchanged the AgNPs size distribution and their position inside the  $\text{SiO}_2$  matrix.

By ion implantation technique, it has been demonstrated the possibility of accurate tuning of the AgNPs average size, surface density and position with respect to the free surface [Benzo et al., 2013]. Nevertheless, for implanted doses larger than  $3 \times 10^{16}$  ions/cm<sup>2</sup>, sputtering and diffusion effects towards the free surface limit the amount of Ag that can be introduced in the dielectric and thus the

final average diameter of the formed nanocrystals, that cannot exceed 15 nm. To obtain bigger AgNPs and a larger silver amount, another elaboration technique has been applied, as described in the next section.

Table IV.1: Parameters used to elaborate the samples by ion implantation.

Sample	Ag <sup>+</sup> Implantation conditions			
	Energy, $E$ [keV]	Dose, $\phi$ [10 <sup>16</sup> ions/cm <sup>2</sup> ]	Density current, $I$ [ $\mu$ A]	Time, $t$ [hours]
<b>E1</b>	10	0.715	5	4.5
<b>E2</b>	10	3.8	5	22

## 2.2. Plasma deposition process

As described in Chapter III the plasma deposition process consists of an axially-asymmetric RF capacitively-coupled discharge maintained at 13.56 MHz at low gas pressure that successfully combines metal sputtering (PVD) and plasma polymerization (PECVD) [Despax and Raynaud, 2007]. It allows a fine control over the size and density of the metal nanoparticles along with homogeneous dispersion for metallic concentrations from a few percent up to 100% (continuous metallic nanolayer).

Table IV.2: Parameters used to elaborate AgNPs by sputtering deposition process (PVD).

Sample	Ag deposition conditions (PVD step)				
	Applied Power, $P$ [W]	Self-bias Voltage, $V_{dc}$ [V]	Ar pressure, $p$ [Pa]	Ar flow, [sccm]	Time, $t$ [sec]
<b>E3</b>	10	- 390	5.2	2.8	10
<b>E4</b>	10	- 390	5.2	2.8	30

The AgNPs single layer was deposited on thermally grown SiO<sub>2</sub> thin films on Si substrate by means of Ag sputtering of the powered electrode (silver target) in argon plasma sustained at low gas pressure. It was subsequently covered by a high quality very thin SiO<sub>2</sub> plasma layer during the plasma

polymerization step to form the stack. The evolution of the AgNPs with the plasma operating conditions was described in details in Chapter III. The selected plasma operating conditions for the sputtering process leading to the deposition of AgNPs are presented in Table IV.2. As mentioned above after the PVD step, the AgNPs plane was covered by a very thin SiO<sub>2</sub> layer deposited in the same plasma reactor. In the latter deposition step, the plasma is obtained in a mixture of argon (Ar)-hexamethyldisiloxane (HMDSO, [CH<sub>3</sub>]<sub>6</sub>Si<sub>2</sub>O)-oxygen (O<sub>2</sub>) (Chapter III). The deposition of SiO<sub>2</sub> is performed for a fixed deposition time  $t$  (to always achieve the same thickness as the deposition time controls the layers thickness) and a constant RF power  $P$  (Table IV.3). The relatively high applied power for the plasma polymerization phase ensures deposition of high quality plasma silica layers. Details of sample preparation, including the cleaning procedure of substrates, and elaboration process as well as the optimized parameters for both sputtering and silica deposition steps, and the plasma process monitoring are given in Chapter II and Chapter III.

Table IV.3: Parameters used to elaborate the SiO<sub>2</sub> plasma layer by PECVD.

Sample	SiO <sub>2</sub> <sup>Plasma</sup> deposition conditions (PECVD step)								
	Applied Power, $P$ [W]	Self-bias Voltage, $V_{dc}$ [V]	Total Pressure, $p_{tot}$ [Pa]	Ar flow [sccm]	O <sub>2</sub> flow [sccm]	HMDSO injection time, $t_{on}$ [sec]	HMDSO period, $T = t_{on} + t_{off}$ [sec]	HMDSO average flow [sccm]	Time, $t$ [sec]
E3	120	- 880	7.68	2.8	1.25	3.1	5	0.25	30
E4									

### 3. Description of the theoretical model used for simulation of plasmonic structures

The optical frequency range ( $3 \times 10^{11}$  Hz –  $3 \times 10^{16}$  Hz) extends from far-infrared (FIR) to vacuum-ultraviolet (VUV) spectral regions with longest and shortest wavelength of 1 mm and 10 nm, respectively. Since the atomic dimensions are of the order of 0.1 nm, matter behaves as continuum at the optical frequencies and below (microwave and radiofrequency range). Although the discrete atomic structure of matter induces strong spatial variation of the quantities describing optical fields, the response at macroscopic level is smooth and usually detected by light probes in the optical range. The nanostructured materials can be considered as a mixture of individual components each of them possessing their own continuum-like optical response. The advantage of treating a nanostructured material as a mixture having continuum behavior is the possibility of finding the macroscopic

(averaged) field quantities by using approximate treatment (effective media approximation, EMA). If the composite material consists of dissimilar regions that are small compared to the wavelength of probing light but large enough to express their own dielectric identity, the local fields and the subsequently obtained averaged quantities are impacted by the presence of screening charge that develops at the boundaries between regions [Aspnes, 2011]. The screening charge modifies locally the electric field which yields modifications in the averaged macroscopic polarization. However, under certain conditions we can perform a second average and find the dielectric function, but the one that describes the macroscopic response of the nanocomposite material to the applied field. If the geometry of the nanostructured material is sufficiently simple so that we can solve the Maxwell equations analytically, we can obtain expression relating the averaged dielectric function to the structural parameters of the nanocomposites on the basis of EMA. We have performed such treatment on the nanocomposites elaborated in this work and described above plasmonic structures by using the prototype of EMA, the one developed by Garnett [Garnett, 1904].

The physical situation that we wish to describe is an ensemble of AgNPs included in a silica matrix. Following the EMA rules, and in particular the Maxwell-Garnett approximation, we convert this heterogeneous system in a homogeneous effective media. To describe the interaction between the AgNPs and the electromagnetic wave we limit the case to the quasi-static approximation. This consideration is based on the fact that the size of AgNPs in the system is much smaller than the wavelength of the external electric field in the visible range. Additional condition is that the density of AgNPs inclusions (their volume fraction) remains small so that their impact on the system can be considered as perturbation only. Accordingly, the electromagnetic field does not experience the detailed structure of the nanocomposite.

The effective permittivity of the media  $\epsilon_{eff}$  is then available according to the Clausius Mossotti relation where  $N$  is the number of NPs in a unit volume,  $V$  and  $\epsilon_m$  is the dielectric permittivity of the host matrix:

$$\frac{\epsilon_{eff} - \epsilon_m}{\epsilon_{eff} + 2\epsilon_m} = \frac{N\alpha}{3\epsilon_m}. \quad (IV.1)$$

After introducing the volume fraction of AgNPs  $f = NV$  in the silica matrix and by replacement of  $\alpha$  by its expression for NPs of spherical shape ( $\alpha = 2$ ) [Garnett, 1904] one finds the general expression of Maxwell-Garnett:

$$\frac{\epsilon_{eff} - \epsilon_m}{\epsilon_{eff} + 2\epsilon_m} = f \frac{\epsilon_{NP} - \epsilon_m}{\epsilon_{NP} + 2\epsilon_m}, \quad (IV.2)$$

with  $\epsilon_{NP}$  representing the dielectric permittivity of the nanoparticles.

For sufficiently small volume fractions the effective permittivity of the media  $\epsilon_{eff}$  takes the form:



$$\varepsilon_{eff} = \varepsilon_m + 3f \varepsilon_m \frac{\varepsilon_{NP} - \varepsilon_m}{\varepsilon_{NP} + 2\varepsilon_m}. \quad (IV.3)$$

As already discussed in Chapter I (Section 6.3) when scaling down to nanometer size, the optical response of metals is affected by three main features: size, shape and surrounding medium of the metal [Kreibig and Vollmer, 1995; Maier, 2007]. The complex dielectric function of nanoparticles becomes size dependent. Assuming metallic spherical nanoparticles, their complex dielectric function can be written as:

$$\varepsilon_{NP}(\omega, D_{NP}) = \varepsilon_{IB}(\omega) - \frac{\omega_p^2}{\omega^2 + i\gamma(D_{NP})\omega}, \quad (IV.4)$$

where  $\varepsilon_{IB}(\omega)$  is the part of complex dielectric function due to the interband transitions in bulk metals and  $\gamma(D_{NP})$  is related to the damping parameter  $\gamma_b$  accounting for collisions of electrons with other electrons, crystal lattice (phonons), lattice defects, or impurities and considering the size effect of nanoparticles (see Chapter I, Eq. I.21). Accordingly, the size dependency of the dielectric function remains negligible on its real part while its imaginary part is significantly impacted.

Considering the dielectric permittivity of the nanoparticles as given by Eq. IV.4 in the expression of effective permittivity of the media (Eq. IV.3) allows for accounting the size effects imposed by the AgNPs in the theoretical model of plasmonic structures.

## 4. Numerical procedure for the simulations

Schematic representation of the modeled plasmonic structures is given in Fig. IV.1. The plasmonic structures are considered as multi-layer systems. Each of the layers is described by its dielectric permittivity. The layers containing AgNPs are taken as effective media and are represented by the corresponding effective dielectric permittivity. As can be noticed on the figure such consideration of the plasmonic structure offers the possibility to describe double layer of NPs with different size and volume fraction. This stratified structure is well adapted to account for different physical situations that can arise in the stack representation according to the type of applied elaboration method.

The dielectric properties of the Si-substrate were taken from [Palik, 1985] for the whole wavelength range, those of the SiO<sub>2</sub> layer from SOPRA Database [SOPRA Database, 1999] and the AgNPs dielectric function was calculated according Eq. IV.4 by using the optical properties of bulk silver [Palik, 1985]. As input parameters in the model we start with guesses for the thicknesses of different layers in the structure and the corresponding volume fractions of the NPs. After convergence of the model calculations the output parameters of the simulation are as listed in the Fig. IV.1 along with ellipsometric spectra ( $\tan(\Psi)$  and  $\cos(\Delta)$ ) in the 250 – 850 nm wavelength range, corresponding to the considered structure. These theoretical spectra were compared with experimental ellipsometric spectra.

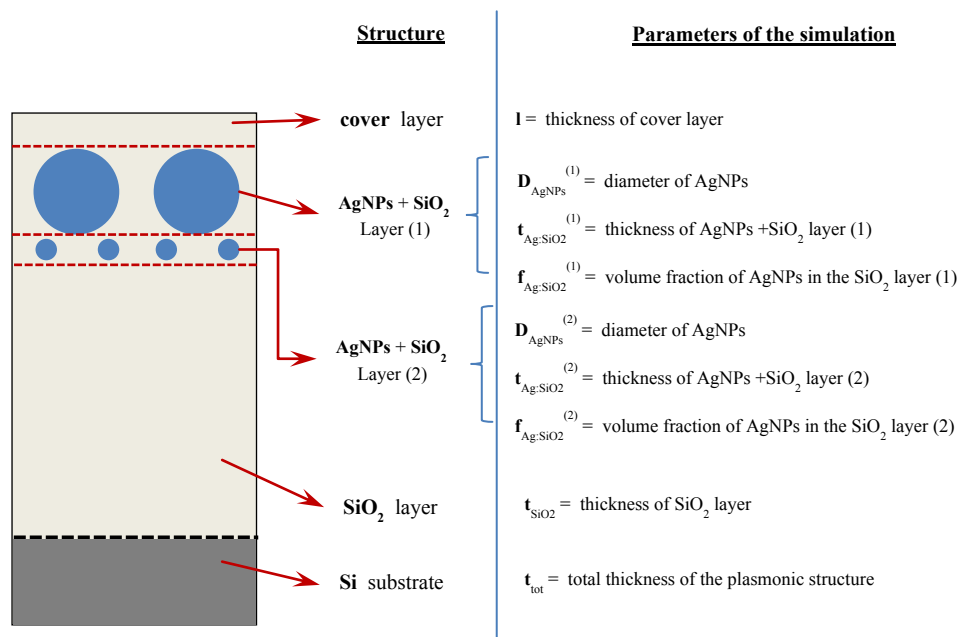


Figure IV.1: Schematic representation of the plasmonic structures and parameters issued from the model.

The developed numerical code runs on Matlab software [Matlab, 2012] and uses Abeles formalisms for calculations of the electric field in multilayer systems. More information on the basis and the adopted hypotheses is given elsewhere [Larivière et al., 1992; Poinsothe, 2006; M. Bayle, 2014].

The experimental ellipsometric spectra to compare with on a given plasmonic structure were acquired with a SOPRA GES5 spectroscopic ellipsometer in the wavelength range from 250 to 850 nm at incidence angle of 75°. Systematically the parameters of tested plasmonic structures obtained from modelling were compared with results extracted from TEM observations of the same samples.

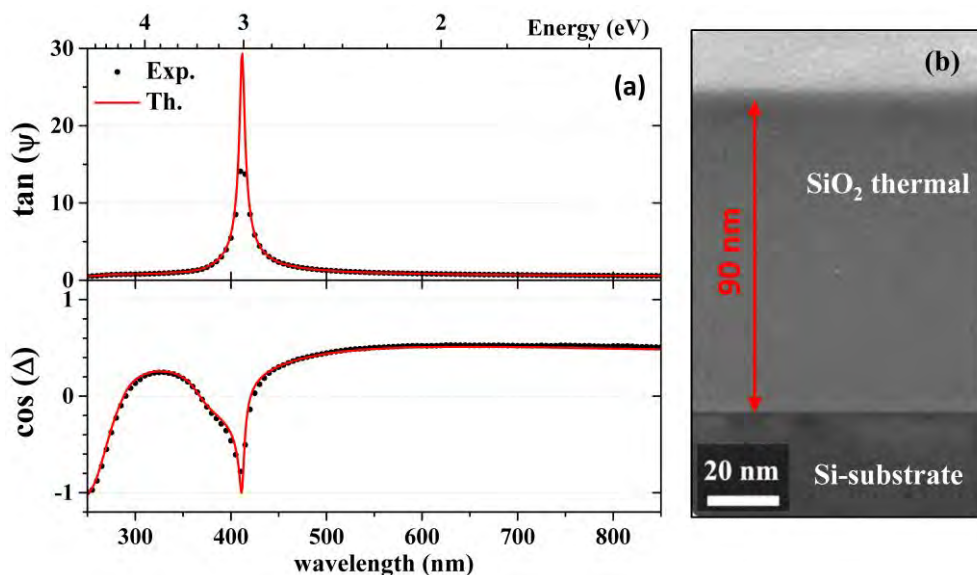


Figure IV.2: Benchmark of the model: (a) ellipsometric spectra of pristine SiO<sub>2</sub> layer grown on Si substrate as recorded experimentally (dots) and as obtained from modelling (red line), and (b) XSTEM Bright Field images of the pristine SiO<sub>2</sub> layer.

Before going further in the modeling of plasmonic substrates we have used a 90 nm thick SiO<sub>2</sub> layer grown on Si-substrate as a model benchmark. The obtained from modelling results are shown in Fig. IV.2 along with the experimentally recorded spectra. This test-sample approves the theoretical model and the selected numerical procedure. Several indicators are used to estimate the sensitivity and uniqueness of the model. The first estimate is related to quality of the comparison between the model-generated ellipsometric spectra and the experimentally obtained ones in the entire spectral range. Additional verification for the benchmark sample is performed by using the EMA model for ellipsometric spectra processing on the WinElli Software available by SOPRA [SOPRA Database, 1999]. The XS-TEM image of the studied benchmark sample is shown in Fig. IV.2(b) as complementary indicator for comparison of the obtained SiO<sub>2</sub> layer thickness.

## 5. Results and discussions

### 5.1. Advantages of the model describing the dielectric response of plasmonic structures

The advantage of using two different in their basic principles but complementary in terms of final solution physical methods to elaborate the plasmonic structures is above all the possibility to cover different architectures of the nanostructures, evolution of the size, density and shape of the AgNPs and the nanometric distance from the sample free surface.

Figure IV.3 represents the obtained from modelling and the experimentally recorded ellipsometric spectra on the implanted sample E1. The XS-TEM of this sample is also shown in the figure.

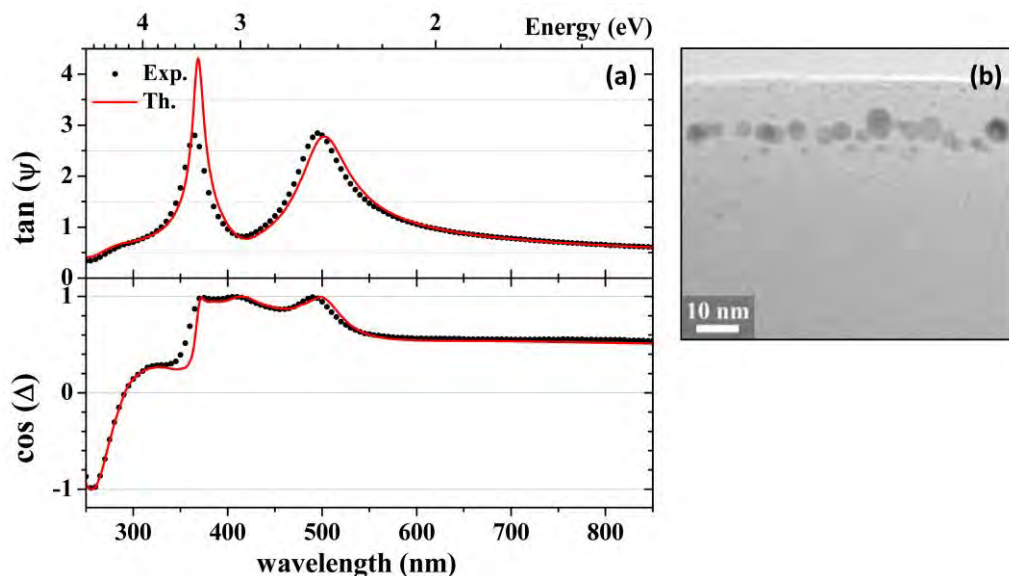


Figure IV.3: (a) ellipsometric spectra as recorded experimentally (dots) and as obtained from modelling (red line), and (b) XS-TEM Bright Field images of the implanted sample E1

The parameters of the plasmonic structure obtained from modelling and those extracted from the TEM-images processing are summarized in Table IV.4. A strong particularity of this sample E1 is the

presence of a second plane of AgNPs in-depth of the sample. In this case the constituent layers of the modeled structure are five, as represented in Fig. IV.1. This sample testifies for the appropriateness of the developed theoretical model with respect to the stratified structure comprising effective media with different size and volume fraction of the AgNPs. The represented plasmonic structure on Fig. IV.4 corresponds to the plasma deposited sample E3.

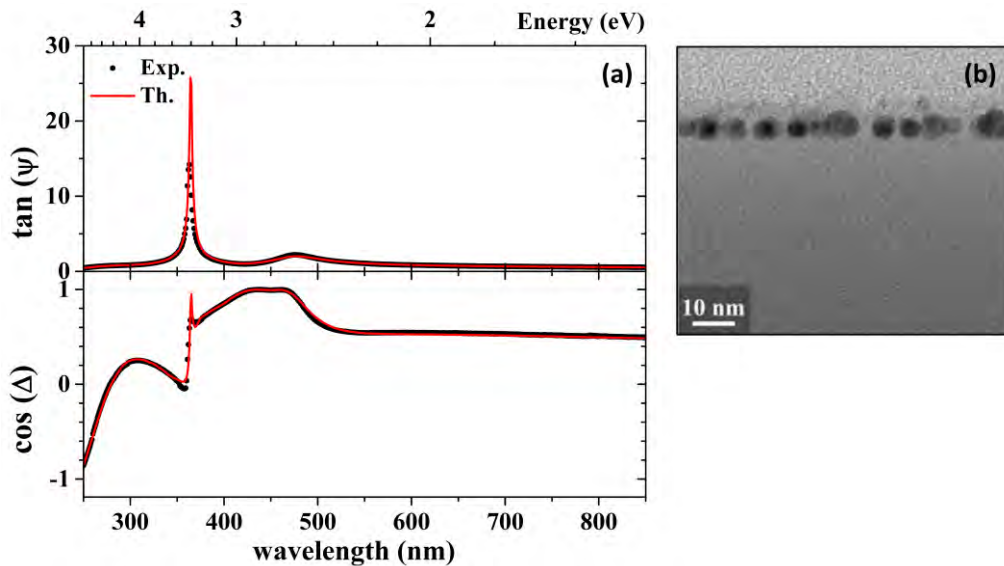


Figure IV.4: (a) ellipsometric spectra as recorded experimentally (dots) and as obtained from modelling (red line), and (b) XS-TEM Bright Field images of the plasma deposited sample E3.

The planarity of the AgNPs layer in this case allows for model-generated ellipsometric spectra identical to the experimentally recorded ones. The very slight waviness of the sample surface imposed by the plasma deposition method (Chapter III) does not lead to depolarization of the probe light in the entire wavelength range.

One can notice the excellent agreement between the parameters describing the two plasmonic structures (E1 and E3) obtained from modeling of the ellipsometric spectra and those extracted from TEM measurements (Table IV.4). The common point of these two examples is that their structural parameters completely satisfy the hypotheses of the Maxwell-Garnett approximation. The AgNPs are spherical in shape. They are well aligned in a plane so that they form a single layer in which the thickness of the effective media can be considered equal to the diameter of the AgNPs. The AgNPs volume fraction is small enough not to induce strong modification of the electromagnetic field and can be considered as perturbation only.

Table IV.4 Parameters describing the studied samples E1 and E3 as obtained from ellipsometry and TEM.

Parameters	Sample E1		Sample E3	
	SE	TEM	SE	TEM
Cover layer thickness - l (nm)	7.0	7.0 ± 2.0	5.0	4.7 ± 0.5
Layer 1: thickness - $t_{\text{Ag:SiO}_2}^{(1)}$ (nm)	9.0	10.0 ± 0.5	6.0	6.0 ± 0.3
AgNPs size - $D_{\text{AgNPs}}^{(1)}$ (nm)	9.0	7.0 ± 2.0	6.0	6.0 ± 1.0
Volume fraction of AgNPs - $f_{\text{Ag:SiO}_2}^{(1)}$	0.13	0.13	0.17	0.16
Eccentricity - $e_e$	n/a	0.35	n/a	0.36
Layer 2: thickness - $t_{\text{Ag:SiO}_2}^{(2)}$ (nm)	4.0	4.1 ± 0.5	n/a	n/a
AgNPs size - $D_{\text{AgNPs}}^{(2)}$ (nm)	4.0	3.2 ± 0.9	n/a	n/a
$f_{\text{Ag:SiO}_2}^{(2)}$	0.042	0.012	n/a	n/a
Silica layer thickness - $t_{\text{SiO}_2}$ (nm)	75.0	69.0 ± 3.0	75.5	76.0 ± 4.0
Total thickness of the structure - $t_{\text{tot}}$ (nm)	95.0	90.0 ± 5.0	86.5	87.0 ± 4.0

## 5.2. Critical assessment of the applicability of the model

Departure from the hypotheses of the Maxwell-Garnett approximation leads to a strong discrepancy between the model-generated and the experimentally obtained ellipsometric spectra. This is demonstrated on Fig. IV.5 for the implanted sample E2 and on Fig. IV.6 for the plasma deposited sample E4.

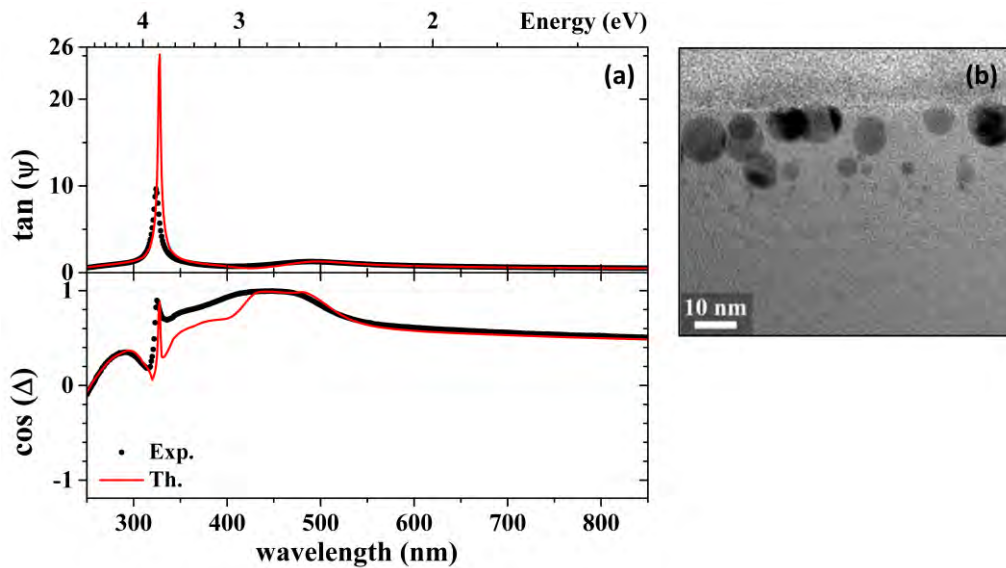


Figure IV.5: (a) ellipsometric spectra as recorded experimentally (dots) and as obtained from modelling (red line), and (b) XS-TEM Bright Field images of the plasma deposited sample E2.

The discrepancy occurs mainly in the wavelength range around 400 nm where the surface plasmon resonance response is detected. It results from dispersion of AgNPs in a band that cannot be represented by one or two layers of aligned AgNPs for the implanted sample E2 and from the evolution in shape of the AgNPs from spherical to prolate spheroid for the plasma deposited sample E4. Additional reason is the large size-distribution of AgNPs for both samples (E2 and E4).

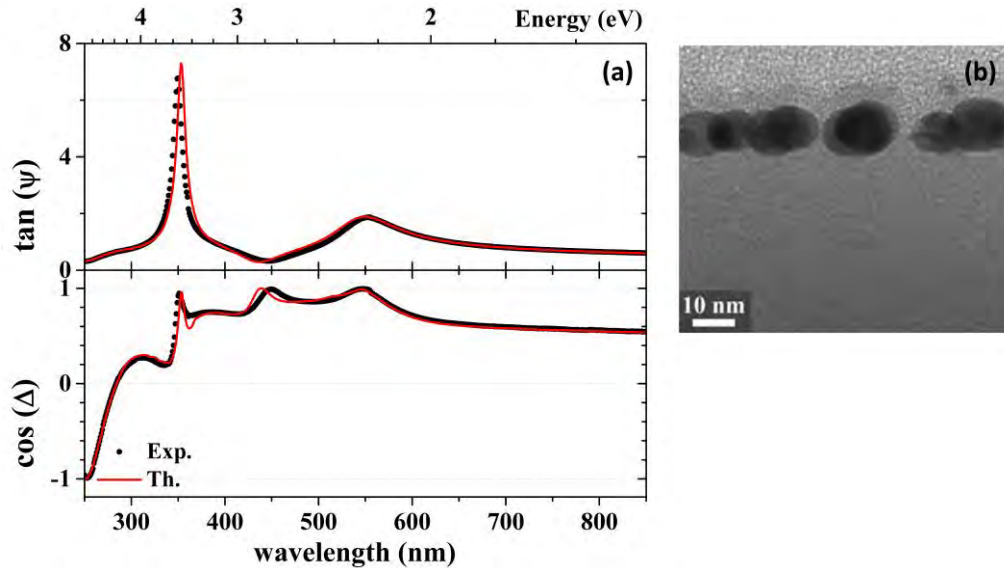


Figure IV.6: (a) ellipsometric spectra as recorded experimentally (dots) and as obtained from modelling (red line), and (b) XS-TEM Bright Field images of the plasma deposited sample E4.

The parameters describing samples E2 and E4 obtained from modelling the ellipsometric spectra and those extracted from TEM images are given in Table IV.5. The largest error stems from the AgNPs size as obtained from SE and TEM measurements which prevents from correct description of the thickness and dielectric function of the effective media and further reflects on the calculation of the thickness of SiO<sub>2</sub> layer on which the AgNPs rely. Additional error results from the poor calculation of the SiO<sub>2</sub> cover layer thickness. Finally, some of the errors accumulate to arrive to more than 10% difference in the total thickness as for the sample E4 or compensate as for sample E2 but the uniqueness of the solution is not guaranteed.

Eccentricity-based statistical analysis of the two implanted samples (E1 and E2) and the two plasma deposited samples (E3 and E4) based on TEM-images processing gives additional information on the influence of AgNPs shape evolution and the AgNPs size distribution on the theoretical model hypotheses. The analysis was performed on a large ensemble of AgNPs and is shown in Fig. IV.7 for the four samples. At least 1100 AgNPs have been considered for each sample. Different levels of eccentricity refer to different shapes of the NPs starting from zero for spherical NP and evolving to 0.8 for a spheroid shape for which the minor axis is 40% smaller than the major axis.



Table IV.5 Parameters describing the studied samples E2 and E4 as obtained from ellipsometry and TEM

Parameters	Sample E2		Sample E4	
	SE	TEM	SE	TEM
Cover layer thickness - $l$ (nm)	0.5	$5.0 \pm 4.0$	5.0	$5.6 \pm 0.4$
Layer 1: thickness - $t_{\text{Ag:SiO}_2}^{(1)}$ (nm)	9.0	$18.0 \pm 2.0$	12.0	$13.0 \pm 1.0$
AgNPs size - $D_{\text{AgNPs}}^{(1)}$ (nm)	9.0	$8.0 \pm 2.0$	12.0	$7.9 \pm 4.0$
Volume fraction of AgNPs - $f_{\text{Ag:SiO}_2}^{(1)}$	0.169	0.10	0.211	0.20
Eccentricity - $e_e$	n/a	0.37	n/a	0.45
Layer 2: thickness - $t_{\text{Ag:SiO}_2}^{(2)}$ (nm)	4.0	$6.8 \pm 0.7$	n/a	n/a
AgNPs size - $D_{\text{AgNPs}}^{(2)}$ (nm)	4.0	$3.2 \pm 0.8$	n/a	n/a
$f_{\text{Ag:SiO}_2}^{(2)}$	0.19	0.08	n/a	n/a
Silica layer thickness - $t_{\text{SiO}_2}$ (nm)	60.5	$47.0 \pm 2.0$	74.5	$83.0 \pm 4.0$
Total thickness of the structure - $t_{\text{tot}}$ (nm)	74.0	$72.0 \pm 4.0$	91.5	$102.0 \pm 5.0$

The excellent agreement between theoretical and experimental ellipsometric spectra is observed for plasmonic structures (samples E1 and E3) containing AgNPs with shape close to spherical one. The permitted level of eccentricity of AgNPs is limited to 0.4 in order to fulfill the hypotheses of Maxwell-Garnett approximation. Moreover, the size distribution of AgNPs should be quite narrow. Large size distribution of AgNPs leads to ill-defined effective dielectric permittivity of the corresponding layer.

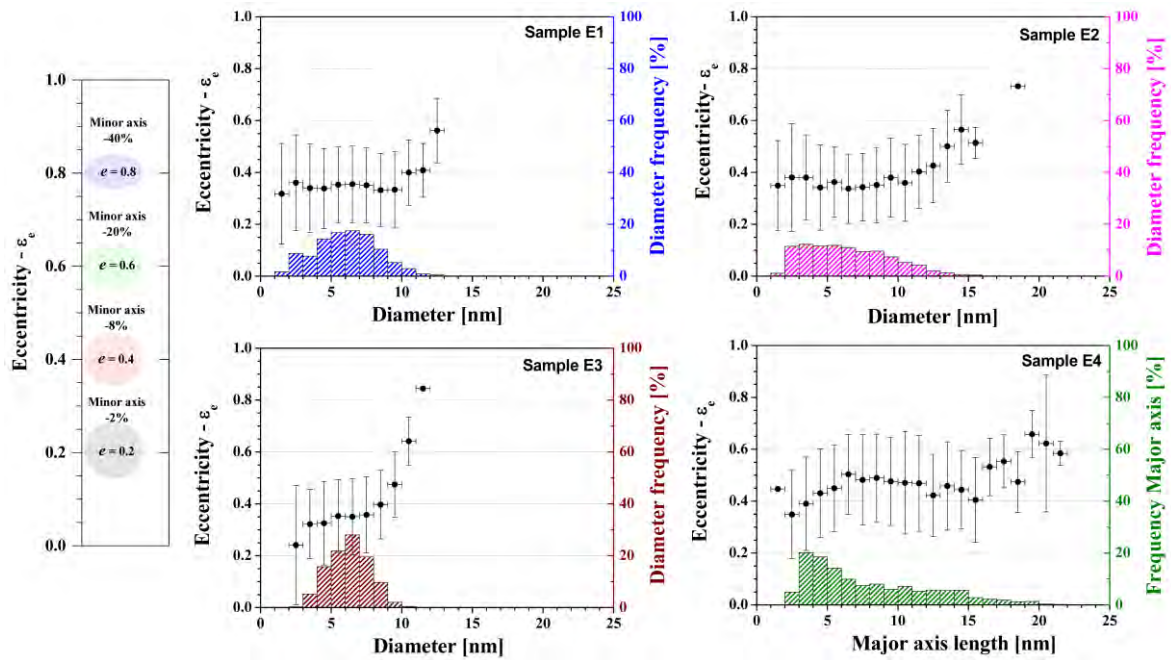


Figure IV.7: Eccentricity of the AgNPs in the studied samples: implanted samples E1 and E2, and plasma deposited samples E3 and E4. Analysis based on minimum 1100 AgNPs per sample. Left panel: evolution of the NPs shape for different eccentricity levels.

When the large size distribution is accompanied by eccentricity level over 0.4, the error accumulation in the calculated ellipsometric spectra leads to a large discrepancy of the obtained parameters of plasmonic structures compared to TEM observations although the mean square error (MSE) that quantifies the difference between theoretically obtained and experimentally recorded spectra remains small like in the case of sample E4.

## **6. Conclusions**

The results presented in this Chapter concern the development, test and application of a fully predictive model appropriate for interpretation of ellipsometric spectra recorded on plasmonic structures. The model is based on the quasistatic approximation of the classical Maxwell-Garnett formalism, however accounting for the electronic confinement effect through the damping parameter. It is found that excellent agreement between theoretically calculated and experimentally recorded spectra can be achieved for quasi-spherical AgNPs with volume fraction in the host matrix up to 15-17%. Additionally, a narrow size distribution of the AgNPs is required in order to allow representation of the thickness of the effective media layer by the diameter of the AgNPs. Eccentricity-based statistical analysis of the samples shows that a level of 0.4 of the eccentricity of AgNPs should not be exceeded in order to remain in the frame of Maxwell-Garnett approximation.

Further improvement of the theoretical model with respect to correlation with experimentally recorded spectra will be performed. In particular, the results interpretation will be related to the theoretical model sensitivity. This includes calculation of the mean square error (MSE) curve that quantifies the difference between model and experience for all regressed quantities. Other indicators to consider will be the figure of merit (or 90% confidence limit), two-parameters correlation to indicate the independency nature of any two fit parameters. Moreover, the uniqueness test of the model will be performed to guarantee the less than 10% Unique Range which spans above and below the best fit that provide 10% variance on the global MSE minimum when compare theoretical and experimental ellipsometric spectra.





# Chapter V: Assessing bio-available silver released from silver nanoparticles embedded in silica layers using the green algae *Chlamydomonas reinhardtii* as bio-sensors

---

## 1. Introduction

Because of their antimicrobial properties, the silver nanoparticles (AgNPs) have the potential to impact on human health and environmental equilibrium. These issues have been addressed by no less than 25 reviews during the period 2008-2015 [Hansen and Baun, 2012; Reidy et al., 2013; Haider and Kang, 2015; Le Ouay and Stellacci, 2015].

The biological activity of AgNPs is twofold. It is either closely related to the activity of ionic Ag ( $\text{Ag}^+$ ) and the AgNPs themselves resulting in protein denaturation at different cell locations; specially sensible are those enzymes of the respiratory chain and transport channels [Holt and Bard, 2005; Despax et al., 2011]. The development of reliable diagnostic methods for evaluating the biological activity of AgNPs, and to disentangle the contribution of the silver ions and silver nanoparticles to the whole antibacterial effect of AgNPs [Agnihotri et al., 2013], would be an asset for the appropriate design and use of silver-based nanotechnologies.

The modulation of the silver ion release from AgNPs would eventually allow the release of the appropriate dose of  $\text{Ag}^+$  for biomedical uses and protecting thus the environmental equilibrium [Liu et al., 2010; Sabella et al., 2014]. One of the methods to control Ag release from AgNPs is by their inclusion in nanocomposite materials. The host matrices can stabilize AgNPs and at the same time allow a controlled release of ionic silver and or AgNPs to inhibit the microbial colonization and biofilms formation for biological and medical applications [Despax et al., 2011; Beer et al., 2012; Alissawi et al., 2013].

In this chapter, we propose an original method for assessing the release and biocide activity of silver released from AgNPs embedded in silica ( $\text{SiO}_2$ ) matrix submersed in water. It is based on the photosynthesis of the green alga *Chlamydomonas reinhardtii* used as a sensible and reliable sensor of ionic silver. This unicellular alga with well-known genetics is a simple model of eukaryotes [Merchant et al., 2007] and extensively applied for toxicity tests. During the last years, this alga has been used as a bio-sensor for measuring the dissolved silver released from silver nanoparticles, under realistic exposure scenarios [Navarro et al., 2008b; Navarro et al., 2015].

The two physical approaches were applied to elaborate the nanocomposite structures (previous Chapters): (i) low energy ion beam synthesis and (ii) combined silver sputtering and plasma polymerization allow fabricating of a single layer of AgNPs embedded in thin silica films at controlled nanometric distance beneath the free surface. To relate the silver release from the elaborated structures with their microbial activity, the structural and optical properties of the resulting composite layers were studied by Transmission Electron Microscopy (TEM) and by optical reflectance, respectively. The silver release was measured through Inductively Coupled Plasma-Mass Spectrometry (ICP-MS). The short-term toxicity of AgNPs to photosynthesis in *Chlamydomonas reinhardtii* was studied using fluorometry. The working hypothesis is the following: the amount of biologically active silver (bio-available  $-\text{Ag}_{\text{bioav}}^-$ , and operationally defined as that provoking effect on the algal photosynthesis mechanism) would mainly depend on both the density of silver nanoparticles and their in-depth location below the free surface. The role of the host silica matrix in the process of silver release is discussed as well.

## 2. Experimental

### 2.1. Synthetic procedures

The samples used for this study, and the conditions for their elaboration, have been described in the previous Chapters. To recall the structures we will say that these contain a single layer of AgNPs embedded in silica layers at a controlled distance from the free surface elaborated by two physical methods: ion implantation and plasma deposition process. For clarity of presentation the samples elaborated by ion implantation are called hereafter “implanted samples” and labelled E1 and E2. The elaboration of these samples has been described in details in a past work [Benzo et al., 2013] and recalled in Chapter I (section 2.3.3) and Chapter IV. The layers have been implanted at fixed energy  $E$  of the  $\text{Ag}^+$  ions and with two ion doses  $\phi$  (see Table V.1).

Table V.1: Parameters used to elaborate the samples by ion implantation.

Sample	$\text{Ag}^+$			
	Implantation conditions			
	Energy, $E$ [keV]	Dose, $\phi$ [ $10^{16}$ ions/cm $^2$ ]	Density current, $I$ [ $\mu\text{A}$ ]	Time, $t$ [hours]
<b>E1</b>	10	0.715	5	4.5
<b>E2</b>	10	3.8	5	22

The ion density current plays a key role for the silver diffusion in the silica matrix and has been fixed to 5  $\mu\text{A}$  for all the implantations. As mentioned in Chapter I, under these conditions the nucleation of the AgNPs takes place during the implantation process without the need of any annealing step. These two samples present a quasi 2D array of AgNPs, with similar mean diameter and surface density and therefore a similar initial Ag amount in the NPs. The main difference consists in the distance of the AgNPs from the free surface, which slightly increases when increasing the implantation dose. The experimental conditions for their elaboration are summarized in the Table V.1. To recover the matrix damage and protect the AgNPs from fast oxidation (Benzo et al., 2011) a post-implantation rapid-thermal-annealing was carried out under  $\text{N}_2$  atmosphere at  $500^\circ\text{C}$  for 30 minutes. The choice of the annealing time and temperature was restricted as to maintain unchanged the AgNPs size distribution and their position inside the  $\text{SiO}_2$  matrix.

Table V.2: Parameters used to elaborate AgNPs by sputtering deposition process (PVD).

Sample	Ag deposition conditions (PVD step)				
	Applied Power, $P$ [W]	Self-bias Voltage, $V_{dc}$ [V]	Ar pressure, $p$ [Pa]	Ar flow, [sccm]	Time, $t$ [sec]
<b>E4</b>	10	- 390	5.2	2.8	30
<b>E5</b>	80	- 995	5.2	2.8	5

Table V.3: Parameters used to elaborate the  $\text{SiO}_2$  plasma layer by PECVD.

Sample	$\text{SiO}_2^{\text{Plasma}}$ deposition conditions (PECVD step)								
	Applied Power, $P$ [W]	Self-bias Voltage, $V_{dc}$ [V]	Total Pressure, $p_{tot}$ [Pa]	Ar flow [sccm]	$\text{O}_2$ flow [sccm]	HMDSO injection time, $t_{on}$ [sec]	HMDSO period, $T = t_{on} + t_{off}$ [sec]	HMDSO average flow [sccm]	Time, $t$ [sec]
<b>E4</b>	120	- 880	7.68	2.8	1.25	3.1	5	0.25	30
<b>E5</b>									

The second type of used samples are those prepared by plasma deposition process and called “plasma deposited samples”. These are samples E4 and E5. A change in the plasma operation conditions for silver sputtering time was made in order to obtain even bigger AgNPs than those used in Chapter IV. The conditions for elaboration of the SiO<sub>2</sub> plasma cover layer were the same as in Chapter IV. To avoid any misleading the plasma operation conditions for elaboration of samples E4 and E5 are given in Tables V.2 and V.3.

## 2.2. Structural and optical characterization of the nanocomposite layer

Microscopy imaging was performed using a field emission Transmission Electron Microscope, FEI Tecnai™ F20 microscope operating at 200 kV, equipped with a spherical aberration corrector dedicated for high quality High Resolution Electron Microscopy (HREM) images with an increased signal/noise ratio and nearly no delocalization effect at surfaces and interfaces. To achieve observation, specimens transparent to electrons have been prepared in accordance with the standard procedure, *i.e.*, mechanical polishing and Ar<sup>+</sup> ion milling in both cross-section (XS) and plan view (PV) configurations. The former configuration is used for the accurate measurement of the position of AgNPs with respect to the free surface while the later one allows measurement of the total Ag-amount contained within the NPs by deduction from their size-distribution and surface density.

Optical reflectance spectra of the samples were recorded using a Cary 5000 UV-visible spectrometer to check the evolution of the LSPR resonance that is expected around 410 nm for spherical AgNPs embedded in silica. Moreover the choice of the thickness of the nanocomposite layer around 90 nm provides antireflective conditions in the UV-visible range. The combination of these two effects results in a “plasmonic interference” phenomenon that has been shown to be very sensitive to small changes in the optical path of the nanocomposite layer [Carles et al. 2011, Cacciato et al., 2015].

## 2.3. Experimental procedure for silver release assessment

To evaluate the silver release, we have followed the procedure schematized in Fig. II.18 of Chapter II. In a first step, we introduce 6ml of 10mM 3-morpholinepropanesulfonic acid (MOPS) solution at adjusted

pH = 7.5 (buffered water) in each one of three flasks. The buffered water was prepared in accordance with the procedure given in reference Navarro et al., 2008b. We use one of the flasks as negative control (black flask - control). In the second flask we add an appropriate amount of silver nitrate salt (AgNO<sub>3</sub>) (blue flask - control Ag<sup>+</sup>) dissolved in pure water. This flask is used to follow the toxicity effect of a well-known amount of dissolved silver (Ag<sup>+</sup> ions) on the algae. Under the adopted experimental conditions, the AgNO<sub>3</sub> is completely dissociated [Navarro et al., 2008b]. In the third flask we add a solid sample with AgNPs embedded in thin silica layers (red flask - AgNPs). In order to compare the different samples, the same surface (4 cm<sup>2</sup>) of samples is used in all cases. All flasks are gently shaken at 90 rpm at room temperature in the dark. In order to improve the silver release from

the samples, immersion duration of 20 h was chosen as it has been shown in the literature that the most important delivery of silver takes place during the first 24 h of immersion [Saulou et al., 2009]. In a second step we remove the solid sample from the solution and take 2 ml from each flask for ICP-MS measurements to evaluate the total amount of silver in solution. In a third step, we add algae in the 3 mL of solution left up to a concentration of 0.15 O.D.<sub>685</sub> (O.D.<sub>685</sub> stands for optical density at wavelength 685 nm). More details are given in Chapter II (section 6).

After one hour of the algae exposure, we perform the fluorometry measurements on 2 ml of solution. To ensure normal activity of algae, the solution was kept under continuous illumination of 65  $\mu\text{Mol photons s}^{-1}\text{cm}^{-1}$ . To avoid the algae aggregation and sedimentation, the solution was continuously shaken at 90 rpm during the experiment.

#### **2.4. Inductively Coupled Plasma–Mass Spectrometry measurements**

Analysis of  $^{107}\text{Ag}$  was carried out with a quadrupole ICP–MS instrument (Agilent 7500), equipped with a babington nebulizer and a double pass spray chamber. Samples were evaporated in a hot plate and re-dissolved in 2 ml  $\text{HNO}_3$  1%, transferred to polyethylene vials and maintained at 4°C until ICP-MS analysis. The linear calibration curve was adopted between 0.003 and 5  $\mu\text{M}$  Ag in 10 mM MOPS (buffered at pH = 7.5) to account for any matrix effect. It was prepared from TraceCERT® Ag standard solution for ICP (1000 mg/l) (Fluka Analytical) and the same procedure as for samples (evaporation and re-dissolution in  $\text{HNO}_3$  1%) was followed before measurement in the ICP. The calibration curve was recorded at every measuring sequence. Important instrumental settings, like plasma position, radiofrequency power, nebulizer gas flow, and lens voltage were carefully optimized before analysis.

#### **2.5. Algal culture**

*Chlamydomonas reinhardtii* culture was prepared according to the procedures described in reference [Le Faucheur et al., 2005]. *Chlamydomonas reinhardtii* shows a good absorption in the red part of light spectrum around 685 nm [Berberoglu et al., 2008]. In short, experimental batch cultures were prepared by transferring an inoculum of algae (approx.  $1 \times 10^5$  cells/mL with an O.D.<sub>685</sub> 0.05) to fresh growth media [Le Faucheur et al., 2005]. Algae were grown during 72 h until reaching exponential growth phase at 25°C with continuous illumination of 120  $\mu\text{Mol photons s}^{-1}\text{cm}^{-1}$  (Philips Coolwhite TLD 15W fluorescent lamps) and shaken at 90 rpm. Experimental cell densities ( $6 \times 10^5$  cells/mL, 0.15 O.D.<sub>685</sub>) were obtained by centrifuging (1500 g, 10 min) and then resuspending the cell pellet in the appropriate volume of 10 mM MOPS (adjusted to pH = 7.5).

#### **2.6. Fluorometry measurement**

The algal photosynthetic yield of the photosystem II in light was measured by fluorometry using a PHYTO-PAM (Heinz Walz GmbH) equipped with an Optical Unit ED-101US/MP. This parameter

reflects the efficiency of the photochemical energy conversion process [Schreiber et al., 1995]. Each fluorometry experiment was repeated twice and three fluorometry measurements were taken for each experimental condition. Photosynthetic yield measured by fluorometry was not affected by the algal translocation into MOPS (for details see references Navarro et al., 2015 and Navarro et al., 2008b).

### 3. Results and discussion

#### 3.1. Structural analysis: silver reservoir in nanocomposite layer

The structural characteristics of the samples (size distribution, location and density of the AgNPs, silver amount, *etc.*) have been analyzed by TEM. Figure V.1 shows Bright Field TEM and HREM images of a typical elaborated structure. These images refer to sample E1. In the cross-section view shown in Fig. V.1a it is possible to distinguish two important zones for our study: (i) the nanometric layer of AgNPs embedded in SiO<sub>2</sub> and (ii) the nanometric SiO<sub>2</sub> cover layer. Figure V.1b represents plan-view of the same sample. HREM image (Fig. V.1c) of an isolated particle shows interplanar distance of 2.36 Å characteristic of Ag (111) planes. This verification appears necessary for all samples in order to know the initial state of the AgNPs before their immersion in solution and following interaction with algae.

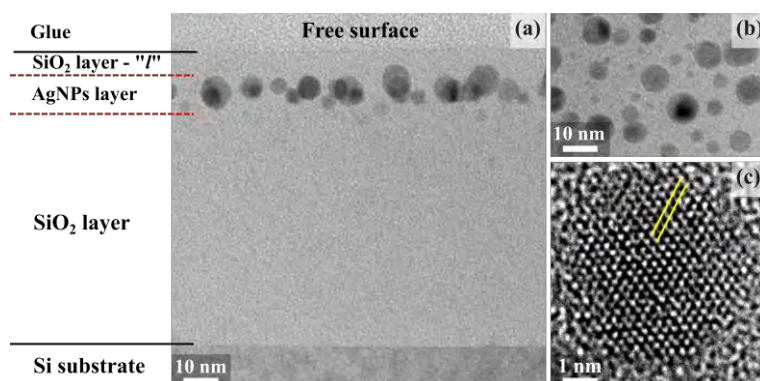


Figure V.1: (a) XS-TEM and (b) PV-TEM Bright Field images of the implanted sample E1 describing the typical architecture of the samples. (c) HREM image of an isolated nanoparticle oriented following (110) zone axis.

TEM observations reveal that the selected experimental conditions for sample synthesis lead to formation of: (i) spherical-like AgNPs covered by a flat thin dielectric silica layer for the implanted samples (Fig. V.2a-b, e-f) and (ii) prolate spheroid AgNPs with a conformal silica cover layer for the deposited samples (Fig. V.2c-d, g-h). These results are in accordance with the enlarged capacities of the two physical elaboration methods to control the parameters of the embedded AgNPs and the characteristics of the silica cover layer. The ion implantation process preserves the composition of the host matrix and respects the planarity of the surface (Fig. V.2a-b). The plasma deposition processes are known to be conformal to the surface on which the layer is deposited. This surface conformity

allows coatings of patterned substrates. In this study, as the plasma deposited SiO<sub>2</sub> cover layer is very thin, it envelops the AgNPs and spreads between them, finally imposing a slight waviness on the surface (Fig. V.2c-d).

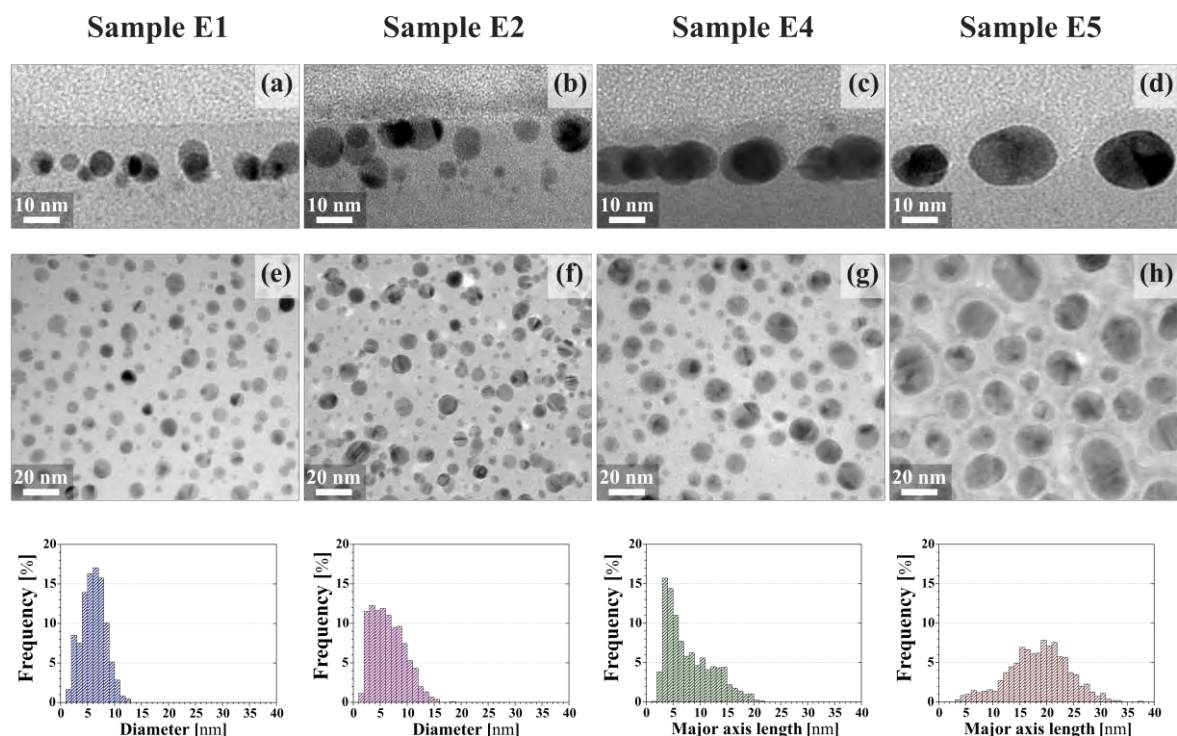


Figure V.2: (a)-(d) Bright Field XS-TEM zooming on the upper part of the nanocomposite layers and (e)-(h) PV-TEM images of the samples exploited for silver release measurement and associated size-distribution.

From the PV-TEM images we have determined on more than 1000 AgNPs the size-distribution (Fig. V.2), the mean size and the surface density. The obtained results are summarized in Table V.1. For the implanted samples, we observe similar AgNPs mean diameter with different doses, 6.1 nm and 6.5 nm for samples E1 and E2, respectively, and a similar surface density of AgNPs (Fig. V.2e-f). When increasing the dose, a saturation of the quantity of implanted Ag is indeed observed due to sputtering effects and Ag diffusion towards the surface, as reported earlier [Benzo et al., 2013]. This saturation effect is accompanied by localization of the AgNPs closer to the free surface. In both samples E1 and E2, some small AgNPs are also formed slightly deeper in the silica layer in the tail of the rather wide implanted ion profile. The implanted sample with the lower dose (sample E1), *i.e.*, during the shortest implantation time (Table V.1), presents a size-distribution in good agreement with the theoretical distributions predicted by the Lifshitz–Slyosov–Wagner (LSW) theory for Ostwald ripening, as observed in a previous work [Carles et al., 2009]. When increasing the implanted dose and thus the implantation time (sample E2), the size histogram evolves towards a log-normal distribution. This evolution is related to the system’s memory loss of initial nucleation and growth processes, which take



place for no uniform solute concentration (*e.g.* implantation) [Espiau de Lamaestre and H. Bernas, 2006].

Concerning the plasma deposited samples (samples E4 and E5), the major axis length of the observed prolate spheroid AgNPs increases, scaling up from 7.9 nm to 18.5 nm (Fig. V.2g-h). This behavior is explained by the respective role of the injected power in the gas discharge and the sputtering time on the formation and organization of AgNPs, when shifting from low-injected power for long time (Fig. V.2g) to high-injected power for short time (Fig. V.2h) (Table V.2). Moreover, the distribution of the AgNPs size population evolves from log-normal (sample E4) to normal (Gaussian) one (sample E5). The log-normal distribution of AgNPs cannot be simply explained on the basis of nucleation and pure growth mechanisms during the deposition process. Most likely, the Ostwald ripening also takes place when the AgNPs are deposited at low injected power in the plasma for longer times. The AgNPs size increase is accompanied here by surface density decrease (Table V.3). This effect is a direct consequence of the increased injected power in the plasma. Scaling up the injected power to such a high level imposes an increase of the self-bias voltage to almost 1 kV (Table V.2) which impacts the deposition of AgNPs in two ways. It leads (*i*) to a strong intensification of the flow of sputtered Ag-atoms increasing thus the rate of pure growth of AgNPs and (*ii*) to a rise of the mean energy of both main categories of species in the plasma, electrons and heavy particles (ions, excited and ground state atoms), which means that the Ag-atoms arrive at the sample surface with higher kinetic energy determining a higher surface diffusion to favor nucleation and growth mechanisms of AgNPs.

For an accurate description of the silver release process, we have introduced three characteristic parameters of the AgNPs assemblies that can play a significant role in the Ag<sup>+</sup> release when the samples are immersed in solution. The first one is the maximum amount of silver in the silica layer (“initial Ag reservoir”)  $K$  in molar unit.

Considering each nanoparticle as a prolate spheroid (sphere being a particular case where the two axes are equal) the total Ag mass per unit surface ( $G_{Ag}$ ) stored inside the AgNPs for each sample can be evaluated from the following expression:

$$G_{Ag} = \frac{\rho_{Ag}}{S} \frac{\pi}{6} \sum_i B_i C_i^2 \quad (\text{V.1})$$

where  $\rho_{Ag}$  is the silver density,  $B_i$  is the major and  $C_i$  is the minor axis length of each AgNP, and  $S$  is the total surface of the analyzed image. Hence, one can calculate the initial Ag reservoir as the maximum amount of releasable silver if all the AgNPs are completely dissolved in the solution. Considering the total Ag mass per unit surface,  $G_{Ag}$  and the total surface ( $4 \text{ cm}^2$ ) of each sample immersed in 6 mL of MOPS, we estimate this initial Ag reservoir  $K$  in molar units. Owing to the elaboration conditions  $K$  increases from sample E1 to sample E5 by a factor of three (Fig. V.3b and Table V.3).

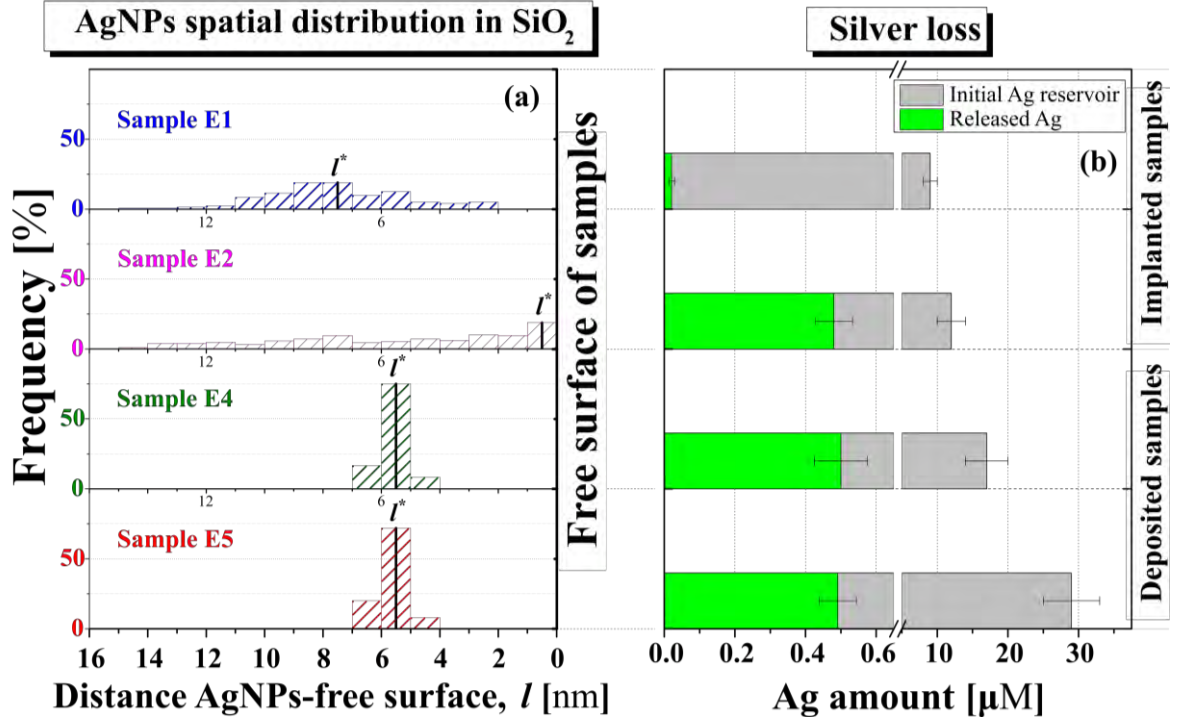


Figure V.3: (a) Spatial distribution of the AgNPs with respect to the free surface (distance  $l$ ) for each sample; the most probable distance  $l^*$  is indicated; (b) Initial Ag reservoir (grey bar) and released silver (green bar) for each sample.

The second parameter to be estimated from size and surface density measurements is the total surface of AgNPs, called  $M$ . Owing to the synthesis conditions  $M$  is similar for samples E2, E4 and E5 (see Table V.3).

Finally, the third essential parameter extracted from the XS-TEM images is the distance  $l$  separating each AgNP from the free silica surface (Fig. V.1a). To characterize the AgNPs spatial dispersion in SiO<sub>2</sub> layer we evaluate the average distance  $l_{mean}$  and the most probable distance  $l^*$ . The latter is defined as the distance where the greatest number of particles ( $N_{MAX}$ ) are located. In the case of implanted samples, we observe a non-negligible spatial distribution of the AgNPs in the layer (Fig. V.3a). The small satellite AgNPs that are formed below the main layer are neglected in the procedure, being far from the surface and containing a very small Ag amount. The values  $l_{mean}$  are 7.4 nm and 5.3 nm for samples E1 and E2, with a standard deviation  $\sigma$  of 2.4 nm and 4.2 nm, respectively. This spatial dispersion simply reflects the width of the implantation profile. As shown in Fig. V.3a where the histograms of distances (with a step of 1 nm) are reported, the values  $l^*$  are 7.5 nm and 0.5 nm for sample E1 and E2, with  $N_{MAX}$  equal to 19.0% and 18.8% of the total number of NPs, respectively (Fig. V.3a). In spite of a large spatial dispersion of AgNPs for sample E2, a consistent number of NPs are located just under the free surface. On the contrary, for the plasma deposited samples that have conformal cover layer, the dispersion of the distances is reduced (Fig. V.3a). The values of  $l_{mean}$  are 5.6 nm and 5.7 nm for sample E4 and E5, respectively, with a standard deviation  $\sigma$  of 0.4 nm for both

samples. Moreover, the most probable distance  $l^*$  is identical for these two samples and equals to 5.5 nm, *i.e.*, very close to the averaged value, with  $N_{\text{MAX}}$  that overcomes 70 % (Fig. V.3a). This is a proof of the good reproducibility in terms of deposition of the SiO<sub>2</sub> cover layer, whatever the size and shape of AgNPs.

Table V.3: AgNPs characteristics directly measured on TEM images (mean size, density, average distance and the most probable distance to the free surface) and deduced from these values (total AgNPs surface, initial Ag reservoir). The released silver measured by ICP-MS is also given. The percentage refers to the initial Ag reservoir  $K$ .

Structural Characteristics	Implanted samples		Deposited samples	
	E1	E2	E4	E5
Mean size [nm]	6.1	6.5	7.9	18.5
St. Dev. of size-distribution [nm]	2.2	3.0	4.3	5.6
AgNPs surface density [ $10^{11}$ NPs/cm <sup>2</sup> ]	$10.4 \pm 0.7$	$10.1 \pm 0.8$	$6.9 \pm 0.4$	$1.7 \pm 0.2$
Average distance AgNPs-free surface, $l_{\text{mean}}$ [nm]	7.4	5.3	5.6	5.5
St. Dev. of the average distance, $\sigma$ [nm]	2.4	4.2	0.4	0.4
The most probable distance AgNPs-free surface, $l^*$ [nm]	7.5	0.5	5.5	5.5
Total AgNPs surface, $M$ [cm <sup>2</sup> ]	$4.7 \pm 0.5$	$5.4 \pm 0.5$	$5.6 \pm 0.6$	$5.7 \pm 0.6$
Initial Ag reservoir, $K^a$ [ $\mu\text{M}$ ]	$9 \pm 1$	$12 \pm 2$	$17 \pm 3$	$29 \pm 4$
Released silver <sup>b</sup> [ $\mu\text{M}$ ]	0.021 (0.2%)	0.491 (4.1%)	0.500 (2.9%)	0.480 (1.7%)
St. Dev. of the released silver [ $\mu\text{M}$ ]	0.008	0.053	0.075	0.053

<sup>a</sup> The initial Ag reservoir  $K$  can be considered as the maximum amount of releasable silver if all the AgNPs are completely dissolved in the solution.

<sup>b</sup> The detection threshold of ICP-MS measurement of released silver is 0.003  $\mu\text{M}$ .

The above described characteristic parameters ( $K$ ,  $M$ ,  $l_{\text{mean}}$  and  $l^*$ ) are listed in Table V.3 for the four analyzed samples. The precision on size and distance values, near 5%, is linked to the magnification uncertainty in conventional TEM.

## 3.2. Silver release in water

### 3.2.1. ICP-MS analysis

The measurements of the Ag amount released in solution were performed by ICP-MS and the results are reported in Table V.3. Two lessons can be learned from these data. First, for the plasma deposited samples E4 and E5, which present a low dispersion of distances, identical values of  $l^*$  (Fig. V.3a) and similar values of  $M$  (see Table V.3), the final Ag release is rather identical (Fig. V.3b), independently of their initial Ag reservoir,  $K$  (E5 contains 74 % more Ag atoms per unit surface compared to E4).

Second, for the implanted samples, although  $M$  is multiplied only by 1.15 and  $K$  by 1.3 when going from E1 to E2 (Table V.3), the loss of silver is multiplied by 20 (from 0.2% of the initial Ag reservoir for E1 to 4.1 % for E2). As shown in Fig. V.3a, the main difference between these two samples lies in the value  $l^*$  (7.5 nm in E1 compared to 0.5 nm in E2). Finally, from these observations one can conclude that in all the explored samples: (i) the number of available Ag atoms in the AgNPs is largely sufficient and is not a limiting factor for the release, and (ii) the key parameter that governs the Ag release is the most probable distance  $l^*$  (see Fig. V.3a).

More quantitatively, the threshold distance is between 5.5 and 7.5 nm since sample E1 has a very weak Ag release. The most efficient silver release is observed for sample E2, which has the same average distance as samples E4 and E5 ( $l_{mean} \sim 5.5$  nm) but a large number of AgNPs closer to the free surface (Fig. V.3a). As it will be commented later, this could be explained by the fact that the driving force for silver release is the penetration of water molecules into silica. As a matter of fact, the diffusion length of water molecules well compares with critical values of  $l$  as it can reach few nanometers at room temperature, especially if the matrix is damaged as in the case of ion implantation.

### 3.2.2. TEM Analysis

In Fig. V.4a-b, the Bright Field XS-TEM images (taken in regions of the specimen with similar thicknesses) show the impact of immersion in buffered water on sample E2. We present this sample because the percentage of released silver was the greatest one among all nanocomposite layers.

Comparing the TEM images before (Fig. V.4a) and after (Fig. V.4b) water immersion, we observe at a first sight a sensible decrease of the number of AgNPs touching the free surface. It means that the silver release is accompanied by shrinkage of the AgNPs located closely to the free surface. The distribution of the distance  $l$  between AgNPs and the free surface is plotted in Fig. V.4a-b before and after water immersion. After plunging and comparing with the as-implanted sample, the AgNPs surface density remains unchanged meanwhile the distance  $l^*$  increases from 0.5 nm to 5.5 nm. This means that the number of AgNPs touching the free surface ( $l < 1$  nm) strongly decreases while those buried more deeply with distance  $5 < l < 6$  nm significantly increases. Beyond 6 nm the shape of the distance distribution does not change significantly. This shows that the critical distance beyond which the silver release is negligible, is around 6 nm. This result is in good agreement with the threshold distance (between 5.5 and 7.5 nm) for silver release found in Section 3.2.1.

Concerning the size-distributions measured from PV-TEM images (Fig. V.4c) one observes a net decrease of the class of AgNPs with size larger than 6 nm, and simultaneously a relative increase of the classes ranging between 3 and 5 nm. Both evolutions confirm the shrinkage of the largest AgNPs located close to the free surface after interaction with water.

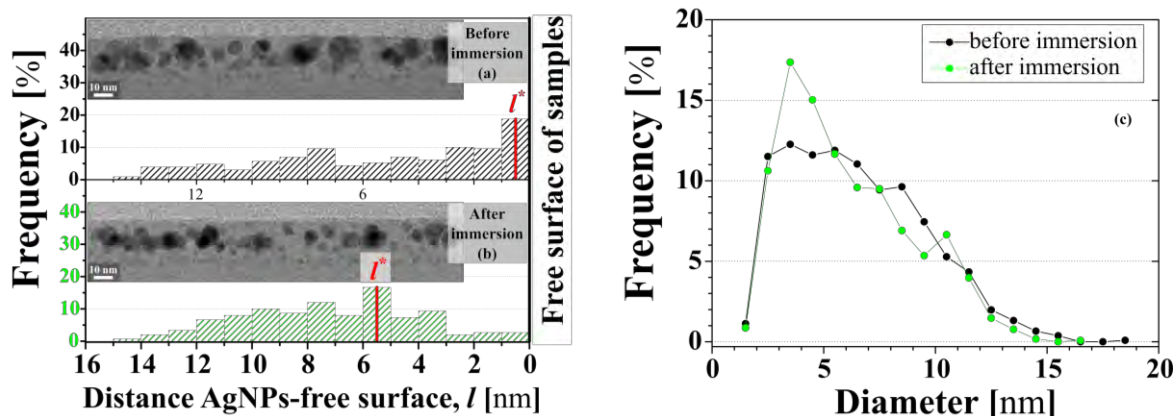


Figure V.4: XS-TEM of sample E2 and the associated spatial distribution of distance  $l$  before (a) and after (b) immersion in buffered water. (c) AgNPs size-distributions, measured from PV-TEM images, before (black) and after (green) immersion in buffered water. The lines in the graph are shown as guide to the eye.

The Ag-atom loss can be estimated from the PV-TEM images of these samples as the difference between the Ag reservoir before (initial Ag reservoir,  $12 \pm 2 \mu\text{M}$ ) and after water immersion ( $11 \pm 2 \mu\text{M}$ ). Even if the cumulated error bar on this measurement is large (30 %) this value is of the same order of magnitude as the one measured by ICP-MS (4.1 %).

### 3.2.3. Optical Analysis

Another point in the current study concerning the evolution of the silver amount is the possible oxidation of the AgNPs during water immersion. To elucidate this point we have used reflectance spectroscopy to check the presence of pure metallic AgNPs in the elaborated nanostructures [Carles et al., 2009]. Visible-UV reflectance spectra are particularly easy to obtain experimentally and display a notable sensitivity to the presence of this kind of NPs in the dielectric matrix. This enhanced sensitivity is a direct consequence of the design of our specific nanocomposites that combine strong absorption at the LSPR (near 410 nm for spherical AgNPs in  $\text{SiO}_2$ ) and antireflective effect of the multilayer structure (near 600 nm for the AgNPs- $\text{SiO}_2$  nanocomposite layer). Hence, we can detect modification in the AgNPs assembly as a modulation of the reflectance spectrum in the 400-500 nm range [Carles et al., 2011; Chapter III]. Figure V.5 shows the reflectance spectra of samples E1 (Fig. V.5a) and E2 (Fig. V.5b) for which the Ag loss percentage is respectively minimal and maximal before (black points) and after (colored points) plunging in buffered water. In both cases, we observe the presence of the LSPR (indicated with an arrow) even after the interaction of the nanocomposites with water. The presence of LSPR indicates that there is still a significant amount of NPs made of pure silver inside the silica layer. For sample E1, which has lost only 0.2% of Ag released in solution, the two spectra are nearly identical.

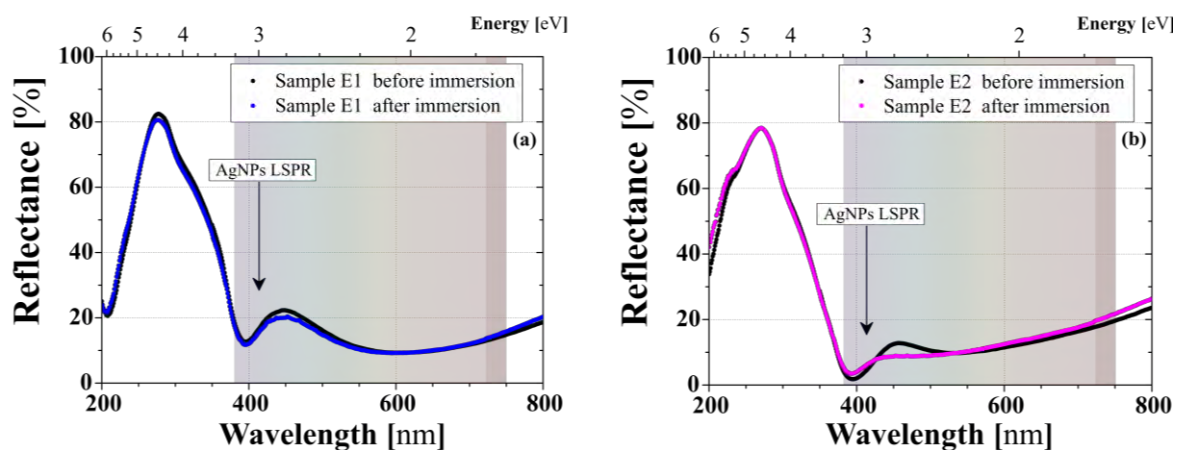


Figure V.5: Reflectance spectra of: (a) samples E1 and (b) sample E2, before (black lines) and after buffered water immersion (colored lines).

For sample E2, for which the silver release is accompanied by AgNPs shrinkage, a change in the reflectance spectrum is clearly observed. This can be interpreted as changes in the average diameter and in the depth position of the AgNPs, which modify both the plasmonic signature and the interference conditions. Correlation between these non-destructive and rapid optical observations and our detailed analyses for a quantitative evaluation of the Ag release is of prime interest for forthcoming in situ characterizations. Presence of AgNPs made of pure silver after water immersion qualifies the analyzed nanocomposites as reusable. They can be successfully applied for optical spectroscopy in liquid environment or for bio-sensors, for example.

### 3.3. Silver toxicity on algal photosynthesis

The toxicity of the silver released from AgNPs embedded in silica matrices was assessed as the inhibition of the photosynthetic activity of the green algae *Chlamydomonas reinhardtii*. As it has been demonstrated previously [Navarro et al., 2008b], under these experimental conditions the toxicity to the algal photosynthesis is due to the dissolved silver bioavailable for the algae ( $Ag_{bioav}$ ). The evaluation of  $Ag_{bioav}$  released from the AgNPs embedded in the different nanocomposites requires removing the samples from solution before the addition of algae. That would avoid the interaction of the reactive oxygen species produced by algae and the AgNPs present in the nanocomposites [Navarro et al., 2015]. Moreover, the use of  $AgNO_3$  as a positive control for  $Ag_{bioav}$  toxicity, would allow estimating the amount of  $Ag_{bioav}$  released from nanocomposites based on the toxicity to the photosynthesis (Fig. V.6).

Toxicity of AgNPs and  $AgNO_3$  were examined upon short-term exposures (1 and 2h) in order to minimize accumulation of algal products in the exposure media and thus changes in the silver speciation [Navarro et al., 2008b]. The photosynthetic values of all the experiments are presented as percentage of the respective controls. These percentages are plotted as function of the released silver,

measured by ICP-MS. In Fig. V.6 we show the reduction of the photosynthetic yield of  $\text{AgNO}_3$  solution, after 1 hour exposure assessed by concentration-response experiments (black circles).

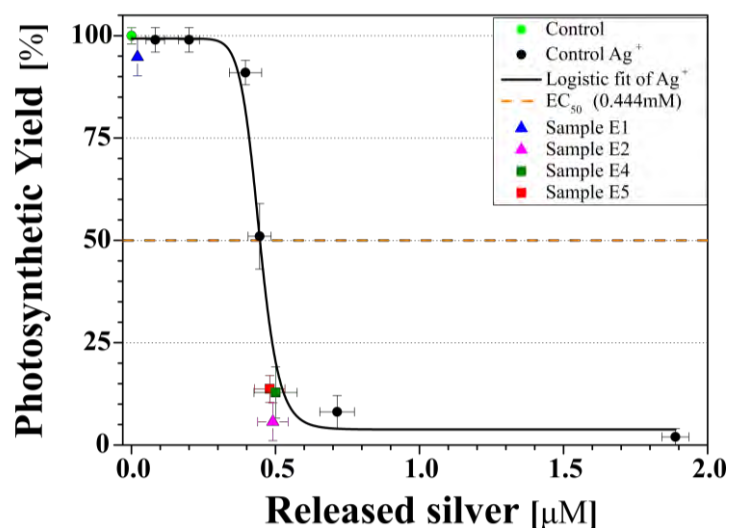


Figure V.6: Fluorometry measurements of solutions containing silver released from the elaborated samples and photosynthetic yield concentration-response curve of  $\text{AgNO}_3$ , after 1 hour. The black line traces the four-parameters logistic fit. The  $\text{EC}_{50}$  value is reported.

A four-parameter logistic fitting permits to evaluate the toxicity of  $\text{AgNO}_3$ , hence the  $\text{Ag}_{\text{bioav}}$ , by defining the half maximal effective concentration ( $\text{EC}_{50}$ ) of released silver corresponding to a reduction of 50% of the photosynthetic yield:  $\text{EC}_{50} = 0.444 \mu\text{M}$  (Fig. V.6).

In the same figure the toxicity effect of samples containing AgNPs (colored symbols) on algal photosynthesis is also evaluated by the corresponding reduction of the photosynthetic yield. For sample E1 (blue triangle), the amount of released silver is not enough to provoke a significant decrease of the photosynthetic yield. The toxicity of Ag released from the other samples is comparable with the toxicity of  $\text{Ag}^+$  from  $\text{AgNO}_3$  (Fig. V.6) indicating that the released silver from synthesized samples is bio-available for algae. Measurements of  $\text{O.D.}_{685}$  of the algae solutions were carried out twice, 3 minutes and 2 hours after the algae injection, to follow the silver toxicity impact on the algal population (Fig. V.7). For each solution, the recorded  $\text{O.D.}_{685}$  changes confirm the silver toxicity trend observed in the fluorometry measurements.

To reveal the origin of the observed silver toxicity to algae (silver ions  $\text{Ag}^+$  and/or AgNPs), we performed fluorometry measurements of solutions in presence of cysteine, known as a strong silver ligand [Navarro et al., 2008b]. The equimolar complexation of  $\text{Ag}^+$  by cysteine has been previously demonstrated in similar experimental conditions [Navarro et al., 2008b; Navarro et al., 2015]. Owing to the 30% of AgNPs located at 2 nm or less from the free silica surface, sample E2 is the favorite candidate to assess the source of released silver. In Fig. V.8, we represent the fluorometry measurements, taken 1 hour after the algae injection, of a solution containing silver released from sample E2 and two different amounts of cysteine.

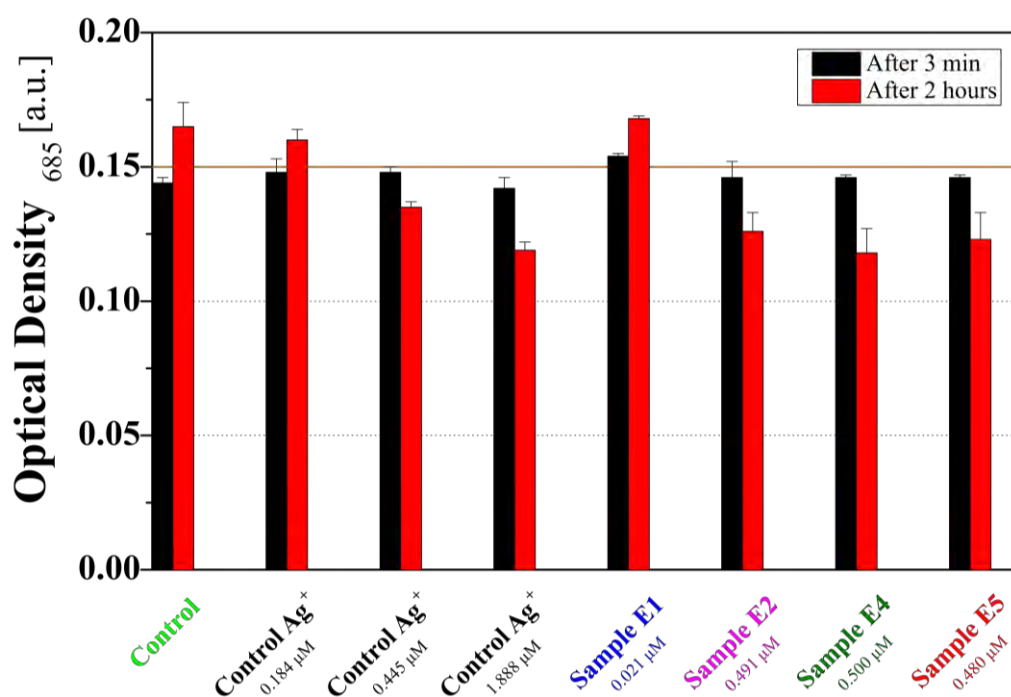


Figure V.7: Measurements of the Optical Density at 685nm of the algae solutions carried out twice, 3 minutes and 2 hours after the algae injection. These measurements assess the toxicity trend of silver observed in the fluorometry analysis.

We compare the fluorometry values obtained on sample E2 (magenta triangles) with the ones of a reference solution containing  $\text{AgNO}_3$  at concentration of  $0.714 \pm 0.060 \mu\text{M}$  and different amounts of cysteine (black circles). Cysteine concentrations of about  $0.7 - 0.9 \mu\text{M}$  abolishes the toxicity of  $\text{Ag}^+$  (from  $\text{AgNO}_3$ ) to the algae photosynthesis, confirming both the key role of  $\text{Ag}^+$  on explaining the observed toxicity to the algal photosynthesis and the equimolar complexation of cysteine and  $\text{Ag}^+$  [Navarro et al., 2008b; Navarro et al., 2015].

Sample E2 presents a partial restoring of the algae photosynthesis when the cysteine concentration is about  $0.35 \mu\text{M}$ , indicating the presence of a higher amount of  $\text{Ag}^+$  in solution. Further addition of cysteine ( $1.5 \mu\text{M}$ ) in this case also abolishes the toxicity to the algal photosynthesis. This finding agrees with other studies [Navarro et al., 2008b; Navarro et al., 2015] confirming that all the toxicity exerted by the suspension after contact with sample E2 is due to the presence of  $\text{Ag}^+$  in the solution.

Merging the information obtained from fluorometry and TEM observations makes possible to conclude that the silver released in solution from the embedded AgNPs is prevalently ionic silver.



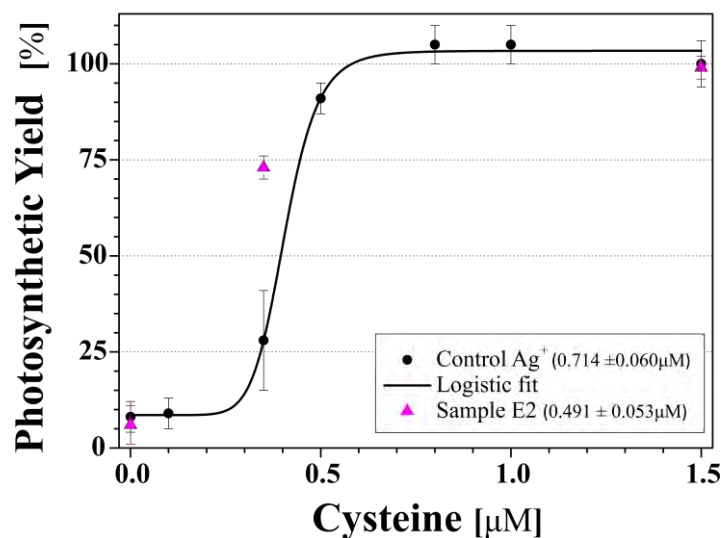


Figure V.8: Algal photosynthetic yield measurements, after 1 hour of exposure to silver released from sample E2 or to a fixed concentration of  $\text{AgNO}_3$  ( $0.714 \mu\text{M}$ ) and different amounts of cysteine. The black line traces the four-parameters logistic fit.

### 3.4. Proposed mechanisms for $\text{Ag}^+$ release: water molecules uptake in silica matrix

The architecture of the samples used in this study is particularly well adapted to control the silver release and as a consequence the toxicity of these nanocomposite layers. Indeed, the embedded AgNPs are located close to the free surface and well separated from each other providing possibility to maximize the AgNPs surface. The nanometric distance between the AgNPs layer and the free surface, *i.e.* the cover silica layer, acts as a barrier layer protecting the metallic silver against quick disappearance and/or a premature aging, mainly through oxidation of AgNPs [Benzo et al., 2011].

However, for the  $\text{Ag}^+$  release to be initiated the water molecules should arrive at the surface of AgNPs. The properties of the surrounding matrix are of primary importance when nanocomposite structures containing metal nanoparticles are exposed to external aging agents (air, aqueous media, different solvents, etc.). The release of  $\text{Ag}^+$  is found to be faster when the host matrix is less stable, like for hydrophilic amorphous oxygenated hydrocarbon matrix (a-CH:O) [Körner et al., 2010; Drábik et al., 2015] where the oxygen functional groups allow quicker water penetration. Increasing the hydrophobicity of the host matrix, like for the amorphous organosilicon matrices (a-SiOC:H) [Saulou et al., 2009; Beer et al., 2012; Alissawi et al., 2013], leads to slower  $\text{Ag}^+$  release mainly due to the delayed water molecules uptake. Increasing the matrix stability through densification, like for the amorphous  $\text{SiO}_2$  matrices (this work), allows fine tuning of the  $\text{Ag}^+$  release.

The absorption of  $\text{H}_2\text{O}$  molecules from the air has been studied in very thin implanted  $\text{SiO}_2$  matrix (less than 10 nm) [Schmidt et al., 2002; Claverie et al., 2006]. The large number of broken bonds in the  $\text{SiO}_4$ -tetrahedra due to displaced Si and O atoms during implantation process results in rearrangements of the fundamental ring structure within the glassy network in which moisture from the ambient can be absorbed. Water molecules adsorb on the surface and damage-enhanced diffusion in the matrix can take place. Therefore, chemical reactions of the implanted impurities with hydrogen

and oxygen are expected. There are two possibilities for the adsorption and room temperature inward diffusion of water molecules into ion-damaged SiO<sub>2</sub>. Either the water molecules directly diffuse into the open SiO<sub>2</sub> network because H<sub>2</sub>O is a molecule with small diameter (less than 0.3 nm), or the H<sub>2</sub>O molecules dissociate at the SiO<sub>2</sub> surface and H<sup>+</sup> and OH<sup>-</sup> ions diffuse into SiO<sub>2</sub>. The O-rich molecules and complexes are driven in the layers up to some 10 nm in depth. Actually, the absorption and final concentration of water molecules are only limited by the degree of damage, *i.e.* the concentration of defects in the SiO<sub>2</sub> matrix.

In the case of Ag implanted silica, annealing of the layers at low temperature (400–500°C) under N<sub>2</sub> atmosphere allows a partial recovering of the implantation damage as the total recovering of a stoichiometric SiO<sub>2</sub> requires higher temperature. This annealing step of the silica cover layer is nevertheless sufficient to avoid, or at least to retard the penetration of O rich complexes from the air [Benzo et al., 2011]. In the present work we demonstrate that the recovered implanted silica allow a strong interaction silver-water reactive species up to 3 nm in depth (Fig. V.4a-b). Over this value, the penetration of H<sub>2</sub>O reactive species should decrease (Fig V.4b) and becomes negligible at depths greater than 7 nm, as confirmed by the low amount of released silver from sample E1. This critical depth can be compared with the diffusion length of water vapour in silica found in the literature, which is 3 nm in one week. [Muscat et al., 2001]. Water diffusion seems to be enhanced in our samples. This is due to lower silica-matrix density and higher porosity comparing to pure thermal silica, in particular for the implanted samples.

The stability of SiO<sub>2</sub> matrix in the plasma deposited samples when exposed to water media is also a defect dependent process. It is determined by the very small amount of residual CH-groups present in the silica network due to the plasma polymerization deposition process used to obtain the plasma silica cover layer. Other structural defects in the silica network arrangement during the plasma deposition are not excluded.

Accurate quantitative comparison of the Ag<sup>+</sup> release for different types of host matrices is not possible as the sample surface characteristics are usually not reported in the literature but the main trend confirms that the highest rate of Ag<sup>+</sup> release appears during the first 24 hours. As far as the mechanism of Ag<sup>+</sup> release is concerned it was shown [Schmidt et al., 2003; Molleman and Hiemstra, 2015] that the consecutive steps of oxygen-silver interaction are related to initial O<sub>2</sub> physisorption followed by O<sub>2</sub> molecularly chemisorbed state and sticking of O<sub>2</sub> to the silver clusters. Generally, the adsorption probability of O<sub>2</sub> increases with the AgNPs size. This mechanism is complemented by the intrinsic properties of the SiO<sub>2</sub> matrix, in particular by the thickness of the cover layer. However, as discussed in Chapter I, the small AgNPs are easily oxidized [Bi et al., 2002] due to the free energy changes depending both of surface and curvature effect of the nanosized particle. If the oxidative dissolution of Ag ions from “free” AgNPs has already been modeled in the literature by using DFT approaches [Molleman and Hiemstra, 2015], the atomic scale modeling of this process for embedded NPs coupled to the modeling of Ag<sup>+</sup> diffusion in silica should be of great help in understanding the reactional

mechanisms and driving forces implied in  $\text{Ag}^+$  release. In particular, a key point will be the modeling of the  $\text{SiO}_2/\text{Ag}$  interface for hydrated silica and the study of the influence of water content on the mechanisms of Ag ion diffusion.

#### 4. Towards reusable nanocomposite samples: assessment of the Ag release from already used nanocomposites

Earlier in this Chapter we have demonstrated that the amount of released in solution Ag is only of few percentages of the total Ag amount stored in the nanocomposite layer as AgNPs. It was also shown that the stratified structure of the layers, a single layer of AgNPs embedded in silica matrix, remains after water immersion although some structural modifications appear. An addition, the optical analysis confirmed the metallic character of AgNPs left in the nanocomposite structure after water immersion. These findings encouraged us to launch a study of the possibility to reuse the nanocomposite samples to access and to assess a second Ag release in the water solution. Fig. V.9 shows ICP-MS measurements of the second Ag release from each one of the already used nanocomposite samples after 24h immersion in buffered water.

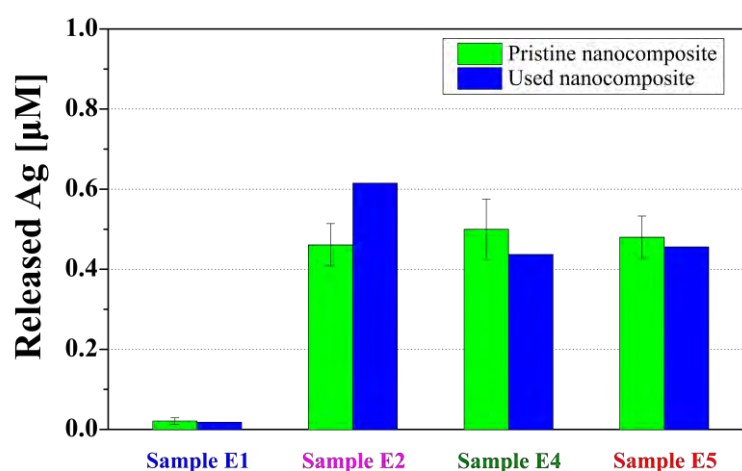


Figure V.9: Comparison of Ag released from a pristine nanocomposite (green column) with a used one (blue column).

The general trend is that all samples release Ag when re-immersed in water. Moreover, the released Ag amount from reused nanocomposite samples is comparable to one from the pristine nanocomposite samples. This behavior is expected for samples E1 for which the analysis from first immersion in water shows no changes in the structure and almost no release of Ag. The amount of Ag released after second immersion in water of sample E2 is a bit higher than the first try in spite of the sensible decrease of the number of AgNPs touching the free surface (Figure V.4). This result can be explained by the presence of a large number of big particles localized close to the free surface. One can also

suppose an increase of the matrix porosity due to the departure of Ag atoms from the AgNPs leaving behind structural defects in the surrounding matrix. Such mechanism can facilitate the Ag release for this sample. Concerning the plasma deposited samples E4 and E5, the Ag amount released from the pristine nanocomposites and the reused ones is similar. This finding allows us to consider both nanocomposite structures, implanted samples and plasma deposited ones, as candidate systems that release a constant amount of Ag in solution over time, finding applications in sensors. Further analysis however, and statistic measurements have to be performed in order to confirm the observed trends and to evaluate the stability of the nanocomposite structures with respect to the Ag release.

## 5. Conclusions

This work presents an original method to assess the release of Ag from AgNPs embedded in silica matrices, based on the  $Ag_{\text{biov}}$  toxicity to the algal photosynthetic activity. The distance of the AgNPs to the free surface of the silica matrix was found to be the key parameter controlling the silver release. Depending on that distance, the release of silver is found to vary between 0.2 and 4.1% of the initial Ag-amount present in the samples. The TEM observations after immersion in water indicate that the Ag release is accompanied by shrinkage of the AgNPs that are located in the immediate proximity of the free surface meanwhile the AgNPs density remains unchanged, suggesting that these AgNPs are the source of the silver released into the solution. Reflectance measurements confirm the presence of pure metallic silver in the NPs after water immersion.

The toxicity of silver released from these nanocomposites to algal photosynthesis is comparable to similar concentrations of  $Ag^+$  released from  $AgNO_3$ . This result, together with the ability of cysteine to abolish the toxicity of experimental suspensions, demonstrates that most of the silver released from nanocomposites was in the form of  $Ag^+$ . As for the release of ionic silver, contact of water molecules with the AgNPs is necessary, being this step strongly dependent on the properties of the surrounding matrix. Our findings show a physical approach to modulate the activity of silver nanostructured layers. These nanocomposites are thus good candidates as coatings for inhibiting the development of microbial films on solid surfaces by controlled dose of the antimicrobial agent.



# Chapter VI: Physico-chemical characterization of the interaction of red fluorescent protein - DsRed with thin silica layers containing AgNPs

---

## 1. Introduction

Increasingly, the microbial adhesion, and following biofilm formation, on dielectric surfaces causes major complications in the biomedical domain and food industry. The general context of this PhD work is the attempt to answer biofilm formation issues by designing nanocomposite materials containing AgNPs to address the underlying mechanisms. We have demonstrated in Chapter V that the first condition, necessary for fabricating biocide nanocomposites which is their capacity to release  $\text{Ag}^+$ , is fulfilled. Indeed, our AgNPs embedded in silica are able to release Ag ions and we can modulate this release by playing with the distance of the AgNPs to the dielectric free surface, in other words with the thickness of the silica cover layer.

In this context and based on previously observed modifications of the protein structure of the model yeast *Saccharomyces cerevisiae*, induced by the interaction at contact of the microorganisms with AgNPs [Saulou et al., 2010], the current study focuses on the physico-chemical characterization of the interactions of proteins with AgNPs. Two proteins were used for the study: the well-studied bovine serum albumin (BSA) which, as a model protein, served to the preliminary step of this investigation and the Discosoma Red fluorescent protein (DsRed) used because of its fluorescent properties holding great promise for applications in biotechnology and cell biology. However, before being used for rational engineering, knowledge on the behavior of DsRed and the underlying mechanisms relating its structural stability and adsorption properties on silica surfaces is highly demanded.

The fluorescent proteins are a family of proteins of 25 – 30 kDa, mainly applied to study the organization and function of living systems [Matz et al., 1999; Baird et al., 2000; Vrzheschch et al., 2000; Wall et al., 2000; Chudakov et al., 2010]. The most extensively characterized member of this family is the green fluorescent protein (GFP). The recently cloned from reef coral *Discosoma sp.* DsRed protein [Matz et al., 1999] has the longest, for a wild-type spontaneously fluorescent protein, excitation and emission maxima at 558 nm and 583 nm, respectively. The DsRed is tetrameric in nature and a spectrally distinct companion or substitute for the GFP.

A variety of experimental techniques have been employed to access and to assess the structural properties of adsorbed proteins on solid surfaces leading to formulation of a number of common trends [Arai and Norde, 1990; Matz et al., 1999; Baird et al., 2000; Vrzheschch et al., 2000; Wall et al., 2000; Larsericdotter et al., 2005; Vo-Dinh, 2005; Barth, 2007; Hughes, 2012; Jachimska and Pajor, 2012].

It is generally acknowledged that proteins having strong internal coherence adsorb on hydrophobic surfaces. However, the electrostatic attraction is necessary for their adsorption on hydrophilic surfaces. In contrary, proteins with much lower structural stability adsorb freely on both hydrophobic and hydrophilic surfaces, even under unfavorable conditions of hydrophilic, electrostatically repelling surfaces. Most of the applied diagnostic methods are adapted for studying the structural stability of proteins in solution. Nevertheless, some advanced diagnostic methods are based on probing proteins adsorbed on solid surfaces after dehydration. It is the case, for example, with matrix assisted laser desorption/ionization (MALDI) [Larsen et al., 2005; Hughes, 2012] or the FTIR spectroscopy [Barth, 2007; Gruian et al., 2012].

In this chapter we report results on the interaction of DsRed proteins with solid silica surfaces containing or not AgNPs. It also demonstrates a way to explore very small quantities of proteins, which allows investigation of rare proteins and/or of proteins demanding costly procedures for their extraction. Finally, when properly dimensioned, AgNPs embedded close to the free surface of anti-reflective thin SiO<sub>2</sub> layer can be used as substrates allowing detection of chemical substances on their surfaces [Carles et al., 2011]. In this context, we illustrate preliminary results about SERS effect of DsRed protein deposited on these kinds of Ag nanocomposite substrate elaborated by plasma processes and LE-IBS. This part of my work was performed in close collaboration with Marvine Soumbo during his Master degree training of 6 months at LAPLACE laboratory in collaboration with CEMES and LGC laboratory.

## **2. Experimental conditions**

### **2.1. SiO<sub>2</sub> thin film preparation**

For the part of this study concerning SiO<sub>2</sub> layers without AgNPs, 100 nm-thick silica layers, were thermally grown on intrinsic Si-substrates at 1100°C under slightly oxidizing atmosphere using a N<sub>2</sub>-O<sub>2</sub> gas mixture containing 1.0% of O<sub>2</sub>. Before being exposed to protein deposition, the SiO<sub>2</sub>/Si substrates were consecutively cleaned in ethanol (95% vol.) and acetone (95% vol.) and then rinsed in deionized water. The deionized water was filtered through 200 nm pore size filter. The rinsing procedure continued until attaining zero surface conductivity on the SiO<sub>2</sub> surfaces. Cleaning the SiO<sub>2</sub> surface is an essential step in this study because of avoiding electrostatic interactions and offering a better control of the experimental conditions. It was performed in a clean room with well controlled environmental conditions, temperature and relative humidity.

The SiO<sub>2</sub> layers containing AgNPs were the already described in previous Chapters layers elaborated by plasma deposition processes and LE-IBS.

## 2.2. DsRed protein and preparation procedure

DsRed (Fig. VI.1a) is a tetrameric protein (120 kDa, 4 x 225 aa) derived from a coral (*Discosoma sp.*) having the intrinsic property of emitting a red fluorescence. DsRed has a maximum excitation wavelength of 558 nm (green light). It has a large "tail" at high energy (wavelength of maximum emission at 583 nm). DsRed forms a very stable tetrameric structure [Verkhusha and Lukyanov, 2004]. The chromophore of DsRed is formed of amino acids 66-68 (Gln-Tyr-Gly). Its maturation takes place through a folding mechanism and intramolecular rearrangement comprising 5 steps (Fig. VI.1b): (1) rearrangement of the chromophore by twisting, (2) cyclization, (3) dehydration, (4) oxidation and (5) the dehydrogenation at Gln. After the last step, the protein becomes fluorescent. DsRed also is stable between pH 5 and 12 [Vrzheschch et al., 2000]. The chromophore of DsRed is shown in Fig. VI.1c.

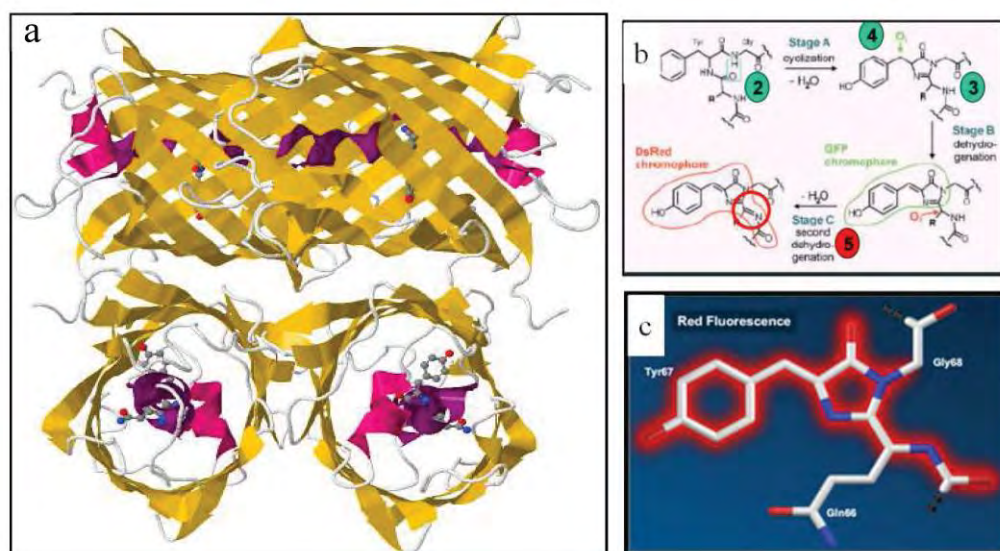


Figure VI.1: (a) Secondary structure of DsRed, (b) the five stages of the formation of the chromophore of DsRed and (c) the chromophore of DsRed.

DsRed was purchased from Biovision. According to the SDS-PAGE, the recombinant DsRed was at least 97% pure and in a freeze dried form. A stock solution of DsRed was made to a concentration of 1 mg/mL in water for injectable preparations (European Pharmacopoeia, COOPER) [European Pharmacopoeia, 2008]. The pH-value of water for injection was measured to 7.0 with conductivity of 1.2  $\mu\text{S}/\text{cm}$ . The pH-value of DsRed stock solution was also determined to 7.0 and its stability was repetitively controlled during all the measurements. The assays were performed at room temperature (23°C). Aliquots of DsRed stock solution were diluted 4-20 times into water for injectable preparations for characterization of DsRed sessile droplets with different protein concentrations.



### **2.3. Deposition of DsRed proteins on the silica layers containing or not AgNPs**

Sessile droplets of different concentrations of DsRed and with very small volume ( $3.8 \pm 0.1 \mu\text{L}$ ) were deposited on the surface of silica layers by using Digidrop goniometer, a Contact Angle Meter from GBX Scientific Instruments to measure the adhesion process of DsRed proteins on silica surfaces. The droplets were deposited with microsyringe Gastight 1700 series fixed on the goniometer giving the possibility of fine control of the droplet volume. To record and analyze the sessile droplets a Visiodrop software was coupled to the contact angle meter. The measurement precision of the applied method is of  $\pm 0.1^\circ$  degree. The results given in this work are averaged over three independent measurements per sample.

Optical images of sessile droplets after their dehydration were recorded with a digital microscope Keyence VHX-1000. The droplet diameter ( $d$ ) was measured on the images using the associated to the microscope VHX 1.3.0.7 software. The other parameters of the dehydrated droplet: thickness ( $e$ ) measured inside the droplet just before the droplet ring, droplet ring width ( $l$ ) and droplet ring height ( $h$ ), were measured with a 2D surface profilometer Alpha-Step IQ from KLA-Tencor. The photoluminescence emission of the DsRed was excited with an argon ion laser operating at 514 nm. The emitted light was dispersed using a Jobin Yvon spectrometer with a 150 grooves/mm grating. FTIR spectra were acquired with a Bruker Vertex 70 spectrometer in transmission mode in the range  $400 - 4000 \text{ cm}^{-1}$  with a resolution of  $2 \text{ cm}^{-1}$  to obtain information about the composition of dehydrated protein layers. The transmission mode was attainable due to the transparency of the used intrinsic Si-substrates to infrared light.

## **3. Study of the interaction DsRed/SiO<sub>2</sub> surfaces**











The interaction of DsRed proteins with SiO<sub>2</sub> surfaces was analyzed on the basis of the adhesion process of diluted protein solutions when approaching the SiO<sub>2</sub> surface, their subsequent behavior during the droplet dehydration, and the related DsRed morphological modifications.

### **3.1. Adsorption and optical properties of DsRed sessile droplets**

The adsorption of DsRed proteins on silica surfaces is an interdependent process involving the protein concentration, the solution in which the proteins are diluted, the silica surface state and the environmental air conditions. When a droplet containing given concentration of proteins is brought to a contact with a solid surface, the organization and protein behavior rely primarily on the Contact Angle Hysteresis (CAH) at the solid-vapor and liquid-vapor interfaces [Chen et al., 1991; Delmas et al., 2011; Deegan et al., 2012; Trantum et al., 2013]. The dehydration process however, involves mechanisms related to irreversible thermodynamic functions giving rise to mechanical hysteresis, due to topographical surface defects, and to chemical hysteresis associated with rearrangements of chemical groups due to positional and orientational changes of the surface molecules. To reveal the

DsRed interaction with the SiO<sub>2</sub> surface we compare the measured advancing contact angles when droplets with very small volume of the control solution (water for injection, pH = 7.0) and of the DsRed (concentration of 0.05 g/L diluted in the control solution) are brought to contact (Table VI.1).

Table VI.1: Dehydration dynamics of sessile droplets.

$\theta_A^a$	$\theta_R^b$	$\theta_R$	$\theta_R$	$\theta_R$
t = 1 s	t = 1 min	t = 5 min	t = 10 min	t = 15 min
Control solution sessile droplet, pH = 7.0 and 23°C				
 55.3°	 51.2°	 50.4°	 47.3°	 26.8°
DsRed sessile droplet with 0.05g/L, pH = 7.0 and 23°C				
 65.4°	 60.1°	 40.3°	 5.0°	 n/a

<sup>a</sup> Advancing contact angle -  $\theta_A$ .

<sup>b</sup> Receding contact angle -  $\theta_R$ .

<sup>c</sup> Standard deviation of the contact angle measurements for all the presented times does not exceed  $\pm 1.7^\circ$ .

The obtained value for the control solution ( $\theta_A = 55.3^\circ$ ) is consistent with values measured on SiO<sub>2</sub> surfaces with deionized water ( $\theta_A = 54.7^\circ$ ) confirming the hydrophilic nature of the used SiO<sub>2</sub> surfaces. The contact angle measured with DsRed is higher ( $\theta_A = 65.4^\circ$ ) suggesting chemical hysteresis induced by the presence of proteins and their organization on the silica surface. Most likely the DsRed proteins adsorb on the SiO<sub>2</sub> surface with their polar side chains towards the available a-polar bonds of the clean SiO<sub>2</sub> surface. The droplet diameter is determined at the moment of contact and remains constant till full dehydration of the droplet.

The very small droplet volume leads to a rapid dehydration. The dehydration process of DsRed (c = 0.05 g/L) solution is completed for 10 min at 23°C. In the same experimental conditions, the water droplet is not evaporated for the same duration; it lasts for almost 20 min. It is also worth to notice that whereas the contact angle of the control solution is preserved for the whole process of dehydration except at the very end due to very small residues present in the water for injection, i.e. the contact angle remains almost constant, the contact angle for different DsRed solutions varies with time (Fig. VI.2) expressing a CAH. The latter observation is related to the adsorption of proteins on the SiO<sub>2</sub> surface. The physical description of this effect is the following. The DsRed proteins deposit at the contact line due to surface tension interactions. They pin the contact line and prevent from receding during the evaporation process. Consequently, they impose a diffusion-limited evaporation process with a larger evaporation rate at the edge as for the water droplet the evaporation is rather uniform over the droplet surface.

Figure VI.2 shows the DsRed behavior during dehydration for different protein concentrations. The droplet dehydration is more rapid for small concentrations of DsRed (up to 0.1 g/L). The linear decrease over time of the contact angle is common for all the studied DsRed concentrations. This effect can be related to a large surface energy variation on the droplet profile close to the triple line (solid-liquid-vapor) and to protein adsorption mechanisms induced by the liquid convective drive inside the droplet (Marangoni effect) [Trantum et al., 2013]. According to theory, a region with high surface tension exerts a pulling force on neighboring regions with lower surface tension inducing a flow across the gradient. For an evaporating droplet [Deegan et al., 2000], the contact line is the place where the lowest surface tension occurs. It will induce an outward flow resulting in accumulation of proteins at the contact line. Given the dependence of Marangoni stress on the contact angle, it is stronger for larger contact angles [Hu and Larson, 2005], the dehydration process takes longer times for larger DsRed concentrations as observed here. Additional reason, to the surface energy variation, is the tetrameric nature of the DsRed protein that can be at the origin of imprisonment of extremely small volumes of water, thus slightly delaying the dehydration process. However, to go further in this explanation by quantification of the dehydration process a thorough theoretical analysis must be performed considering also in details the proteins as surfactant in the sessile droplets.

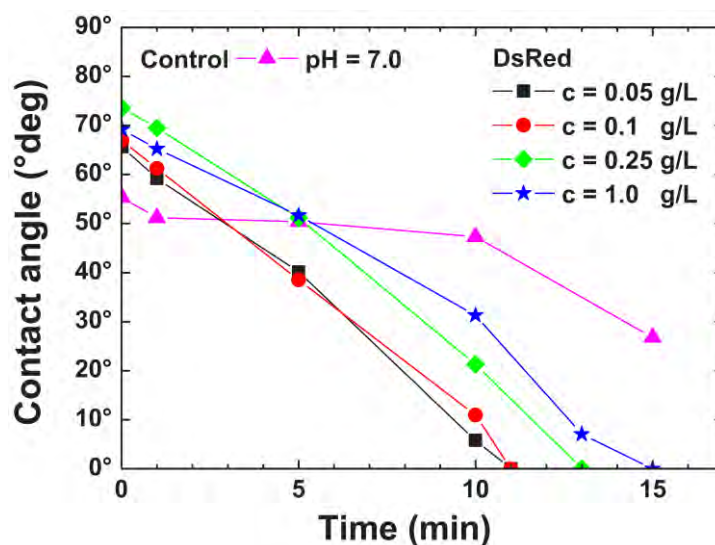




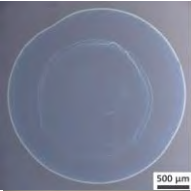

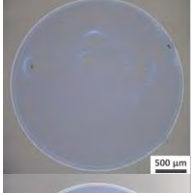

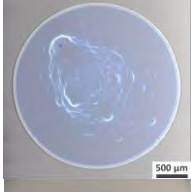

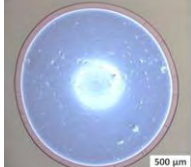
Figure VI.2: Measured contact angles at pH = 7.0 and 23°C as a function of time during sessile droplet dehydration for different concentrations of DsRed.

Table VI.2 summarizes the characteristics of sessile droplets with different concentrations of DsRed diluted in water for injection (pH = 7.0) studied at room temperature (23°C). Due to the hydrophilic properties of SiO<sub>2</sub> surface the measured contact angles for droplets containing DsRed proteins remain in the range  $\theta_A = 65^\circ - 75^\circ$  determining the interaction as hydrophilic one, however with larger contact angles for larger DsRed concentrations. Because of the adsorption of the proteins on the silica surface, the wettability of the DsRed droplet is reduced in comparison with water for injection (control solution

droplet). The increased standard deviation for larger DsRed concentrations reflects the dynamic character of the interaction between DsRed proteins and silica surface in relation with the large DsRed-interfaces imposed by its tetramerization [Wall et al., 2000].

The optical images of dehydrated DsRed droplets indicate that the visual aspect of the sessile droplet becomes more homogeneous with increasing DsRed concentrations. The droplet diameter ( $d$ ) remains almost unchanged over the wide DsRed concentration range from 0.05 to 1.0 g/L. A slight reduction of the diameter of dehydrated droplets is observed with increasing concentration of DsRed. As it is shown in Table VI.2, all the other droplet characteristics (droplet thickness,  $e$ , measured inside the droplet, just before the droplet ring, droplet ring width,  $l$ , and droplet ring height,  $h$ ) are increased when the concentration of DsRed in solution is larger. It means that the DsRed adsorbs on the entire area covered by the droplet with preferential deposition close to the triple line as discussed earlier.

Table VI.2: Dehydration dynamics of sessile droplets.

DsRed (g/L)	Droplet image at 1s	Contact angle $-\theta_A$	Optical image after dehydration	Dehydrated sessile droplet <sup>a</sup>
Control pH=7.0		54.3° ± 0.1°	n/a	n/a
0.05		65.4° ± 0.2°		$d = 2.8 \text{ mm};$ $e = 20 \text{ nm};$ $l = 46 \text{ }\mu\text{m};$ $h = 0.6 \text{ }\mu\text{m}$
0.10		65.5° ± 1.6°		$d = 2.8 \text{ mm};$ $e = 30 \text{ nm};$ $l = 67 \text{ }\mu\text{m};$ $h = 1.4 \text{ }\mu\text{m}$
0.25		73.7° ± 1.5°		$d = 2.7 \text{ mm};$ $e = 30 \text{ nm};$ $l = 84 \text{ }\mu\text{m};$ $h = 3.0 \text{ }\mu\text{m}$
1.00		72.0° ± 2.7°		$d = 2.6 \text{ mm};$ $e = 60 \text{ nm};$ $l = 200 \text{ }\mu\text{m};$ $h = 5.2 \text{ }\mu\text{m}$

<sup>a</sup> The DsRed sessile droplet characteristics after dehydration are as follows:  $d$  is the droplet diameter;  $e$  is the droplet thickness measured inside the droplet, just before the droplet ring;  $l$  is the droplet ring width; and  $h$  is the droplet ring height.

The obtained results imply that the thickness of the adsorbed DsRed layer on solid surfaces (SiO<sub>2</sub>) can finely be controlled by the protein concentration. Moreover, the DsRed layer thickness can be varied

in the nanometer range. DsRed layers as thin as 20 nm ( $c = 0.05$  g/L) can be deposited. The characteristics of dehydrated DsRed droplets are important to be determined for future Raman and fluorescence spectroscopy studies of DsRed adsorbed on silica surfaces requiring very thin protein layers.

The photoluminescence (PL) of the DsRed inside sessile droplet was excited using the 514 nm line of an Argon laser focused to  $1 \mu\text{m}^2$  spot size. The incident laser power was limited to 5 mW in order to avoid laser induced heating and subsequent degradation of the samples. Uniform regions of the dehydrated droplets containing DsRed ( $\text{pH} = 7.0$ ) with different concentrations were selected for the optical measurements. During measurements, the photoluminescence signal of the DsRed exhibited photo-bleaching on the time scale of 2 minutes [Garcia-parajo et al., 2001; Lounis et al., 2001]. After 3 minutes the PL intensity was quite stable and the spectra were acquired with 10 s accumulation time. The so-obtained photoluminescence spectra are presented in figure VI.3. As can be noticed PL emission increases with increasing DsRed concentration. However, it does not scale up linearly most likely due to quenching induced by protein aggregation at high concentration (Fig. VI.3, inset). The PL emission band is peaking at 590 nm. The slight red-shift with respect to the DsRed emission in solution (583 nm) [Matz et al., 1999] can be attributed to conformation effects and to interaction of the DsRed with the silica substrate.

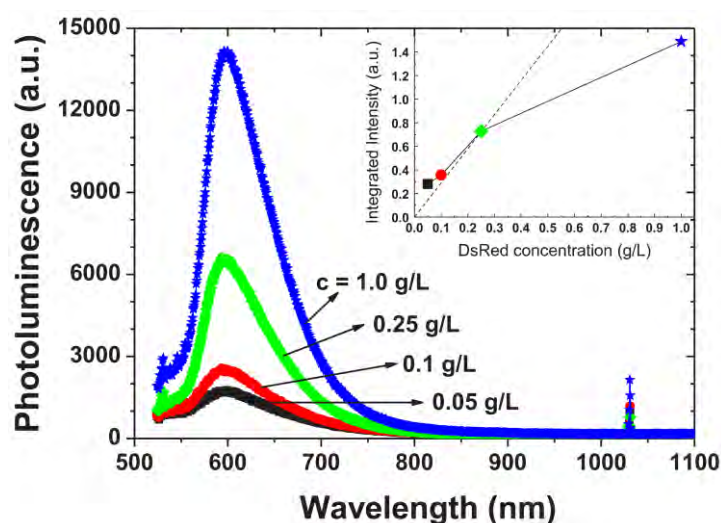


Figure VI.3: Photoluminescence spectra of DsRed dehydrated droplets adsorbed on  $\text{SiO}_2$  surface for different concentrations at  $\text{pH} = 7.0$  and  $23^\circ\text{C}$ . The inset represents the integrated intensity of the photoluminescence peak as a function of the DsRed concentration.

### 3.2. On the possibility to perform FTIR analysis of dehydrated DsRed adsorbed on solid surfaces

The recorded FTIR spectrum of dehydrated DsRed droplet ( $c = 1.0$  g/L,  $\text{pH} = 7.0$ ) adsorbed on  $\text{SiO}_2$  surface is presented in figure VI.4. Due to the fine protein layer thickness after dehydration, the concentration of 1.0 g/L is the only one authorizing acquisition of FTIR spectra in transmission mode.

For lower concentrations the dehydrated protein layer is very thin to allow detectable absorbance. The FTIR spectrum contains all characteristic bond vibrations of the SiO<sub>2</sub> layer and those typically associated with the secondary structure of proteins. The three typical TO modes of amorphous silicon dioxide, the Si-O-Si rocking vibration at 457 cm<sup>-1</sup>, the symmetric stretching mode at 810 cm<sup>-1</sup>, and the asymmetric stretching mode at 1067 cm<sup>-1</sup>, are clearly observable on the spectrum [Kirk, 2001]. One can also notice the SiO<sub>2</sub> characteristic shoulder centered around 1250 cm<sup>-1</sup>.

In general, the protein structures are relatively unstable when exposed to solid surfaces, allowing internal protein regions to interact with the surface. Proteins tend to unfold in this case. Protein denaturation is often associated with complete loss of their secondary structure. The recorded FTIR spectrum (Fig. VI.4) suggests that the DsRed protein is not fully denaturated after dehydration and adsorption on the silica surface in accordance with the observed photoluminescence. The Amide I band with peaks centered at 1654 cm<sup>-1</sup>, assigned the protein  $\alpha$ -helix, and the one at 1684 cm<sup>-1</sup>, belonging to the protein  $\beta$ -sheet are well present on the spectrum [Barth, 2007]. Amide II band centered at 1530 cm<sup>-1</sup>, and most likely the Amide III band around 1340 cm<sup>-1</sup>, are also detectable. Other bands on the spectrum are the Amide A (N-H) one (3300-3500 cm<sup>-1</sup>) and the C-H bonds in CH<sub>3</sub> environment (symmetric at 2900 cm<sup>-1</sup> and asymmetric at 2960 cm<sup>-1</sup> stretching bonds). The large band around 670 cm<sup>-1</sup> can be attributed to possible N-H out-of-plane bending vibrations (640 – 750 cm<sup>-1</sup>) [Smith, 1999]. Further studies will be directed to deconvolution of the FTIR spectrum consistent with identification of positions of the protein secondary structure and possible protein-protein interactions. However the applied here procedure to study dehydrated proteins adsorbed on solid surfaces by FTIR analysis in transmission mode offers the possibility to work on reduced quantities of proteins, especially for quite costly proteins, like DsRed and/or for rare proteins. This attempt will be further developed to extract information about the structural stability of proteins

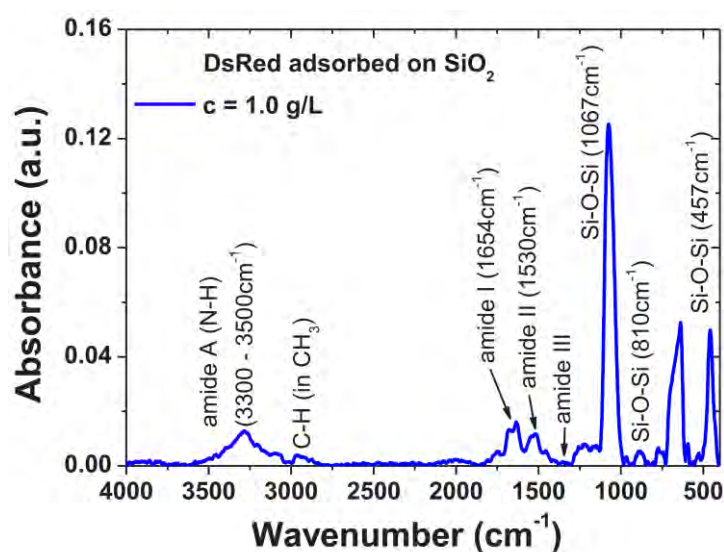


Figure VI.4: FTIR spectrum of DsRed dehydrated droplet adsorbed on SiO<sub>2</sub> surface for c = 1.0 g/L at pH = 7.0 and 23°C.

## **4. Preliminary results of SERS effect of DsRed proteins deposited on AgNPs based plasmonic substrates**

### **4.1. Selection of samples for the SERS study**

Fabrication of nanostructured substrates for molecular plasmonics is hampered by the requirement to maintain on large areas, in a reproducible way, a well-defined spacing between metallic nanostructures and molecules: their mutual interaction is indeed governed by the local topography of the electromagnetic field [Maier, 2007]. In that sense, the emission of a fluorescent molecule placed in the vicinity of a metallic nanostructure can be either amplified or quenched, depending on its position and orientation [Bharadwaj et al., 2007; Sau et al., 2010]. Hence, the separation between emitting or scattering objects deposited near plasmonic antenna has to remain constant in the range of few nanometers and be easily tunable. In that sense, our nanocomposites samples, with delta-layers of AgNPs at tunable nanometric distances from the silica surface are designed to be efficient SERS substrates. They combine several advantages: (i) the choice goes with AgNPs which possess the best features to realize plasmonic antennae, (ii) the AgNPs are embedded in silica matrix which avoids their dissemination and/or their alteration, while preserving their plasmonic properties and retaining the surface reusable and (iii) the thickness of the whole structure is specifically parametrized to provide antireflective effects and to add optical enhancement to the plasmonic effect. In SERS applications, the control over both field enhancement and plasmon resonance is of importance for a high amplification of the Raman signal (“hot spots”) coming from the deposited molecules. It is therefore interesting to select samples with either (i) a percolated array of particles, to exploit the localization by disorder effects of electromagnetic modes [Cang et al., 2011] or (ii) a high density of big particles to exploit the field enhancement in small gaps between particles [Schuck et al., 2005]. In any case, it is necessary to incorporate a large amount of big AgNPs in the plane.

Preliminary promising tests of SERS effects have been performed on the implanted samples [Carles et al., 2011]. Raman signal originating in a micrometer-sized droplet of pure pyridine molecules that have been deposited on the free surface of one of our plasmonic devices was recorded. The Raman signal originating from implanted areas was compared to that recorded on AgNPs-free zones. By taking into account that most of the signal comes from the volume of the liquid located around the focal point of the microscope objective (around 1  $\mu\text{m}$ -thick), we have deduced that the enhancement of the signal coming from molecules located at the near vicinity of the substrate (in a sub-nanometer range), was of several orders of magnitude (around  $10^3$  to  $10^4$ ). This was typical of a SERS gain expected from the solely electromagnetic field mechanism. Indeed, in our case the chemical mechanism is excluded due to the presence of a dielectric spacer between the metal surface and the molecules. Although these preliminary results were promising further efforts had to be done for a precise quantitative analysis. In particular, the surface coverage of AgNPs in the studied implanted sample was quite low (<20%) to achieve the best conditions for a strong SERS effect. More recently



SERS has been demonstrated on 2D sheets (graphene and TMD) deposited on top of the dielectric surface of our implanted samples, evidencing the efficient coupling between the embedded AgNPs and these layers [M. Bayle, 2014].

For the present SERS study on DsRed, we have selected two samples studied and described in the previous Chapters, elaborated with each of the two techniques: the E2 (implanted sample) and the E5 (plasma deposited sample). Again, the two elaboration techniques are complementary and give the prospect to consider different physical situations. From the series of elaborated and studied plasmonic substrates by each of the techniques (LE-IBS and plasma deposition), these 2 samples represent the highest rate of big AgNPs localized close to each other, which should lead to hot spots, and at vicinity of the free surface. The structural characteristics of these two samples are nevertheless clearly different: the AgNPs are quite large for the plasma deposited sample – E5 with mean size of 18.5 nm and surface fraction of 42.6 % while for the implanted sample E2, they are of mean size 6.5 nm and covering a surface in the plane of 32.8 %. In addition, the AgNPs are all located at a distance of 5.5 nm from the surface for sample E5 for which the cover layer is conformal to the AgNPs while, even if the average distance to the surface is 5.3 nm for sample E2, the in-depth distribution of AgNPs is not narrow and a significant part of the AgNPs are touching the dielectric surface. At last, due to the different elaboration techniques the free surface remains flat for sample E2 but having waviness for sample E5 due to the tiny cover layer, with “peaks” on top of the AgNPs and “dips” in between two AgNPs. The width of the formed dips increases with the AgNPs size and for sample E5 is evaluated from the XS-TEM image to be of around 4 nm (red dashed line).

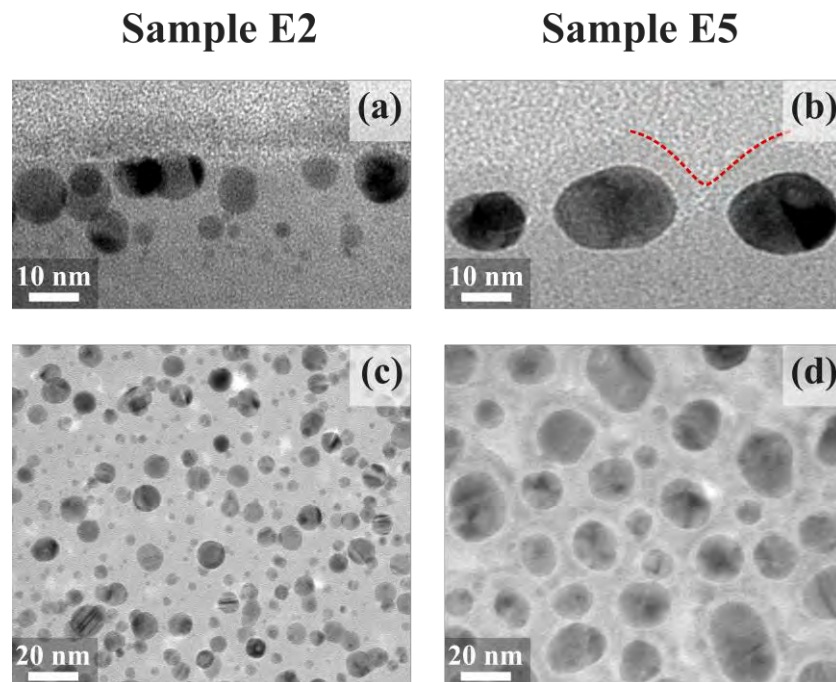


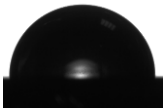
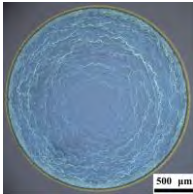
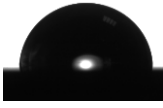
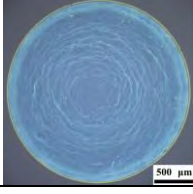
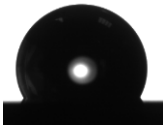
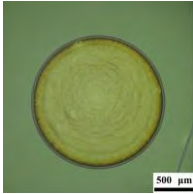
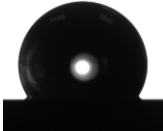

Figure VI.5: (a) and (b) XS and (c) and (d) PV TEM images of the two samples tested for SERS effect on DsRed



## 4.2. Interaction of DsRed with thin silica layers with embedded AgNPs

Table VI.3 summarizes all the morphological characteristics obtained for droplets containing two DsRed concentrations (0.1 and 0.25 g/L) deposited on thin silica layers with embedded AgNPs. The droplet spreads and reaches the maximum diameter immediately after contact. After droplet dehydration the visual appearance of the protein layer is more homogeneous when the Ag content in the substrate increases (Table VI.3).

Table VI.3: Characteristic DsRed droplets on samples E2 and E5, for concentrations of 0.1 and 0.25 g / L at pH = 7.0 and 23°C.

Elaboration process	DsRed (g/L)	Droplet image at 1s	Contact angle - $\theta_A$	Optical image after dehydration	Dehydrated sessile droplet
<b>LE-IBS (E2)</b>	0.10		91.8°		$d = 2.4$ mm
	0.25		89.7°		$d = 2.4$ mm
<b>Plasma deposited samples (E5)</b>	0.10		117.8°		$d = 1.7$ mm
	0.25		120.8°		$d = 1.8$ mm

Substantial increase with respect to the contact angle is observed for the silica layers containing AgNPs. The interaction of DsRed proteins with these nanocomposite substrates presents rather hydrophobic character ( $\theta_A \geq 90^\circ$ ). The measured contact angles are of  $90^\circ$  for the implanted samples and of  $120^\circ$  for the plasma deposited samples. To recall, contact angles of only  $65.5^\circ$  and  $73.7^\circ$  were measured for the silica layers without AgNPs for DsRed concentration of 0.1 and 0.25 g/L, respectively. It signifies that in presence of AgNPs one observes a transition from hydrophilic to hydrophobic character of the DsRed interaction. However, nothing changes from the point of view of DsRed solution. The observed transition is solely due to the surface of silica layer when AgNPs are embedded in it. Different reasons might be at the origin of the transition from hydrophilic to

hydrophobic character for the interaction of DsRed with silica layers without and with AgNPs. Typically polar bonds (C-C or  $\text{CH}_x$  ( $x < 2$ ) groups) drive the surface hydrophobic. Given the used precursor (HMDSO) for the plasma polymerization process to obtain the cover silica layer (Chapter 3) the plasma deposited samples most likely contain a small amount of  $\text{CH}_x$  ( $x < 2$ ) groups which are activated after the cleaning procedure. Another reason is the surface waviness for the plasma deposited samples (Chapter 5). Although the surface of the implanted samples is flat, the implantation process itself causes damages in the silica matrix after  $\text{Ag}^+$  implantation. Some of the  $\text{SiO}_4$ -tetrahedra are with broken bonds and the ring structure is rearranged due to displacement of O and Si atoms during the implantation. In addition, Ag nanocomposite substrates elaborated by plasma processes have higher contact angles ( $120^\circ$ ) than ones elaborated by LE-IBS ( $90^\circ$ ). This influences the final diameter of the sessile droplet resulting in the reduction of its diameter when the contact angle increases (Table VI.3). To go further in the understanding of this issue complementary studies combining contact angle measurements in dynamic mode and x-ray photoelectron spectroscopy (XPS) to quantify the surface composition are necessary.

### **4.3. SERS effect on DsRed proteins deposited on AgNPs based nanocomposites**

Here we present the preliminary results of SERS obtained for DsRed protein with dehydrated droplet concentration of 0.25g/L deposited on samples E2 and E5. Raman spectra were recorded by using a high resolution Raman spectrometer (Horiba Jobin-Yvon Xplora) equipped with three lasers 532, 632 and 785 nm and a standard confocal microscope. The 532 nm laser was used for this experiment. The laser beam was focused on a uniform area of the DsRed using a x100 objective. To avoid possible degradation of proteins due to laser heating, the intensity and time exposure of the incident beam were limited to 1% of its maximum (about 0.15 mW) and 1s, respectively.

Figure VI.6 presents the experimental Raman spectra of DsRed obtained using the two different substrates (E2 and E5). A theoretical spectrum of DsRed was used as reference to identify the protein signature (black spectrum). The characteristics vibration frequencies of DsRed molecular bonds correspond to the band positions in the Raman spectrum. The average spectrum for each substrate was calculated from the accumulation of 10 acquired spectra.

A strong SERS effect of DsRed protein is observed for sample E5 elaborated by plasma processes (Fig. VI.6). In particular, a blinking effect is observed, corresponding to intensity fluctuations of the different Raman peaks. This is due to changes and fluctuations in the molecular orientation and conformation of DsRed protein under the laser excitation (532 nm). On the contrary, the Raman signal is low when the DsRed proteins are deposited on top of the sample elaborated by LE-IBS (E2) and the phenomenon of "blinking" is not detected. The difference in behavior between these two samples can be ascribed to several factors: (i) the highest surface fraction of AgNPs for the sample E5 leading to a high concentration of hot spots, (ii) the effect of the surface waviness which allows trapping of

proteins in the dips in between two AgNPs where; the size of the DsRed protein (molecular weight of the DsRed monomer is 27.6 kDa) being 4.2 nm *i.e.*, comparable to the dip width.

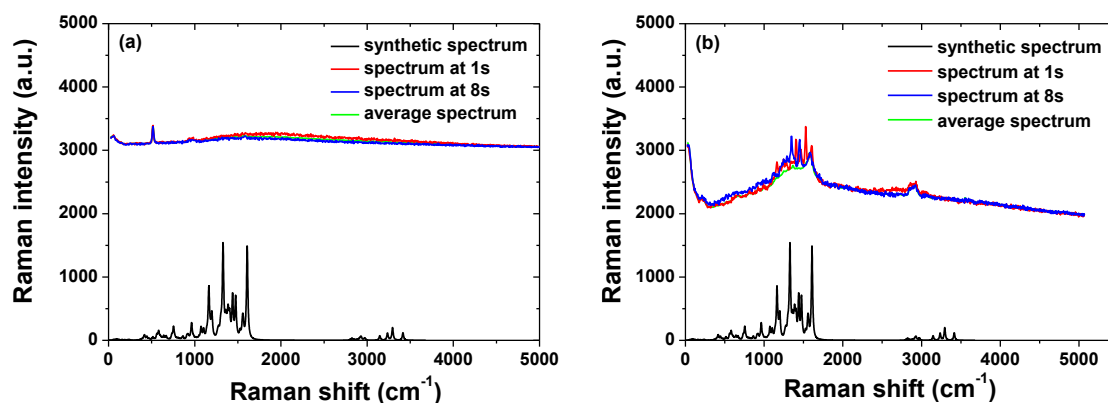


Figure VI.6: Raman spectra obtained with the laser at excitation wavelength of 532nm: (a) E2 sample elaborated by LE-IBS and (b) E5 plasma deposited sample.

## 5. Conclusions

Physico-chemical analysis of the interactions of red fluorescent protein, DsRed with thermal SiO<sub>2</sub> surfaces was performed aiming at identification of the relation between structural stability of DsRed proteins and their adsorption behavior. The obtained characteristics of dehydrated DsRed droplets imply that the thickness of the adsorbed DsRed protein layer on solid surfaces can finely be tuned by the protein concentration. The measured contact angles of very small droplets containing different concentration of DsRed proteins deposited on silica layers without AgNPs determine the interaction as hydrophilic one, however with larger contact angles for larger DsRed concentrations. Transition from hydrophilic to rather hydrophobic interaction of DsRed is observed when the silica layers contain AgNPs. The adsorption of DsRed on SiO<sub>2</sub> surfaces and the following dehydration processes do not lead to complete protein denaturation. The photoluminescence emission of dehydrated DsRed proteins adsorbed on SiO<sub>2</sub> layers is preserved and found to peak at 590 nm, which is slightly red-shifted compared to the reported value for a solution (583 nm). The procedure for recording FTIR spectra in transmission mode confirms the possibility to explore the protein secondary structure after dehydration and adsorption on SiO<sub>2</sub> surfaces. It also largely supports future spectroscopic studies about the behavior of the proteins with modified surfaces (less hydrophilic), taking advantage of the silica layer and the fact that its surface can be easily functionalized. Potential modification of the DsRed excitation and emission spectra due to the DsRed-SiO<sub>2</sub> interactions in solution will also be addressed further. Finally, preliminary results of SERS effect obtained for DsRed proteins deposited on top of the AgNPs based nanocomposite substrates were presented in this Chapter. The sample elaborated by plasma processes with the highest surface fraction of AgNPs, located at 5 nm from the dielectric surface, conformal to the AgNPs with waviness imposed by the nanoparticles, shows promising SERS properties SERS properties to study the interaction of DsRed proteins with AgNPs.

# Conclusions and outlooks

---

The objectives of this PhD was to develop multifunctional nanocomposites based on Ag nanoparticles embedded in dielectric matrices allowing controlled release of Ag (under  $\text{Ag}^+$  and/or AgNPs forms) as antibacterial agent. This should allow both to target the type of microorganism to fight and to deliver it the right dose for its inhibition, while preserving the surrounding microflora. To achieve these objectives we have proposed to use the multifunctionality of Ag nanoparticles, which are both (i) plasmonic antennas for detecting interaction with microorganisms and (ii) ion reservoirs known for their antibacterial properties. In order to stabilize the nanoparticles and control the toxic dose (i.e. the released  $\text{Ag}^+$  ion concentration) the AgNPs were embedded in silica matrix and positioned at varying distances from the surface of the substrate, on which microorganisms will adhere.

Specific silica layers containing AgNPs were developed by two very different but complementary processes: (i) low energy ion beam synthesis and (ii) combined silver sputtering and plasma polymerization. These techniques allow elaboration of a single layer of AgNPs embedded in silica films at defined nanometer distances (from 0 to 7 nm) beneath the free surface. Concerning the deposition technique, specially developed for the purpose of this work, we have shown how the key parameters of the embedded nanostructures (size, density, shape, and distance to the surface) can be controlled by tuning the elaboration conditions combining silver sputtering and plasma polymerization in successive deposition steps. By coupling these samples to the ones elaborated by LE-IBS, we obtained two routes for fabricating of a single layer of AgNPs embedded in thin silica films at controlled nanometric distance beneath the free surface. They offer the possibility to explore different AgNPs size distributions, shapes of the AgNPs, surface densities and particularly their separation from the free surface. The structural and optical properties of the nanocomposites were studied by transmission electron microscopy, reflectance spectroscopy and ellipsometry. This last technique, coupled to modelling based on the quasi-static approximation of the classical Maxwell-Garnett formalism however, accounting for the electronic confinement effect through the damping parameter, has been shown to be an extremely efficient diagnostic tool for the detection of small variations in the size and density of AgNPs.

To assess the ability of the AgNPs embedded in dielectrics (silica layers) to release controlled amounts of Ag ions, we have developed an original method where the evaluation of the dose and the biocidal activity of the ion  $\text{Ag}^+$  has been leached using a eukaryotic model system, *Chlamydomonas reinhardtii*. The photosynthetic system of these green algae has been used as sensitive and reliable biosensor to detect bio-available ionic silver in solution. Distance of the AgNPs to the free surface of the nanocomposite was found to be the key parameter affecting the silver release. Depending on that distance, the release of silver is found to vary between 0.2 and 4.1% of the initial Ag amount present in the samples. The TEM observations after immersion in buffered water indicate that the Ag release is

accompanied by shrinkage of the AgNPs that are located in the immediate proximity of the free surface meanwhile the AgNPs density remains unchanged, suggesting that these AgNPs are the source of the silver released into the solution. The toxicity of silver released from these nanocomposites to algal photosynthesis is comparable to similar concentrations of  $\text{Ag}^+$  released from  $\text{AgNO}_3$ . This result, together with the ability of cysteine to abolish the toxicity of experimental suspensions, demonstrates that most of the silver released from our nanocomposites was in the form of  $\text{Ag}^+$  and exclude the implication of released AgNPs. For the release of ionic silver, penetration till and contact of water molecules with the AgNPs is necessary, being this step strongly dependent on the matrix properties. Our findings show a physical approach to modulate the activity of silver nanostructured surfaces. These nanocomposites are thus good candidates as coatings for inhibiting the development of microbial films on solid surfaces.

To go further in the understanding of underlying mechanisms of adhesion of microorganisms to dielectric surfaces, physico-chemical analysis of the interactions of red fluorescent protein (*Discosoma Red* - DsRed) with thermal  $\text{SiO}_2$  surfaces was performed aiming at identification of the relation between structural stability of DsRed proteins and their adsorption behavior. The obtained characteristics of dehydrated DsRed droplets imply that the thickness of the adsorbed DsRed protein layer on solid surfaces can finely be tuned by the protein concentration. The measured contact angles of very small droplets containing different concentration of DsRed proteins determine their interaction with silica layers as hydrophilic one, however with larger contact angles for larger DsRed concentrations. The adsorption of DsRed on  $\text{SiO}_2$  surfaces and the following dehydration processes do not lead to complete protein denaturation. The photoluminescence emission of dehydrated DsRed proteins adsorbed on  $\text{SiO}_2$  layers is preserved and found to peak at 590 nm, which is slightly red-shifted compared to the reported value for a solution (583 nm). The procedure for recording FTIR spectra in transmission mode confirms the possibility to explore the protein secondary structure after dehydration and adsorption on  $\text{SiO}_2$  surfaces. Finally, we present preliminary results of SERS effect obtained for DsRed proteins deposited on top of our AgNPs based nanocomposite substrates. The sample elaborated by plasma processes with the highest surface fraction of AgNPs, located at 5 nm from the dielectric conformal surface, shows promising SERS properties.

The preliminary results of SERS effects encourage us to pursue in the future optimization of the elaboration conditions in order to get the highest SERS enhancement. For the plasma deposited samples, where a quasi-percolated 2D array is obtained, the influence of the thickness of the cover layer and the imposed by the cover layer waviness of the surface will be for example further examined. Concerning the samples elaborated by LE-IBS, the improved low temperature ion implantation system that will be available at CEMES very soon, should allow inserting in the matrix a higher amount of Ag by suppressing its diffusion towards the surface during the implantation process. 2D percolated arrays of AgNPs should be hence formed during the post-implantation annealing process and will be better candidates for plasmonic enhancement.

Shortly, the next step would be to use these anti-bacterial nanocomposites in “real conditions” to treat the overgrowth of microorganisms for instance *Candida albicans* IP48.72, that can colonize the surfaces of surgical instruments, implantable devices (prosthesis, stents) or percutaneous (catheter) and the walls of the rooms of interventions in hospitals. This study will be performed in collaboration with LGC laboratory in Toulouse.

In parallel, it would be interesting to perform an in-depth study of the Ag ions release mechanisms and of their diffusion through the thin silica cover layer. Dedicated experiments will be carried out in order to better understand the Ag ions release after water immersion, implying FTIR, XPS and STEM-EELS and EDX. In particular, the formation and existence of Ag<sub>2</sub>O thin shell surrounding the AgNPs will be tracked. The effect on the release of the density (porosity) of the cover layer will be also explored by progressive change of the matrix composition. In addition, the oxidative dissolution of Ag ions from “free” AgNPs has already been modelled in the literature by using DFT approaches. Nevertheless the atomic scale modelling of this process for embedded NPs coupled to the modelling of Ag<sup>+</sup> diffusion in silica should be of great help in understanding the reactional mechanisms and driving forces implied in Ag release. Such considerations are already under discussions and shortly be launched with SINanO group of CEMES.

In a long term, this type of extensive study of both the properties of nanocomposite materials themselves and the interaction of metallic nanoparticles with biological-like molecules and biological targets (proteins and cells) is highly demanded to fully uncover the principal effects caused by these materials as well as their side effects. The widespread application of nanoscale metallic nanocomposites challenges many agencies and stakeholders to assess and to balance benefits against the possible health-care hazards and environmental risks. The above particular point represents the main motivation line to pursue in the future this kind of multidisciplinary study on rational engineering of nanocomposite materials in order to better understand their behaviour and to create multifunctional nanocomposites which will reply to issues related to safe application in customer products following the “safe-by-design” concept.



# References

---

- [Adams and Kramer, 1999] N. W. H. ADAMS, J. R. KRAMER. Potentiometric Determination of Silver Thiolate Formation Constants Using a Ag<sub>2</sub>S Electrode, *Aquatic Geochemistry*, 1999, **5**, 1-11. DOI: [10.1023/A:1009699617808](https://doi.org/10.1023/A:1009699617808)
- [Agnihotri et al., 2013] S. AGNIHOTRI, S. MUKHERJI, S. MUKHERJI. Immobilized silver nanoparticles enhance contact killing and show highest efficacy: elucidation of the mechanism of bactericidal action of silver, *Nanoscale*, 2013, **5**, 7328-7340. DOI: [10.1039/c3nr00024a](https://doi.org/10.1039/c3nr00024a)
- [Alissawi et al., 2012] N. ALISSAWI, V. ZAPOROJTCHENKO, T. STRUNSKUS, T. HRKAC, I. KOCABAS, B. ERKARTAL, V. S. K. CHAKRAVADHANULA, L. KIENLE, G. GRUNDMEIER, D. GARBE-SCHÖNBERG, F. FAUPEL. Tuning of the ion release properties of silver nanoparticles buried under a hydrophobic polymer barrier, *J. Nanopart. Res.*, 2012, **14**, 928. DOI: [10.1007/s11051-012-0928-z](https://doi.org/10.1007/s11051-012-0928-z)
- [Alissawi et al., 2013] N. ALISSAWI, T. PETER, T. STRUNSKUS, C. EBBERT, G. GRUNDMEIER, F. FAUPEL. Plasma-polymerized HMDSO coatings to adjust the silver ion release properties of Ag/polymer nanocomposites, *J. Nanopart. Res.*, 2013, **15**, 2080. DOI: [10.1007/s11051-013-2080-9](https://doi.org/10.1007/s11051-013-2080-9)
- [An and Friedman, 1998] Y. H. AN, R. J. FRIEDMAN. Concise Review of Mechanisms of Bacterial Adhesion to Biomaterial Surfaces, *J. Biomed. Mat. Res.*, 1998, **43**, 338-348. DOI: [10.1002/\(SICI\)1097-4636\(199823\)43:3<338::AID-JBM16>3.0.CO;2-B](https://doi.org/10.1002/(SICI)1097-4636(199823)43:3<338::AID-JBM16>3.0.CO;2-B)
- [Arai and Norde, 1990] T. ARAI, W. NORDE. The behavior of some model proteins at solid-liquid interfaces 1. Adsorption from single protein solutions, *Colloids and Surfaces*, 1990, **51**, 1-15. DOI: [10.1016/0166-6622\(90\)80127-P](https://doi.org/10.1016/0166-6622(90)80127-P)
- [Arai et al., 2006] N. ARAI, H. TSUJI, K. UENO, T. MATSUMOTO, N. GOTOH, K. AADACHI, H. KOTAKI, Y. GOTOH, J. ISHIKAWA. Formation of silver nanoparticles aligned near the bottom of SiO<sub>2</sub> film on silicon substrate by negative-ion implantation and post-annealing, *Nuclear Instruments and Methods in Physics Research B*, 2006, **242**, 217-220. DOI: [10.1016/j.nimb.2005.08.018](https://doi.org/10.1016/j.nimb.2005.08.018)
- [Arai et al., 2007] N. ARAI, H. TSUJI, K. ADACHI, H. KOTAKI, Y. GOTOH, J. ISHIKAWA. Silver Negative-Ion Implantation into Thermally Grown Thin SiO<sub>2</sub> Film on Si Substrate and Heat Treatment for Formation of Silver Nanoparticles, *Jpn. J. Appl. Phys.*, 2007, **46**, 6260-6266. DOI: [10.1143/JJAP.46.6260](https://doi.org/10.1143/JJAP.46.6260)
- [Aspnes, 2011] D. E. ASPNES. Plasmonics and effective-medium theories, *Thin Solid Films*, 2011, **519**, 2571-2574. DOI: [10.1016/j.tsf.2010.12.081](https://doi.org/10.1016/j.tsf.2010.12.081)
- [Atwater and Polman, 2010] H. A. ATWATER, A. POLMAN. Plasmonics for improved photovoltaic devices, *Nat. Mater.*, 2010, **9**, 205-213. DOI: [10.1038/NMAT2629](https://doi.org/10.1038/NMAT2629)
- [Aumaille et al., 2000] K. AUMAILLE, C. VALLEE, A. GRANIER, A. GOULLET, F. GABORIAU, G. TURBAN. A comparative study of oxygen/organosilicon plasmas and thin SiO<sub>x</sub>C<sub>y</sub>H<sub>z</sub> films deposited in a helicon reactor, *Thin Solid Films*, 2000, **359**, 188-196. DOI: [10.1016/S0040-6090\(99\)00883-4](https://doi.org/10.1016/S0040-6090(99)00883-4)
- [Axson et al. 2015] J. L. AXSON, D. I. STARK, A. L. BONDY, S. S. CAPRACOTTA, A. D. MAYNARD, M. A. PHILBERT, I. L. BERGIN, A. P. AULT. Rapid Kinetics of Size and pH-Dependent Dissolution and Aggregation of Silver Nanoparticles in Simulated Gastric Fluid, *J. Phys. Chem. C*, 2015, **119**, 20632-20641. DOI: [10.1021/acs.jpcc.5b03634](https://doi.org/10.1021/acs.jpcc.5b03634)
- [Backx et al., 1981] C. BACKX, C.P.M. DE GROOT, P. BILOEN. Adsorption of oxygen on Ag(110) studied by high resolution ELS and TPD, *Surface Science*, 1981, **104**, 300-317. DOI: [10.1016/0039-6028\(81\)90137-0](https://doi.org/10.1016/0039-6028(81)90137-0)



- [Bae et al., 2010] E. BAE, H.-J. PJARK, J. LEE, Y. KIM, J. YOON, K. PARK, K. CHOI, J. YI. Bacterial Cytotoxicity of the Silver Nanoparticle related to Physicochemical Metrics and Agglomeration Properties, *Environ. Toxicol. Chem.*, 2010, **29**, 2154-2160. DOI: [10.1002/etc.278](https://doi.org/10.1002/etc.278)
- [Baffou and Quidant, 2013] G. BAFFOU, R. QUIDANT. Thermo-plasmonics: using metallic nanostructures as nano-sources of heat, *Laser Photonics Rev.*, 2013, **7**, 171-187. DOI: [10.1002/lpor.201200003](https://doi.org/10.1002/lpor.201200003)
- [Baida et al., 2009] H. BAIDA, P. BILLAUD, S. MARHABA, D. CHRISTOFILOS, E. COTTANCIN, A. CRUT, J. LERMÉ, P. MAIOLI, M. PELLARIN, M. BROYER, N. DEL FATTI, F. VALLÉE. Quantitative Determination of the Size Dependence of Surface Plasmon Resonance Damping in Single Ag@SiO<sub>2</sub> Nanoparticles, *Nano Lett.*, 2009, **9**, 3463-3469. DOI: [10.1021/nl901672b](https://doi.org/10.1021/nl901672b)
- [Baird et al., 2000] G. S. BAIRD, D. A. ZACHARIAS, R. Y. TSIEN. Biochemistry, mutagenesis, and oligomerization of DsRed, a red fluorescent protein from coral, *PNAS*, 2000, **97**, 11984-11989. DOI: [10.1073/pnas.97.22.11984](https://doi.org/10.1073/pnas.97.22.11984)
- [Baker et al., 2005] C. BAKER, A. PRADHAN, L. PAKSTIS, D. J. POCHAN, S. I. SHAH. Synthesis and Antibacterial Properties of Silver Nanoparticles, *J. Nanosci. Nanotech.*, 2005, **5**, 244-249. DOI: [10.1166/jnn.2005.034](https://doi.org/10.1166/jnn.2005.034).
- [Barillo and Marx, 2014] D. J. BARILLO, D. E. MARX. Silver in medicine: A brief history BC 335 to present, *Burns*, 2014, **40S**, S3-S8. DOI: [10.1016/j.burns.2014.09.009](https://doi.org/10.1016/j.burns.2014.09.009)
- [Barni et al., 2012] R. BARNI, S. ZANINI, C. RICCARDI. Characterization of the Chemical Kinetics in an O<sub>2</sub>/HMDSO RF Plasma for Material Processing, *Advances in Physical Chemistry*, 2012, **2012**, articleID 205380, 1-6. DOI: [10.1155/2012/205380](https://doi.org/10.1155/2012/205380)
- [Barth, 2007] A. BARTH. Infrared spectroscopy of proteins, *Biochimica et Biophysica Acta*, 2007, **1767**, 1073-1101. DOI: [10.1016/j.bbabi.2007.06.004](https://doi.org/10.1016/j.bbabi.2007.06.004)
- [Bayle et al., 2014] M. BAYLE, P. BENZO, N. COMBE, C. GATEL, C. BONAFOS, G. BENASSAYAG, R. CARLES. Experimental investigation of the vibrational density of states and electronic excitations in metallic nanocrystals, *Physical Review B*, 2014, **89**, 195402. DOI: [10.1103/PhysRevB.89.195402](https://doi.org/10.1103/PhysRevB.89.195402)
- [Bayle et al., 2015] M. BAYLE, C. BONAFOS, P. BENZO, G. BENASSAYAG, B. PÉCASSOU, L. KHOMENKOVA, F. GOURBILLEAU, R. CARLES. Ag doped silicon nitride nanocomposites for embedded plasmonics, *Applied Physics Letters*, 2015, **107**, 101907. DOI: [10.1063/1.4930940](https://doi.org/10.1063/1.4930940)
- [Bayle, 2014] M. BAYLE. Architectures plasmoniques enterrées : élaboration, propriétés optiques et applications, PhD dissertation, Université Paul Sabatier (France), 2014.
- [Beer et al., 2012] C. BEER, R. FOLDBJERG, Y. HAYASHI, D. S. SUTHERLAND, H. AUTRUP. Toxicity of silver nanoparticles—Nanoparticle or silver ion?, *Toxicology Letters*, 2012, **208**, 286-292. DOI: [10.1016/j.toxlet.2011.11.002](https://doi.org/10.1016/j.toxlet.2011.11.002)
- [Behra et al., 2013] R. BEHRA, L. SIGG, M. J. D. CLIFT, F. HERZOG, M. MINGHETTI, B. JOHNSTON, A. PETRI-FINK, B. ROTHEN-RUTISHAUSER. Si Bioavailability of silver nanoparticles and ions: from a chemical and biochemical perspective, *J. R. Soc. Interface*, 2013, **10**, 0396. DOI: [10.1098/rsif.2013.0396](https://doi.org/10.1098/rsif.2013.0396)
- [Bell and Kramer, 1999] R. A. BELL, J. R. KRAMER. STRUCTURAL CHEMISTRY AND GEOCHEMISTRY OF SILVER-SULFUR COMPOUNDS: CRITICAL REVIEW, *Environmental Toxicology and Chemistry*, 1999, **18**, 9-22. DOI: [10.1002/etc.5620180103](https://doi.org/10.1002/etc.5620180103)
- [Belmonte et al., 2011] T. BELMONTE, G. ARNOULT, G. HENRION, T. GRIES. Nanoscience with non-equilibrium plasmas at atmospheric pressure, *Environ. J. Phys. D: Appl. Phys.*, 2011, **44**, 363001. DOI: [10.1088/0022-3727/44/36/363001](https://doi.org/10.1088/0022-3727/44/36/363001)

- [Benassayag et al., 2000] G. BENASSAYAG, W. SANT, F. OLIVIE, A. SEGUELA, C. ARMAND, F. VOILLOT, A. CLAVERIE. New design of a decelerator module for ultra low energy implantation, *Ion Implantation Technology*, 2000. Conference on, 2000, 384-387. DOI: [10.1109/2000.924168](https://doi.org/10.1109/2000.924168)
- [Benassayag et al., 2012] G. BENASSAYAG, C. FARCAU, P. BENZO, L. CATTANEO, C. BONAFOS, B. PECASSOU, A. ZWICK, R. CARLES. 3D patterning of Ag nanoparticles by ULE ion implantation and stencil soft lithography for plasmonic device applications, *Nuclear Instruments and Methods in Physics Research B*, 2012, **272**, 214-217. DOI: [10.1016/j.nimb.2011.01.068](https://doi.org/10.1016/j.nimb.2011.01.068)
- [Benton and Drake, 1932] A. F. BENTON, L. C. DRAKE. The dissociation pressure of silver oxide below 200°, *J. Am. Chem. Soc.*, 1932, **54**, 2186-2194. DOI: [10.1021/ja01345a005](https://doi.org/10.1021/ja01345a005).
- [Benzo et al., 2011] P. BENZO, L. CATTANEO, C. FARCAU, A. ANDREOZZI, M. PEREGO, G. BENASSAYAG, B. PECASSOU, R. CARLES, BONAFOS. Stability of Ag nanocrystals synthesized by ultra-low energy ion implantation in SiO<sub>2</sub> matrices, *J. Appl. Phys.*, 2011, **109**, 103524. DOI: [10.1063/1.3592254](https://doi.org/10.1063/1.3592254)
- [Benzo et al., 2013] P. BENZO, C. BONAFOS, M. BAYLE, R. CARLES, L. CATTANEO, C. FARCAU, G. BENASSAYAG, B. PECASSOU, D. MULLER. Controlled synthesis of buried delta-layers of Ag nanocrystals for near-field plasmonic effects on free surfaces, *J. Appl. Phys.*, 2013, **113**, 193505. DOI: [10.1063/1.4804171](https://doi.org/10.1063/1.4804171)
- [Berberoglu et al., 2008] H. BERBEROGLU, L. PILON, A. MELIS. Radiation characteristics of *Chlamydomonas reinhardtii* CC125 and its truncated chlorophyll antenna transformants tla1, tlaX and tla1-CW<sup>+</sup>, *International Journal of Hydrogen Energy*, 2008, **33**, 6467-6483. DOI: [10.1016/j.ijhydene.2008.07.071](https://doi.org/10.1016/j.ijhydene.2008.07.071)
- [Bergmann, 2014] A E. BERGMANN. Dépôts sous vide par procédés plasma – principes, *Techniques de l'ingénieur*, 2014, M1663.
- [Bernoux et al., 2003] F. BERNOUX, J.-P. PIEL, B. CASTELLON, C. DEFRANOUX, J.-H. LECAT, P. BOHER, J.-L. STEHLE. Ellipsométrie - Théorie, *Techniques de l'ingénieur*, 2003, R6490 V1
- [Beyene et al., 2010] H. T. BEYENE, V. S. K. CHAKRAVADHANULA, C. HANISCH, M. ELBAHRI, T. STRUNSKUS, V. ZAPOROJTCHENKO, L. KIENLE, F. FAUPEL. Preparation and plasmonic properties of polymer-based composites containing Ag–Au alloy nanoparticles produced by vapor phase co-deposition, *J. Mater. Sci.*, 2010, **45**, 5865-5871. DOI: [10.1007/s10853-010-4663-5](https://doi.org/10.1007/s10853-010-4663-5)
- [Beyer et al., 1975] H. BEYER, P. A. JACOBS, J. B. UYTTERHOEVEN. Behaviour of Transition Metal Ions in Zeolites, Part 2.-Kinetic Study of the Reduction and Reoxidation of Silver-Y Zeolites, *J. Chem. Soc., Faraday Trans. 1*, 1976, **72**, 674-685. DOI: [10.1039/F19767200674](https://doi.org/10.1039/F19767200674)
- [Bharadwaj et al., 2007] P. BHARADWAJ, P. ANGER, L. NOVOTNY. The Nanoplasmonic enhancement of single-molecule fluorescence, *Nanotechnology*, 2007, **18**, 044017. DOI: [10.1088/0957-4484/18/4/044017](https://doi.org/10.1088/0957-4484/18/4/044017)
- [Bi et al., 2002] H. BI, W. CAI, C. KAN, L. ZHANG, D. MARTIN, F. TRÄGER. Optical study of redox process of Ag nanoparticles at high temperature, *J. Appl. Phys.*, 2002, **92**, 7491-7497. DOI: [10.1063/1.1518147](https://doi.org/10.1063/1.1518147)
- [Birks et al., 2006] N. BIRKS, G. H. MEIER, F. S. PETTIT. *Introduction to High Temperature Oxidation of Metals*, 2006, Edward Arnold.
- [Bohdansky et al., 1980] J. BOHDANSKY, J. ROTH, H. L. BAY. An analytical formula and important parameters for low-energy ion sputtering, *J. Appl. Phys.*, 1980, **51**, 2861-2865. DOI: [10.1063/1.327954](https://doi.org/10.1063/1.327954)

[Bonafos et al., 2001] C. BONAFOS, B. COLOMBEAU, A. ALTIBELLI, M. CARRADA, G. BENASSAYAG, B. GARRIDO, M. LÓPEZ, A. PÉREZ-RODRÍGUEZ, J.R. MORANTE, A. CLAVERIE. Kinetic study of group IV nanoparticles ion beam synthesized in SiO<sub>2</sub>, *Nuclear Instruments and Methods in Physics Research B*, 2001, **178**, 17-24. DOI: [10.1016/S0168-583X\(01\)00497-9](https://doi.org/10.1016/S0168-583X(01)00497-9)

[Bonafos et al., 2002] C. BONAFOS, B. COLOMBEAU, M. CARRADA, A. ALTIBELLI, A. CLAVERIE. Simulations of the ripening of 3D, 2D and 1D objects, *Materials Science and Engineering*, 2002, **B88**, 112-117. DOI: [10.1016/S0921-5107\(01\)00861-3](https://doi.org/10.1016/S0921-5107(01)00861-3)

[Bonafos et al., 2004] C. BONAFOS, M. CARRADA, N. CHERKASHIN, H. COFFIN, D. CHASSAING, G. BENASSAYAG, A. CLAVERIE, T. MÜLLER, K. H. HEINIG, M. PEREGO, M. FANCIULLI, P. DIMITRAKIS, P. NORMAND. Manipulation of two-dimensional arrays of Si nanocrystals embedded in thin SiO<sub>2</sub> layers by low energy ion implantation, *J. Appl. Phys.*, 2004, **95**, 5696. DOI: [10.1063/1.1695594](https://doi.org/10.1063/1.1695594)

[Bonafos et al., 2005]. C. BONAFOS, H. COFFIN, S. SCHAMM, N. CHERKASHIN, G. BENASSAYAG, P. DIMITRAKIS, P. NORMAND, M. CARRADA, V. PAILLARD, A. CLAVERIE. Si nanocrystals by ultra-low-energy ion beam-synthesis for non-volatile memory applications, *Solid-State Electronics*, 2005, **49**, 1734-1744. DOI: [10.1016/j.sse.2005.10.001](https://doi.org/10.1016/j.sse.2005.10.001)

[Bonafos et al., 2012] C. BONAFOS, M. CARRADA, G. BENASSAYAG, S. SCHAMM-CHARDON, J. GROENEN, V. PAILLARD, B. PECASSOU, A. CLAVERIE, P. DIMITRAKIS, E. KAPETANAKIS, V. IOANNOU-SOUGLERIDIS, P. NORMAND, B. SAHU, A. SLAOUI. Si and Ge nanocrystals for future memory devices, *Materials Science in Semiconductor Processing*, 2012, **15**, 615-626. DOI: [10.1016/j.mssp.2012.09.004](https://doi.org/10.1016/j.mssp.2012.09.004)

[Brett, 2006] D. W. BRETT. A discussion of silver as an antimicrobial agent: alleviating the confusion, *Ostomy Wound Manage*, 2006, **52**, 34-41.

[Briandet et al., 1999] R. BRIANDET, V. LERICHE, B. CARPENTIER, M.-N. BELLON-FONTAINE. Effects of the Growth Procedure on the Surface Hydrophobicity of *Listeria monocytogenes* Cells and Their Adhesion to Stainless Steel, *J. Food Prot.*, 1999, **62**, 994-998.

[Bukhtiyarov et al., 2003] V. I. BUKHTIYAROV, M. HÄVECKER, V. V. KAICHEV, A. KNOP-GERICKE, R. W. MAYER, R. SCHLÖGL. Atomic oxygen species on silver: Photoelectron spectroscopy and x-ray absorption studies, *Physical Review B*, 2003, **67**, 235422. DOI: [10.1103/PhysRevB.67.235422](https://doi.org/10.1103/PhysRevB.67.235422).

[Cacciato et al., 2015] G. CACCIATO, M. BAYLE, A. PUGLIARA, C. BONAFOS, M. ZIMBONE, V. PRIVITERA, M. G. GRIMALDI, R. CARLES. Enhancing carrier generation in TiO<sub>2</sub> by a synergistic effect between plasmon resonance in Ag nanoparticles and optical interference, *Nanoscale*, 2015, **7**, 13468-13476. DOI: [10.1039/c5nr02406d](https://doi.org/10.1039/c5nr02406d)

[Cai et al., 1998] W. CAI, H. ZHONG, L. ZHANG. Optical measurements of oxidation behavior of silver nanometer particle within pores of silica host, *J. Appl. Phys.*, 1998, **83**, 1705-1710. DOI: [10.1063/1.366888](https://doi.org/10.1063/1.366888).

[Camacho et al., 2008] J. J. CAMACHO, M. SANTOS, L. DIAZ, J. M. L. POYATO. Optical emission spectroscopy of oxygen plasma induced by IR CO<sub>2</sub> pulsed laser, *J. Phys. D: Appl. Phys.*, 2008, **41**, 215206. DOI: [10.1088/0022-3727/41/21/215206](https://doi.org/10.1088/0022-3727/41/21/215206)

[Campbell, 1985] C. T. CAMPBELL. The Atomic and molecular oxygen adsorption on Ag(111), *Surface Science*, 1985, **157**, 43-60. DOI: [10.1016/0039-6028\(85\)90634-X](https://doi.org/10.1016/0039-6028(85)90634-X).

[Canet et al., 1992] P. CANET, C. LAURENT, J. AKINNIFESI, B. DESPAX. Dielectric properties of gold-containing plasma-polymerized thin films, *J. Appl. Phys.*, 1992, **72**, 2423-2431. DOI: [10.1063/1.351587](https://doi.org/10.1063/1.351587)

- [Cang et al., 2011] H. CANG, A. LABNO, C. LU, X. YIN, M. LIU, C. GLADDEN, Y. LIU, X. ZHANG. Probing the electromagnetic field of a 15-nanometre hotspot by single molecule imaging, *Nature*, 2011, **469**, 385-388 DOI: [10.1038/nature09698](https://doi.org/10.1038/nature09698)
- [Carles et al., 2009] R. CARLES, C. FARCAU, C. BONAFOS, G. BENASSAYAG, B. PECASSOU, A. ZWICK. The synthesis of single layers of Ag nanocrystals by ultra-low-energy ion implantation for large-scale plasmonic structures, *Nanotechnology*, 2009, **20**, 355305. DOI: [10.1088/0957-4484/20/35/355305](https://doi.org/10.1088/0957-4484/20/35/355305)
- [Carles et al., 2011] R. CARLES, C. FARCAU, C. BONAFOS, G. BENASSAYAG, M. BAYLE, P. BENZO, J. GROENEN, A. ZWICK. Three Dimensional Design of Silver Nanoparticle Assemblies Embedded in Dielectrics for Raman Spectroscopy Enhancement and Dark-Field Imaging, *ACS Nano*, 2011, **5**, 355305. DOI: [10.1021/nn202767p](https://doi.org/10.1021/nn202767p)
- [Carles et al., 2015] R. CARLES, M. BAYLE, P. BENZO, G. BENASSAYAG, C. BONAFOS, G. CACCIATO, V. PRIVITERA. Plasmon-resonant Raman spectroscopy in metallic nanoparticles: Surface-enhanced scattering by electronic excitations, *Physical Review B*, 2015, **92**, 174302. DOI: [10.1103/PhysRevB.92.174302](https://doi.org/10.1103/PhysRevB.92.174302)
- [Castellano et al., 2007] J. J. CASTELLANO, S. M. SHAFII, F. KO, G. DONATE, T. E. WRIGHT, R. J. MANNARI, W. G. PAYNE, D. J. SMITH, M. C. ROBSON. Comparative evaluation of silver-containing antimicrobial dressings and drugs, *Int. Wound J.*, 2007, **4**, 114-122. DOI: [10.1111/j.1742-481X.2007.00316.x](https://doi.org/10.1111/j.1742-481X.2007.00316.x)
- [Chaloupka et al., 2010] K. CHALOUPKA, Y. MALAM, A. M. SEIFALIAN. Nanosilver as a new generation of nanoparticle in biomedical applications, *Trends in Biotechnology*, 2010, **28**, 580-588. DOI: [10.1016/j.tibtech.2010.07.006](https://doi.org/10.1016/j.tibtech.2010.07.006)
- [Chapman, 1980] B. CHAPMAN. *Glow discharge processes: Sputtering and Plasma Etching*, 1980, Wiley.
- [Chaudhry et al., 2008] Q. CHAUDHRY, M. SCOTTER, J. BLACKBURN, B. ROSS, A. BOXALL, L. CASTLE, R. AITKEN, R. WATKINS. Applications and implications of nanotechnologies for the food sector, *Food Additives and Contaminants*, 2008, **25**, 241-258. DOI: [10.1080/02652030701744538](https://doi.org/10.1080/02652030701744538)
- [Chen et al., 1991] Y. L. CHEN, C. A. HELM, J. N. ISRAELACHVILI. Molecular Mechanisms Associated with Adhesion and Contact Angle Hysteresis of Monolayer Surfaces, *J. Phys. Chem.*, 1991, **95**, 10736-10747. DOI: [10.1021/j100179a041](https://doi.org/10.1021/j100179a041)
- [Chernousova and Eppel, 2013] S. CHERNOUSOVA AND M. EPPEL. Silver as Antibacterial Agent: Ion, Nanoparticle, and Metal, *Angew. Chem. Int. Ed.*, 2013, **52**, 1636-1653. DOI: [10.1002/anie.201205923](https://doi.org/10.1002/anie.201205923)
- [Cho et al., 2012] W. J. CHO, Y. KIM, J. K. KIM. Ultrahigh-Density Array of Silver Nanoclusters for SERS Substrate with High Sensitivity and Excellent Reproducibility, *ACS Nano*, 2012, **6**, 249-255. DOI: [10.1021/nn2035236](https://doi.org/10.1021/nn2035236)
- [Choi et al. 2009] O. CHOI, T. E. CLEVENGER, B. DENG, R. Y. SURAMPALLI, L. ROSS, JR. M Role of sulfide and ligand strength in controlling nanosilver toxicity, *Water research*, 2009, **43**, 1879-1886. DOI: [10.1016/j.watres.2009.01.029](https://doi.org/10.1016/j.watres.2009.01.029)
- [Chopra, 2007] I. CHOPRA. The increasing use of silver-based products as antimicrobial agents: a useful development or a cause for concern?, *Journal of Antimicrobial Chemotherapy*, 2007, **59**, 587-590. DOI: [10.1093/jac/dkm006](https://doi.org/10.1093/jac/dkm006)
- [Chudakov et al., 2010] D. M. CHUDAKOV, M. V. MATZ, S. LUKYANOV, AND K. A. LUKYANOV. Fluorescent Proteins and Their Applications in Imaging Living Cells and Tissues, *Physiol. Rev.*, 2010, **90**, 1103-1163. DOI: [10.1152/physrev.00038.2009](https://doi.org/10.1152/physrev.00038.2009)

- [Claverie et al., 2006] A. CLAVERIE, C. BONAFOS, G. BENASSAYAG, S. SCHAMM, N. CHERKASHIN, V. PAILLARD, P. DIMITRAKIS, E. KAPETENAKIS, D. TSOUKALAS, T. MULLER, B. SCHMIDT, K. H. HEINIG, M. PEREGO, M. FANCIULLI, D. MATHIOT, M. CARRADA, P. NORMAND. Materials Science Issues for the Fabrication of Nanocrystal Memory Devices by Ultra Low Energy Ion Implantation, *Diffusion in Solids and Liquids*, 2006, **258**, 531-541. DOI: [10.4028/www.scientific.net/DDF.258-260.531](https://doi.org/10.4028/www.scientific.net/DDF.258-260.531)
- [Consalvey et al., 2005] M. CONSALVEY , R. G. PERKINS , D. M. PATERSON, G. J. C. UNDERWOOD. PAM fluorescence: a beginners guide for benthic diatomists, *Diatom Research*, 2005, **20**, 1-22. DOI: [10.1080/0269249X.2005.9705619](https://doi.org/10.1080/0269249X.2005.9705619)
- [Coronado and Schatz, 2003] E. A. CORONADO, G. C. SCHATZ. Surface plasmon broadening for arbitrary shape nanoparticles: A geometrical probability approach, *J. Chem. Phys.*, 2003, **119**, 3926-3934. DOI: [10.1063/1.1587686](https://doi.org/10.1063/1.1587686)
- [Costerton et al., 1999] J. W. COSTERTON, P. S. STEWART, E. P. GREENBERG. Bacterial Biofilms: A Common Cause of Persistent Infections, *Science*, 1999, **284**, 1318-1322. DOI: [10.1126/science.284.5418.1318](https://doi.org/10.1126/science.284.5418.1318)
- [Cumberland and Lead, 2013] S. A. CUMBERLAND, J. R. LEAD. Synthesis of NOM-Capped Silver Nanoparticles: Size, Morphology, Stability, and NOM Binding Characteristics, *ACS Sustainable Chem. Eng.*, 2013, **1**, 817-825. DOI: [10.1021/sc400063r](https://doi.org/10.1021/sc400063r)
- [Czanderna, 1964] A. W. CZANDERNA. The Adsorption of Oxygen on Silver, *J. Phys. Chem.*, 1964, **68**, 2765-2771. DOI: [10.1021/j100792a005](https://doi.org/10.1021/j100792a005)
- [Deegan et al., 2000] R. D. DEEGAN, O. BAKAJIN, T. F. DUPONT, G. HUBER, S. R. NAGEL, T. A. WITTEN. Contact line deposits in an evaporating drop, *Phys. Rev. E*, 2000, **62**, 756-765. DOI: [10.1103/PhysRevE.62.756](https://doi.org/10.1103/PhysRevE.62.756)
- [Delmas et al., 2011] M. DELMAS, M. MONTHIOUX, T. ONDARÇUHU. Contact Angle Hysteresis at the Nanometer Scale, *Phys. Rev. Lett.*, 2011, **106**, 136102. DOI: [10.1103/PhysRevLett.106.136102](https://doi.org/10.1103/PhysRevLett.106.136102)
- [Despax and Flouttard, 1989] B. DESPAX, J. L. FLOUTTARD. Synthesis of gold-carbon composites by simultaneous sputtering and plasma polymerization of propane in R.F. capacitively coupled diode system (13.56 MHz), *Thin Solid Films*, 168 (1989) 81-88. *Appl. Phys.*, 1989, **168**, 81-88. DOI: [10.1016/0040-6090\(89\)90691-3](https://doi.org/10.1016/0040-6090(89)90691-3)
- [Despax and Raynaud, 2007] B. DESPAX, P. RAYNAUD. Deposition of “Polysiloxane” Thin Films Containing Silver Particles by an RF Asymmetrical Discharge, *Plasma Process. Polym.*, 2007, **4**, 127-134. DOI: [10.1002/ppap.200600083](https://doi.org/10.1002/ppap.200600083)
- [Despax et al., 2011] B. DESPAX, C. SAULOU, P. RAYNAUD, L. DATAS, M. MERCIER-BONIN. Transmission electron microscopy for elucidating the impact of silver-based treatments (ionic silver versus nanosilver-containing coating) on the model yeast *Saccharomyces cerevisiae*, *Nanotechnology*, 2011, **22**, 175101. DOI: [10.1088/0957-4484/22/17/175101](https://doi.org/10.1088/0957-4484/22/17/175101)
- [Dilonardo et al., 2010] E. DILONARDO, A. MILELLA, F. PALUMBO, G. CAPITANI, R. D’AGOSTINO, F. FRACASSI. One-Step Plasma Deposition of Platinum Containing Nanocomposite Coatings, *Plasma Process. Polym.*, 2010, **7**, 51-58. DOI: [10.1002/ppap.200900118](https://doi.org/10.1002/ppap.200900118)
- [Donnelly, 1990] V. M. DONNELLY. Optical diagnostic techniques for low pressure plasma processing, *Plasma-Surface Interactions and Processing of Materials*, 1990, **176**, 57-93. DOI: [10.1007/978-94-009-1946-4\\_3](https://doi.org/10.1007/978-94-009-1946-4_3)

- [Drábik et al., 2015] M. DRÁBIK, J. PEŠIČKA, H. BIEDERMAN, D. HEGEMANN. Long-term aging of Ag/a-C:H:O nanocomposite coatings in air and in aqueous environment, *Sci. Technol. Adv. Mater.*, 2015, **16**, 025005. DOI: [10.1088/1468-6996/16/2/025005](https://doi.org/10.1088/1468-6996/16/2/025005)
- [Duran et al., 2007] N. DURAN, P. D. MARCATO, G. I. H. DE SOUZA, O. L. ALVES, E. ESPOSITO. Antibacterial Effect of Silver Nanoparticles Produced by Fungal Process on Textile Fabrics and Their Effluent Treatment, *J. Biomed. Nanotechnol.*, 2007, **3**, 203-208. DOI: [10.1166/jbn.2007.022](https://doi.org/10.1166/jbn.2007.022)
- [Eckardt et al., 1984] H. ECKARDT, L. FRITSCHKE, J. NOFFKE. Self-consistent relativistic band structure of the noble metals, *J. Phys. F: Met. Phys.*, 1984, **14**, 97-112. DOI: [10.1088/0305-4608/14/1/013](https://doi.org/10.1088/0305-4608/14/1/013)
- [El Badawy et al., 2010] A. M. EL BADAWY, T. LUXTON, R. G. SILVA, K. G. SCHECKEL, M. T. SUIDAN, T. M. TOLAYMAT. Impact of Environmental Conditions (pH, Ionic Strength, and Electrolyte Type) on the Surface Charge and Aggregation of Silver Nanoparticles Suspensions, *Environ. Sci. Technol.*, 2010, **44**, 1260-1266. DOI: [10.1021/es902240k](https://doi.org/10.1021/es902240k)
- [El Badawy et al., 2011] A. M. EL BADAWY, R. G. SILVA, K. G. SCHECKEL, M. T. SUIDAN, T. M. TOLAYMAT. I Surface Charge-Dependent Toxicity of Silver Nanoparticles, *Environ. Sci. Technol.*, 2011, **45**, 283-287. DOI: [10.1021/es1034188](https://doi.org/10.1021/es1034188)
- [El Badawy et al., 2012] A. M. EL BADAWY, K. G. SCHECKEL, M. SUIDAN, T. TOLAYMAT. The impact of stabilization mechanism on the aggregation kinetics of silver nanoparticles, *Science of the Total Environment*, 2012, **429**, 325-331. DOI: [10.1016/j.scitotenv.2012.03.041](https://doi.org/10.1016/j.scitotenv.2012.03.041)
- [Elechiguerra et al., 2005a] J. L. ELECHIGUERRA, J. L. BURT, J. R. MORONES, A. CAMACHO-BRAGADO, X. GAO, H. H. LARA, M. J. YACAMAN. Interaction of silver nanoparticles with HIV-1, *E Journal of Nanobiotechnology* 2005, **3:6** doi:, 2005, **3**, 1-10. DOI: [10.1186/1477-3155-3-6](https://doi.org/10.1186/1477-3155-3-6)
- [Elechiguerra et al., 2005b] J. L. ELECHIGUERRA, L. LARIOS-LOPEZ, C. LIU, D. GARCIA-GUTIERREZ, A. CAMACHO-BRAGADO, M. J. YACAMAN. Corrosion at the Nanoscale: The Case of Silver Nanowires and Nanoparticles, *Chem. Mater.*, 2005, **17**, 6042-6052. DOI: [10.1021/cm051532n](https://doi.org/10.1021/cm051532n)
- [Espiau de Lamaestre and H. Bernas, 2006] R. ESPIAU DE LAMAËSTRE, H. BERNAS. Significance of lognormal nanocrystal size distributions, *Physical Review B*, 2006, **73**, 125317. DOI: [10.1103/PhysRevB.73.125317](https://doi.org/10.1103/PhysRevB.73.125317)
- [European Pharmacopoeia, 2008] European Directorate for the Quality of Medicines - Council of Europe (COE), European Pharmacopoeia 6th Edition: Supplement 6.3, BDC, 2008
- [Evanoff and Chumanov, 2005] D. D. EVANOFF JR., G. CHUMANOV. Synthesis and Optical Properties of Silver Nanoparticles and Arrays, *ChemPhysChem*, 2005, **6**, 1221-1231. DOI: [10.1002/cphc.200500113](https://doi.org/10.1002/cphc.200500113)
- [Fabrega et al., 2009] J. FABREGA, S. R. FAWCETT, J. C. RENSHAW, J. R. LEAD. M Silver Nanoparticle Impact on Bacterial Growth: Effect of pH, Concentration, and Organic Matter, *Environ. Sci. Technol.*, 2009, **43**, 7285-7290. DOI: [10.1021/es803259g](https://doi.org/10.1021/es803259g)
- [Farcau et al., 2010] C. FARCAU, C. BONAFOS, P. BENZO, G. BENASSAYAG, R. CARLES. Combining elastic and resonant inelastic optical spectroscopies for multiscale probing of embedded nanoparticle architectures, *J. Appl. Phys.*, 2010, **108**, 093516. DOI: [10.1063/1.3506680](https://doi.org/10.1063/1.3506680)
- [Favia et al., 2000] P. FAVIA, M. VULPIO, R. MARINO, R. D'AGOSTINO, R. P. MOTA, M. CATALANO. Plasma-Deposition of Ag-Containing Polyethyleneoxide-Like Coatings, *Plasmas and Polymers*, 2000, **5**, 1-14. DOI: [10.1023/A:1009517408368](https://doi.org/10.1023/A:1009517408368)

- [Feng et al., 2000] Q. L. FENG, J. WU, G. Q. CHEN, F. Z. CUI, T. N. KIM, J. O. KIM. A mechanistic study of the antibacterial effect of silver ions on *Escherichia coli* and *Staphylococcus aureus*, *J. Biomed. Mater. Res*, 2000, **52**, 662-668. DOI: [10.1002/1097-4636\(20001215\)52:4<662::AID-JBM10>3.0.CO;2-3](https://doi.org/10.1002/1097-4636(20001215)52:4<662::AID-JBM10>3.0.CO;2-3)
- [Fleischmann et al., 1974] M. FLEISCHMANN, P. J. HEMDRA, A. J. MCQUILLAN. Raman spectra of pyridine adsorbed at a silver electrode, *Chemical Physics Letters*, 1974, **26**, 163-166. DOI: [10.1016/0009-2614\(74\)85388-1](https://doi.org/10.1016/0009-2614(74)85388-1)
- [Foldbjerg and Autrup, 2013] R. FOLDBJERG, H. AUTRUP. Mechanisms of Silver Nanoparticle Toxicity, *Arch. Bas. App. Med.*, 2013, **1**, 5-15.
- [Forouhi and Bloomer, 1986] A. R. FOROUI, I. BLOOMER. Optical dispersion relations for amorphous semiconductors and amorphous dielectrics, *Physical Review B*, 1986, **34**, 7018-7026. DOI: [10.1103/PhysRevB.34.7018](https://doi.org/10.1103/PhysRevB.34.7018)
- [Fortin and Campbell, 2001] C. FORTIN, P. G. C. CAMPBELL. Thiosulfate Enhances Silver Uptake by a Green Alga: Role of Anion Transporters in Metal Uptake, *Environ. Sci. Technol.*, 2001, **35**, 2214-2218. DOI: [10.1021/es0017965](https://doi.org/10.1021/es0017965)
- [Franey et al., 1985] J. P. FRANNEY, G. W. KAMMLOTT, T. E. GRAEDEL. The corrosion of silver by atmospheric sulphurous gases, *Corrosion Science*, 1985, **25**, 133-143. DOI: [10.1016/0010-938X\(85\)90104-0](https://doi.org/10.1016/0010-938X(85)90104-0)
- [Garcia-parajo et al., 2001] M. F. GARCIA-PARAJO, M. KOOPMAN, E. M. H. P. VAN DIJK, V. SUBRAMANIAM, N. F. VAN HULST. The nature of fluorescence emission in the red fluorescent protein DsRed, revealed by single molecule detection, *PNAS*, 2001, **98**, 14392-14397. DOI: [10.1073/pnas.251525598](https://doi.org/10.1073/pnas.251525598)
- [Garnett, 1904] J. C. M. GARNETT. Colours in Metal Glasses and in Metallic Films, *Philos. Trans. R. Soc. A Math. Phys. Eng. Sci.*, 1904, **203**, 385-420.
- [Glover et al., 2011] R. D. GLOVER, J. M. MILLER, J. E. HUTCHISON. Generation of Metal Nanoparticles from Silver and Copper Objects: Nanoparticle Dynamics on Surfaces and Potential Sources of Nanoparticles in the Environment, *ACS Nano*, 2011, **5**, 8950-8957. DOI: [10.1021/nn2031319](https://doi.org/10.1021/nn2031319)
- [Gondikas et al., 2012] A. P. GONDIKAS, A. MORRIS, B. C. REINSCH, S. M. MARINAKOS, G. V. LOWRY, H. HSU-KIM. Cysteine-Induced Modifications of Zero-valent Silver Nanomaterials: Implications for Particle Surface Chemistry, Aggregation, Dissolution, and Silver Speciation, *Environ. Sci. Technol.*, 2012, **46**, 7037-7045. DOI: [10.1021/es3001757](https://doi.org/10.1021/es3001757)
- [Goujon et al., 2004] M. GOUJON, T. BELMONTE, G. HENRION. OES and FTIR diagnostics of HMDSO/O<sub>2</sub> gas mixtures for SiO<sub>x</sub> deposition assisted by RF plasma, *Surface and Coatings Technology*, 2004, **188-189**, 756-761. DOI: [10.1016/j.surfcoat.2004.07.048](https://doi.org/10.1016/j.surfcoat.2004.07.048)
- [Graedel et al., 1985] T. E. GRAEDEL, J. P. FRANNEY, G. J. GUALTIERI, G. W. KAMMLOTY, D. L. MALM. On the mechanism of silver and copper sulfidation by atmospheric H<sub>2</sub>O and OCS, *Corrosion Science*, 1985, **25**, 1163-1180. DOI: [10.1016/0010-938X\(85\)90060-5](https://doi.org/10.1016/0010-938X(85)90060-5)
- [Gruian et al., 2012] C. GRUIAN, E. VANEA, S. SIMON, V. SIMON. FTIR and XPS studies of protein adsorption onto functionalized bioactive glass, *Biochimica et Biophysica Acta*, 2012, **1824**, 873-881. DOI: [10.1016/j.bbapap.2012.04.008](https://doi.org/10.1016/j.bbapap.2012.04.008)
- [Gupta et al., 1998] A. GUPTA, M. MAYNES, S. SILVER. Effects of Halides on Plasmid-Mediated Silver Resistance in *Escherichia coli*, *Appl. Environ. Microbiol.*, 1998, **64**, 5042-5045.

- [Haider and Kang, 2015] A. HAIDER, I.-K. KANG. Preparation of Silver Nanoparticles and Their Industrial and Biomedical Applications: A Comprehensive Review, *J. Advances in Materials Science and Engineering*, 2015, **2015**, 1-16. DOI: [10.1155/2015/165257](https://doi.org/10.1155/2015/165257)
- [Hansen and Baun, 2012] S. F. HANSEN, A. BAUN. When enough is enough, *Nature Nanotechnology*, 2012, **7**, 409-411. DOI: [10.1038/nnano.2012.115](https://doi.org/10.1038/nnano.2012.115)
- [Hartland, 2011] G. V. HARTLAND. Optical Studies of Dynamics in Noble Metal Nanostructures, *Chem. Rev.*, 2011, **111**, 3858-3887. DOI: [10.1021/cr1002547](https://doi.org/10.1021/cr1002547)
- [Hatchett and White, 1996] D. W. HATCHETT, H. S. WHITE. Electrochemistry of Sulfur Adlayers on the Low-Index Faces of Silver, *J. Phys. Chem.*, 1996, **100**, 9854-9859. DOI: [10.1021/jp953757z](https://doi.org/10.1021/jp953757z)
- [He et al., 2011] D. HE, A. M. JONES, S. GARG, A. N. PHAM, T. D. WAITE. Silver Nanoparticle-Reactive Oxygen Species Interactions: Application of a Charging-Discharging Model, *J. Phys. Chem. C*, 2011, **115**, 5461-5468. DOI: [10.1021/jp111275a](https://doi.org/10.1021/jp111275a)
- [He et al., 2012a] L. W. HE, Y.-T. ZHOU, W. G. WAMER, M. D. BOUDREAU, J.-J. YIN. Mechanisms of the pH dependent generation of hydroxyl radicals and oxygen induced by Ag nanoparticles, *Biomaterials*, 2012, **33**, 7547-7555. DOI: [10.1016/j.biomaterials.2012.06.076](https://doi.org/10.1016/j.biomaterials.2012.06.076)
- [He et al., 2012b] D. HE, J. J. DORANTES-ARANDA, T. D. WAITE. Silver Nanoparticle - Algae Interactions: Oxidative Dissolution, Reactive Oxygen Species Generation and Synergistic Toxic Effects, *Environ. Sci. Technol.*, 2012, **46**, 8731-8738. DOI: [10.1021/es300588a](https://doi.org/10.1021/es300588a)
- [He et al., 2012c] D. HE, S. GARG, T. D. WAITE. H<sub>2</sub>O<sub>2</sub>-Mediated Oxidation of Zero-Valent Silver and Resultant Interactions among Silver Nanoparticles, Silver Ions, and Reactive Oxygen Species, *Langmuir*, 2012, **28**, 10266-10275. DOI: [10.1021/la300929g](https://doi.org/10.1021/la300929g)
- [Hegemann et al., 1999] D. HEGEMANN, U. VOHRER, C. OEHR, R. RIEDEL. Deposition of SiO<sub>x</sub> films from O<sub>2</sub>/HMDSO plasmas, *Surface and Coatings Technology*, 1999, **116-119**, 1033-1036. DOI: [10.1016/S0257-8972\(99\)00092-4](https://doi.org/10.1016/S0257-8972(99)00092-4)
- [Henglein, 1988] A. HENGLEIN. Mechanism of reactions on colloidal microelectrodes and size quantization effects, *Topics in Current Chemistry*, 1988, **143**, 113-180. DOI: [10.1007/BFb0018073](https://doi.org/10.1007/BFb0018073)
- [Henry, 1998] W. Z. C. R. HENRY. Surface studies of supported model, *Surface Science Reports*, 1998, **31**, 231-325. DOI: [10.1016/S0167-5729\(98\)00002-8](https://doi.org/10.1016/S0167-5729(98)00002-8)
- [Hilfiker et al., 2008] J. N. HILFIKER, N. SINGH, T. TIWALD, D. CONVEY, S. M. SMITH, J. H. BAKER, H. G. TOMPKINS. Survey of methods to characterize thin absorbing films with Spectroscopic Ellipsometry, *Thin Solid Films*, 2008, **516**, 7979-7989. DOI: [10.1016/j.tsf.2008.04.060](https://doi.org/10.1016/j.tsf.2008.04.060)
- [Hollstein et al., 1977] T. HOLLSTEIN, U. KREIBIG, F. LEIS. Optical Properties of Cu and Ag in the Intermediate Region between Pure Drude and Interband Absorption, *Phys. Stat. Sol. (b)*, 1977, **83**, 545-556. DOI: [10.1002/pssb.2220820217](https://doi.org/10.1002/pssb.2220820217)
- [Holt and Bard, 2005] K. B. HOLT, A. J. BARD. Interaction of Silver(I) Ions with the Respiratory Chain of *Escherichia coli*: An Electrochemical and Scanning Electrochemical Microscopy Study of the Antimicrobial Mechanism of Micromolar Ag<sup>+</sup>, *Biochemistry*, 2005, **44**, 13214-13223. DOI: [10.1021/bi0508542](https://doi.org/10.1021/bi0508542)
- [Hotze et al., 2010] E. M. HOTZE, T. PHENRAT, G. V. LOWRY. Nanoparticle Aggregation: Challenges to Understanding Transport and Reactivity in the Environment, *J. Environ. Qual.*, 2010, **39**, 1909-1924. DOI: [10.2134/jeq2009.0462](https://doi.org/10.2134/jeq2009.0462)



- [Hoyle and Costerton, 1991] J. D. HOYLE BD, J. W. COSTERTON. Bacterial resistance to antibiotics: The role of biofilms, *Prog Drug Res*, 1991, **37**, 91-105. DOI: [10.1007/978-3-0348-7139-6\\_2](https://doi.org/10.1007/978-3-0348-7139-6_2)
- [Hu and Larson, 2005] H. HU, R. G. LARSON. Analysis of the effect of Marangoni stresses on the microflow in an evaporating sessile droplet, *Langmuir*, 2005, **21**, 3972-3980. DOI: [10.1021/la0475270](https://doi.org/10.1021/la0475270)
- [Hughes, 2012] A. B. HUGHES. *Amino Acids, Peptides and Proteins in Organic Chemistry: Volume 5 Analysis and Functions of Amino Acids and Peptides*, 2012, Wiley.
- [Ivask et al., 2014] A. IVASK, A. ELBADAWY, C. KAWETEERAWAT, D. BOREN, H. FISCHER, Z. JI, C. H. CHANG, R. LIU, T. TOLAYMAT, D. TELESCA, J. I. ZINK, Y. COHEN, P. A. HOLDEN, H. A. GODWIN. Toxicity Mechanisms in *Escherichia coli* Vary for Silver Nanoparticles and Differ from Ionic Silver, *ACS Nano*, 2014, **8**, 374-386. DOI: [10.1021/nn4044047](https://doi.org/10.1021/nn4044047)
- [Jachimska and Pajor, 2012] B. JACHIMSKA, A. PAJOR. Physico-chemical characterization of bovine serum albumin in solution and as deposited on surfaces, *Bioelectrochemistry*, 2012, **87**, 138-146. DOI: [10.1016/j.bioelechem.2011.09.004](https://doi.org/10.1016/j.bioelechem.2011.09.004)
- [Jenney and Anderson, 2000] C. R. JENNEY, J. M. ANDERSON. Adsorbed serum proteins responsible for surface dependent human macrophage behavior, *J. Biomed Mater. Res.*, 2000, **49**, 435-447. DOI: [10.1002/\(SICI\)1097-4636\(20000315\)49:4<435::AID-JBM2>3.0.CO;2-Y](https://doi.org/10.1002/(SICI)1097-4636(20000315)49:4<435::AID-JBM2>3.0.CO;2-Y)
- [Jiang et al., 2004] H. JIANG, S. MANOLACHE, A. C. LEE WONG, F. S. DENES. Plasma-Enhanced Deposition of Silver Nanoparticles onto Polymer and Metal Surfaces for the Generation of Antimicrobial Characteristics, *Journal of Applied Polymer Science*, 2004, **93**, 1411-1422. DOI: [10.1002/app.20561](https://doi.org/10.1002/app.20561)
- [Jones et al., 2011] M. R. JONES, K. D. OSBERG, R. J. MACFARLANE, M. R. LANGILLE, C. A. MIRKIN. Templated Techniques for the Synthesis and Assembly of Plasmonic Nanostructures, *Chem. Rev.*, 2011, **111**, 3736-3827. DOI: [10.1021/cr1004452](https://doi.org/10.1021/cr1004452)
- [Katz et al., 1999] G. KATZ, Y. ZEIRI, R. KOSLOFF. Non-adiabatic charge transfer process of oxygen on metal surface, *Surface Science*, 1999, **425**, 1-14. DOI [10.1016/S0039-6028\(98\)00909-1](https://doi.org/10.1016/S0039-6028(98)00909-1).
- [Kay and Hecq, 1984] E. KAY, M. HECQ. Metal clusters in plasma polymerized matrices: Gold, *J. Appl. Phys.*, 1984, **55**, 340-374. DOI: [10.1063/1.333082](https://doi.org/10.1063/1.333082)
- [Kilin et al., 2008] D. S. KILIN, O. V. PREZHDO, Y. XIA. Shape-controlled synthesis of silver nanoparticles: *Ab initio* study of preferential surface coordination with citric acid, *Chemical Physics Letters*, 2008, **458**, 113-116. DOI: [10.1016/j.cplett.2008.04.046](https://doi.org/10.1016/j.cplett.2008.04.046)
- [Kilty and Sachtler, 1974] P. A. KILTY, W. M. SACHTLER. The mechanism of the selective oxidation of ethylene to ethylene oxide, *Catal. Rev. Sci. Eng.*, 1974, **10**, 1-16. DOI: [10.1080/01614947408079624](https://doi.org/10.1080/01614947408079624).
- [Kirk, 1988] C. T. KIRK. Quantitative analysis of the effect of disorder-induced mode coupling on infrared absorption in silica, *Physical Review B*, 1988, **38**, 1255-1273. DOI: [10.1103/PhysRevB.38.1255](https://doi.org/10.1103/PhysRevB.38.1255)
- [Kirk, 2001] C. T. KIRK. Quantitative analysis of the effect of disorder-induced mode coupling on infrared absorption in silica, *Phys. Rev. B*, 1988, **38**, 1255-1273. DOI: [10.1103/PhysRevB.38.1255](https://doi.org/10.1103/PhysRevB.38.1255)
- [Kittel, 2004] C. KITTEL. *Introduction to Solid State Physics*, 2004, Wiley.
- [Kittler et al., 2010] S. KITTLER, C. GREULICH, J. DIENDORF, M. KÖLLER, M. EPPLE. Toxicity of Silver Nanoparticles Increases during Storage Because of Slow Dissolution under Release of Silver Ions, *Chem. Mater.*, 2010, **22**, 4548-4554. DOI: [10.1021/cm100023p](https://doi.org/10.1021/cm100023p)

- [Klasen, 2000] H. J. KLASEN. Historical review of the use of silver in the treatment of burns, *Burns*, 2000 **26**, 117-130. DOI: [10.1016/S0305-4179\(99\)00108-4](https://doi.org/10.1016/S0305-4179(99)00108-4)
- [Körner et al., 2009] E. KÖRNER, G. FORTUNATO, D. HEGEMANN. Influence of RF Plasma Reactor Setup on Carboxylated Hydrocarbon Coatings, *Plasma Process. Polym.*, 2009, **6**, 119-125. DOI: [10.1002/ppap.200800102](https://doi.org/10.1002/ppap.200800102)
- [Körner et al., 2010] E. KÖRNER, M. H. AGUIRRE, G. FORTUNATO, A. RITTER, J. RÜHE, D. HEGEMANN. Formation and Distribution of Silver Nanoparticles in a Functional Plasma Polymer Matrix and Related Ag<sup>+</sup> Release Properties, *Plasma Process. Polym.*, 2010, **7**, 619-625. DOI: [10.1002/ppap.200900163](https://doi.org/10.1002/ppap.200900163)
- [Körner et al., 2012] E. KÖRNER, B. HANSELMANN, P. CIERNIAK, D. HEGEMANN. Tailor-Made Silver Release Properties of Silver-Containing Functional Plasma Polymer Coatings Adjusted Through a Macroscopic Kinetics Approach, *Plasma Chem Plasma Process*, 2012, **32**, 619-627. DOI: [10.1007/s11090-012-9362-3](https://doi.org/10.1007/s11090-012-9362-3)
- [Kortshagen, 2009] U. KORTSHAGEN. Nonthermal plasma synthesis of semiconductor nanocrystals, *J. Phys. D: Appl. Phys.*, 2009, **42**, 113001. DOI: [10.1088/0022-3727/42/11/113001](https://doi.org/10.1088/0022-3727/42/11/113001)
- [Kozai et al., 2012] T. D. YOSHIDA KOZAI, N. B. LANGHALS, P. R. PATEL, X. DENG, H. ZHANG, K. L. SMITH, J. LAHANN, N. A. KOTOV, D. R. KIPKE. Ultrasmall implantable composite microelectrodes with bioactive surfaces for chronic neural interfaces, *Nature materials*, 2012, **11**, 1065-1073. DOI: [10.1038/nmat3468](https://doi.org/10.1038/nmat3468)
- [Kreibig and Vollmer, 1985] U. KREIBIG, M. VOLLMER. *Optical properties of metal clusters*, 1985, Springer. DOI: [10.1007/978-3-662-09109-8](https://doi.org/10.1007/978-3-662-09109-8)
- [Kvítek et al., 2008] L. KVÍTEK, A. PANÁČEK, J. SOUKUPOVÁ, M. KOLÁŘ, R. VEČEŘOVÁ, R. PRUCEK, M. HOLECOVÁ, R. ZBOŘIL. Effect of Surfactants and Polymers on Stability and Antibacterial Activity of Silver Nanoparticles (NPs), *J. Phys. Chem. C*, 2008, **112**, 5825-5834. DOI: [10.1021/jp711616v](https://doi.org/10.1021/jp711616v)
- [Kylián et al., 2013] O. KYLIÁN, A. CHOUKOUROV, H. BIEDERMANRRIN. Nanostructured plasma polymers, *Thin Solid Films*, 2013, **548**, 1-17. DOI: [10.1016/j.tsf.2013.09.003](https://doi.org/10.1016/j.tsf.2013.09.003)
- [Lacy et al., 1996] W. B. LACY, J. M. WILLIAMS, L. A. WENZLER, T. P. BEEBE JR., J. M. HARRIS. Characterization of SiO<sub>2</sub>-Overcoated Silver-Island Films as Substrates for Surface-Enhanced Raman Scattering, *Anal. Chem.*, 1996, **68**, 1003-1011. DOI: [10.1021/ac950860b](https://doi.org/10.1021/ac950860b)
- [Lamendola et al., 1997] R. LAMENDOLA, R. D'AGOSTINO, F. FRACASSI. Thin film deposition from hexamethyldisiloxane fed glow discharges, *Plasmas and Polymers*, 1997, **2**, 147-164. DOI: [10.1007/BF02766151](https://doi.org/10.1007/BF02766151)
- [Larivière et al., 1992] G. P. LARIVIÈRE, J. M. FRIGERIO, J. RIVORY, F. ABELÈS. Estimate of the degree of inhomogeneity of the refractive index of dielectric films from spectroscopic ellipsometry, *Appl. Opt.*, 1992, **31**, 6056-6061. DOI: [10.1364/AO.31.006056](https://doi.org/10.1364/AO.31.006056)
- [Larsericsdotter et al., 2005] H. LARSERICSDOTTER, S. OSCARSSON, J. BUIJS. Structure, stability, and orientation of BSA adsorbed to silica, *J. Colloid Interface Sci.*, 2005, **289**, 26-35. DOI: [10.1016/j.jcis.2005.03.064](https://doi.org/10.1016/j.jcis.2005.03.064)
- [Lartundo-Rojas, 2007] L. LARTUNDO-ROJAS. Influence de l'adsorption de protéine (BSA) sur le comportement électrochimique et la composition de surface d'un alliage Fe-17Cr en solution aqueuse, *Thèse de l'Université Paris VI*, 2007. HAL Id: [pastel-00004963](https://hal.archives-ouvertes.fr/pastel-00004963)

- [Laurent and Kay, 1989] C. LAURENT, E. KAY. Properties of metal clusters in polymerized hydrocarbon versus fluorocarbon matrices, *J. Appl. Phys.*, 1989, **65**, 1717-1723. DOI: [10.1063/1.342944](https://doi.org/10.1063/1.342944)
- [Le Faucheur et al., 2005] S. LE FAUCHEUR, R. BEHRA, L. SIGG. Phytochelatin induction, cadmium accumulation, and algal sensitivity to free cadmium ion in *Scenedesmus Vacuolatus*, *Environmental Toxicology and Chemistry*, 2005, **24**, 1731-1737. DOI: [10.1897/04-394R.1](https://doi.org/10.1897/04-394R.1)
- [Le Ouay and Stellacci, 2015] B. LE OUAY, F. STELLACCI. Antibacterial activity of silver nanoparticles: A surface science insight, *Nano Today*, 2015, **10**, 339-354. DOI: [10.1016/j.nantod.2015.04.002](https://doi.org/10.1016/j.nantod.2015.04.002)
- [Le Ru et al., 2006] E. C. LE RU, M. MEYER, P. G. ETCHEGOIN. Proof of Single-Molecule Sensitivity in Surface Enhanced Raman Scattering (SERS) by Means of a Two-Analyte Technique, *J. Phys. Chem. B*, 2006, **110**, 1944-1948. DOI: [10.1021/jp054732v](https://doi.org/10.1021/jp054732v)
- [Lee and Mather, 1977] J. I. LEE, A. E. MATHER. Solubility of Hydrogen Sulfide in Water, *Berichte der Bunsengesellschaft für physikalische Chemie*, 2004, **81**, 1020-1023. DOI: [10.1002/bbpc.19770811029](https://doi.org/10.1002/bbpc.19770811029)
- [Levard et al., 2011]. C. LEVARD, B. C. REINSCH, F. M. MICHEL, C. OUMAH, G. V. LOWRY, G. E. BROWN, JR. Sulfidation Processes of PVP-Coated Silver Nanoparticles in Aqueous Solution: Impact on Dissolution Rate, *Environ. Sci. Technol.*, 2011, **45**, 5260-5266. DOI: [10.1021/es2007758](https://doi.org/10.1021/es2007758)
- [Levard et al., 2012] C. LEVARD, E. M. HOTZE, G. V. LOWRY, G. E. JR. BROWN. Environmental Transformations of Silver Nanoparticles: Impact on Stability and Toxicity, *Environ. Sci. Technol.*, 2012, **46**, 6900-6914. DOI: [10.1021/es2037405](https://doi.org/10.1021/es2037405)
- [Li et al., 2010] X. LI, J. J. LENHART, H. W. WALKER. Dissolution-Accompanied Aggregation Kinetics of Silver Nanoparticles, *A Langmuir* 2010, 26(22), 16690–16698, 2010, **26**, 16690-16698. DOI: [10.1021/la101768n](https://doi.org/10.1021/la101768n)
- [Lide, 2009] D. R. LIDE. *Handbook of chemistry and physics*, 2009, CRC Press: Boca Raton
- [Lieberman and Lichtenberg, 2005] M. A. LIEBERMAN, A. J. LICHTENBERG. *Principles of plasma discharges and materials processing*, 2005, Wiley. DOI: [10.1002/0471724254](https://doi.org/10.1002/0471724254)
- [Linic et al., 2011] S. LINIC, P. CHRISTOPHER, D. B. INGRAM. Plasmonic-metal nanostructures for efficient conversion of solar to chemical energy, *Nat. Mater.*, 2011, **10**, 911-921. DOI: [10.1038/nmat3151](https://doi.org/10.1038/nmat3151)
- [Liu and Hurt, 2010] J. LIU, R. H. HURT. Ion Release Kinetics and Particle Persistence in Aqueous Nano-Silver Colloids, *Environ. Sci. Technol.*, 2010, **44**, 2169-2175. DOI: [10.1021/es9035557](https://doi.org/10.1021/es9035557)
- [Liu et al., 1998] Z. LIU, H. WANG, H. LI. Controlled synthesis of buried delta-layers of Ag nanocrystals for near-field plasmonic effects on free surfaces, *Appl. Phys. Lett.*, 1998, **72**, 1823-961. DOI: [10.1063/1.121196](https://doi.org/10.1063/1.121196)
- [Liu et al., 2010] J. LIU, D. A. SONSHINE, S. SHERVANI, R. H. HURT. Controlled Release of Biologically Active Silver from Nanosilver Surfaces, *ACS Nano*, 2010, **4**, 6903-6913. DOI: [10.1021/nn102272n](https://doi.org/10.1021/nn102272n)
- [Lok et al., 2007] C.-N. LOK, C.-M. HO, R. CHEN, Q.-Y. HE, W.-Y. YU, H. SUN, P. K.-H. TAM, J.-F.U CHIU, C.-M. CHE. Silver nanoparticles: partial oxidation and antibacterial activities, *J Biol Inorg Chem*, 2007, **12**, 527-534. DOI: [10.1007/s00775-007-0208-z](https://doi.org/10.1007/s00775-007-0208-z)

[Losurdo et al., 2009] M. LOSURDO, M.L BERGMAIR, G. BRUNO, D. CATTELAN, C. COBET, A. DE MARTINO, K. FLEISCHER, Z. DOHCEVIC-MITROVIC, N. ESSER, M. GALLIET, R. GAJIC, D. HEMZAL, K. HINGERL, J. HUMLICEK, R. OSSIKOVSKI, Z. V. POPOVIC, O. SAXL. Spectroscopic ellipsometry and polarimetry for materials and systems analysis at the nanometer scale: state-of-the-art, potential, and perspectives, *J. Nanopart. Res.*, 2009, **11**, 1521-1554. DOI: [10.1007/s11051-009-9662-6](https://doi.org/10.1007/s11051-009-9662-6)

[Lounis et al., 2001] B. LOUNIS, J. DEICH, F. I. ROSELL, S. G. BOXER, W. E. MOERNER. Photophysics of Ds Red, a Red Fluorescent Protein, from the Ensemble to the Single-Molecule Level, *J. Phys. Chem. B*, 2001, **105**, 5048-5054. DOI: [10.1021/jp010116x](https://doi.org/10.1021/jp010116x)

[Loza et al., 2014] K. LOZA, J. DIENDORF, C. SENGSTOCK, L. RUIZ-GONZALEZ, J. M. GONZALEZ-CALBET, M. VALLET-REGI, M. KÖLLERB, M. EPPLE. The dissolution and biological effects of silver nanoparticles in biological media, *J. Mater. Chem. B*, 2014, **2**, 1634-1643. DOI: [10.1039/c3tb21569e](https://doi.org/10.1039/c3tb21569e)

[Lukaszewicz, 2011] K. LUKASZKOWICZ. Review of nanocomposite thin films and coatings deposited by PVD and CVD technology, *Nanomaterials*, 2011, chapter 7, 145-162. DOI: [10.5772/25799](https://doi.org/10.5772/25799)

[Ma et al., 2012] R. MA, C. LEVARD, S. M. MARINAKOS, Y. CHENG, J. LIU, F. M. MICHEL, G. E. BROWN, JR., G. V. LOWRY. Size-Controlled Dissolution of Organic-Coated Silver Nanoparticles, *Environ. Sci. Technol.*, 2012, **46**, 752-759. DOI: [10.1021/es201686j](https://doi.org/10.1021/es201686j).

[Madigan et al., 2012] M. T. MADIGAN, J. M. MARTIN, D. A. STAHL, D. P. CLARK. *Brock biology of microorganisms*, 2012, Benjamin Cummings.

[Madigan et al., 2012]. M. T. MADIGAN, J. M. MARTINKO, D. A. STAHL, D. P. CLARK. *Brock Biology of Microorganisms*, 2012, Benjamin Cummings.

[Magni et al., 2001] D. MAGNI, CH. DESCHENAUX, CH. HOLLENSTEIN, A. CREATORE, P. FAYET. Oxygen diluted hexamethyldisiloxane plasmas investigated by means of *in situ* infrared absorption spectroscopy and mass spectrometry, *J. Phys. D: Appl. Phys.*, 2001, **34**, 87-94. DOI: [10.1088/0022-3727/34/1/315](https://doi.org/10.1088/0022-3727/34/1/315)

[Maier et al., 2001] S. A. MAIER, M. L. BRONGERSMA, P. G. KIK, S. MELTZER, A. A. G. REQUICHA, H. A. ATWATER. Plasmonics - A Route to Nanoscale Optical Devices, *Adv. Mater.*, 2001, **13**, 1501-1505. DOI: [10.1002/1521-4095\(200110\)13:19<1501::AID-ADMA1501>3.0.CO;2-Z](https://doi.org/10.1002/1521-4095(200110)13:19<1501::AID-ADMA1501>3.0.CO;2-Z)

[Maier, 2007] S. A. MAITTEL. *Plasmonics: Fundamentals and Applications*, 2007, Springer. DOI: [10.1007/0-387-37825-1](https://doi.org/10.1007/0-387-37825-1)

[Makasheva et al., 2013] K. MAKASHEVA, C. VILLENEUVE-FAURE, S. LE ROY, B. DESPAX, L. BOUDOU, C. LAURENT, G. TEYSSÉDRE. Silver nanoparticles embedded in dielectric matrix: charge transport analysis with application to control of space charge formation, *Annual Report IEEE Conference on Electrical Insulation and Dielectric Phenomena (IEEE CEIDP 2013)*, 2013, **1**, 238-241. DOI: [10.1109/CEIDP.2013.6747079](https://doi.org/10.1109/CEIDP.2013.6747079)

[Marambio-Jones and Hoek, 2010] C. MARAMBIO-JONES, E. M. V. HOEK. A review of the antibacterial effects of silver nanomaterials and potential implications for human health and the environment, *J. Nanopart. Res.*, 2010, **12**, 1531-1551. DOI: [10.1007/s11051-010-9900-y](https://doi.org/10.1007/s11051-010-9900-y)

[Marzbanrad et al., 2015] E. MARZBANRAD, G. RIVERS, P. PENG, B. ZHAO, N. Y. ZHOU. How morphology and surface crystal texture affect thermal stability of a metallic nanoparticle: the case of silver nanobelts and pentagonal silver nanowires, *Phys. Chem. Chem. Phys.*, 2015, **31**, 315-324. DOI: [10.1039/c4cp04129a](https://doi.org/10.1039/c4cp04129a)

[Massines et al., 2003] F. MASSINES, P. SEGUR, N. GHERARDI, C. KHAMPHAN, A. RICARD. Physics and chemistry in a glow dielectric barrier discharge at atmospheric pressure: diagnostics and modelling, *Surface and Coatings Technology*, 2003, **174-175**, 8-14. DOI: [10.1016/S0257-8972\(03\)00540-1](https://doi.org/10.1016/S0257-8972(03)00540-1)

[Matlab, 2012] Matlab, Version R2012b, 2012.

[Matz et al., 1999] M. V. MATZ, A. F. FRADKOV, Y. A. LABAS, A. P. SAVITSKY, A. G. ZARAIISKY, M. L. MARKELOV, S. A. LUKYANOV. Fluorescent proteins from nonbioluminescent Anthozoa species, *Nature Biotechnology*, 1999, **17**, 969-973. DOI: [10.1038/13657](https://doi.org/10.1038/13657)

[McDonnell and Russell, 1999] G. MCDONNELL, A. D. RUSSELL. Antiseptics and Disinfectants: Activity, Action, and Resistance, *Clin. Microbiol. Rev.*, 1999, **12**, 147-179.

[Mcmahon et al., 2005] M.D. MCMAHON, R. LOPEZ, H.M. MEYER III, L.C. FELDMAN, R.F. HAGLUND JR. Rapid tarnishing of silver nanoparticles in ambient laboratory air, *Appl. Phys. B*, 2005, **80**, 915-921. DOI: [10.1007/s00340-005-1793-6](https://doi.org/10.1007/s00340-005-1793-6)

[McPeack et al., 2015] K. M. MCPPEAK, S. V. JAYANTI, S. J. P. KRESS, S. MEYER, S. IOTTI, A. ROSSINELLI, D. J. NORRIS. Plasmonic Films Can Easily Be Better: Rules and Recipes, *ACS Photonics*, 2015, **2**, 326-333. DOI: [10.1021/ph5004237](https://doi.org/10.1021/ph5004237)

[Medasani et al., 2007] B. MEDASANI, Y. H. PARK, I. VASILIEV. Theoretical study of the surface energy, stress, and lattice contraction of silver nanoparticles, *Physical Review B*, 2007, **75**, 235436. DOI: [10.1103/PhysRevB.75.235436](https://doi.org/10.1103/PhysRevB.75.235436)

[Merchant et al., 2007] S. S. MERCHANT, S. E. PROCHNIK, O. VALLON, E. H. HARRIS, S. J. KARPOWICZ, G. B. WITMAN, A. TERRY, A. SALAMOV, L. K. FRITZ-LAYLIN, L. MARÉCHAL-DROUARD, W. F. MARSHALL, L.-H. QU, D. R. NELSON, A. A. SANDERFOOT, M. H. SPALDING, V. V. KAPITONOV, Q. REN, P. FERRIS, E. LINDQUIST, H. SHAPIRO, S. M. LUCAS, J. GRIMWOOD, J. SCHMUTZ, CHLAMYDOMONAS ANNOTATION TEAM, JGI ANNOTATION TEAM, I. V. GRIGORIEV, D. S. ROKHSAR, A. R. GROSSMAN. The *Chlamydomonas* Genome Reveals the Evolution of Key Animal and Plant Functions, *Science*, 2007, **318**, 245-251. DOI: [10.1126/science.1143609](https://doi.org/10.1126/science.1143609)

[Miao et al., 2009] A.-J. MIAO, K. A. SCHWEHR, C. XU, S.-J. ZHANG, Z. LUO, A. QUIGG, P. H. SANTOSCHI. The algal toxicity of silver engineered nanoparticles and detoxification by exopolymeric substance, *Environmental Pollution*, 2009, **157**, 3034-3041. DOI: [10.1016/j.envpol.2009.05.047](https://doi.org/10.1016/j.envpol.2009.05.047)

[Milliere et al., 2016] L. MILLIERE, K. MAKASHEVA, C. LAURENT, B. DESPAX, L. BOUDOU, G. TEYSSÉDRE. Silver nanoparticles as a key feature of a plasma polymer composite layer in mitigation of charge injection into polyethylene under dc stress, *J. Phys. D: Appl. Phys.*, 2016, **49**, 015304. DOI: [10.1088/0022-3727/49/1/015304](https://doi.org/10.1088/0022-3727/49/1/015304)

[Misra et al., 2012] S. K. MISRA, A. DYBOWSKA, D. BERHANU, S. N. LUOMA, E. VALSAMI-JONESIA. The complexity of nanoparticle dissolution and its importance in nanotoxicological studies, *Science of the Total Environment*, 2012, **438**, 225-232. DOI: [10.1016/j.scitotenv.2012.08.066](https://doi.org/10.1016/j.scitotenv.2012.08.066)

[Mitchell and Kiefer, 1988]. B. G. MITCHELL AND D. A. KIEFER. Chlorophyll a specific absorption and fluorescence excitation spectra for light-limited phytoplankton, *Deep Sea Research Part A. Oceanographic Research Papers*, 1998, **35**, 639-663. DOI: [10.1016/0198-0149\(88\)90024-6](https://doi.org/10.1016/0198-0149(88)90024-6)

[Mittelman et al., 2013] A. M. MITTELMAN, A. TAGHAVY, Y. WANG, L. M. ABRIOLO, K. D. PENNELL. Influence of dissolved oxygen on silver nanoparticle mobility and dissolution in water-saturated quartz sand, *J Nanopart Res*, 2013, **15**, 1765. DOI: [10.1007/s11051-013-1765-4](https://doi.org/10.1007/s11051-013-1765-4)

[Moisan and Pelletier, 2006] M. MOISAN, J. PELLETIER. *Physics of Collisional Plasmas*, 2006, Springer. DOI: [10.1007/978-94-007-4558-2](https://doi.org/10.1007/978-94-007-4558-2)

- [Molleman and Hiemstra, 2015] B. MOLLEMAN, T. HIEMSTRA. Surface Structure of Silver Nanoparticles as a Model for Understanding the Oxidative Dissolution of Silver Ions, *Langmuir*, 2015, **31**, 13361-13372. DOI: [10.1021/acs.langmuir.5b03686](https://doi.org/10.1021/acs.langmuir.5b03686)
- [Möller and Eckstein, 1984] W. MÖLLER, W. ECKSTEIN. TRIDYN - A TRIM simulation code including dynamic composition changes, *Nuclear Instruments and Methods in Physics Research Section B: Beam Interactions with Materials and Atoms*, 1984, **2**, 814-818. DOI: [10.1016/0168-583X\(84\)90321-5](https://doi.org/10.1016/0168-583X(84)90321-5)
- [Morones et al., 2005] J. R. MORONES, J. L. ELECHIGUERRA, A. CAMACHO, K. HOLT, J. B. KOURI, J. T. RAMÍREZ, M. J. YACAMAN. The bactericidal effect of silver nanoparticles, *Nanotechnology*, 2005, **16**, 2346-2353. DOI: [10.1088/0957-4484/16/10/059](https://doi.org/10.1088/0957-4484/16/10/059)
- [Mukherjee et al., 2013] S. MUKHERJEE, F. LIBISCH, N. LARGE, O. NEUMANN, L. V. BROWN, J. CHENG, J. B. LASSITER, E. A. CARTER, P. NORDLANDER, N. J. HALAS. Hot Electrons Do the Impossible: Plasmon-Induced Dissociation of H<sub>2</sub> on Au, *Nano Lett.*, 2013, **13**, 240-247. DOI: [10.1021/nl303940z](https://doi.org/10.1021/nl303940z)
- [Mulvaney et al., 1991] P. MULVANEY, T. LINNERT, A. HENGLEIN. Surface Chemistry of Colloidal Silver in Aqueous Solution: Observations on Chemisorption and Reactivity, *J. Phys. Chem.*, 1991, **95**, 7843-7846. DOI: [10.1021/j100173a053](https://doi.org/10.1021/j100173a053)
- [Muscat et al., 2001] A. J. MUSCAT, A. G. THORSNESS, G. MONTAÑO-MIRANDA. Characterization of residues formed by anhydrous hydrogen fluoride etching of doped oxides, *J. Vac. Sci. Technol. A*, 2001, **19**, 1854-486. DOI: [10.1116/1.1372907](https://doi.org/10.1116/1.1372907)
- [Nadworny et al., 2008] P. L. NADWORNÝ, J.F. WANG, E. E. TREDGET, R. E. BURRELL. Anti-inflammatory activity of nanocrystalline silver in a porcine contact dermatitis model, *Nanomedicine: NBM*, 2008, **4**, 241-251. DOI: [10.1016/j.nano.2008.04.006](https://doi.org/10.1016/j.nano.2008.04.006)
- [Nason et al., 1991] T. C. NASON, G. R. YANG, K. H. PARK, T. M. LU. Study of silver diffusion into Si(111) and SiO<sub>2</sub> at moderate temperatures, *J. Appl. Phys.*, 1991, **70**, 1392. DOI: [10.1063/1.349547](https://doi.org/10.1063/1.349547)
- [Navarro et al., 2008a] E. NAVARRO, A. BAUN, R. BEHRA, N. B. HARTMANN, J. FILSER, A.-J. MIAO, A. QUIGG, P. H. SANTSCHI, L. SIGG. Environmental behavior and ecotoxicity of engineered nanoparticles to algae, plants, and fungi, *Ecotoxicology*, 2008, **17**, 372-386. DOI: [10.1007/s10646-008-0214-0](https://doi.org/10.1007/s10646-008-0214-0)
- [Navarro et al., 2008b] E. NAVARRO, F. PICCAPIETRA, B. WAGNER, F. MARCONI, R. KAEGL, N. ODZAK, L. SIGG, R. BEHRA. Toxicity of Silver Nanoparticles to *Chlamydomonas reinhardtii*, *Environ. Sci. Technol.*, 2008, **42**, 8959-8964. DOI: [10.1021/es801785m](https://doi.org/10.1021/es801785m)
- [Navarro et al., 2015] E. NAVARRO, B. WAGNER, N. ODZAK, L. SIGG, R. BEHRA. Effects of Differently Coated Silver Nanoparticles on the Photosynthesis of *Chlamydomonas reinhardtii*, *Environ. Sci. Technol.*, 2015, **49**, 8041-8047. DOI: [10.1021/acs.est.5b01089](https://doi.org/10.1021/acs.est.5b01089)
- [Nelms, 2009] S. M. NELMS. *Inductively Coupled Plasma Mass Spectrometry Handbook*, 2005, Wiley. DOI: [10.1002/9781444305463](https://doi.org/10.1002/9781444305463)
- [Nie and Emory, 1997] S. NIE, S. R. EMORY. Probing Single Molecules and Single Nanoparticles by Surface-Enhanced Raman Scattering, *Science*, 1997, **275**, 1102-1106. DOI: [10.1126/science.275.5303.1102](https://doi.org/10.1126/science.275.5303.1102)
- [NIST] NIST. Atomic Spectra Database (ver. 5.3). [http://physics.nist.gov/PhysRefData/ASD/lines\\_form.html](http://physics.nist.gov/PhysRefData/ASD/lines_form.html)

- [Oates and Mücklich, 1995] T. W. H. OATES, A. MÜCKLICH. Evolution of plasmon resonances during plasma deposition of silver nanoparticles, *Nanotechnology* 16 (2005) 2606–2611, 2005, **16**, 2606-2611. DOI: [10.1088/0957-4484/16/11/023](https://doi.org/10.1088/0957-4484/16/11/023)
- [Ortega et al., 2015] F. G. ORTEGA, M. A. FERNÁNDEZ-BALDO, J. G. FERNÁNDEZ, M. J. SERRANO, M. I. SANZ, J. J. DIAZ-MOCHÓN, J. A. LORENTE, J. RABA. Study of antitumor activity in breast cell lines using silver nanoparticles produced by yeast, *International Journal of Nanomedicine*, 2015, **10**, 2021-2031. DOI: [10.2147/IJN.S75835](https://doi.org/10.2147/IJN.S75835)
- [Pal et al., 1995] A. PAL, D. L. STOKES, J. P. ALARIE, T. VO-DINH. The Selective Surface-Enhanced Raman Spectroscopy Using a Polymer-Coated Substrate, *Anal. Chem.*, 1995, **67**, 3154-3159. DOI: [10.1021/ac00114a009](https://doi.org/10.1021/ac00114a009)
- [Palik, 1985] E. D. PALIK. *Handbook of Optical Constants of Solids*, 1985, Academic Press.
- [Panáček et al., 2006] A. PANÁČEK, M. KOLÁŘ, R. VEČEŘOVÁ, R. PRUCEK, J. SOUKUPOVÁ, V. KRYŠTOF, P. HAMAL, R. ZBOŘIL, L. KVÍTEK. Antifungal activity of silver nanoparticles against *Candida* spp., *Biomaterials*, 2009, **30**, 6333-6340. DOI: [10.1016/j.biomaterials.2009.07.065](https://doi.org/10.1016/j.biomaterials.2009.07.065)
- [Peralta-Video et al., 2011] J. R. PERALTA-VIDEA, L. ZHAO, M. L. LOPEZ-MORENO, G. DE LA ROSA, J. HONG, J. L. GARDEA-TORRESDEY. Nanomaterials and the environment: A review for the biennium 2008–2010, *J. Hazard. Mater.*, 2011, **186**, 1-15. DOI: [10.1016/j.jhazmat.2010.11.020](https://doi.org/10.1016/j.jhazmat.2010.11.020)
- [Peretyazhko et al., 2014] T. S. PERETYAZHKO, Q. ZHANG, V. L. COLVIN. T Size-Controlled Dissolution of Silver Nanoparticles at Neutral and Acidic pH Conditions: Kinetics and Size Changes, *Environ. Sci. Technol.*, 2014, **48**, 11954-11961. DOI: [10.1021/es5023202](https://doi.org/10.1021/es5023202)
- [Perrin et al., 1985] J. PERRIN, B. DESPAX, E. KAY. Optical properties and microstructure of gold-fluorocarbon-polymer composite films, *Phys. Rev. B*, 1985, **32**, 719-732. DOI: [10.1103/PhysRevB.32.719](https://doi.org/10.1103/PhysRevB.32.719)
- [Petrucci et al., 1997] R. H. PETRUCCI, W. S. HARWOOD, G. E. HERRING, J. MADURA. *General Chemistry: Principles and Modern Applications*, 1997, Prentice Hall: New York.
- [Phillips, 1962] V. A. PHILLIPS. Role of Defects in Evaporated Silver Films on the Nucleation of Sulfide “Patches”, *J. Appl. Phys.*, 1962, **33**, 712-717. DOI: [10.1063/1.1702493](https://doi.org/10.1063/1.1702493)
- [Piccapietra et al., 2012] F. PICCAPIETRA, C. GIL ALLUÉ, L. SIGG, R. BEHRA. Intracellular Silver Accumulation in *Chlamydomonas reinhardtii* upon Exposure to Carbonate Coated Silver Nanoparticles and Silver Nitrate, *Environ. Sci. Technol.*, 2012, **46**, 7390-7397. DOI: [10.1021/es300734m](https://doi.org/10.1021/es300734m)
- [Poinsotte, 2006] F. POISOTTE. Son et matière nanostructurée: diffusion Raman et acoustique picoseconde, PhD dissertation, Université Paul Sabatier (France), 2006.
- [Pointu et al., 1997] A. M. POINTU, J. PERRIN, J. JOLLY. Plasmas froids de décharge – applications et diagnostic, *Techniques de l'ingénieur*, 1997, D2835.
- [Polyanskiy, 2016] M. N. POLYANSKIY, Refractive index database, 2016. <http://refractiveindex.info>
- [Pospíšil, 2012] P. POSPÍŠIL. Molecular mechanisms of production and scavenging of reactive oxygen species by photosystem II, *Biochimica et Biophysica Acta*, 2012, **1817**, 218-231. DOI: [10.1016/j.bbabi.2011.05.017](https://doi.org/10.1016/j.bbabi.2011.05.017)

- [Pradier et al., 2005] C. M. PRADIER, C. RUBIO, C. POLEUNIS, P. BERTRAND, P. MARCUS, C. COMPERE. Surface Characterization of Three Marine Bacterial Strains by Fourier Transform IR, X-ray Photoelectron Spectroscopy, and Time-of-Flight Secondary-Ion Mass Spectrometry, Correlation with Adhesion on Stainless Steel Surfaces, *J. Phys. Chem. B*, 2005, **109**, 9540-9549. DOI: [10.1021/jp044705p](https://doi.org/10.1021/jp044705p)
- [Prasad et al., 2005] G. R. PRASAD, S. DANIELS, D. C. CAMERON, B. P. MCNAMARA, E. TULLY, R. O'KENNEDY. PECVD of biocompatible coatings on 316L stainless steel, *Surface & Coatings Technology*, 2005, **200**, 1031-1035. DOI: [10.1016/j.surfcoat.2005.02.009](https://doi.org/10.1016/j.surfcoat.2005.02.009)
- [Prathna et al., 2011] T.C. PRATHNA, N. CHANDRASEKARAN, A. MUKHERJEE. Studies on aggregation behaviour of silver nanoparticles in aqueous matrices: Effect of surface functionalization and matrix composition, *J. Colloids and Surfaces A: Physicochem. Eng. Aspects*, 2011, **390**, 216-224. DOI: [10.1016/j.colsurfa.2011.09.047](https://doi.org/10.1016/j.colsurfa.2011.09.047)
- [Prieto et al., 2012] G. PRIETO, J. ZEČEVIC, H. FRIEDRICH, K. P. DE JONG, P. E. DE JONGH. Towards stable catalysts by controlling collective properties of supported metal nanoparticles, *Nat. Mater.*, 2013, **12**, 34-39. DOI: [10.1038/NMAT3471](https://doi.org/10.1038/NMAT3471)
- [Rai et al., 2009] M. RAI, A. YADAV, A. GADE. Silver nanoparticles as a new generation of antimicrobials, *Biotechnology Advances*, 2009, **27**, 76-83. DOI: [10.1016/j.biotechadv.2008.09.002](https://doi.org/10.1016/j.biotechadv.2008.09.002)
- [Rakić et al., 1998] A. D. RAKIĆ, A. B. DJURIŠIĆ, J. M. ELAZAR, M. L. MAJEWSKI. Optical properties of metallic films for vertical-cavity optoelectronic devices, *Applied Optics*, 1998, **37**, 5271-5283. DOI: [10.1364/AO.37.005271](https://doi.org/10.1364/AO.37.005271)
- [Ramage et al., 2006] G. RAMAGE, J. P. MARTINEZ, J. L. LOPEZ-RIBOT. *Candida* biofilms on implanted biomaterials: a clinically significant problem, *FEMS Yeast Res.*, 2006, **6**, 979-986. DOI: [10.1111/j.1567-1364.2006.00117.x](https://doi.org/10.1111/j.1567-1364.2006.00117.x)
- [Ratner et al., 2004] B. D. RATNER, A. S. HOFFMAN, F. J., SCHOEN, J. E. LEMONS. *Biomaterials Science: An Introduction to Materials in Medicine*, 2004, Academic Press.
- [Reidy et al., 2013] B. REIDY, A. HAASE, A. LUCH, K. A. DAWSON, I. LYNCH. Mechanisms of Silver Nanoparticle Release, Transformation and Toxicity: A Critical Review of Current Knowledge and Recommendations for Future Studies and Applications, *Materials*, 2013, **6**, 2295-2350. DOI: [10.3390/ma6062295](https://doi.org/10.3390/ma6062295)
- [Ren et al., 2007] F. REN, C. Z. JIANG, G. X. CAI, Q. FU, Y. SHI. Fabrication of hollow nanoclusters by ion implantation, *Nuclear Instruments and Methods in Physics Research B*, 2007, **262**, 201-204. DOI: [10.1016/j.nimb.2007.05.024](https://doi.org/10.1016/j.nimb.2007.05.024)
- [Rivas et al., 2001] L. RIVAS, S. SANCHEZ-CORTES, J. V. GARCIA-RAMOS, G. MORCILLO. Growth of Silver Colloidal Particles Obtained by Citrate Reduction To Increase the Raman Enhancement Factor, *Langmuir*, 2001, **17**, 574-577. DOI: [10.1021/la001038s](https://doi.org/10.1021/la001038s)
- [Russell and Hugo, 1994] A. D. RUSSELL, W. B. HUGO. 7 Antimicrobial Activity and Action of Silver, *Prog. Med. Chem.*, 1994, **31**, 351-370. DOI: [10.1016/S0079-6468\(08\)70024-9](https://doi.org/10.1016/S0079-6468(08)70024-9)
- [Rycenga et al., 2011] M. RYCENGA, C. M. COBLEY, J. ZENG, W. LI, C. H. MORAN, Q. ZHANG, D. QIN, Y. XIA. Controlling the Synthesis and Assembly of Silver Nanostructures for Plasmonic Applications, *Chem. Rev.*, 2011, **111**, 3669-3712. DOI: [10.1021/cr100275d](https://doi.org/10.1021/cr100275d)



- [Sabella et al., 2014] S. SABELLA, R. P. CARNEY, V. BRUNETTI, M. A. MALVINDI, N. AL-JUFFALI, G. VECCHIO, S. M. JANES, O. M. BAKR, R. CINGOLANI, F. STELLACCI, P. P. POMPA. A general mechanism for intracellular toxicity of metal-containing nanoparticles, *Nanoscale*, 2014, **6**, 7052-7061. DOI: [10.1039/c4nr01234h](https://doi.org/10.1039/c4nr01234h)
- [Sachan et al., 2013] F. R. SACHAN, V. RAMOS, A. MALASI, S. YADAVALI, B. BARTLEY, H. GARCIA, G. DUSCHER, R. KALYANARAMAN. Oxidation-Resistant Silver Nanostructures for Ultrastable Plasmonic Applications, *Adv. Mater.*, 2013, **25**, 2045-2050. DOI: [10.1002/adma.201204920](https://doi.org/10.1002/adma.201204920)
- [Sakiyama et al., 2004] T. SAKIYAMA, J. TOMURA, K. IMAMURA, K. NAKANISHI. Adsorption characteristics of bovine serum albumin and its peptide fragments on a stainless steel surface, *Colloids and Surfaces B: Biointerfaces*, 2004, **33**, 77-84. DOI: [10.1016/j.colsurfb.2003.08.010](https://doi.org/10.1016/j.colsurfb.2003.08.010)
- [Salh, 2011] R. SALH. Defect Related Luminescence in Silicon Dioxide Network: A Review, *Crystalline Silicon - Properties and Uses*, 2011, **Chapter 8**, 135-172. DOI: [10.5772/22607](https://doi.org/10.5772/22607)
- [Sambhy et al., 2006] V. SAMBHY, M. M. MACBRIDE, B. R. PETERSON, A. SEN. Silver Bromide Nanoparticle/Polymer Composites: Dual Action Tunable Antimicrobial Materials, *J. Am. Chem. Soc.*, 2006, **128**, 9798-9808. DOI: [10.1021/ja061442z](https://doi.org/10.1021/ja061442z)
- [Sardella et al., 2006] E. SARDELLA, P. FAVIA, R. GRISTINA, M. NARDULLI, R. D'AGOSTINO. Plasma-Aided Micro- and Nanopatterning Processes for Biomedical Applications, *Plasma Process. Polym.*, 2006, **3**, 456-469. DOI: [10.1002/ppap.200600041](https://doi.org/10.1002/ppap.200600041)
- [Sau et al., 2010] T. K. SAU, A. L. ROGACH, F. JACKEL, T. A. KLAR, J. FELDMANN. Properties and Applications of Colloidal Nonspherical Noble Metal Nanoparticle, *Advanced Materials*, 2010, **22**, 1805-1825. DOI: [10.1002/adma.200902557](https://doi.org/10.1002/adma.200902557)
- [Saulou et al., 2009] C. SAULOU, B. DESPAX, P. RAYNAUD, S. ZANNA, P. MARCUS, M. MERCIER-BONIN. Plasma deposition of organosilicon polymer thin films with embedded nanosilver for prevention of microbial adhesion, *Applied Surface Science*, 2009, **256S**, S35-S39. DOI: [10.1016/j.apsusc.2009.04.118](https://doi.org/10.1016/j.apsusc.2009.04.118)
- [Saulou et al., 2010] C. SAULOU, F. JAMME, C. MARANGES, I. FOURQUAUX, B. DESPAX, P. RAYNAUD, P. DUMAS, M. MERCIER-BONIN. Synchrotron FTIR microspectroscopy of the yeast *Saccharomyces cerevisiae* after exposure to plasma-deposited nanosilver-containing coating, *Anal. Bioanal. Chem.*, 2010, **396**, 1441-1450. DOI: [10.1007/s00216-009-3316-5](https://doi.org/10.1007/s00216-009-3316-5)
- [Saulou et al., 2012] C. SAULOU, B. DESPAX, P. RAYNAUD, S. ZANNA, A. SEYEUX, P. MARCUS, J.-N. AUDINOT, M. MERCIER-BONIN. Plasma-Mediated Nanosilver-Organosilicon Composite Films Deposited on Stainless Steel: Synthesis, Surface Characterization, and Evaluation of Anti-Adhesive and Anti-Microbial Properties on the Model Yeast *Saccharomyces cerevisiae*, *Plasma Process. Polym.*, 2012, **9**, 324-338. DOI: [10.1002/ppap.201100033](https://doi.org/10.1002/ppap.201100033)
- [Schamm et al., 2008] S. SCHAMM, C. BONAFOS, H. COFFIN, N. CHERKASHIN, M. CARRADA, G. BENASSAYAG, A. CLAVERIE, M. TENCE, C. COLLIEX. Imaging Si nanoparticles embedded in SiO<sub>2</sub> layers by (S)TEM-EELS, *Ultramicroscopy*, 2008, **108**, 346-357. DOI: [10.1016/j.ultramic.2007.05.008](https://doi.org/10.1016/j.ultramic.2007.05.008)
- [Schmidt et al., 2002] B. SCHMIDT, D. GRAMBOLE, F. HERRMANN. Impact of ambient atmosphere on as-implanted amorphous insulating layers, *Nuclear Instruments and Methods in Physics Research B*, 2006, **191**, 482-486. DOI: [10.1016/S0168-583X\(02\)00597-9](https://doi.org/10.1016/S0168-583X(02)00597-9)

- [Schmidt et al., 2003] M. SCHMIDT, A. MASSON, C. BRÉCHIGNAC. Oxygen and Silver Clusters: Transition from Chemisorption to Oxidation, *Phys. Rev. Lett.*, 2003, **91**, 243401. DOI: [10.1103/PhysRevLett.91.243401](https://doi.org/10.1103/PhysRevLett.91.243401)
- [Schreiber et al., 1995] U. SCHREIBER, W. BILGER, C. NEUBAUER. Chlorophyll Fluorescence as a Nonintrusive Indicator for Rapid Assessment of In Vivo Photosynthesis, *Ecophysiology of Photosynthesis*, Springer Study Edition, 1995, **100**, 49-70. DOI: [10.1007/978-3-642-79354-7\\_3](https://doi.org/10.1007/978-3-642-79354-7_3)
- [Schreiber et al., 1995] U. SCHREIBER, W. BILGER, C. NEUBAUER. Chlorophyll Fluorescence as a Nonintrusive Indicator for Rapid Assessment of In Vivo Photosynthesis, *Ecophysiology of Photosynthesis*, Springer Study Edition, 1995, **100**, 49-70. DOI: [10.1007/978-3-642-79354-7\\_3](https://doi.org/10.1007/978-3-642-79354-7_3)
- [Schreiber et al., 2004] U. SCHREIBER. Pulse-amplitude-modulation (PAM) fluorometry and saturation pulse method: an overview, *Chlorophyll a Fluorescence: A Signature of Photosynthesis*, Springer, The Netherlands, 2004, **19**, 279-319. DOI: [10.1007/978-1-4020-3218-9\\_11](https://doi.org/10.1007/978-1-4020-3218-9_11)
- [Schröfel et al., 2014] A. SCHRÖFEL, G. KRATOŠOVÁ, I. ŠAFAŘÍK, M. ŠAFAŘÍKOVÁ, I. RAŠKA, L. M. SHOR. Applications of biosynthesized metallic nanoparticles – A review, *Acta Biomaterialia*, 2014, **10**, 4023-4042. DOI: [10.1016/j.actbio.2014.05.022](https://doi.org/10.1016/j.actbio.2014.05.022)
- [Schuck et al., 2005] P. J. SCHUCK, D. P. FROMM, A. SUNDARAMURTHY, G. S. KINO, W. E. MOERNER. The Improving the Mismatch between Light and Nanoscale Objects with Gold Bowtie Nanoantennas, *Physical Review Letters*, 2005, **94**, 017402. DOI: [10.1103/PhysRevLett.94.017402](https://doi.org/10.1103/PhysRevLett.94.017402)
- [Shahverdi et al., 2007] A. R. SHAHVERDI, A. FAKHIMI, H. R. SHAHVERDI, S. MINAIAN. Synthesis and effect of silver nanoparticles on the antibacterial activity of different antibiotics against *Staphylococcus aureus* and *Escherichia coli*, *Nanomedicine: Nanotechnology, Biology, and Medicine*, 2007, **3**, 168-171. DOI: [10.1016/j.nano.2007.02.001](https://doi.org/10.1016/j.nano.2007.02.001)
- [Sharma et al., 2009] V. K. SHARMA, R. A. YNGARD, Y. LIN. Silver nanoparticles: Green synthesis and their antimicrobial activities, *Advances in Colloid and Interface Science*, 2009, **145**, 83-96. DOI: [10.1016/j.cis.2008.09.002](https://doi.org/10.1016/j.cis.2008.09.002)
- [Shen and Zhu, 2016] L. SHEN, J. ZHU. Heterogeneous surfaces to repel proteins, *Advances in Colloid and Interface Science*, 2016, **228**, 40-54. DOI: [10.1016/j.cis.2015.11.008](https://doi.org/10.1016/j.cis.2015.11.008)
- [Silver et al., 2006] S. SILVER, L. T. PHUNG, G. SILVER. Silver as biocides in burn and wound dressings and bacterial resistance to silver compounds, *J. Ind. Microbiol. Biotechnol.*, 2006, **33**, 627-634. DOI: [10.1007/s10295-006-0139-7](https://doi.org/10.1007/s10295-006-0139-7)
- [Smith, 1999] B. C. SMITH. *Infrared Spectral Interpretation: A Systematic Approach*, 1999, CRC Press.
- [Sondi and Salopek-Sondi, 2004] I. SONDI, B. SALOPEK-SONDI. Silver nanoparticles as antimicrobial agent: a case study on *E. coli* as a model for Gram-negative bacteria, *Journal of Colloid and Interface Science*, 2004, **275**, 177-182. DOI: [10.1016/j.jcis.2004.02.012](https://doi.org/10.1016/j.jcis.2004.02.012)
- [SOPRA Database, 1999] SOPRA Database, WinElli Software by SOPRA S.A., Version 3.04, 1999.
- [Sortiriou and Pratsinis, 2010] G. A. SOTIRIOU, S. E. PRATSINIS. Antibacterial Activity of Nanosilver Ions and Particles, *Environ. Sci. Technol.*, 2010, **44**, 5649-5654. DOI: [10.1021/es101072s](https://doi.org/10.1021/es101072s)
- [Sortiriou and Pratsinis, 2011] G. A. SOTIRIOU, S. E. PRATSINIS. Engineering nanosilver as an antibacterial, biosensor and bioimaging material, *Current Opinion in Chemical Engineering*, 2011, **1**, 1-10. DOI: [10.1016/j.coche.2011.07.001](https://doi.org/10.1016/j.coche.2011.07.001)

- [Sotiriou et al., 2011] G. A. SOTIRIOU, A. TELEKI, A. CAMENZIND, F. KRUMEICH, A. MEYER, SVEN PANKE, S. E. PRATSINIS. Nanosilver on nanostructured silica: Antibacterial activity and Ag surface area, *Chemical Engineering Journal*, 2011, **170**, 547-554. DOI: [10.1016/j.cej.2011.01.099](https://doi.org/10.1016/j.cej.2011.01.099)
- [Sotiriou et al., 2012] G. A. SOTIRIOU, A. MEYER, J. T. N. KNIJNENBURG, S. PANKE, S. E. PRATSINIS. Quantifying the Origin of Released Ag<sup>+</sup> Ions from Nanosilver, *Langmuir*, 2012, **28**, 15929-15936. DOI: [10.1021/la303370d](https://doi.org/10.1021/la303370d)
- [Spinelli and Polman, 2012] P. SPINELLI, A. POLMAN. Prospects of near-field plasmonic absorption enhancement in semiconductor materials using embedded Ag nanoparticles, *Opt. Express*, 2012, **20**, A641-A654. DOI: [10.1364/OE.20.00A641](https://doi.org/10.1364/OE.20.00A641)
- [Stepanov et al., 2000] A. L. STEPANOV, V. A. ZHIKHAREV, D. E. HOLE, P. D. TOWNSEND, I. B. KHAIBULLI. Depth distribution of Cu, Ag and Au ions implanted at low energy into insulators, *Nuclear Instruments and Methods in Physics Research B*, 2000, **166-167**, 26-30. DOI: [10.1016/S0168-583X\(99\)00641-2](https://doi.org/10.1016/S0168-583X(99)00641-2)
- [Stepanov et al., 2013] A. L. STEPANOV, X. XIAO, F. REN, T. KAVETSKYY, Y. N. OSIN. Catalytic and biological sensitivity of TiO<sub>2</sub> and SiO<sub>2</sub> matrices with silver nanoparticles created by ion implantation: a review, *Rev. Adv. Mater. Sci.*, 2013, **34**, 107-122.
- [Stepanov, 2010] A. L. STEPANOV. Synthesis of silver nanoparticles in dielectric matrix by ion implantation: a review, *Rev. Adv. Mater. Sci.*, 2010, **26**, 1-29.
- [Stewart et al., 2008] M. E. STEWART, C. R. ANDERTON, L. B. THOMPSON, J. MARIA, S. K. GRAY, J. A. ROGERS, R. G. NUZZO. Nanostructured Plasmonic Sensors, *Chem. Rev.*, 2008, **108**, 494-521. DOI: [10.1021/cr068126n](https://doi.org/10.1021/cr068126n)
- [Strobel et al., 1999] M. STROBEL. Modeling and Computer Simulation of Ion Beam Synthesis of Nanostructures, PhD dissertation, University of Dreden (Germany), 1999.
- [Stumm et al., 2012] W. STUMM, J. J. MORGAN. *Aquatic Chemistry: Chemical Equilibria and Rates in Natural Waters*, 2012, John Wiley & Sons: New York
- [Suggett et al., 2008] D. J. SUGGETT, M. E. WARNER, D. J. SMITH, P. DAVEY, S. HENNIGE, N. R. BAKER. Photosynthesis and production of hydrogen peroxide by *symbiodinium* (pyrrhophyta) phylotypes with different thermal tolerances, *J. Phycol.*, 2008, **44**, 948-956. DOI: [10.1111/j.1529-8817.2008.00537.x](https://doi.org/10.1111/j.1529-8817.2008.00537.x)
- [Sundaramoorthi et al., 2009] C. SUNDARAMOORTHI, M. KALAIVANI, D. M. MATHEWS, S. PALANISAMY, V. KALAISELVAN, A. RAJASEKARAN. Biosynthesis of silver nanoparticles from *Aspergillus niger* and evaluation of its wound healing activity in experimental rat model, *Int. J. PharmTech Res.*, 2009, **1**, 1523-1529.
- [Takahiro et al., 2012] K. TAKAHIRO, Y. MINAKUCHI, K. KAWAGUCHI, T. ISSHIKI, K. NISHIO, M. SASASE, S. YAMAMOTO, F. NISHIYAMA. Well-ordered arranging of Ag nanoparticles in SiO<sub>2</sub>/Si by ion implantation, *Applied Surface Science*, 2012, **258**, 7322-7326. DOI: [10.1016/j.apsusc.2012.04.001](https://doi.org/10.1016/j.apsusc.2012.04.001)
- [Tejamaya et al., 2012] M. TEJAMAYA, I. RÖMER, R. C. MERRIFIELD, J. R. LEAD. Stability of Citrate, PVP, and PEG Coated Silver Nanoparticles in Ecotoxicology Media, *Environ. Sci. Technol.*, 2012, **46**, 7011-7017. DOI: [10.1021/es2038596](https://doi.org/10.1021/es2038596)
- [Tian et al., 2007] P. J. TIAN, K. K. Y. WONG, C.-M. HO, C.-N. LOK, W.-Y. YU, C.-M. CHE, J.-F. CHIU, P. K. H. TAM. Topical Delivery of Silver Nanoparticles Promotes Wound Healing, *ChemMedChem*, 2007, **2**, 129-136. DOI: [10.1002/cmdc.200600171](https://doi.org/10.1002/cmdc.200600171)

- [Tkachuk et al., 1968] B. V. TKACHUK, V. V. BUSHIN, V. M. KOLOTYRKIN, N. P. SMETANKINA. Polymerization of organosilicon compounds on a metal surface using a glow discharge, *Polymer Science U.S.S.R.*, 1968, **9**, 2281-2289. DOI: [10.1016/S0032-3950\(68\)80031-0](https://doi.org/10.1016/S0032-3950(68)80031-0)
- [Tompkins and Irene, 2005] H. G. TOMPKINS, E. A. IRENE. *Handbook of ellipsometry*, 2005, Springer.
- [Toudert et al., 2008] J. TOUDERT, D. BABONNEAU, L. SIMONOT, S. CAMELIO, T. GIRARDEAU. Quantitative modelling of the surface plasmon resonances of metal nanoclusters sandwiched between dielectric layers: the influence of nanocluster size, shape and organization, *Nanotechnology*, 2008, **19**, 125709. DOI: [10.1088/0957-4484/19/12/125709](https://doi.org/10.1088/0957-4484/19/12/125709)
- [Trantum et al., 2013] J. R. TRANTUM, Z. E. EAGLETON, C. A. PATIL, J. M. TUCKER-SCHWARTZ, M. L. BAGLIA, M. C. SKALA, F. R. HASELTON. Cross-Sectional Tracking of Particle Motion in Evaporating Drops: Flow Fields and Interfacial Accumulation, *Langmuir*, 2013, **29**, 6221-6231. DOI: [10.1021/la400542x](https://doi.org/10.1021/la400542x)
- [Traverse et al., 2008] A. TRAVERSE, C. HUMBERT, C. SIX, A. GAYRAL, B. BUSSON. Nonlinear optical properties of Ag nanoparticles embedded in Si<sub>3</sub>N<sub>4</sub>, *EPL*, 2008, **83**, 64004. DOI: [10.1209/0295-5075/83/64004](https://doi.org/10.1209/0295-5075/83/64004)
- [Tsang et al., 2006] M. TSANG, V. STOLOJAN, C. GIUSCA, H. P. POA, B. SEALY, S. R. P. SILVA, S. P. WONG. Controlled synthesis of buried delta-layers of Ag nanocrystals for near-field plasmonic effects on free surfaces, *J. Vac. Sci. Technol. B*, 2006, **24**, 958-961. DOI: [10.1116/1.2165669](https://doi.org/10.1116/1.2165669)
- [Vasile and G. Smolinsky, 1972] M. J. VASILE, G. SMOLINSKY. Organosilicon films formed by an RF plasma polymerization process, *J. Electrochem. Soc.*, 1972, **119**, 451-455. DOI: [10.1149/1.2404228](https://doi.org/10.1149/1.2404228)
- [Verhoeven, 1975] J. D. VERHOEVEN. *Fundamentals of Physical Metallurgy*, 1975, Wiley.
- [Verkhusha and Lukyanov, 2004] V. V. VERKHUSHA, K. A. LUKYANOV. The molecular properties and applications of Anthozoa fluorescent proteins and chromoproteins, *Nature Biotech.*, 2004, **22**, 289-296. DOI: [10.1038/nbt943](https://doi.org/10.1038/nbt943)
- [Vo-dinh et al., 2005] T. VO-DINH, F. YAN, D. L. STOKES. Plasmonics-Based Nanostructures for Surface-Enhanced Raman Scattering Bioanalysis, *Protein Nanotechnology*, 2005, **300**, 255-283. DOI: [10.1385/1-59259-858-7:255](https://doi.org/10.1385/1-59259-858-7:255)
- [Vo-Dinh, 2005] T. VO-DINH. *Protein Nanotechnology: Protocols, Instrumentation, and Applications at clusters*, 2005, Springer. DOI: [10.1385/1592598587](https://doi.org/10.1385/1592598587)
- [Vrzheshch et al., 2000] P. V. VRZHESHCH, N. A. AKOVBAN, S. D. VARFOLOMEYEV, V. V. VERKHUSHA. Denaturation and partial renaturation of a tightly tetramerized DsRed protein under mildly acidic conditions, *FEBS Letters*, 2000, **487**, 203-208. DOI: [10.1016/S0014-5793\(00\)02344-9](https://doi.org/10.1016/S0014-5793(00)02344-9)
- [Wall et al., 2000] M. A. WALL, M. SOCOLICH, R. RANGANATHAN. The structural basis for red fluorescence in the tetrameric GFP homolog DsRed, *Nature structural biology*, 2000, **7**, 1133-1138. DOI: [10.1038/81992](https://doi.org/10.1038/81992)
- [Wang et al., 2013] J. WANG, G. JIA, X. MU, C. LIU. Quasi-two-dimensional Ag nanoparticle formation in silica by Xe ion irradiation and subsequent Ag ion implantation, *Applied Physics Letters*, **102**, 133102. DOI: [10.1063/1.4799175](https://doi.org/10.1063/1.4799175)
- [Warren et al., 2012] S. C. WARREN, D. A. WALKER, B. A. GRZYBOWSKI. Plasmoelectronics: Coupling Plasmonic Excitation with Electron Flow, *Langmuir*, 2012, **28**, 9093-9102. DOI: [10.1021/la300377j](https://doi.org/10.1021/la300377j)

- [Wasa et al., 2004] K. WASA, M. KITABATAKE, H. ADACHI. *Thin film materials: sputtering of compound materials*, 2004, Springer.
- [Wiley et al., 2004] B. WILEY, T. HERRICKS, Y. SUN, Y. XIA. Polyol Synthesis of Silver Nanoparticles: Use of Chloride and Oxygen to Promote the Formation of Single-Crystal, Truncated Cubes and Tetrahedrons, *Nano Letters*, 2004, **4**, 1733-1739. DOI: [10.1021/nl048912c](https://doi.org/10.1021/nl048912c)
- [Williams and Carter, 2009] D. B. WILLIAMS, C. B. CARTER. *Transmission Electron Microscopy, A Textbook for Materials Science*, 2009, Springer. DOI: [10.1007/978-0-387-76501-3](https://doi.org/10.1007/978-0-387-76501-3)
- [Wyre and Downes, 2002] R. M. WYRE, S. DOWNES. The role of protein adsorption on chondrocyte adhesion to a heterocyclic methacrylate polymer system, *Biomaterials*, 2002, **23**, 357-364. DOI: [10.1016/S0142-9612\(01\)00113-2](https://doi.org/10.1016/S0142-9612(01)00113-2)
- [Xiao et al., 2007] X. H. XIAO, F. REN, J. B. WANG, C. LIU, C. Z. JIANG. Formation of aligned silver nanoparticles by ion implantation, *Materials Letters*, 2007, **61**, 4435-4437. DOI: [10.1016/j.matlet.2007.02.017](https://doi.org/10.1016/j.matlet.2007.02.017)
- [Xiu et al., 2011] Z.-M. XIU, J. MA, P. J. J. ALVAREZ. Differential Effect of Common Ligands and Molecular Oxygen on Antimicrobial Activity of Silver Nanoparticles versus Silver Ions, *Environ. Sci. Technol.*, 2011, **45**, 9003-9008. DOI: [10.1021/es201918f](https://doi.org/10.1021/es201918f)
- [Xiu et al., 2012] Z.-M. XIU, Q.-B. ZHANG, H. L. PUPPALA, V. L. COLVIN, P. J. J. ALVAREZ. Negligible Particle-Specific Antibacterial Activity of Silver Nanoparticles, *Nano Lett.*, 2012, **12**, 4271-4275. DOI: [10.1021/nl301934w](https://doi.org/10.1021/nl301934w)
- [Xu et al., 2006] R. XU, D. WANG, J. ZHANG, Y. LI. Shape-Dependent Catalytic Activity of Silver Nanoparticles for the Oxidation of Styrene, *Chem. Asian J.* 2006, **1**, 888 – 893, 2006, **1**, 888-893. DOI: [10.1002/asia.200600260](https://doi.org/10.1002/asia.200600260)
- [Yang et al., 2012] X. YANG, A. P. GONDIKAS, S. M. MARINAKOS, M. AUFFAN, J. LIU, H. HSU-KIM, J. N. MEYER. Mechanism of Silver Nanoparticle Toxicity Is Dependent on Dissolved Silver and Surface Coating in *Caenorhabditis elegans*, *Environ. Sci. Technol.*, 2012, **46**, 1119-1127. DOI: [10.1021/es202417t](https://doi.org/10.1021/es202417t)
- [Yang et al., 2014] Y. YANG, C. ZHANG, Y. SONG, J. GOU, L. ZHANG, H. ZHANG, J. LIU, Y. XIAN, Y. MA. Tailoring the size and distribution of Ag nanoparticles in silica glass by defects, *Nuclear Instruments and Methods in Physics Research B*, 2014, **321**, 14-18. DOI: [10.1016/j.nimb.2013.12.015](https://doi.org/10.1016/j.nimb.2013.12.015)
- [Yoshida et al., 1973] S. YOSHIDA, T. MURAKAMI, K. TARAMA. Structural Study on Promoting Actions of Titanium Dioxide and Stannic Oxide on Vanadium Pentoxide Catalysts, *Bull. Inst. Chem. Res., Kyoto Univ.*, 1973, **51**, 195-205.
- [Zhang et al., 2005] X. ZHANG, E. M. HICKS, J. ZHAO, G. C. SCHATZ, R. P. VAN DUYN. Electrochemical Tuning of Silver Nanoparticles Fabricated by Nanosphere Lithography, *Nano Lett.*, 2005, **5**, 1503-1507. DOI: [10.1021/nl050873x](https://doi.org/10.1021/nl050873x)
- [Zhang et al., 2011] W. ZHANG, Y. YAO, N. SULLIVAN, Y. CHEN. Modeling the Primary Size Effects of Citrate-Coated Silver Nanoparticles on Their Ion Release Kinetics, *Environ. Sci. Technol.*, 2011, **45**, 4422-4428. DOI: [10.1021/es104205a](https://doi.org/10.1021/es104205a)
- [Zhang et al., 2013] X. ZHANG, Y. L. CHEN, R.-S. LIU, D. P. TSAI. Plasmonic photocatalysis, *Rep. Prog. Phys.*, 2013, **76**, 046401. DOI: [10.1088/0034-4885/76/4/046401](https://doi.org/10.1088/0034-4885/76/4/046401)
- [Zhang, 2009] J. Z. ZHANG. *Optical properties and spectroscopy of nanomaterials*, 2009, World Sci. Pub., London.

[Ziegler et al., 2010] J. F. ZIEGLER, M. D. ZIEGLER, J. P. BIRSACK. SRIM – The stopping and range of ions in matter (2010), *Nuclear Instruments and Methods in Physics Research B*, 2010, **268**, 1818-1823. DOI: [10.1016/j.nimb.2010.02.091](https://doi.org/10.1016/j.nimb.2010.02.091)



# Scientific production

---

- 5 publications in international journals
- 2 publications in referred Conference Publications
- 12 oral communications (**3 as presenting author**) in international conferences
- 12 poster communications in international or national conferences

## Publications in international journals

1. “Algae as fine biosensors to assess bio-available silver released from silica layers with embedded silver nanoparticles”  
**A. Pugliara**, K. Makasheva, B. Despax, M. Bayle, R. Carles, P. Benzo, G. BenAssayag, B. Pécassou, M.-C. Sancho, E. Navarro, Y. Echegoyen, C. Bonafos.  
*Science of the Total Environment* (2016) **565**, 863-871  
DOI : [10.1016/j.scitotenv.2016.02.141](https://doi.org/10.1016/j.scitotenv.2016.02.141)
2. “Controlled elaboration of large-area plasmonic substrates by plasma process”  
**A. Pugliara**, C. Bonafos, R. Carles, B. Despax, K. Makasheva.  
*Materials Research Express* (2015) **2**, 065005  
DOI : [10.1088/2053-1591/2/6/065005](https://doi.org/10.1088/2053-1591/2/6/065005)
3. “Dielectric Engineering of Nanostructured Layers to Control the Transport of Injected Charges in Thin Dielectrics”  
K. Makasheva, C. Villeneuve-Faure, C. Bonafos, C. Laurent, **A. Pugliara**, B. Despax, L. Boudou, and G. Teyssedre.  
*IEEE Trans. Nanotechnology* (2016) **15**, 839-848  
DOI: [10.1109/TNANO.2016.2553179](https://doi.org/10.1109/TNANO.2016.2553179)
4. “Physico-chemical characterization of the interaction of red fluorescent protein - DsRed with thin silica layers”  
M. Soumbo, **A. Pugliara**, M.-C. Monje, C. Roques, B. Despax, C. Bonafos, R. Carles, A. Mlayah, and K. Makasheva.  
*IEEE Trans. NanoBioscience* (2016) **15**, 412-417  
DOI: [10.1109/TNB.2016.2547895](https://doi.org/10.1109/TNB.2016.2547895)
5. “Enhancing carrier generation in TiO<sub>2</sub> by a synergistic effect between plasmon resonance in Ag nanoparticles and optical interference”  
G. Cacciato, M. Bayle, **A. Pugliara**, C. Bonafos, M. Zimbone, V. Privitera, M. G. Grimaldi, R. Carles.  
*Nanoscale* (2015) **7**, 13468  
DOI : [10.1039/c5nr02406d](https://doi.org/10.1039/c5nr02406d)



## Publications in referred Conference Publications

1. “Physico-chemical characterization of the interaction of red fluorescent protein - DsRed with silica layers”  
M. Soumbo, **A. Pugliara**, M-C. Monje, C. Roques, B. Despax, C. Bonafos, R. Carles, A. Mlayah, K. Makasheva  
*IEEE Nanotechnology Materials and Devices Conference (IEEE NMDC 2015)*  
DOI: [10.1109/NMDC.2015.7439280](https://doi.org/10.1109/NMDC.2015.7439280)
2. “Dielectric engineering of nanostructured layers preventing electrostatic charging in thin dielectrics”  
K. Makasheva, C. Villeneuve-Faure, C. Bonafos, C. Laurent, **A. Pugliara**, B. Despax, L. Boudou, G. Teysedre,  
*IEEE Nanotechnology Materials and Devices Conference (IEEE NMDC 2015)*  
DOI: [10.1109/NMDC.2015.7439236](https://doi.org/10.1109/NMDC.2015.7439236)

## Oral communications

1. “Toxicity effect on *Chlamydomonas reinhardtii*: a novel method to study bio-available silver release from a layer of AgNPs embedded in silica matrix”  
**A. Pugliara**, K. Makasheva, B. Despax, M. Bayle, R. Carles, P. Benzo, G. BenAssayag, B. Pécassou, M.C. Sancho, E. Navarro, Y. Echegoyen, I. Sanz, F. Laborda and C. Bonafos.  
*IEEE-NMDC 2014 (Aci castello (IT), October 2014)*
2. “Toxicity evaluation of single layer of silver nanoparticles embedded in silica matrix to photosynthesis in *Chlamydomonas reinhardtii*”.  
**A. Pugliara**, C. Bonafos, M. Bayle, R. Carles, P. Benzo, G. BenAssayag, B. Pécassou, M.C. Sancho, E. Navarro, Y. Echegoyen, I. Sanz, F. Laborda, B. Despax and K. Makasheva.  
*E-MRS spring meeting 2014 (Lille (FR), May 2014) – Symposium N*  
*(“Student award” of Symposium N, orals category)*
3. “Toxicity evaluation of silver nanoparticles embedded in silica matrix to photosynthesis in *Chlamydomonas reinhardtii*”  
**A. Pugliara**, C. Bonafos, M. Bayle, R. Carles, P. Benzo, G. BenAssayag, B. Pécassou, M.C. Sancho, E. Navarro, Y. Echegoyen, I. Sanz, F. Laborda, B. Despax and K. Makasheva.  
*NANOSPAIN 2014 (Madrid (ES), March 2014)*
4. “Plasma based concept for engineering of multifunctional materials with application to synthesis of large-area plasmonic substrates and to control the charge injection in dielectrics”  
**K. Makasheva**, B. Despax, C. Laurent, L. Milliere, C. Villeneuve-Faure, C. Bonafos, **A. Pugliara**, R. Carles, L. Boudou, G. Teysedre.  
*IEEE-NANO 2016 (Sendai (JP), August 2016)*
5. “Multifunctional metallic nanoparticles embedded in dielectrics”  
**C. Bonafos**, **A. Pugliara**, M. Bayle, P. Benzo, A. Mlayah, K. Makasheva, E. Navarro, M. C. Sancho, Y. Echegoyen, G. Benassayag, B. Pécassou, R. Carles.  
*Nanosea 2016, (Catane (IT), July 2016)*

6. “Interaction of red fluorescent protein - DsRed with silver nanoparticles embedded in thin silica layers”  
M. Soumbo, **A. Pugliara**, M.-C. Monje, C. Roques, B. Despax, C. Bonafos, R. Carles, A. Mlayah and K. Makasheva.  
*International Symposium “Advances in nanoparticulate carriers: Applications in diseases and infections (Paris (FR), October 2015)*
7. “Physico-chemical characterization of the interaction of red fluorescent protein - DsRed with silica layers”  
M. Soumbo, **A. Pugliara**, M.-C. Monjé, C. Roques, B. Despax, C. Bonafos, R. Carles, A. Mlayah and K. Makasheva  
*IEEE-NMDC 2015 (Anchorage (US-AK), September 2015)*
8. “Dielectric engineering of nanostructured layers preventing electrostatic charging in thin dielectrics”  
K. Makasheva, C. Villeneuve-Faure, C. Bonafos, C. Laurent, **A. Pugliara**, B. Despax, L. Boudou, G. Teysse, G. Teysse, G. Teysse,  
*IEEE-NMDC 2015 (Anchorage (US-AK), September 2015)*
9. “Excitations électroniques et vibrationnelles, transferts de charges dans les nanoparticules métalliques enterrées”  
R. Carles, **A. Pugliara**, K. Makasheva, A. Mlayah et C. Bonafos,  
*GDR Nacre 2015 (Oléron (FR), September 2015)*
10. “Plasmon enhanced optical response of TiO<sub>2</sub> in the visible range by Ag nanoparticles produced by Low Energy Ion Beam Synthesis”  
G. Cacciato, M. Bayle, **A. Pugliara**, C. Bonafos, M. Zimbone, V. Privitera, M. G. Grimaldi, R. Carles.  
*E-MRS spring meeting 2015 (Lille (FR), May 2015) Symposium H*
11. “TiO<sub>2</sub> subsurface embedded Ag nanoparticles for plasmonic photocatalysis”  
G. Cacciato, M. Bayle, **A. Pugliara**, C. Bonafos, M. Zimbone, V. Privitera, M. G. Grimaldi, R. Carles.  
*IEEE-NMDC 2014 (Catania (IT), October 2014)*
12. “3D design of Ag nanocrystals embedded in dielectrics for imaging and spectroscopy of deposits on surfaces”  
R. Carles, M. Bayle, P. Benzo, A. Pugliara, C. Bonafos, G. Benassayag, and K. Makasheva.  
*International conference – European Program WATER, 2013 (Catania (IT), June 2013)*

## Poster communications

1. “A Plasmonic substrates elaborated by plasma process: optimization of the plasma parameters according to the optical response of the structures”  
**A. Pugliara**, C. Bonafos, R. Carles, P. Benzo, G. BenAssayag, B. Pécassou B. Despax and K. Makasheva.  
*GDR Nacre 2015 (Oléron (FR), September 2015)*
2. “A Plasmonic substrates elaborated by plasma process: optimization of the plasma parameters according to the optical response of the structures”  
**A. Pugliara**, C. Bonafos, R. Carles, B. Despax and K. Makasheva.  
*ISPC 22 (Antwerp (BE), July 2015)*
3. “Algae as fine biosensors to study bio-available silver released from reusable layers with embedded AgNPs”  
**A. Pugliara**, C. Bonafos, M. Bayle, R. Carles, P. Benzo, G. BenAssayag, B. Pécassou, M.-C. Sancho, E. Navarro, Y. Echegoyen, B. Despax and K. Makasheva.  
*E-MRS spring meeting 2015 (Lille (FR), May 2015) Symposium H*
4. “Spectroscopic ellipsometry study of the dielectric response of plasmonic structures containing a layer of silver nanoparticles embedded in silica matrix”  
**A. Pugliara**, M. Bayle, R. Carles, C. Bonafos, B. Despax and K. Makasheva.  
*E-MRS spring meeting 2015 (Lille (FR), May 2015) Symposium H*
5. “A novel method to study bio-available silver released from a layer of AgNPs embedded in silica matrix”  
**A. Pugliara**, K. Makasheva, B. Despax, M. Bayle, R. Carles, P. Benzo, G. BenAssayag, B. Pécassou, M.-C. Sancho, E. Navarro, Y. Echegoyen and C. Bonafos.  
*Journée Surfaces et Interfaces 2015 (Toulouse (FR), January 2015)*
6. “A novel method to study bio-available silver release from a layer of AgNPs embedded in silica matrix through the toxicity effect on *Chlamydomonas reinhardtii*”  
**A. Pugliara**, K. Makasheva, B. Despax, M. Bayle, R. Carles, P. Benzo, G. BenAssayag, B. Pécassou, M.-C. Sancho, E. Navarro, Y. Echegoyen, I. Sanz, F. Laborda and C. Bonafos.  
*GRD Nacre 2014 (St. Aygulf (FR), September 2014)*
7. “Optical response of delta-layer of silver nanoparticles embedded near the free surface of thin silica matrix”  
**A. Pugliara**, K. Makasheva, B. Despax, M. Bayle, R. Carles, P. Benzo, G. BenAssayag, B. Pécassou and C. Bonafos.  
*Workshop – “Nano-matériaux, nano-objets pour la détection et les capteurs” – Fondation de Cooperation Scientifique RTRA STAE (Nailloux (FR), December 2013)*
8. “Optical signature of delta-layer of silver nanoparticles embedded in silica matrix elaborated through Low Energy Ion Beam Synthesis or combined silver sputtering and Plasma Enhanced Chemical Vapour Deposition”  
**A. Pugliara**, K. Makasheva, B. Despax, M. Bayle, R. Carles, P. Benzo, G. BenAssayag, B. Pécassou and C. Bonafos.  
*Nanoworkshop 2013, 6th International Workshop on Polymer/Metal Nanocomposites (Toulouse (FR), September 2013)*

9. “On the application of Surface Enhanced Raman Scattering to study the interaction of DsRed fluorescent proteins with silver nanoparticles embedded in thin silica layers”  
M. Soumbo, **A. Pugliara**, A. Mlayah, , M-C. Monjé, C. Roques, B. Despax, C. Bonafos, R.Carles, and K. Makasheva.  
*IEEE-NMDC 2016 (Toulouse (FR), October 2016)*
  
10. “Mise en évidence par spectroscopie Raman exaltée de l’interaction des protéines fluorescentes DsRed avec des nanoparticules d’argent enterrées dans des couches minces de silice”  
M. Soumbo, A. Mlayah, **A. Pugliara**, M-C. Monjé, C. Roques, B. Despax, C. Bonafos, R.Carles and K. Makasheva.  
*GDR PMSE 2016 (Toulouse (FR), June 2016)*
  
11. “Metal nanostructures for plasmonic TiO<sub>2</sub> photocatalysis”  
G. Cacciato, F. Ruffino, M. Zimbone, R. Reitano, M. Bayle, **A. Pugliara**, C. Bonafos, R. Carles, V. Privitera and M. G. Grimaldi.  
*E-MRS spring meeting 2015 (Lille (FR), May 2015) Symposium B*  
*(“Student award” of Symposium B, posters category)*
  
12. “Etude des interactions protéines/nanoparticules d’argent, impliquées dans les mécanismes d’adhérence des biofilm”  
M. Soumbo, M-C. Monjé, C. Roques, **A. Pugliara**, B. Despax, C. Bonafos, R.Carles, A. Mlayah and K. Makasheva.  
*GDR Ingénierie des biosystèmes : de la cellule au procédé 2015 (Aubière (FR), April 2015)*



# Abstract

---

## **Elaboration of thin nanocomposite layers based on Ag nanoparticles embedded in silica for controlled biocide properties**

Silver nanoparticles (AgNPs) because of their strong biocide activity are widely used in health-care sector, food industry and various consumer products. Their huge surface-volume ratio enhances the silver release compared to the bulk material, leading to an increased toxicity for microorganisms sensitive to this element. This work presents an assessment of the biocide properties on algal photosynthesis of small (<20 nm) AgNPs embedded in silica layers. Two physical approaches were used to elaborate these nanocomposites: (i) low energy ion beam synthesis and (ii) combined silver sputtering and plasma polymerization. These techniques allow elaboration of a single layer of AgNPs embedded in silica films at defined nanometer distances (from 0 to 7 nm) beneath the free surface. The structural and optical properties of the nanocomposites were studied by transmission electron microscopy, reflectance spectroscopy and ellipsometry. This last technique, coupled to modelling based on the quasi-static approximation of the classical Maxwell-Garnett formalism, allowed detection of small variations over the size and density of the embedded AgNPs. The silver release from the nanostructures after immersion in buffered water was measured by inductively coupled plasma mass spectrometry. The short-term toxicity of Ag to the photosynthesis of green algae, *Chlamydomonas reinhardtii*, was assessed by fluorometry. Embedding AgNPs reduces their interactions with the buffered water, protecting the AgNPs from fast oxidation. The release of bio-available silver (impacting on the algal photosynthesis) is controlled by the depth at which AgNPs are located for the given host silica matrix. This provides a procedure to tailor the biocide effect of nanocomposites containing AgNPs. By coupling the controlled antimicrobial properties of the embedded AgNPs and their quality as plasmonic antenna, these coatings can be used to detect and prevent the first stages of biofilm formation. Hence, the last part of this work is dedicated to a study of the structural stability and adsorption properties of *Discosoma* recombinant red (DsRed) fluorescent proteins deposited on these dielectric surfaces with perspectives of development of SERS devices.

# Résumé

---

## **Elaboration de couches minces nanocomposites à base de nanoparticules d'Ag enrobées dans la silice pour des propriétés antimicrobiennes contrôlées**

Les nanoparticules (NPs) d'Ag sont très utilisées dans le secteur de la santé, dans l'industrie alimentaire et dans les produits de consommation pour leurs propriétés antimicrobiennes. Le grand rapport surface sur volume des NPs d'Ag permet une augmentation importante du relargage d'Ag comparé au matériau massif et donc une toxicité accrue vis à vis des micro-organismes sensibles à cet élément. Ce travail de thèse présente une évaluation des propriétés antimicrobiennes de petites NPs d'Ag (<20 nm) enrobées dans des matrices de silice sur la photosynthèse d'algues vertes. Deux techniques d'élaboration par voie physique ont été utilisées pour fabriquer ces nanocomposites: (i) l'implantation ionique à basse énergie et (ii) la pulvérisation d'Ag couplée avec la polymérisation plasma. Les propriétés structurales et optiques de ces nanostructures ont été étudiées par microscopie électronique à transmission, réflectivité et ellipsométrie. Cette dernière technique, couplée à un modèle basé sur l'approximation quasi-statique de type Maxwell-Garnett, a permis la détection de petites variations dans la taille et la densité des NPs d'Ag. Le relargage d'argent de ces NPs d'Ag enrobées dans des diélectriques a été mesuré par spectrométrie de masse après immersion dans de l'eau tamponnée. La toxicité à court terme de l'Ag sur la photosynthèse d'algues vertes, *Chlamydomonas reinhardtii*, a été évaluée par fluorométrie. L'enrobage des nanoparticules dans un diélectrique réduit leur interaction avec l'environnement, et les protège d'une oxydation rapide. La libération d'Ag bio-disponible (impactant sur la photosynthèse des algues) est contrôlée par la profondeur à laquelle se trouvent les NPs d'Ag dans la matrice hôte de silice. Cette étude permet d'envisager le design de revêtements à effet biocide contrôlé. En couplant les propriétés antimicrobiennes de ces NPs d'Ag enrobées à leur qualité d'antenne plasmonique, ces nanocomposites peuvent être utilisés pour détecter et prévenir les premières étapes de la formation de biofilms sur des surfaces. Ainsi, une dernière partie de ce travail est dédiée à l'étude de la stabilité et de l'adsorption de protéines fluorescentes *Discosoma* rouges recombinantes (DsRed) sur ces surfaces diélectriques avec la perspective du développement de dispositifs SERS.